5-1-2017

Environmental Changes across the Early Mississippian Carbon Isotope Excursion

Dev Krishna Maharjan
University of Nevada, Las Vegas, devkmaharjan@gmail.com

ENVIRONMENTAL CHANGES ACROSS THE EARLY MISSISSIPPIAN CARBON ISOTOPE EXCURSION

By

Dev Krishna Maharjan

Bachelor of Science – Geology
Trichandra Campus, Nepal
1999

Master of Science – Geology
Tribhuvan University, Nepal
2001

Master of Science – Geology
University of Louisiana Lafayette
2010

A dissertation submitted in partial fulfillment
of the requirements for the

Doctor of Philosophy – Geoscience

Department of Geoscience
College of Science
The Graduate College

University of Nevada, Las Vegas
May 2017

UNLV | GRADUATE COLLEGE

Dissertation Approval

The Graduate College
The University of Nevada, Las Vegas

May 10, 2017

This dissertation prepared by

Dev Krishna Maharjan

entitled

Environmental Changes across the Early Mississippian Carbon Isotope Excursion

is approved in partial fulfillment of the requirements for the degree of

Doctor of Philosophy – Geoscience
Department of Geoscience

Ganqing Jiang, Ph.D.
Examination Committee Chair

Kathryn Hausbeck Korgan, Ph.D.
Graduate College Interim Dean

Stephen M. Rowland, Ph.D.
Examination Committee Member

Elisabeth M. Hausrath, Ph.D.
Examination Committee Member

Rosemarie Came, Ph.D.
Examination Committee Member

Paul Schulte, Ph.D.
Graduate College Faculty Representative

Abstract

Environmental changes across the Early Mississippian carbon isotope excursion

By

Dev Krishna Maharjan

Dr. Ganqing Jiang, Examination Committee Chair
Professor of Geology
University of Nevada, Las Vegas

The Early Mississippian K–O (Kinderhookian-Osagean) $\delta^{13}C$ excursion or TICE (mid-Tournaisian carbon isotope excursion) is characterized by an anomalous carbonate carbon isotope value of ≥5‰ that has been documented from numerous stratigraphic sections across the globe. This $\delta^{13}C$ excursion coincides with global cooling and sea-level fall and predicts a significant change in seawater chemistry. However, sulfate sulfur isotope data across the K-O $\delta^{13}C$ excursion reported in previous studies seem not to be responsive to the carbon cycle. Likewise, a recent study has documented a unidirectional increase in nitrogen isotopes across this excursion, which is not anticipated considering the amount of organic carbon burial required to form the prominent positive $\delta^{13}C$ excursion and its resultant oxygen increase and global cooling. This study aims to understand the coupling between carbon, nitrogen, sulfur and oxygen cycles at this critical transition.

This research uses Early Mississippian carbonate successions from Star Range (SR), Mountain Home Range (MH), and Pahranagat Range (PR) that indicate peritidal, shallow subidal to deep subtidal depositional environment in the Great Basin of western USA. Samples from these sections are analyzed for carbon isotopes ($\delta^{13}C$), sulfur isotopes ($\delta^{34}S$), nitrogen isotopes ($\delta^{15}N$) and oxygen isotopes ($\delta^{18}O$). Additionally, SR samples are analyzed for fluid inclusions,

REEs, major and trace element concentrations. Stratigraphic records from PR and MH sections indicate that the outer shelf section (PR) may be more representative of seawater isotope record. The $\delta^{34}S_{CAS}$ records a ≥7‰ positive anomaly near the peak of the K-O $\delta^{13}C$ excursion. Numerical modeling suggests that pyrite burial rates 5–10 times higher than that of the modern ocean are required to produce the observed $\delta^{34}S_{CAS}$ anomaly in a sulfate-rich Early Mississippian ocean. The aerial and volumetric expansion of sulfate reduction and pyrite burial was likely fused by abundantly available organic matter at the peak of the K-O $\delta^{13}C$ excursion when oxygen minimum zone (OMZ) in the ocean has substantially expanded. At the falling limb of the K-O $\delta^{13}C$ excursion, coupled negative shifts in $\delta^{34}S_{CAS}$ and $\delta^{18}O_{CAS}$ imply increase of sulfide reoxidation in the ocean and pyrite-derived riverine sulfate input, in response to global cooling, sea-level fall, and oxygenation resulted from enhanced organic carbon and pyrite burial, resulting in gradually decreasing the volume of OMZ. Such a change in ocean redox is reflected in the carbon and nitrogen cycles. Stratigraphic records indicate that the deeper-water outer shelf section (PR) show double spikes in both $\delta^{13}C_{carb}$ and $\delta^{13}C_{org}$ with a magnitude up to 7‰ and a negative shift down to 4‰ between the peaks which is more representative of the seawater isotope record. However, considering the sensitivity of $\delta^{15}N$ to redox conditions of depositional environments, the coupled $\delta^{13}C_{carb}$ – $\delta^{15}N$ pattern from the MH section may better record the isotope signature of the oceanic nitrate (NO_3^-) reservoir, while the decoupled $\delta^{13}C_{carb}$ – $\delta^{15}N$ in the PR section reflects involvement of local N-biochemical cycling in periodically developed suboxic-euxinic environments. The increase of $\delta^{15}N$ toward the peak of the K-O $\delta^{13}C$ excursion may record the expansion of oxygen minimum zone (OMZ) in the ocean that promotes water-column denitrification and ^{15}N enrichment in the marine nitrate (NO_3^-) reservoir. The decrease of $\delta^{15}N$ at the falling limb of the K-O $\delta^{13}C$ excursion reflects the shrink of the OMZ and reduces the

water-column denitrification in response to more oxygenated and cooler oceans resulting from enhanced organic carbon burial.

The significant amount of organic carbon burial during Early Mississippian results global cooling and possibly glaciation which is partly supported by the presence of highly depleted $\delta^{18}O$ values, down to –34‰, in SR samples. Block samples from SR and PR are studied for carbon and oxygen isotopes, fluid inclusion, REEs, major and trace elements to investigate the origin and processes involved during carbonate diagenesis. These geochemical data suggest that the carbonate diagenesis took place from a diagenetic fluid originated form freshwater. Importantly, SR samples are from close to or below the unconformity surfaces which may have been altered by glacial melt water with $\delta^{18}O$ values of $\leq$ –15‰. Then, it could have been further modified by a burial diagenesis with geothermal temperature < 200°C to produce the highly depleted $\delta^{18}O$ values down to –34‰. Collectively, carbon, nitrogen, sulfur and oxygen isotope records from Early Mississippian carbonates show a coupled variation in response to the environmental change during this time.

Acknowledgements

Accomplishment of this work has been only possible with the help of numerous honorable people. First, I would never forget to mention my own academic advisor, Dr. Ganqing Jiang, who always emphasizes me to explore a workable scientific problem for future goals. I heartily appreciate him that he allow me a significant amount of time to work on my dissertation with a continuous financial and moral support until the final phase of my dissertation. I also acknowledge my research committee members, Dr. Stephen Rowland, Dr. Elisabeth Hausrath, Dr. Rosemarie Came and a graduate college representative, Dr. Paul Schulte.

I would like to thank Dr. Jean Cline for allowing me to work in her laboratory and providing guidance to understand and collect the data from fluid inclusions from calcite. I also acknowledge Dr. Minghua Ren and Dr. Arya Udry for their help to work in their laboratory. Importantly, my gratitude goes to Dr. Yongbo Peng, Assistant Professor of Research at Louisiana State University, for his valuable time and assistance in sample analyses.

The never lasting memories in my dissertation field work had been accompanied by the "Carbonate Group" and I really appreciate Swapan Sahoo, Leon Taufani, Angel Ventrelli, and Andrew Miller for their valuable time and good moment during field work. Swapan and Leon were the companion during the search of good Mississippian carbonate sections across Utah and Nevada — without their effort the field work would not have been completed on time. I would also like to thank Jeevan Jayakody, Shaimaa Haleem and Zhoujun Xie for their good times during my study.

I acknowledge Maria, Liz, Cynthia and Maribel in the Geoscience department office at UNLV for their assistance and help in processing paper works during my study.

Finally, I am so lucky to have my parents who nurture my life with care and love, always supporting me to take the right way of success. Whatever gratitude I express in words to them is just a tiny. On the other hand, I am grateful to have my beloved wife, Kalpana, who understood my different feelings and situations during the study and gave me a continuous support by any means although she has been taking care of our children Denik and Keden.

Table of contents

List of tables

List of figures

Chapter 1

Introduction

The Early Mississippian marks a critical greenhouse-icehouse transition in Earth history and is characterized by one of the most prominent positive carbonate carbon isotope ($\delta^{13}C_{carb}$) excursions in the Phanerozoic. This $\delta^{13}C_{carb}$ excursion, termed as the K-O (Kinderhookian-Osagean) $\delta^{13}C$ excursion in North America and the TICE (mid-Tournaisian carbon isotope excursion) internationally, has a magnitude of ≥5‰ and has been documented from numerous stratigraphic sections across the globe (e.g., Bruckschen et al., 1999; Mii et al., 1999; Buggisch et al., 2008; Saltzman et al., 2004; Yao et al., 2015). The K-O $\delta^{13}C$ excursion has been interpreted as having formed by enhanced organic carbon burial that preferentially removes ^{13}C-depleted carbon, resulting in ^{13}C-enriched oceanic DIC (dissolved inorganic carbon) reservoir. If a significant amount of organic carbon have been buried during this interval, a remarkable decrease in CO_2 and increase in O_2 in the ocean and atmosphere would be expected to cause global cooling and glaciation, resulting in sea-level fall and changes in seawater chemistry.

Global cooling during the K-O interval is demonstrated by a ≥ 2‰ positive shift in oxygen isotope ($\delta^{18}O$) values across the K-O $\delta^{13}C$ excursion, which may have set the stage for the Late Paleozoic ice age (Mii et al., 1999; Buggisch et al., 2008). Direct evidence for glaciation during K-O $\delta^{13}C$ excursion is still rare, although in the Solimões Basin of northern Brazil locally developed diamictite is found slightly postdating this excursion (Caputo et al., 2008). In contrast, evidence of sea-level fall at or close to K-O boundary is apparent and has been documented from many stratigraphic sections globally (Ross and Ross, 1985; Swennen et al., 1986; Kalvoda, 1989; 2002; Isaacson et al., 1999; Hance et al., 2002; Haq and Al-Qahtani, 2005; Kammer and Matchen, 2008). In response to global cooling and sea-level fall, the ocean geochemical cycles

are expected to change during the K-O interval, particularly the interactions between carbon (C), sulfur (S) and nitrogen (N) cycles. Existing geochemical data from this interval, however, are mostly focused on the $\delta^{13}C_{carb}$ analyses (e.g., Saltzman et al., 2000; Saltzman, 2002, 2004; Katz et al., 2007; Buggsich et al., 2008). Other geochemical data, including sulfur and nitrogen isotopes, are sparsely available but their stratigraphic resolution and spatial distribution are insufficient to evaluate if coupled or decoupled C, S, and N biochemical cycles happened across this critical transition.

Existing carbonate associated sulfate ($\delta^{34}S_{CAS}$) data from the K-O interval are sparse and do not show significant temporal changes across the K-O $\delta^{13}C$ excursion (Kampschulte and Strauss, 2004; Gill et al., 2007). The invariable $\delta^{34}S_{CAS}$ was interpreted as recording the buffering effect of a large Mississippian oceanic sulfate pool (≥28 mM of SO_4^{2-}—the modern ocean sulfate concentration) (Gill et al., 2007). This interpretation, however, was based on a few data points from the Confusion Range section of western Utah where the Early Mississippian strata are highly condensed with potential stratigraphic discontinuities. To better constrain the sulfur isotope variation across the K-O $\delta^{13}C$ excursion, a dataset with higher resolution in stratigraphically more complete sections is needed.

Existing nitrogen isotope records from South China show a 3‰ unidirectional increase across the K-O $\delta^{13}C$ excursion that has been interpreted as recording the onset of a long-term shift in the locus of denitrification from continental shelf sediments to continental margin oxygen-minimum zone in response to cooling and sea-level fall (Algeo et al., 2014; Yao et al., 2015). This is in contrast to the nitrogen isotope response to Quaternary and Pleistocene glacial-interglacial cycles, during which water-column denitrification decreases rather than increases

during glaciation. Since the existing data are obtained from a single location, additional nitrogen isotope analyses are needed in a broad paleogeographic context.

Some unusually negative $\delta^{18}O_{carb}$ values are present in the Lower Mississippian strata (Katz et al., 2006) and have been interpreted as recording isotope signatures of hydrothermally modified, meteoric fluids. Similar low $\delta^{18}O_{carb}$ values are present in the geological record but are interpreted as signature of glacially-influenced seawater or meteoric water (Zhao et al., 2010; Zhou et al., 2013; Wang et al., 2014). In the southern Great Basin, unusually negative $\delta^{18}O$ values are present at different levels of the Mississippian strata and they show variations at macro- and micro-scales. Understanding the origin of these unusually negative $\delta^{18}O$ values may help to constrain the meteoric diagenetic environment and more importantly, the isotopic signature of surface water of the K-O interval.

My PhD dissertation study aims for obtaining an integrated carbon, oxygen, sulfur and nitrogen isotope record for the K-O internal in the southern Great Basin, western U.S.A. and for a better understanding of the Earth systems changes associated with a major perturbation of the global carbon cycle. The dissertation contains three chapters, each of which focuses on a paleoclimate-paleoceanographic isotope geochemical proxy.

Chapter 2 focuses on the sulfur cycle across the K-O $\delta^{13}C$ excursion. Paired carbonate associate sulfate (CAS) sulfur isotopes ($\delta^{34}S_{CAS}$), pyrite sulfur isotopes ($\delta^{34}S_{PY}$) and CAS oxygen isotopes ($\delta^{18}O_{CAS}$) across the K-O $\delta^{13}C$ excursion are obtained from a deeper-water outer shelf section in the Pahranagat Range (PR), Nevada, and a shallower water section in the Mountain Home Range (MH), Utah. The isotope records reveal ≥7‰ positive $\delta^{34}S_{CAS}$ anomaly near the peak of the K-O $\delta^{13}C$ excursion. The large magnitude and short duration (shorter than that of $\delta^{13}C$) of this positive $\delta^{34}S_{CAS}$ anomaly requires an unusual pyrite burial event that could happen

only if enhanced sulfate reduction and pyrite burial expanded from sediments to ocean water-column. Numerical modeling suggests that pyrite burial rates 5-10 times higher than that of the modern ocean are required to form the positive $\delta^{34}S_{CAS}$. The sulfur isotope data demonstrate a much more dynamic sulfur cycle than previously thought.

Chapter 3 discusses the organic carbon ($\delta^{13}C_{org}$) and nitrogen isotope ($\delta^{15}N$) changes across the K-O $\delta^{13}C$ excursion. Comparison of paired $\delta^{13}C_{carb}$ and $\delta^{13}C_{org}$ data from the deep-water PR section and shallow-water MH section suggest that the 7‰ magnitude and double spikes from the PR section are more representative of the K-O $\delta^{13}C$ excursion in the Great Basin and maybe in other sections globally. However, the coupled $\delta^{13}C_{carb}$–$\delta^{15}N$ pattern from the MH section may better record the N-isotope signature of the oceanic nitrate (NO_3^-) reservoir. Results suggest increase of water-column denitrification at or near the peak of the K-O $\delta^{13}C$ excursion and decrease of water-column denitrification afterwards, recording the expansion and shrink of oxygen-minimum zone (OMZ), respectively, in response to changes in organic carbon production and burial during the K-O carbon cycle.

Chapter 4 discusses the origin of unusually low $\delta^{18}O$ values (as low as –34‰) in Early Mississippian carbonates. In addition to $\delta^{13}C$ and $\delta^{18}O$ analyses, fluid inclusions and REE+Y data from block samples are used to understand the origin of depleted $\delta^{18}O$ values and to track the isotope composition of diagenetic fluids. Results suggest the low $\delta^{18}O$ values from fractured wackestones of the Pahranagat Range section were derived from deeply charged meteoric water alteration at geothermal temperatures up to 150°C. Samples along the unconformities from the Star Range section might have been altered by glacial melt water with $\delta^{18}O$ values ≤ –15‰ (SMOW), supporting glacial advance to low latitude during the Early Mississippian.

References

Algeo, T.J., Meyers, P.A., Robinson, R.S., Rowe, H., Jiang, G.Q., 2014. Icehouse-greenhouse variations in marine denitrification. Biogeosciences 11, 1273-1295.

Bruckschen, P., Oesmann, S., Veizer, J., 1999. Isotope stratigraphy of the European Carboniferous: proxy signals for ocean chemistry, climate and techonics. Chemical Geology 161, 127-163.

Buggisch, W., Joachimski, M.M., Sevastopulo, G., Morrow, J.R., 2008. Mississippian $\delta^{13}C_{carb}$ and conodont apatite $\delta^{18}O$ records− Their relation to the Late Palaeozoic Glaciation. Palaeogeography, Palaeoclimatology, Palaeoecology 268, 273-292.

Gill, B.C., Lyons, T.W., Saltzman, M.R., 2007. Parallel, high-resolution carbon and sulfur isotope records of the evolving Paleozoic marine sulfur reservoir. Palaeogeography, Palaeoclimatology, Palaeoecology 256, 156-173.

Hance, L., Devuyst, F.-X., and Poty, E., 2002. Sequence stratigraphy of the Belgium Lower Carboniferous—Tentative correlation with the British Isles, in: Hills, L.V., Henderson, C.M., and Bamber, E.W., (Eds.), Carboniferous and Permian of the World: Canadian Society of Petroleum Geologists Memoir 19, pp. 41–51.

Haq, B.U. and Al-Qahtani, A.M., 2005. Phanerozoic cycles of sea-level change on the Arabian Platform. Geoarabia 10, 127-160.

Isaacson, P., Hladil, J., Shen, J., Kalvoda, J., Grader, G., 1999. Late Devonian (Famennian) glaciation in South America and marine offlap on other continents. Abhandlungen-Geologischen Bundesanstalt 54, 239-258.

Kalvoda, J., 1989. Tournaisian events in Moravia (Czechoslovakia) and their significance. Courier Forschungsinstitut Senckenberg 117, 353–358.

Kalvoda, J., 2002, Late Devonian–Early Carboniferous Foraminiferal Fauna: Zonations, Evolutionary Events, Paleobiogeography and Tectonic Implications. Brno, Czech Republic, Folia, Geologia 39, Masaryk University, 213 p.

Kammer, T.W., Matchen, D.L., 2008, Evidence for eustasy at the Kinderhookian-Osagean (Mississippian) boundary in the United States: Response to late Tournaisian glaciation?, in: Fielding, C.R., Frank, T.D., and Isbell, J.L., (Eds.), Resolving the Late Paleozoic Ice Age in Time and Space: Geological Society of America Special Paper 441, pp. 261–274.

Kampschulte, A., Strauss, H., 2004. The sulfur isotopic evolution of Phanerozoic seawater based on the analysis of structurally substituted sulfate in carbonates. Chemical Geology 204, 255-286.

Katz, D.A., Eberli, G.P., Swart, P.K., Smith Jr, L.B., 2006. Tectonic-hydrothermal brecciation associated with calcite precipitation and permeability destruction in Mississippian carbonate reservoirs, Montana and Wyoming. American Association of Petroleum Geologist Bulletin 90, 1803-1841.

Katz, D.A., Buoniconti, M.R., Montañez, I.P., Swart, P.K., Eberli, G.P., Smith, L.B., 2007. Timing and local perturbations to the carbon pool in the lower Mississippian Madison Limestone, Montana and Wyoming. Palaeogeography, Palaeoclimatology, Palaeoecology 256, 231-253.

Mii, H.S., Grossman, E.L., Yancey, T.E., 1999. Carboniferous isotope stratigraphies of North America: Implications for Carboniferous paleoceanography and Mississippian glaciation. Geological Society of America Bulletin 111, 960-973.

Ross, C.A., Ross, J.R.P., 1985. Late Paleozoic Depositional Sequences are Synchronous and Worldwide. Geology 13, 194-197.

Saltzman, M.R., Gonzalez, L.A., Lohmann, K.C., 2000. Earliest Carboniferous cooling step triggered by the Antler Orogeny? Geology 28, 347-350.

Saltzman, M.R., Groessens, E., Zhuravlev, A.V., 2004. Carbon cycle models based on extreme changes in $\delta^{13}C$: an example from the lower Mississippian. Palaeogeography, Palaeoclimatology, Palaeoecology 213, 359-377.

Saltzman, M.R., 2002. Carbon and oxygen isotope stratigraphy of the Lower Mississippian (Kinderhookian-lower Osagean), western United States: Implications for seawater chemistry and glaciation. Geological Society of America Bulletin 114, 96-108.

Swennen, R., Bless, M.J., Bouckaert, J., Razina, T.P., Simakov, K.V., 1986. Evaluation of transgression-regression events in the Upper Famennian-Tournaisian strata of the southeastern Omolon area (NE-Siberia, USSR). Annales De La Société Géologique De Belgique 109, 237-248.

Wang, W., Zhou, C., Guan, C., Yuan, X., Chen, Z., Wan, B., 2014. An integrated carbon, oxygen, and strontium isotopic studies of the Lantian Formation in South China with implications for the Shuram anomaly. Chemical Geology 373, 10-26.

Yao, L., Qie, W., Luo, G., Liu, J., Algeo, T.J., Bai, X., Yang, B., Wang, X., 2015. The TICE event: Perturbation of carbon-nitrogen cycles during the mid-Tournaisian (Early Carboniferous) greenhouse-icehouse transition. Chemical Geology 401, 1-14.

Zhao, Y., Zheng, Y., 2010. Stable isotope evidence for involvement of deglacial meltwater in Ediacaran carbonates in South China. Chemical Geology 271, 86-100.

Zhao, Y.-Y., Zheng, Y.-F., 2013. Geochemical constraints on the origin of post-depositional fluids in sedimentary carbonates of the Ediacaran system in South china. Precambrian Research 224, 341-363.

Chapter 2

The dynamic sulfur cycle across the Early Mississippian positive $\delta^{13}C$ excursion*

Abstract

The Early Mississippian strata host a large positive carbon isotope ($\delta^{13}C$) excursion with a magnitude of ≥5‰ that has been documented from numerous successions across the globe. This $\delta^{13}C$ excursion, informally referred to as the TICE (mid-Tournaisian carbon isotope excursion) or K-O (Kinderhookian-Osagean) $\delta^{13}C$ excursion, coincides with global cooling and sea-level fall and predicts significant changes in weathering fluxes and the inventory of oceanic sulfate. However, sparsely available sulfate sulfur isotope data across the K-O $\delta^{13}C$ excursion in literature seem not to be responsive to the perturbation of the carbon cycle. To better understand the coupling of sulfur and carbon cycles at this critical transition, we have analyzed paired carbonate associate sulfate (CAS) sulfur isotopes ($\delta^{34}S_{CAS}$), pyrite sulfur isotopes ($\delta^{34}S_{PY}$) and CAS oxygen isotopes ($\delta^{18}O_{CAS}$) across the K-O $\delta^{13}C$ excursion from two sections in the southern Great Basin, western U.S.A. The two sections represent peritidal and outer shelf depositional environments of a west-dipping carbonate platform. Stratigraphic analyses indicate that isotope profiles from the outer shelf section may be more representative of the seawater isotope record. At the rising limb of the K-O $\delta^{13}C$ excursion, stable $\delta^{34}S_{CAS}$ and $\delta^{34}S_{PY}$ and constant sulfur isotope fractionations ($\Delta^{34}S = \delta^{34}S_{CAS} - \delta^{34}S_{PY}$) suggest that the sulfur cycle was "decoupled" from the carbon cycle, possibly due to the buffering effect of a large marine sulfate reservoir. A

This chapter is prepared as a manuscript for EPSL:
Dev Maharjan, Ganqing Jiang, and Yongbo Peng, The dynamic sulfur cycle across the Early Mississippian positive $\delta^{13}C$ excursion

7‰ positive $\delta^{34}S_{CAS}$ anomaly, accompanied by negative shifts in $\delta^{34}S_{PY}$, $\delta^{18}O_{CAS}$, and $\delta^{13}C$ and increase of $\Delta^{34}S$ up to 45‰, is found near the peak of the K-O $\delta^{13}C$ excursion. The large magnitude (≥7‰) and short duration (shorter than that of $\delta^{13}C$) of this positive $\delta^{34}S_{CAS}$ anomaly, if it is representative of seawater sulfate isotope signature, requires an unusual pyrite burial event that could happen only if enhanced sulfate reduction and pyrite burial expanded from sediments to ocean water column. The aerial and volumetric expansion of sulfate reduction and pyrite burial was likely fused by abundantly available organic matter at the peak of the K-O $\delta^{13}C$ excursion, during which organic carbon production and burial may have reached maximum and the oxygen minimum zone (OMZ) in the ocean has substantially expanded. Numerical modeling suggests that pyrite burial rates 5–10 times higher than that of the modern ocean are required to produce the observed $\delta^{34}S_{CAS}$ anomaly in a sulfate-rich Early Mississippian ocean. At the falling limb of the K-O $\delta^{13}C$ excursion, coupled negative shifts in $\delta^{34}S_{CAS}$ and $\delta^{18}O_{CAS}$ imply increase of sulfide reoxidation in the ocean and pyrite-derived riverine sulfate input, in response to global cooling, sea-level fall, and oxygenation resulted from enhanced organic carbon and pyrite burial. Collectively, the integrated carbon, sulfur, and CAS-oxygen isotope data demonstrate a much more dynamic sulfur cycle across the K-O $\delta^{13}C$ excursion than previously suggested.

Key words: sulfur isotopes, Early Mississippian, carbon isotope excursion, Great Basin, western United States

1. Introduction

The Early Mississippian (ca. 359–346 Ma) marks a transition from Late Devonian greenhouse climate to Permo-Carboniferous ice age (e.g., Beerling, 2002; Berner, 2003; Mii et al., 1999; Fielding et al., 2008; Grossman et al., 2008; Buggisch et al., 2008; Isbell et al., 2003,

2012; Montañez and Poulsen, 2013). During this critical transition a prominent positive carbon isotope ($\delta^{13}C$) excursion with a magnitude of ≥+5%, informally referred to as the TICE (mid-Tournaisian carbon isotope excursion; Yao et al., 2015) or K-O (Kinderhookian-Osagean) $\delta^{13}C$ excursion (Saltzman, 2002), has been documented from numerous sections across the globe (e.g., Budai et al., 1987; Bruckshen and Veizer, 1997; Saltzman, 2002, 2003a, 2003b; Saltzman et al., 2000; 2004; Katz et al., 2007; Buggisch et al., 2008; Qie et al., 2011). Temporally across the K-O $\delta^{13}C$ excursion, oxygen isotopes of brachiopod calcite (Mii et al., 1999; Grossman et al., 2008; Giles et al., 2012) and conodont apatite (e.g., Buggisch et al., 2008) suggest a 7–10ºC seawater temperature drop. Stratigraphic studies also document a major unconformity indicative of substantial sea-level fall at or near the peak of the K-O $\delta^{13}C$ excursion (e.g., Ross and Ross, 1985; Swennen et al., 1986; Kalvoda, 1989; 2002; Isaacson et al., 1999; Hance et al., 2002; Haq and Al-Qahtani, 2005; Kammer and Matchen, 2008). The coincidence of a positive $\delta^{13}C$ excursion, global cooling, and sea-level fall implies the coupling of the global carbon cycle and Early Mississippian climate change in general (e.g., Mii et al., 1999; Katz et al., 2007; Buggisch et al., 2008; Yao et al., 2015). However, the detailed relationship between perturbations of the carbon cycle and paleoclimate-paleoceanographic events remains largely unresolved.

A particular point related to the Early Mississippian carbon cycle is the sulfur isotope response to the increase of organic carbon burial and atmosphere-ocean oxygenation implied by the K-O $\delta^{13}C$ excursion. Conservative mass balance calculation suggested 7.5×10^{19} to 1.5×10^{20} g carbon burial associated with the K-O $\delta^{13}C$ excursion (Saltzman et al., 2004), which amounts to 1–3 times of the total global hydrocarbon reserves including oil, gas, and coals (~5,000 Gt C; 1 Gt = 10^{15} g carbon; Dickens et al., 1995). Because each mole of organic carbon burial would leave one mole of oxygen in the atmosphere and ocean, significant oxygen increase

and enhanced sulfide reoxidation across the K-O $\delta^{13}C$ excursion are expected. Meanwhile, because burial of organic carbon is commonly accompanied by pyrite burial (Berner and Canfield, 1989), the oceanic sulfate pool may also have changed significantly (e.g., Sim et al., 2015). Altogether it is anticipated that the sulfur isotopes of both carbonate associated sulfate ($\delta^{34}S_{CAS}$) and pyrite ($\delta^{34}S_{PY}$) would show large temporal variations across the K-O $\delta^{13}C$ excursion.

In contrast to these intuitive expectations, sparsely available $\delta^{34}S_{CAS}$ data across the K-O $\delta^{13}C$ excursion do not show notable temporal variations (Fig. 1; Strauss, 1997; Kampschulte and Strauss, 2004; Gill et al., 2007). The invariable $\delta^{34}S_{CAS}$ across the K-O $\delta^{13}C$ excursion was interpreted as recording a large Mississippian oceanic sulfate pool (≥28 mM of SO_4^{2-}—the modern ocean sulfate concentration) that may have been insensitive to changes in sulfur fluxes (Gill et al., 2007). This interpretation, however, is based on a few data points across the K-O $\delta^{13}C$ excursion in the Confusion Range of western Utah where the Early Mississippian strata are highly condensed with potential stratigraphic discontinuities (Giles and Dickinson, 1995). It is uncertain if the lack of $\delta^{34}S_{CAS}$ variation is due to insufficient sample resolution or a true record of an irresponsive, large Mississippian oceanic sulfate pool. Earlier $\delta^{34}S$ data from Mississippian whole-rock carbonates and brachiopods (Kampschulte and Strauss, 2004) and evaporites (Strauss, 1997) were also sparse and insufficient to evaluate the relationship between carbon and sulfur isotopes (Fig. 1).

To further explore the Early Mississippian sulfur cycle and in particular, to test the stability of sulfur isotopes in the Early Mississippian ocean, we have conducted paired $\delta^{34}S_{CAS}$–$\delta^{34}S_{PY}$ analyses across the K-O $\delta^{13}C$ excursion (or TICE) in two stratigraphic sections in the southern Great Basin, western United States (Fig. 2). We also report CAS oxygen isotope

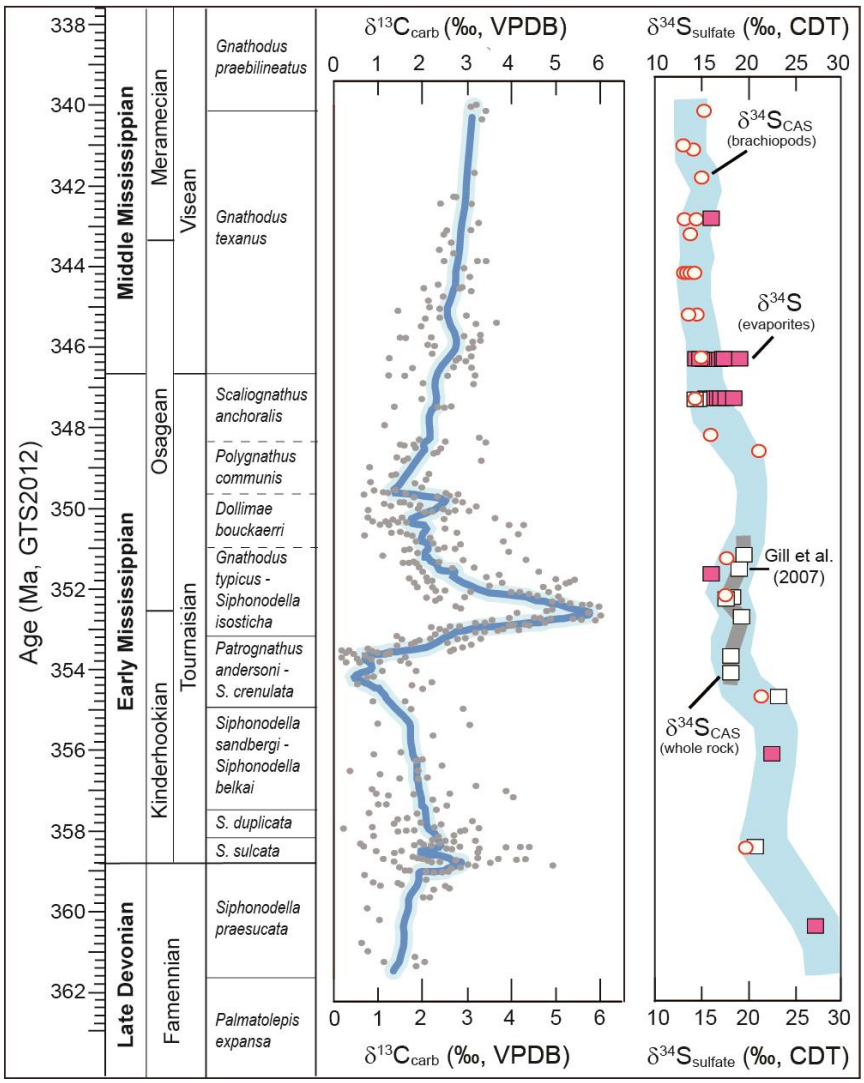

Fig. 1. Summary of available carbonate carbon ($\delta^{13}C_{carb}$) and sulfate sulfur ($\delta^{34}S_{sulfate}$) isotope data from latest Devonian to Early–Middle Mississippian (ca. 362–340 Ma). Existing data show no significant change in $\delta^{34}S_{sulfate}$ across the Kinderhookian-Osagean (K-O) or middle Tournaisian (TICE) $\delta^{13}C_{carb}$ excursion. Data source: $\delta^{13}C_{carb}$ data are from Buggisch et al. (2008); $\delta^{34}S$ data of evaporates are from Strauss (1997); whole-rock $\delta^{34}S_{CAS}$ across the K-O $\delta^{13}C_{carb}$ excursion are from Gill et al. (2007); $\delta^{34}S_{CAS}$ of brachiopods, whole-rock $\delta^{34}S_{CAS}$ in addition to Gill et al. (2007), and the overall $\delta^{34}S_{sulfate}$ trend are from Kampschulte and Strauss (2004).

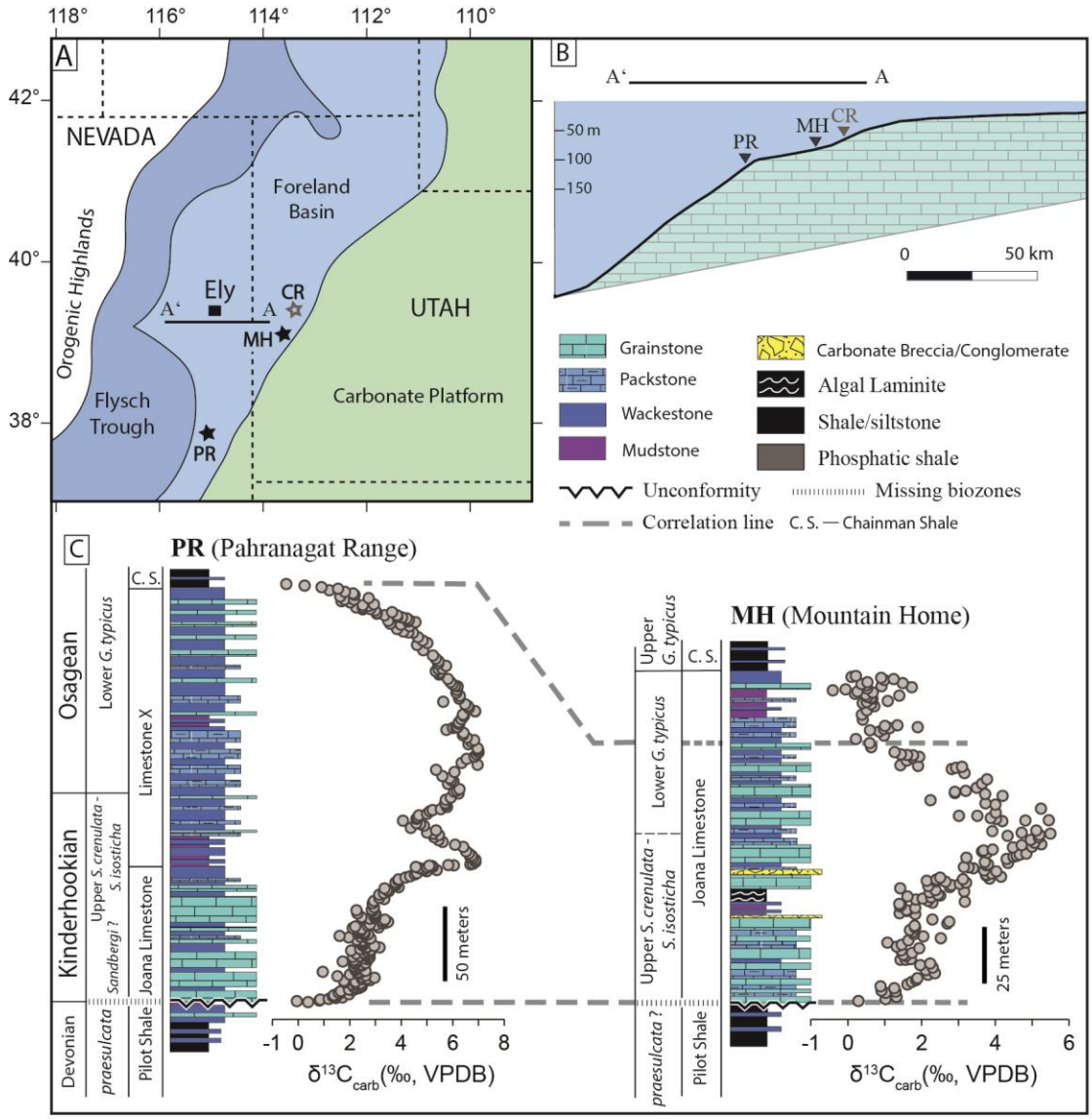

Fig. 2. (A) General paleogeographic reconstruction of the Antler foreland basin during Early Mississippian (Giles, 1996). PR–Pahranagat Range section near Alamo, Nevada; MH–Mountain Home section, western Utah; CR–Confusion Range section, western Utah, studied by Gill et al. (2007). (B) Relative paleogeographic position of studied sections across an east-to-west transect (line A–A') of the Early Mississippian carbonate ramp (after Giles, 1996). (C) Biostratigraphic (Singler, 1987; Poole and Sandberg, 1991) and $\delta^{13}C_{carb}$ chemostratigraphic (this study) correlation of the Pahranagat Range (PR) and Mountain Home (MH) sections.

($\delta^{18}O_{CAS}$) data from the same set of samples, which may provide constraints on the relative rates of sulfate reduction and sulfide reoxidation in the ocean and inputs from oxidative weathering of pyrites (e.g., Böttcher et al., 2001; Turchyn and Schrag, 2004; Bottrell and Newton, 2006; Antler et al., 2013; Schobben et al., 2015). The integration of carbon, sulfur, and oxygen isotope data allows to evaluate the sulfur isotope response to enhanced organic carbon/pyrite burial and oxygen increase implied by the K-O $\delta^{13}C$ excursion.

2. Geological background and stratigraphic sections

Early Mississippian strata in the southern Great Basin were deposited from a carbonate ramp in the craton side of the Antler foreland basin (Fig. 2; Giles, 1996). This foreland basin was developed over the early Paleozoic passive margin of western North America during the Antler orogeny (Late Devonian–Mississippian), when the Roberts Mountains allochthon thrust over the west-facing continental margin (Speed and Sleep, 1982). Cratonward thrusting formed a contractional belt extending over 2300 km from southern California to British Columbia (Smith et al., 1993) and flexural downwarping created accommodation space for the deposition of retrogradational Mississippian carbonate-shale sequences in the Great Basin (Giles and Dickinson, 1995; Giles, 1996).

We focus on two Early Mississippian sections (Fig. 2) at the Mountain Home (MH) Range of western Utah (GPS: N38º35′44.7″, W113º56′19.5″) and the southern Pahranagat Range (PR) near Alamo, Nevada (GPS: N37º23′35.7″, W115º16′5.4″). In both sections, the Early Mississippian Joana Limestone unconformably overlies the late Devonian Pilot Shale, with 1-3 earliest Mississippian conodont biozones missing (Singler, 1987; Poole and Sandberg, 1991; Giles, 1996). In the PR section (Fig. 2C), the 86-m-thick Joana Limestone is dominated by crinoid-rich grainstone and packstone, and the overlying 186-m-thick Limestone X consists

mainly of lime mudstone and wackestone, with subordinate packstone and grainstone interbeds. The contact between the Joana Limestone and Limestone X is marked by abrupt lithological change possibly recording a flooding surface. Yet evidence for subaerial exposure or erosion have not been observed at the transition. The Limestone X is overlain by siltstone, shale, and silty limestone of the Chainman Shale, but the contact is mostly covered in the studied section and its adjacent areas. Conodonts of upper *S. crenulata–S. isosticha* zone (Kinderhookian) and lower *G. typicus* zone (Osagean) were found from the upper Joana Limestone and Limestone X (Singler, 1987). Regional stratigraphic correlation suggested that the lower Joana Limestone may cover the *S. sandibergi*–lower *S. crenulata* zones (Poole and Sandberg, 1991; Giles, 1996).

In the MH section (Fig. 2C), the 152-m-thick Joana Limestone covers the upper *S. crenulata–S. isosticha* (Kinderhookian) and lower *G. typicus* (Osagean) conodont zones (Poole and Sandberg, 1991), but it is uncertain if the Devonian-Carboniferous boundary is located within the underlying Pilot Shale (Giles and Dickinson, 1995; Giles, 1996). The lower part (0–60 m) of the Joana Limestone consists mainly of packstone and grainstone, with wackestone, lime mudstone, and microbial limestone interbeds. Dissolution cavities and reworked karst breccias are seen at 40 m and 60 m, indicating subaerial exposure and potential erosion. The upper part (60–152 m) of the Joana Limestone shows decrease of grainstone and increase of wackestone and lime mudstone, indicating a shift toward deeper-water depositional environments (Giles, 1996). Abrupt change from cherty wackestone-packstone of the uppermost Joana Limestone to phosphatic shale of the Chainman Shale records a major flooding surface (Giles, 1996; Saltzman et al., 2004).

Previous studies have reported the K-O $\delta^{13}C$ excursion from the PR section (Saltzman et al., 2000; Saltzman, 2002), but in those studies isotope analyses did not cover the top of the

Limestone X and the uppermost $\delta^{13}C$ values (+4‰ to +4.5‰) in this section did not return back to pre-excursion $\delta^{13}C$ values (near 0‰). For the purposes of chemostratigraphic correlation and of obtaining paired carbon, sulfur, and CAS oxygen isotope data, we have re-sampled and analyzed the $\delta^{13}C$–$\delta^{18}O$ of the PR section at higher stratigraphic resolution. The new $\delta^{13}C$ profile of the PR section shows a complete K-O $\delta^{13}C$ excursion and $\delta^{13}C$ chemostratigraphic correlation with the MH section (Fig. 2C) indicates that the deposition of the Chainman Shale must have been strongly diachronous: the lower Chainman Shale in Pahranagat Range may be time-equivalent to the uppermost Joana Limestone in Mountain Home and other western Utah sections.

3. Analytical methods

We collected samples at ≤1 m resolution for carbonate carbon and oxygen isotope analyses. A total of 470 carbon and oxygen isotope analyses were conducted at the Las Vegas Isotope Science (LVIS) lab at the University of Nevada, Las Vegas, using a Kiel-IV carbonate device connected to a Delta V Plus mass spectrometer. Analytical reproducibility monitored by NBS-19 and an internal standard was better than 0.1‰ for both $\delta^{13}C_{carb}$ and $\delta^{18}O$ values (reported as in per mil relative to V-PDB).

Large samples were collected for sulfur isotope analyses from homogenous and thick beds, avoiding visible fractures, veins, and caliche. To minimize the potential modern atmospheric sulfate contamination to carbonate-associated sulfate (Peng et al., 2014), samples for sulfur isotope analyses were cut into slabs to remove any weathered surfaces: only the central, clean part of each sample is used for powdering and further analyses. About 200–500g clean samples were crushed to homogenous powders in a shatter box for subsequent chemical

extraction. For horizons that have sulfur isotope data, the carbonate carbon and oxygen isotope analyses used the same sample powders.

Sulfate extraction follows a modified procedure of Wotte et al. (2012). Sample powders (60–120 g) were immersed in 10% NaCl solution under constant magnetic stirring at room temperature overnight and repeat three to five times until no sulfate was present in filtered solutions. Rinsed samples were dissolved with 2N HCL to release carbonate associated sulfate (CAS). The solution was filtered in three steps using vacuum filtration and the filtrate was reacted with saturated barium chloride to precipitate barium sulfate. The barium sulfate powder was rinsed with deionized water and separated by centrifugation. All collected $BaSO_4$ samples were further purified with a DDARP method (Bao, 2006).

Acid insoluble residue from CAS extraction was rinsed with deionized water, dried at room temperature and homogenized for pyrite extraction, following the chromium reduction procedure specified in Canfield et al. (1986). Pyrite extraction was performed under nitrogen gas by addition of 6N HCI and 0.4M reduced chromium chloride solution. The reaction was proceeded for 2 hours to collect silver sulfide by allowing hydrogen *sulfide gas* to bubble through a sodium citrate buffer (pH = 4) into a silver nitrate (0.1 M) trap.

During sample preparation, we paid particular attention to obtain reliable sulfur and oxygen isotope data with multiple dissolution, rinse, and filtration steps. Some sulfate may have been lost through these steps and the absolute CAS concentration values may be lower than those obtained from a single dissolution-rinse-filtration step. Therefore, the CAS concentration data reported here should be used with caution: they may only record relative CAS abundances.

Sulfur isotope analyses of extracted sulfate and sulfide was conducted using a vario MICRO cube elemental analyzer coupled with an Isoprime 100 mass spectrometer in the Oxy-

Anion Stable Isotope Consortium (OASIC) at the Louisiana State University. Samples were loaded into tin capsules and combusted at 1000°C in the elemental analyzer. The combustion was catalyzed by ~2 mg of vanadium pentoxide and the resulting SO_2 is admitted to the mass spectrometer via a Conflow interface. Sulfur isotopes were calibrated using NBS-127, IAEA-S1, and IAEA-S3 and are reported in per mil (‰) relative to the V-CDT (Vienna Canyon Diablo Troilite). Reproducibility determined by NBS-127 and internal standards is better than 0.3‰.

The oxygen isotope composition of extracted barium sulfate was measured on CO produced through pyrolysis of each sample using a Temperature Conversion Elemental Analyzer (TC-EA) connected to a Thermo MAT 253 mass spectrometer. Results are reported in per mil (‰) relative to VSMOW (Standard mean ocean water). Reproducibility monitored by an internal standard is better than 0.3‰.

4. Results

Carbon isotope data from the PR section (Figs. 2C and 3A; Supplementary Table S1) show a complete K-O $\delta^{13}C$ excursion: $\delta^{13}C$ values rise from near 1‰ at the base of the Joana Limestone to highest values up to +7‰ in the lower-middle Limestone X and return back to pre-excursion values of ~1‰ near the top of the Limestone X. A secondary 'negative' shift with $\delta^{13}C$ values down to +4‰ occurs within the $\delta^{13}C$ plateau in the lower Limestone X. This feature has been reported in Saltzman et al. (2000) and Saltzman (2002), but their analyses did not reach the top of the K-O $\delta^{13}C$ excursion. Oxygen isotope values from this section mostly fall between –8‰ and –2‰; only a few samples have $\delta^{18}O$ values lower than –8‰ or higher than –2‰ (Fig. 5A). No significant $\delta^{13}C$–$\delta^{18}O$ co-variation is observed for the entire dataset or in any particular interval.

The $\delta^{34}S_{CAS}$ show stable values of 21–25‰ at the rising limb of the K-O $\delta^{13}C$ excursion; reach the highest values of 26–29‰ slightly after the first $\delta^{13}C$ peak; and have a 10‰ decrease down to 16–19‰ after the $\delta^{13}C$ peak (Fig. 3A). The $\delta^{34}S_{PY}$ values (5–14‰) are slightly more variable than $\delta^{34}S_{CAS}$ across the rising limb of the K-O $\delta^{13}C$ excursion and show a negative 'excursion' (down to –15.6‰) coincident with the secondary 'negative' $\delta^{13}C$ shift. Similar to $\delta^{34}S_{CAS}$, a negative shift in $\delta^{34}S_{PY}$ from 10–12‰ to 2–4‰ occurs at the falling limb of the $\delta^{13}C$ excursion. The sulfur isotope offset ($\Delta^{34}S = \delta^{34}S_{CAS} - \delta^{34}S_{PY}$) mostly fall between 10‰ and 20‰, with the exception of the basal Limestone X where $\Delta^{34}S$ reaches the highest value of 45‰. No $\delta^{34}S_{CAS}$–$\delta^{18}O_{carb}$ (R^2=0.02; Fig. 3B) or $\delta^{34}S_{CAS}$–$\delta^{34}S_{PY}$ (R^2<0.01; Fig. 3C) co-variation is observed. The $\delta^{18}O_{CAS}$ (Fig. 3A) show an increase from 16‰ to 22–24‰ toward the $\delta^{13}C$ peak, a negative 'excursion' parallel to that of $\delta^{34}S_{PY}$, and a decline down to 15–17‰ at the falling limb of the K-O $\delta^{13}C$ excursion. There is no correlation between $\delta^{18}O_{CAS}$ and $\delta^{18}O_{carb}$ (R^2=0.003; Fig. 3D), indicating that CAS and carbonate oxygen isotopes were derived from different sources and/or processes.

In the MH section (Figs. 2C and 4A; Table S1), the K-O $\delta^{13}C$ excursion starts with values of near 1‰ at the base of the Joana Limestone; reaches peak values of 5–5.5‰ in the middle; and returns back to near 0‰ in the upper Joana Limestone. Comparing with that of the PR section, the magnitude of the K-O excursion is 1.5–2‰ smaller and the double $\delta^{13}C$ spikes seen in PR are not present in this section. In addition, $\delta^{13}C$ return back to pre-excursion values about 40 m below the Chainman Shale/Joana Limestone contact, implying that the base of the Chainman Shale is not a synchronous time line across the southern Great Basin (Fig. 6). Carbonate oxygen isotope values fall between –8% and –2‰ and show no co-variation with $\delta^{13}C$

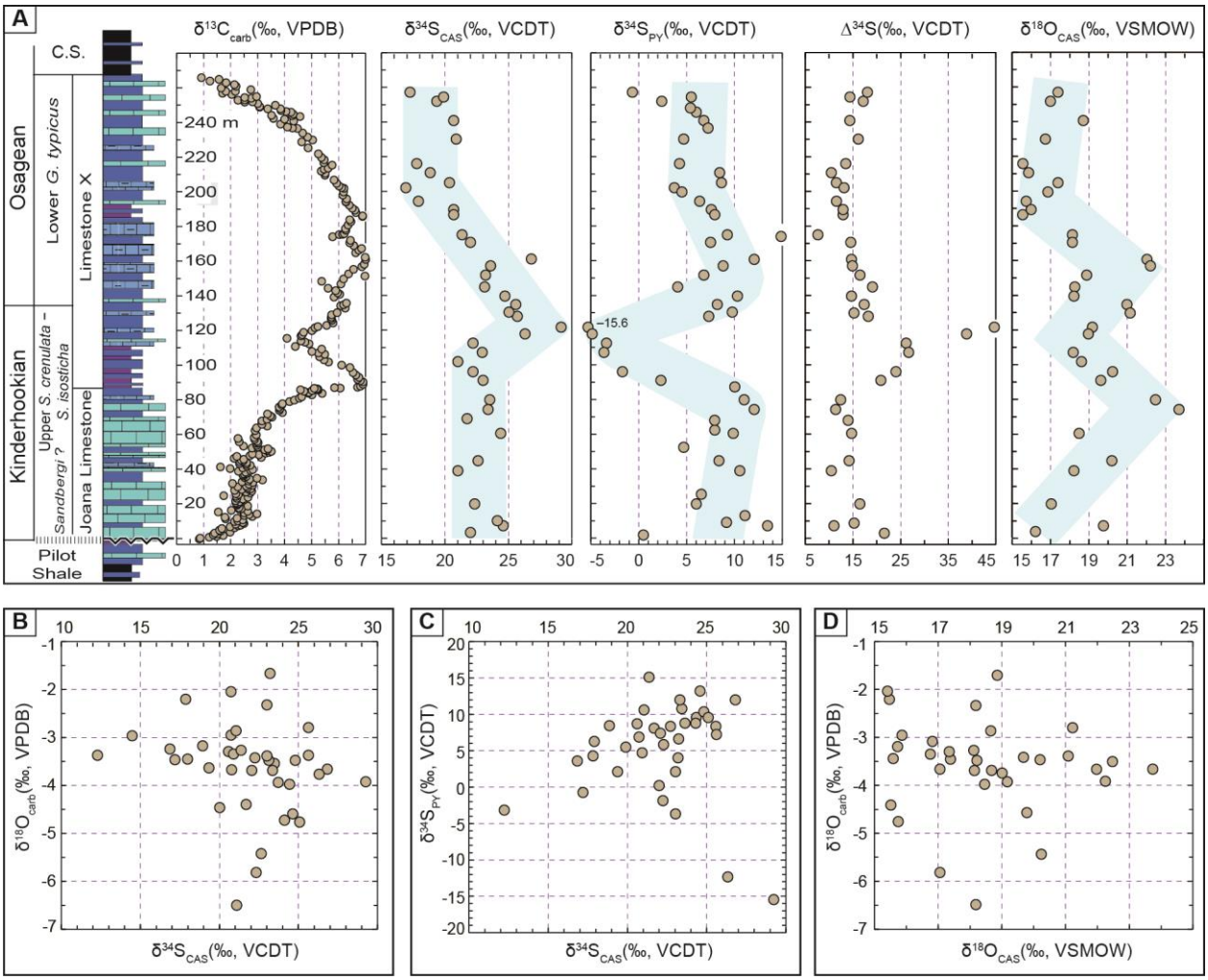

Fig. 3. (A) Carbonate carbon ($\delta^{13}C_{carb}$), carbonate-associate sulfur ($\delta^{34}S_{CAS}$), pyrite sulfur ($\delta^{34}S_{PY}$), and CAS oxygen ($\delta^{18}O_{CAS}$) isotope profiles from the Pahranagat Range section. The sulfur isotope difference ($\Delta^{34}S$) is calculated by $\Delta^{34}S = \delta^{34}S_{CAS} - \delta^{34}S_{PY}$. (B–D) Cross-plots of $\delta^{34}S_{CAS}$ vs. δ^{18}Ocarb (B), $\delta^{34}S_{CAS}$ vs. $\delta^{34}S_{PY}$ (C) and $\delta^{18}O_{CAS}$ vs. $\delta^{18}O_{carb}$ (D).

in general (R^2=0.22; Fig. 4B). However, the 20 m interval below the exposure surface (from 40 m to 60 m) has significant $\delta^{13}C$–$\delta^{18}O$ co-variation (R^2=0.54; Fig. 5C).

The magnitude of temporal $\delta^{34}S_{CAS}$ variations in the MH section is smaller than that of the PR section. Except for the two data points at the base of the Joana limestone that may be

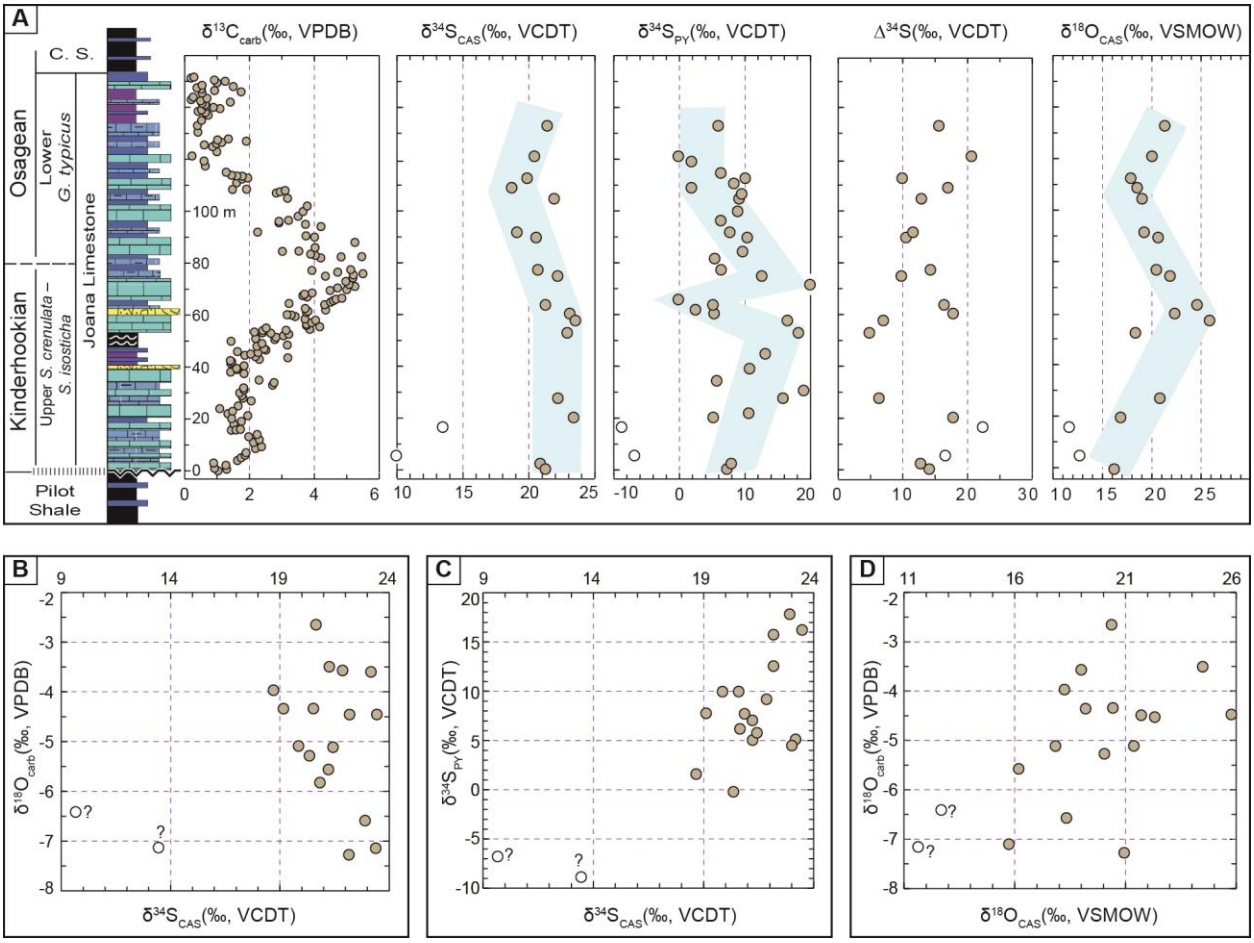

Fig. 4. (A) Carbonate carbon ($\delta^{13}C_{carb}$), carbonate-associate sulfur ($\delta^{34}S_{CAS}$), pyrite sulfur ($\delta^{34}S_{PY}$), $\Delta^{34}S$ ($\Delta^{34}S = \delta^{34}S_{CAS} - \delta^{34}S_{PY}$), and CAS oxygen ($\delta^{18}O_{CAS}$) isotope profiles from the Mountain Home section. (B–D) Cross-plots of $\delta^{34}S_{CAS}$ vs. $\delta^{18}O_{carb}$ (B), $\delta^{34}S_{CAS}$ vs. $\delta^{34}S_{PY}$ (C) and $\delta^{18}O_{CAS}$ vs. $\delta^{18}O_{carb}$ (D). The two data points with question mark (?) are possibly of diagenetic origin.

diagenetically altered (see below), most $\delta^{34}S_{CAS}$ values fall between 19‰ and 24‰. Although $\delta^{34}S_{CAS}$ show a decrease from 24% to 19‰ at the falling limb of the K-O $\delta^{13}C$ excursion, the magnitude of variation is ≤5‰. The $\delta^{34}S_{PY}$ show temporal variations similar to those of the PR section, including an increase in $\delta^{34}S_{PY}$ at the rising limb of the $\delta^{13}C$ excursion, a negative $\delta^{34}S_{PY}$ 'excursion' near the $\delta^{13}C$ peak, and an up to 10‰ decrease in $\delta^{34}S_{PY}$ across the falling limb of

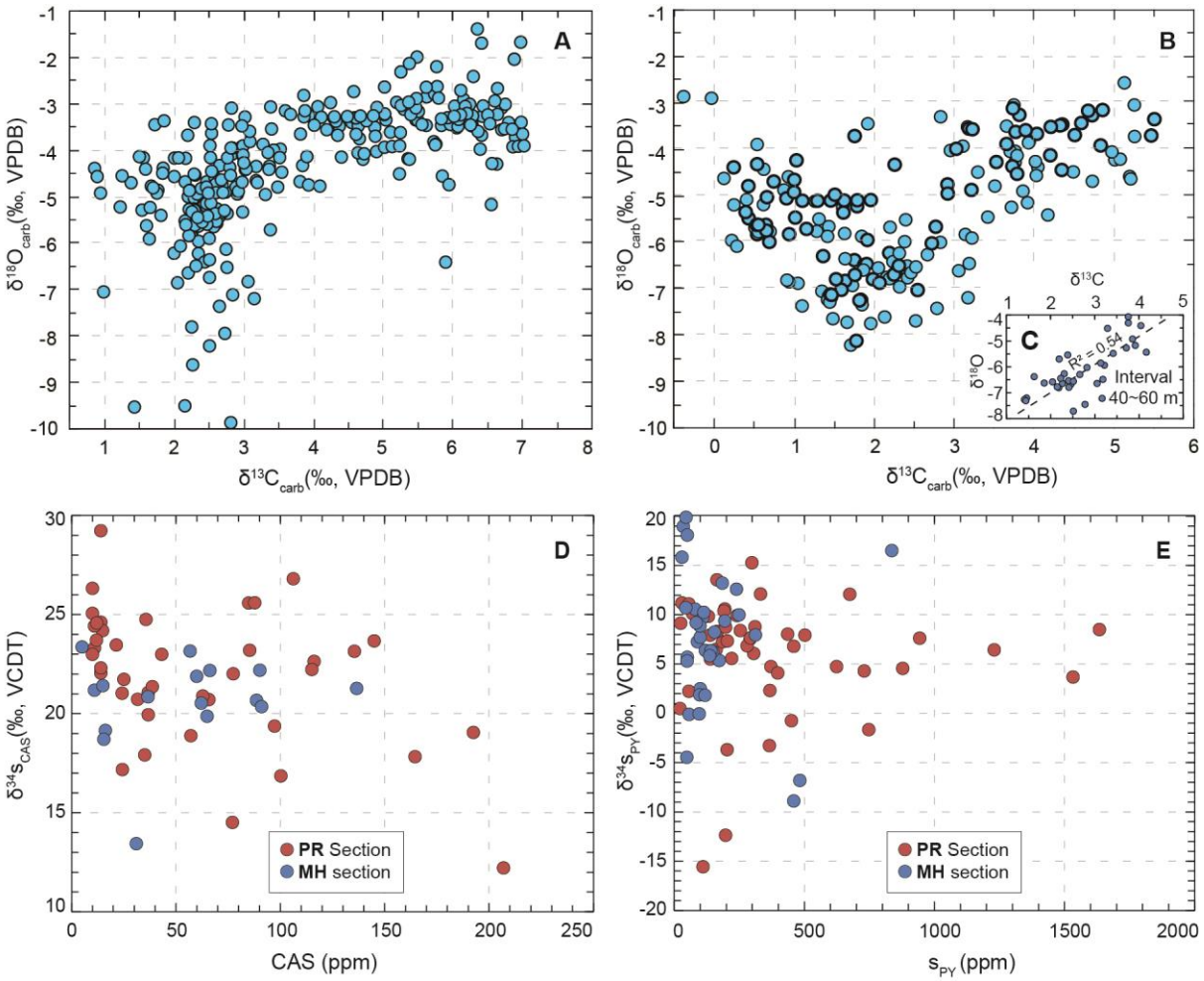

Fig. 5. Cross-plots of $\delta^{13}C_{carb}$ vs. $\delta^{18}O_{carb}$ from the Pahranagat Range (PR) section (A) and Mountain Home (MH) section (B). Overall there is no $\delta^{13}C$–$\delta^{18}O$ co-variation in both sections. However, in the MH section $\delta^{13}C$ and $\delta^{18}O$ show a weak co-variation (R^2=0.54) for the 20-m-thick interval (40–60 m) below a karst unconformity (inset in B). (C) Cross-plot of $\delta^{34}S_{CAS}$ vs. CAS concentrations from the PR (red dots) and MH (blue dots). (D) Cross-plot of $\delta^{34}S_{PY}$ vs. sulfide sulfur (S_{PY}) concentrations from the PR (red dots) and MH (blue dots). No co-variation between sulfur isotopes and sulfate/sulfide concentrations is observed.

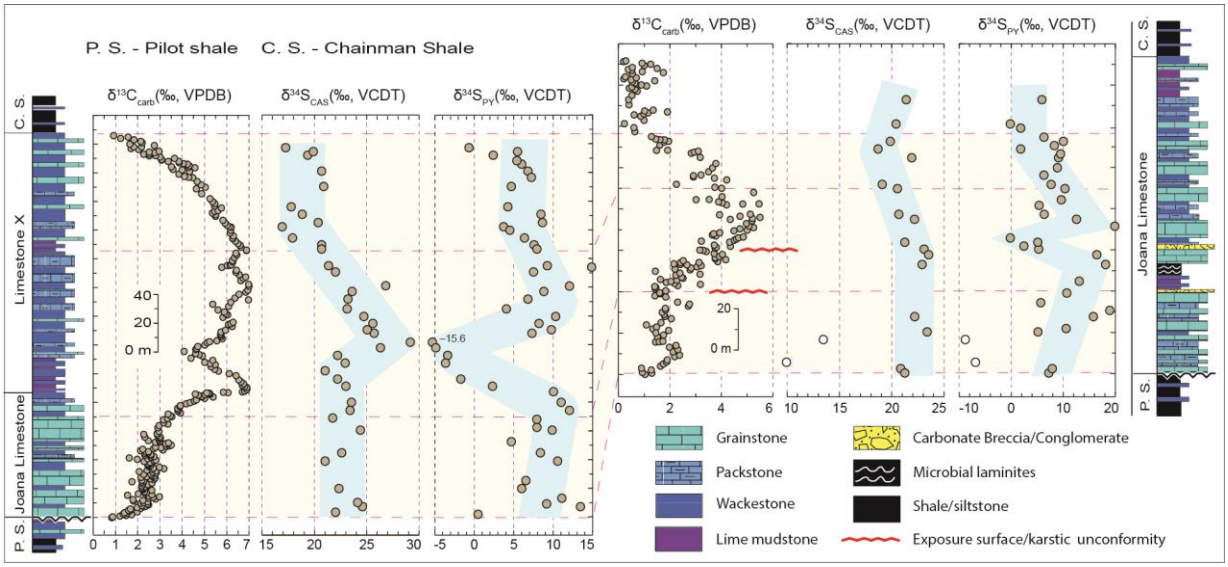

Fig. 6. Comparison of carbon and sulfur isotope profiles between Pahranagat Range (left panel) and Mountain Home (right panel) sections. Although the general trend of $\delta^{13}C_{carb}$, $\delta^{34}S_{CAS}$ and $\delta^{34}S_{PY}$ are similar, the magnitude of temporal $\delta^{13}C$ and $\delta^{34}S$ changes in the Pahranagat Range (PR) is much larger than those in the Mountain Home (MH) section. The presence of karstic unconformities at 40 m and 60 m in the MH section, the overall shallow-water facies, and the much smaller stratal thickness (152 m in MH vs. 270 m in PR for the $\delta^{13}C_{carb}$ excursion) raise the possibility that the smaller magnitude of $\delta^{13}C$ and $\delta^{34}S$ variations in the MH sections is due to incomplete stratigraphic record (erosion or condensed strata). In this case, the isotope record in the PR section (left panel) may be more representative of the seawater isotope signature across the K-O $\delta^{13}C$ excursion. The dashed correlation lines are tentative on the basis of the $\delta^{13}C_{carb}$ excursion and facies change and a comprehensive sequence stratigraphic study is required to confirm.

the $\delta^{13}C$ excursion (Fig. 5A). The $\Delta^{34}S$ mostly fall between 10‰ and 20‰, except for the few data points below the exposure surface at 60 m. No obvious co-variation is observed among $\delta^{18}O_{carb}$, $\delta^{34}S_{CAS}$, and $\delta^{34}S_{PY}$ (Fig. 5B and C). The $\delta^{18}O_{CAS}$ show a 10‰ increase from 16‰ to 26‰ toward the $\delta^{13}C$ peak and 8‰ decrease in the falling limb of the $\delta^{13}C$ excursion (Fig. 5A). Similar to that of the PR section, no significant $\delta^{18}O_{CAS}$–$\delta^{18}O_{carb}$ co-variation is observed.

5. Discussions

5.1. Preservation of primary isotope signatures

Significant temporal variations in $\delta^{13}C$, $\delta^{34}S_{CAS}$, and $\delta^{18}O_{CAS}$ are observed from both PR and MH sections (Figs. 3, 4, and 6), but the magnitude of isotope changes differs between the two sections, raising concerns about potential diagenetic alteration of isotope signatures. Numerous studies have discussed about meteoric and burial diagenetic alterations of $\delta^{13}C_{carb}$ and concluded that in most cases, $\delta^{13}C_{carb}$ values are rock buffered because carbon is a major element in carbonates but a trace element in diagenetic fluids (e.g., Banner and Hanson, 1990; Kaufman et al., 1991; Kaufman and Knoll, 1995; Jacobson and Kaufman, 1999). Exceptions may include meteoric and burial diagenetic environments with high fluid/rock ratios that reset $\delta^{18}O_{carb}$ to that of the fluids and partially alter $\delta^{13}C_{carb}$ values (invariable $\delta^{18}O_{carb}$ with variable $\delta^{13}C_{carb}$; Allen and Matthews, 1982; Swart, 2015) or diagenetic environments that result in co-varying $\delta^{13}C_{carb}$ and $\delta^{18}O_{carb}$ (e.g., Jacobson and Kaufman, 1999; Derry, 2010; Oehlert and Swart, 2014; Swart, 2008, 2015). In general, variable $\delta^{18}O_{carb}$ values and the lack of $\delta^{13}C_{carb}$–$\delta^{18}O_{carb}$ co-variation (Fig. 5A and B), plus the persistence of the K-O $\delta^{13}C$ excursion across the globe (e.g., Mii et al., 1998; Saltzman 2002, 2003; Saltzman et al., 2000; 2004; Buggisch et al., 2008; Yao et al., 2015), all suggest $\delta^{13}C$ signature close to that of ancient seawater. However, the co-varying $\delta^{13}C_{carb}$–$\delta^{18}O_{carb}$ below the exposure surface (interval 40–60 m; Figs. 5C and Fig. 6) in the MH section suggests at least partial diagenetic alteration and potentially, stratigraphic truncation that may have caused the absence of the double $\delta^{13}C$ spikes seen in the PR section.

Diagenetic alteration of $\delta^{34}S_{CAS}$ and $\delta^{18}O_{CAS}$ is not fully understood, but past work has shown that $\delta^{34}S_{CAS}$ trends are well preserved in Precambrian-Paleozoic stratigraphic successions (e.g., Kampschulte et al., 2001; Kah et al., 2004; Kampschulte and Strauss, 2004; Gill et al.,

2011; Jones and Fike, 2013; Sim et al, 2015). Seawater $\delta^{34}S_{CAS}$ may be altered during burial diagenesis when bacterial sulfate reduction (BSR) progressively enriches ^{34}S in pore water sulfate that, if it is fully incorporated into CAS, would project a maximum $\delta^{34}S_{CAS}$ increase up to +9‰ (Swart, 2015). However, the actual $\delta^{34}S_{CAS}$ changes through pore-water BSR are much smaller than the modeled maximum value (e.g., Rennie and Turchyn, 2014) because (1) at shallow burial depth close to the seawater-sediment interface, pore-water sulfate exchanges with that of the overlying seawater (e.g., Antler et al., 2013) and (2) at deeper burial depth, quantitative or near quantitative sulfate reduction in pore water would eventually diminish sulfur isotope fractionation (leading to low $\Delta^{34}S$) and taper off $\delta^{34}S_{CAS}$ change (Sim et al., 2011; Fike et al., 2015; Gomes and Hurtgen, 2015; Sim et al., 2015). Observations from modern environments also confirm that seawater $\delta^{34}S_{CAS}$ are mostly preserved in carbonates that host active BSR and authigenic carbonate precipitation (Lyons et al., 2004). Thus, the positive $\delta^{34}S_{CAS}$ shift with high $\Delta^{34}S$ seen in the PR section (in Fig. 3A) is unlikely an artifact resulting from pore-water sulfate reduction. This notion is further supported by the negative $\delta^{18}O_{CAS}$ shift at the same stratigraphic level because pore-water sulfate reduction increases rather than decreases $\delta^{18}O_{CAS}$ in both shallow and deep water environments (Antler et al., 2013).

Meteoric diagenesis may lower CAS concentrations of carbonates, but previous studies indicated that it has little or no effect on $\delta^{34}S_{CAS}$ (Gill et al., 2008). The CAS concentrations in both PR and MH sections are generally low (mostly 15–250 ppm; but see methods section for potential sulfate loss through multiple rinsing and purification steps) and a significant portion of samples (particularly in the MH section) do not have enough sulfate for $\delta^{34}S_{CAS}$ analyses (Table S1). However, there is no $\delta^{34}S_{CAS}$–CAS (Fig. 5D) and $\delta^{18}O_{carb}$–$\delta^{34}S_{CAS}$ (Figs. 3B and 4B) correlation that may indicate $\delta^{34}S_{CAS}$ change through diagenetic loss of CAS. The range of

$\delta^{34}S_{CAS}$ values (mostly 15–25‰) from the PR and MH sections are also similar to those reported from diagenetically screened, well-preserved Early Mississippian brachiopods and evaporites (Fig. 1; Strauss, 1997; Kampschulte et al., 2001; Kampschulte and Strauss, 2004), supporting the preservation of seawater or near-seawater $\delta^{34}S_{CAS}$ signature.

Pyrite reoxidation during exposure or artificial incorporation of contaminant sulfate during sample preparation may lower $\delta^{34}S_{CAS}$ values (Marenco et al., 2008; Peng et al., 2014). The few samples that have anomalously low $\delta^{34}S_{CAS}$ values away from the general trend in the MH section (e.g., MH-5.7 and MH-15.7; Fig. 4) may fall into this category, but the general lack of correlation between $\delta^{34}S_{CAS}$ and S_{PY} ($R^2<0.1$; Table S1) and high $\Delta^{34}S$ values across the $\delta^{34}S_{CAS}$ maximum do not support a systematic shift from pyrite-derived sulfate contamination. Similarly, the lack of $\delta^{18}O_{CAS}$–$\delta^{18}O_{carb}$ correlation and the similar absolute $\delta^{18}O_{CAS}$ values in two sections (Figs. 3 and 4) suggest an overall preservation of CAS oxygen isotope signature. Collectively, we believe that primary or near primary $\delta^{34}S_{CAS}$, $\delta^{34}S_{PY,}$ and $\delta^{18}O_{CAS}$ trends are preserved in the PR and MH sections. Diagenesis may be the cause of the 2–4‰ scatter within the isotope trends (Figs. 3 and 4) and the few outliers distinct from the temporal trends (cf. Marenco et al., 2013; Rennie and Turchyn, 2014).

5.2. Spatial variation of isotope trends

If the isotope trends (Figs. 3 and 4) record temporal changes of primary or near primary seawater signature, the variable magnitude of isotope excursions between the two sections raises questions about their representativeness of the seawater isotope record. This is particularly evident for $\delta^{34}S_{CAS}$: In the PR section, $\delta^{34}S_{CAS}$ increase from ~23‰ to ~29‰ within a 20-m-thick interval, followed by a 11‰ decrease from ~29‰ to ~18‰ in the next 80 m; while in the MH section, $\delta^{34}S_{CAS}$ changes are within 5‰ (Fig. 6). The smaller magnitude of $\delta^{34}S_{CAS}$ change

across the K-O $\delta^{13}C$ excursion in the MH section is comparable with that documented from the Confusion Range, western Utah (Fig. 7; Gill et al., 2007). Potential causes of such spatial isotope variations (Figs. 6 and 7) may include (1) local isotope departure from average seawater signature or (2) incomplete isotope record in proximal, shallow-water sections due to non-deposition, stratigraphic truncation, and low sample resolution.

Current stratigraphic observations seem to favor the second interpretation. The larger $\delta^{34}S_{CAS}$ and $\delta^{34}S_{PY}$ variations in the distal section at PR (Fig. 3) are obtained from fine-grained lime mudstone and wackestone that were deposited below fair-weather wave base, from which no exposure surface has been observed. In contrast, exposure surface and karst unconformity near the $\delta^{13}C$ peak are common in the proximal shallow-water section at MH (Figs. 4 and 6). Particularly, the karst unconformity expressed by locally reworked karst breccias at 60 m in the MH section (Fig. 8) seems to be a regional unconformity that has been documented in other proximal sections in western Utah (Giles, 1996). Although the amount of stratigraphic truncation by this unconformity requires further investigation, its influence on the $\delta^{13}C_{carb}$ values of underlying strata is demonstrated by the $\delta^{13}C_{carb}$–$\delta^{18}O_{carb}$ co-variation (R^2=0.54) in the MH section (Fig. 5C) and by the abrupt $\delta^{13}C_{carb}$ change in the Confusion Range section (Fig. 7). In addition, reworking of sediments in proximal shallow-water (above storm wave base) environments could have also contributed to the relatively more scatted $\delta^{34}S_{PY}$ and smaller $\Delta\delta^{34}S$ values seen in the MH section (c.f., Aller et al., 2010; Fike et al., 2015). For these reasons, we consider that the isotope record from the PR section (Fig. 3) may be more complete and better reflect seawater chemical changes. Therefore, in the following discussions we focus on the isotope record from the PR section, but keep in mind that if future studies confirm that the PR

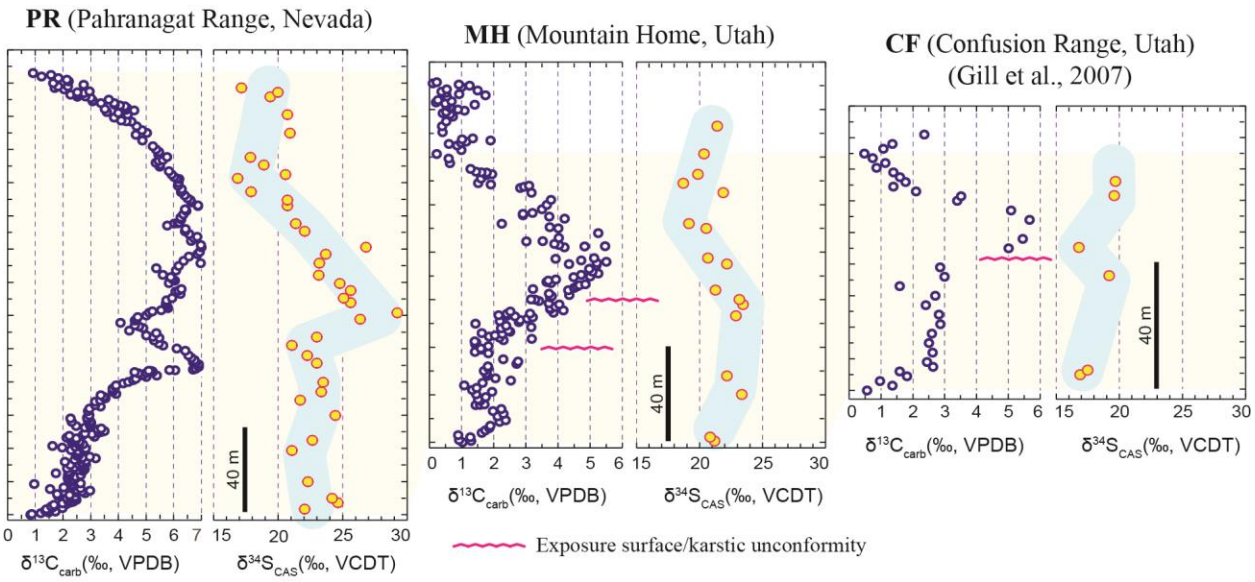

Fig. 7. Comparison of $\delta^{13}C_{carb}$ and $\delta^{34}S_{CAS}$ profiles from the PR and MH sections with those from the Confusion Range section (CF; Gill et al., 2007). The presence of karstic unconformities and the significantly smaller thickness across the K-O $\delta^{13}C$ excursion in both MH and CF sections seem to support that the $\delta^{13}C_{carb}$ and $\delta^{34}S_{CAS}$ profiles from the PR section are more complete and more representative of the temporal changes in seawater isotope signature.

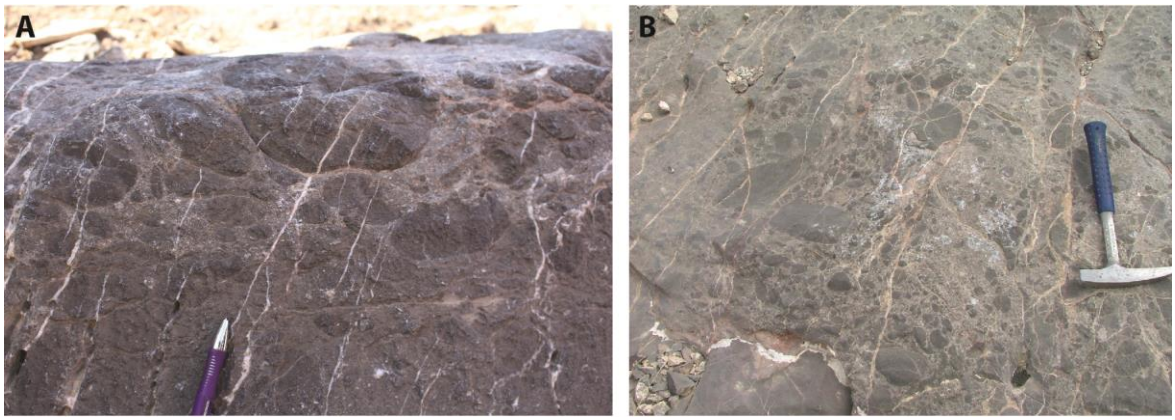

Fig. 8. Field photographs of the paleokarst breccias at 60 m of the Mountain Home section (See Figs. 2 and 4 for stratigraphic position). (A) Profile view of the karst breccia. (B) Surface view of the karst breccia. Pencil (12 cm long) and hammer (33 cm long) for scale.

isotope changes record local departure from average seawater signature, the interpretations are justifiable.

5.3. Interpreting the temporal sulfur isotope changes

The $\delta^{34}S$ of the marine sulfate reservoir is controlled by the rate and isotope composition of sulfur fluxes into and out of the ocean. The primary sulfur inputs to the oceans are riverine sulfate resulting from weathering of sulfide- and sulfate-bearing minerals and emissions from volcanic/hydrothermal systems (Bottrell and Newton, 2006; Fike et al., 2015). Riverine and hydrothermal sulfate has $\delta^{34}S$ values in the range of 0–8‰, which are much lower than that of the marine sulfate reservoir ($\delta^{34}S \approx 20‰$). Therefore, enhanced riverine and/or hydrothermal sulfate input, if its effect exceeds that of the sulfur outputs, may cause a negative shift in $\delta^{34}S$ values of the marine sulfate reservoir. The major sulfur outputs of the ocean are through the burial of calcium sulfate (gypsum, barite, and CAS) and pyrite in sediments. Because the precipitation of calcium sulfate from seawater involves minimal isotope fractionation (1–2‰; Raab and Spiro, 1991), burial of calcium sulfate has limited impact on the seawater sulfur isotope composition. In contrast, pyrite burial may result in positive shift in $\delta^{34}S$ of seawater sulfate because pyrite formed through microbial sulfate reduction has $\delta^{34}S$ values 4–66‰ lower than its original sulfate (Canfield, 2001; Canfield et al., 2010; Sim et al., 2011). Within this framework, the positive shift in $\delta^{34}S_{CAS}$ across the K-O $\delta^{13}C$ excursion (Fig. 3) can be interpreted as resulting from enhanced pyrite burial, whereas the subsequent negative $\delta^{34}S_{CAS}$ shift may record greater contributions from riverine sulfate input, particularly sulfide-derived sulfate.

While such a simple interpretation seems to be consistent with enhanced organic carbon burial that has driven the K-O $\delta^{13}C$ excursion (Saltzman et al., 2000, 2004) because organic carbon and pyrite burial is often closely associated (Raiswell and Berner, 1986), the shorter

duration of the positive $\delta^{34}S_{CAS}$ anomaly (Fig. 3) contradicts with the reservoir size and response time of carbon and sulfur. In spite of the many similarities in carbon and sulfur cycles in modern oceans (Fike et al., 2015), the marine sulfate reservoir (~1.3×10^{21} g of S; Bottrell and Newton, 2006) is much larger than the dissolved inorganic carbon (DIC) reservoir (~3.8×10^{19} g of C; Dickens, 1995). In contrast, the annual flux of carbon (~1.5×10^{15} g C/yr) into and out of the ocean is much larger than the sulfur fluxes (~1.0×10^{14} g S/yr). As a result, the response time of the oceanic sulfate reservoir (10^7 years) is much longer than that of the DIC reservoir (10^5 years), except for the times in early Earth history when the sulfate reservoir was much smaller than that of the modern ocean (Kah et al, 2004; Algeo et al., 2015; Gomes and Hurtgen, 2015). Steady-state modeling of the sulfur cycle across the positive $\delta^{13}C$ excursions of late Cambrian (Gill et al., 2011), late Ordovician (Jones and Fike, 2013), late Devonian (Sim et al., 2015), and Cretaceous (Owens et al., 2013) all demonstrated a delayed $\delta^{34}S$ response to $\delta^{13}C$ changes when sulfate concentrations are higher than 5 mM. The faster change in $\delta^{34}S_{CAS}$ near the peak values of the K-O $\delta^{13}C$ excursion requires either low sulfate concentrations (<5 mM; Gomes and Hurtgen, 2015; Sim et al., 2015) or a dynamic sulfur cycle that involves change in sulfur isotope fractionation (Jones and Fike, 2013) and pyrite formation/burial through water column sulfate reduction, instead of sulfate reduction primarily within sediments like in the modern ocean (Fike et al., 2015). Although the size of the marine sulfate reservoir is believed to have been highly variable over Earth history (Kah et al., 2004; Halevy et al., 2012; Wortmann and Paytan, 2012; Gomes and Hurtgen, 2015), low oceanic sulfate concentration (<5 mM) during the Mississippian seems less likely because most of the modeling results based on geological and geochemical data portray high atmospheric pO_2 and well-oxygenated Mississippian oceans (Berner and Canfield, 1989; Kampschulte et al., 2001, 2004; Berner, 2004, 2006; Gill et al., 2007).

The marked increase of $\Delta^{34}S$ associated with the positive $\delta^{34}S_{CAS}$ anomaly and the opposite $\delta^{34}S_{CAS}$ and $\delta^{34}S_{PY}$ trends (Fig. 3) provide constraints for a dynamic sulfur cycle. Changes in $\Delta^{34}S$ during microbial sulfate reduction (MSR) are related to sulfate concentrations, sulfate reduction rates, and sulfur recycling through sulfide reoxidation and sulfur disproportionation. In general, high sulfate concentration (>1 mM or unlimited sulfate supply; Habicht et al., 2002; Canfield et al., 2010; Sim et al., 2011), low sulfate reduction rate (e.g., Habicht and Canfield, 2001; Sim et al., 2011; Wing and Halvey, 2014), and active sulfur recycling (Canfield and Teske, 1996) can result in larger sulfur isotope fractionation or $\Delta^{34}S$, but none of these factors acts to increase pyrite burial required for a positive $\delta^{34}S_{CAS}$ shift. This implies the decoupling of factors that influence the sulfur isotope fractionation from pyrite burial (e.g., Levitt et al., 2013). The increase of $\Delta^{34}S$ and $\delta^{34}S_{CAS}$ occurs at the peak of the K-O $\delta^{13}C$ excursion, presumably the time interval of highest organic carbon production and burial. The most parsimonious scenario would be that high primary production significantly expanded the oxygen minimum zone (OMZ) and abundantly available organic carbon fueled sulfate reduction (cf. Leavitt et al., 2013) in the ocean water column instead of only in the sediments, resulting in a pyrite burial event and a positive $\delta^{34}S_{CAS}$ shift. Active sulfate reduction in sulfate-replete OMZ produced sulfides and elemental sulfur that went through reoxidation and disproportionation and eventually produced ^{34}S-depleted pyrites. In sulfide-enriched environments, sulfate reduction rate is unnecessarily much higher than the early stages due to the toxicity of H_2S to sulfate reduction. Laboratory and modeling studies indicated that high H_2S concentrations may slow down the sulfate reduction rate and increase the isotope fractionation (e.g., Reis et al., 1992; Oleszkiewicz et al., 1989; Cooney et al., 1996; Wing and Halevy, 2014). Thus, the combined effects of oxidative recycling of sulfur species and moderate sulfate reduction rates (e.g., cell-

specific sulfate reduction rates or csSRR ≤5 fmol $H_2S.cell^{-1}d^{-1}$; Wing and Halevy, 2014) explain the negative shift in $\delta^{34}S_{PY}$ and the positive shift in $\Delta^{34}S$. Subsequent reoxidation and shrink of the expanded OMZ, possibly caused by cooling and increased oxygenation due to organic carbon and pyrite burial, add sulfide-derived sulfate to the ocean and quickly shift the $\delta^{34}S_{CAS}$ and $\delta^{34}S_{PY}$ back to background values.

The dynamic sulfur cycle is supported by the negative $\delta^{13}C$ shift accompanying the sulfur isotope anomalies (Fig. 3). The expansion of OMZ and sulfate reduction adds ^{13}C-depleted bicarbonate to the ocean ($SO_4^{2-} + 2CH_2O \rightarrow H_2S + 2HCO_3^-$), lowering the $\delta^{13}C$ values of DIC and carbonates precipitated from seawater. The negative $\delta^{13}C$ shift at the peak of the K-O $\delta^{13}C$ excursion, although it is not present in all sections reported, appears in several successions globally, including the Samaria Mountain section in Idaho (Saltzman, 2002), Clark Fork Canyon section in Wyoming (Saltzman, 2003), Fitchville Ridge section in central Utah (Saltzman, 2003), and sections in the Dinant Basin of Belgium and Northern Urals of Russia (Saltzman et al., 2004). The lack of this negative $\delta^{13}C$ shift in some sections is likely due to incomplete stratigraphic records in shallow-water settings, such as in the Mountain Home and Confusion Range sections (Fig. 7). The K-O $\delta^{13}C$ excursion is stratigraphically "self-destructive": increase of organic carbon burial would result in global cooling and sea-level fall and form unconformities in shallow-water environments. Unconformities and exposure surfaces are indeed present at or near the peak the K-O $\delta^{13}C$ excursion in the Great Basin area (e.g., Fig. 7), across the entire United States (Lane and Brenckle, 2005; Kammer and Matchen, 2008) and in South China (Jiang, unpublished data). Therefore, only at relatively deep-water environments the complete $\delta^{13}C$ and $\delta^{34}S$ records are preserved. In this context, the $\delta^{13}C$ and $\delta^{34}S$ patterns seen in the outer shelf-slope section (Figs. 3 and 7) may record a global rather than local seawater

signature, although a more comprehensive stratigraphic framework covering broader areas in different basins is required to confirm.

If the positive $\delta^{34}S_{CAS}$ and negative $\delta^{34}S_{PY}$ anomalies (Fig. 3) record a global signature, one of the challenges is the large magnitude (7‰) of $\delta^{34}S_{CAS}$ shift in a sulfate-rich ocean. Many studies directly or indirectly suggested that the sulfate concentrations in the Mississippian ocean may be close to or even higher than that of the modern ocean (Berner and Canfield, 1989; Kampschulte et al., 2001, 2004; Berner, 2004, 2006; Gill et al., 2007). Assuming that a pyrite burial event happened in the Mississippian ocean with a sulfate reservoir comparable with that of the modern ocean (~28 mM or ~1.3 × 10^{21} g S; Bottrell and Newton, 2006), we do a simple steady-state mass balance calculation using the following equation:

$$M_{TX} \times \delta^{34}S_{TX} = (M_{TX} - M_{PY}) \times \delta^{34}S'_{TX} + M_{PY} \times \delta^{34}S_{PY} \quad (1)$$

Where M_{TX} and $\delta^{34}S_{TX}$ are the total mass and isotope value of the marine sulfate reservoir, respectively; M_{PY} and $\delta^{34}S_{PY}$ are the mass and isotope value of pyrite buried (or removed) from the ocean; and $\delta^{34}S'_{TX}$ are the isotope value of the marine sulfate reservoir after the pyrite burial event. After adjustment, equation (1) can be simplified as:

$$M_{PY} = \frac{M_{TX} \times (\delta^{34}S'_{TX} - \delta^{34}S_{TX})}{\delta^{34'}{}_{TX} - \delta^{34}S_{PY}} \quad (2)$$

Using the data displayed in Fig. 3, $(\delta^{34'}{}_{TX} - \delta^{34}S_{PY})$ is the $\Delta^{34}S$ (we use the highest value of 45‰) and $(\delta^{34}S'_{TX} - \delta^{34}S_{TX})$ is the magnitude of $\delta^{34}S_{CAS}$ shift (7‰). The amount of pyrite burial (M_{PY}) is in the range of 2.0×10^{20} g S or 15% of the marine sulfate reservoir. Assuming that the positive $\delta^{34}S_{CAS}$ shift took 0.5 million years (myr) to reach the peak value, it amounts to an annual pyrite burial rate of 4.0×10^{14} g S/yr, which is about 6 times of the estimated modern annual burial rate (~6.0 ×10^{13} g S/yr; Bottrell and Newton, 2006). Considering that pyrite burial in the modern ocean occurs mostly in sediments and the K-O $\delta^{13}C$ excursion is

arguably the largest $\delta^{13}C$ excursion in the Phanerozoic, during which pyrite formation may have expanded to the water column, a pyrite burial rate a few times higher than that of the modern ocean is not outrageously unrealistic.

This simple mass balance calculation, however, did not consider the riverine input that lowers the $\delta^{34}S$ of seawater. To better constrain the sulfur isotope responses to input and output fluxes, we use the box model of Sim et al. (2015) to track the temporal changes in the size and isotope composition of the marine sulfate reservoir:

$$\frac{d}{dt}M = F_{in} - \left(F_{PY} + F_{evap}\right) \quad (3)$$

$$\frac{d}{dt}\left[\delta^{34}S_{SO_4}\right] = \frac{F_{in} \times \left(\delta_{in} - \delta^{34}S_{SO_4}\right) - F_{PY} \times \Delta^{34}S}{M} \quad (4)$$

Where M is the mass of the marine sulfate reservoir (moles); F_{in} is the input flux to the ocean (moles/year); F_{PY} and F_{evap} are the burial fluxes of pyrite and evaporites (moles/year), respectively; δ_{in} and $\delta^{34}S_{SO_4}$ are the isotope compositions of input flux and the marine sulfate reservoir, respectively; and $\Delta^{34}S$ is the isotope fractionation. Following Sim et al. (2015), the weathering and magmatic inputs are combined as a single input flux (F_{in}) and we assume that this flux did not change. The $\Delta^{34}S$ changes from 15‰ to 45‰, following the temporal $\Delta^{34}S$ obtained from the K-O interval (Fig. 3). The other initial conditions are adopted from Sim et al. (2015). For a comparison we also run the model using the input and output fluxes specified in Bottrell and Newton (2006).

The duration of the K-O $\delta^{13}C$ excursion is estimated as 2–4 million years (Saltzman et al., 2004; Buggisch et al., 2008; Yao et al., 2015) and we take an average of 3 million years. We model the $\delta^{34}S_{SO4}$ response to a 0.5-myr pyrite burial event in a sulfate-rich ocean. Using the initial conditions specified in Sim et al. (2015), a 7‰ positive $\delta^{34}S_{SO4}$ shift requires to increase

F_{PY} more than 10 times within 0.5 million years (Fig. 9A). When the inputs and outputs of Bottrell and Newton (2006) are used, the increase of pyrite burial is within 5-10 times (Fig. 9B). With lower sulfate concentrations, the required pyrite burial decreases accordingly. That means that, within uncertainties of estimated sulfur input and output fluxes, an increase of pyrite burial by 5–10 times explains the isotope patterns observed in the K-O interval, even if the early Mississippian ocean had the sulfate concentrations similar to that of the modern ocean (~28 mM).

5.4. Implications of the temporal $\delta^{18}O_{CAS}$ variations

Oxygen isotopes of marine sulfate ($\delta^{18}O_{SO4}$) are mainly controlled by input from continental weathering and the reflux of isotopically modified sulfate through sulfate reduction and sulfide reoxidation (e.g., Turchyn and Schrag, 2004, 2006; Bottrell and Newton, 2006; Markovic et al., 2016). Sulfate derived from weathering of evaporites and pyrites has $\delta^{18}O_{SO4}$ values of 11–13‰ (VSMOW; the same hereafter) and –4‰ to +2‰, respectively. Riverine sulfate, which is a mixture of evaporite- and pyrite-derived sulfate, has $\delta^{34}S_{SO4}$ values in the range of –2‰ to +7‰, depending on the relative importance of pyrite- vs. evaporite-derived sulfate contribution (Bottrell and Newton, 2006). Modern seawater sulfate has $\delta^{18}O_{SO4}$ values of ~9.3‰, which is higher than that of the riverine input and is regulated by microbial sulfate reduction (MSR) and sulfide reoxidation (Lloyd, 1968; Turchyn and Schrag, 2004, 2006). During MSR, sulfate reducers preferentially remove ^{16}O through oxygen exchanges between intracellular sulfite (SO_3^{2-}) and ambient water, resulting in high $\delta^{18}O_{SO4}$ up to 29‰ in residual sulfate (Antler et al., 2013; Markovic et al., 2016). Microbial sulfide reoxidation (or disproportionation) produces sulfate that has $\delta^{18}O_{SO4}$ 8–21‰ higher than that of seawater ($\delta^{18}O \approx$ 0‰). In contrast, direct (abiotic) sulfide reoxidation produces sulfate that has $\delta^{18}O_{SO4}$ values

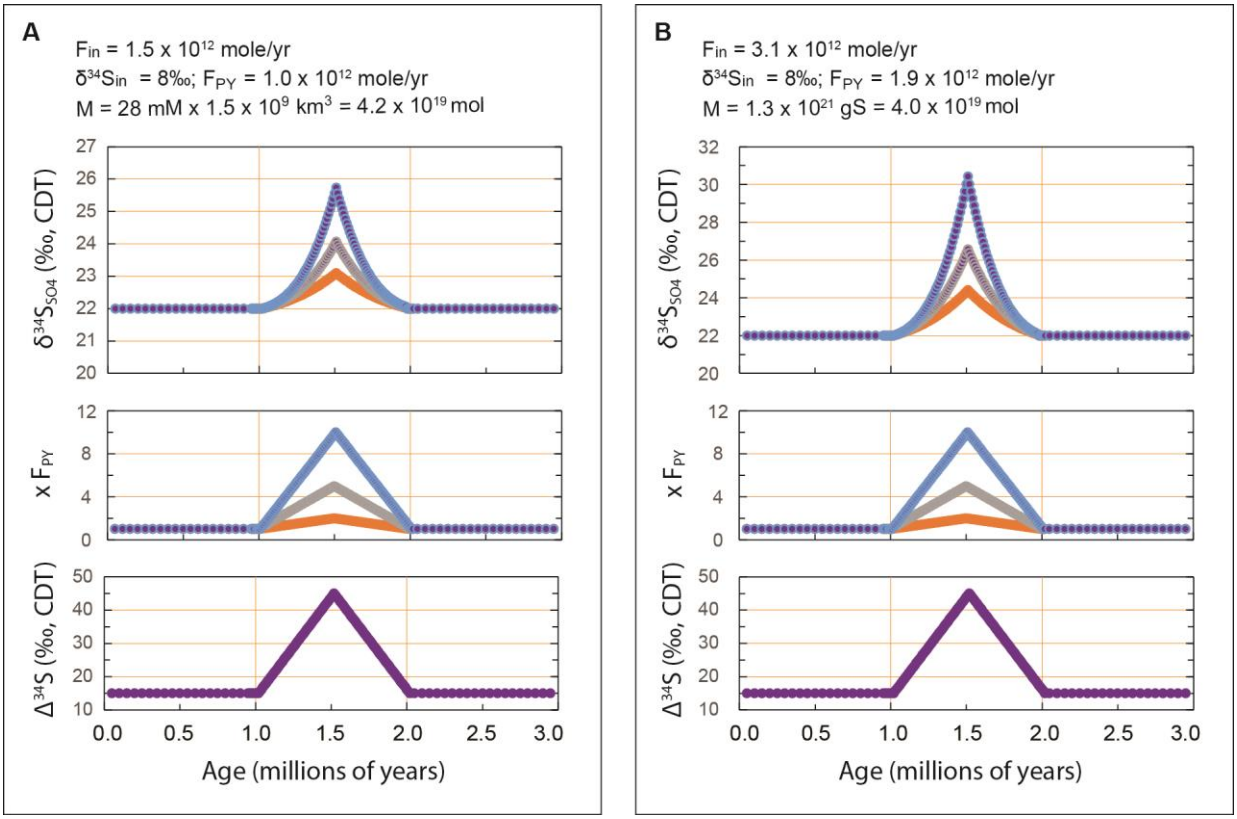

Fig. 9. Modeling the $\delta^{34}S_{SO4}$ response to a 0.5-myr pyrite burial event within the 3-myr K-O $\delta^{13}C$ excursion, assuming that the sulfate concentrations in early Mississippian oceans are similar to that of the modern ocean (~28 mM). (A) Using the input and output fluxes specified in Sim et al. (2015) and the temporal $\Delta^{34}S$ change from 15‰ to 45‰ obtained from the K-O interval (Fig. 3), a 7‰ positive shift in $\delta^{34}S_{SO4}$ requires an increase of pyrite burial by more than 10 times. (B) Using the input and output fluxes of Bottrell and Newton (2006), a 7‰ shift in $\delta^{34}S_{SO4}$ requires an increase of pyrite burial by 5–10 times.

similar to seawater $\delta^{18}O$ (Böttcher et al., 2001, 2005; Antler et al., 2013; Markovic et al., 2016). Within this framework, positive shift in $\delta^{18}O_{SO4}$ reflects enhanced sulfate reduction and/or microbial sulfide reoxidation, whereas negative shift in $\delta^{18}O_{SO4}$ may record increase of direct sulfide reoxidation and/or pyrite-derived riverine sulfate input. Because riverine input and pyrite burial influence both $\delta^{34}S_{SO4}$ and $\delta^{18}O_{SO4}$, decoupled $\delta^{34}S_{SO4}$ and $\delta^{18}O_{SO4}$ must involve changes

in the pathways of sulfide reoxidation, which has large impact on $\delta^{18}O_{SO4}$ but less significant net effects on $\delta^{34}S_{SO4}$ (Turchyn and Schrag, 2004, 2006; Turchyn et al., 2009).

The $\delta^{18}O_{CAS}$ from PR and MH sections shows an 8–10‰ increase at the rising limb of the K-O $\delta^{13}C$ excursion, but $\delta^{34}S_{CAS}$ at the same interval has limited variations (Figs. 3 and 4). This apparently decoupled $\delta^{18}O_{CAS}$–$\delta^{34}S_{CAS}$ suggests that in addition to increase of sulfate reduction, microbial sulfide reoxidation (disproportionation) contributed a large portion to the increase of $\delta^{18}O_{CAS}$. Similar decoupled $\delta^{18}O_{CAS}$–$\delta^{34}S_{CAS}$ patterns have been observed from the Cenozoic (Turchyn and Schrag, 2006) and middle Cretaceous (Turchyn et al., 2009) records, which have been ascribed to changes in the pathways of sulfide reoxidation. When high organic carbon burial dominates continental shelves, high rates of sulfate reduction in less oxic environments promote microbial sulfide reoxidation and raise $\delta^{18}Oso_4$ in seawater sulfate. When organic matter is deposited in more oxic shelves or deep-water environments, direct sulfide reoxidation dominates and $\delta^{18}Oso_4$ decreases (Turchyn and Schrag, 2006). Microbial sulfide reoxidation is most effective in anoxic sediments and water column where sulfide oxidizing bacteria thrive and utilize nitrate or iron/manganese oxyhydroxides as electron acceptors (e.g., Turchyn et al., 2009). The parallel increase of $\delta^{18}O_{CAS}$ and $\delta^{13}C$ (Figs. 3 and 4) is consistent with the potential aerial expansion of anoxic organic-rich sediments and water column favorable for sulfide oxidizers, as specified in Turchyn and Schrag (2006), which is an anticipated outcome of enhanced organic production and burial required for the 5-6‰ shift in $\delta^{13}C$. A more recent study (Antler et al., 2013), however, suggested that the recycling of sulfite (SO_3^{2-}) during MSR controls the $\delta^{18}Oso_4$ of porewater sulfate: in environments with high sulfate reduction rates (e.g., estuaries and marginal marine environments), sulfate reducing bacteria maintain low rate of sulfite reoxidation, resulting in slower increase of $\delta^{18}O_{SO4}$ relative to $\delta^{34}S_{SO4}$; while in environments

with low sulfate reduction rates (e.g., deep ocean), $\delta^{18}O_{SO4}$ increases faster than $\delta^{34}S_{SO4}$. These observations are the opposite of what has been described in Turchyn and Schrag (2006), but isotope analyses and modeling are limited to porewater sulfate; the influence of which to the secular isotope change of seawater sulfate awaits for further confirmation.

The negative shift in $\delta^{18}O_{CAS}$ at the peak of the K-O $\delta^{13}C$ excursion, which is better recorded in the PR section (Fig. 3), is most likely formed by direct sulfide reoxidation in response to the expansion of water-column euxinia. As discussed earlier, the fast positive $\delta^{34}S_{CAS}$ shift at the same stratigraphic interval requires a prominent pyrite burial event resulted from the aerial expansion of oxygen minimum zone (OMZ). Enhanced sulfate reduction and H_2S production in spatially expanded OMZ would inevitably increase direct sulfide reoxidation and lower the $\delta^{18}O$ of sulfate (e.g., Turchyn et al., 2009), although in such environments microbial sulfide disproportionation could also exist (e.g., Turchyn et al., 2009). As OMZ shrank, sulfate reduction shifts from water column to sediments and sulfide reoxidation change back to the pathway of microbial disproportionation that returns $\delta^{18}O_{CAS}$ back to high values.

The coupled negative shift in $\delta^{18}O_{CAS}$ and $\delta^{34}S_{CAS}$ at the falling limb of the K-O $\delta^{13}C$ excursion is best explained by the increase of sulfide-derived sulfate, likely from combined sources of pyrite weathering and direct sulfide reoxidation in the ocean. After the peak of a ≥5‰ $\delta^{13}C$ excursion, pervasive organic carbon burial could have resulted in increase of oxygen in the water column and atmosphere, global cooling, and sea-level fall. Global cooling may increase the solubility of oxygen in the ocean and sea-level fall reduces shelf areas, both of which may have acted to shift microbial disproportionation to direct sulfide reoxidation (Turchyn and Schrag, 2004, 2006; Markovic et al., 2016). High atmosphere oxygen facilitates oxidative pyrite weathering, which may also have contributed to the negative $\delta^{18}O_{CAS}$ and $\delta^{34}S_{CAS}$ shift. The

much larger magnitude of $\delta^{18}O_{CAS}$ and $\delta^{34}S_{CAS}$ change during the K-O, compared to that of the Cenozoic record (cf. Turchyn and Schrag, 2006; Markovic et al., 2016), may relate to more dynamic carbon and sulfur cycles across one of the largest Phanerozoic $\delta^{13}C$ excursions, which requires further quantitative exploration in the future.

5.5. Summary of the dynamic sulfur cycle across the K-O $\delta^{13}C$ excursion

The integrated $\delta^{13}C$, $\delta^{34}S_{CAS}$, $\delta^{34}S_{PY}$, and $\delta^{18}O_{CAS}$ data from the PR section, if they are representative of the seawater isotope records, demonstrate a dynamic sulfur cycle across the K-O $\delta^{13}C$ excursion (Fig. 10). At the rising limb of the K-O $\delta^{13}C$ excursion, increased organic carbon production and burial may have led to aerial expansion of organic-rich (anoxic) sediments and potentially suboxic environments near the sediment/water interface (Fig. 10A). Microbial sulfate reduction (MSR) and sulfide reoxidation (disproportionation) mainly happened in sediments. Pyrite burial certainly increased but had limited effects on the $\delta^{34}S$ of seawater sulfate possibly due to the buffering effect of a large sulfate pool comparable with or even larger than that of the modern ocean (cf. Gill et al., 2011; Jones and Fike, 2013; Sim et al., 2015). In contrast, spatially expanded and intensified microbial sulfide reoxidation in anoxic sediments resulted in a ≥8‰ positive shift in $\delta^{18}O_{CAS}$, in parallel with $\delta^{13}C$.

At the peak of the K-O $\delta^{13}C$ excursion, organic carbon production and burial may have reached the maximum and the oxygen minimum zone was significantly expanded (Fig. 10B). Enhanced sulfate reduction, fed by abundantly available organic carbon, happened not only in sediments, but also in water column, resulting in a pyrite burial event and a positive shift in $\delta^{34}S_{CAS}$. Active sulfur recycling also increased the sulfur isotope fractionation, leading to a negative $\delta^{34}S_{PY}$ anomaly and increase in $\Delta^{34}S$. Sulfate reduction in the water column produced

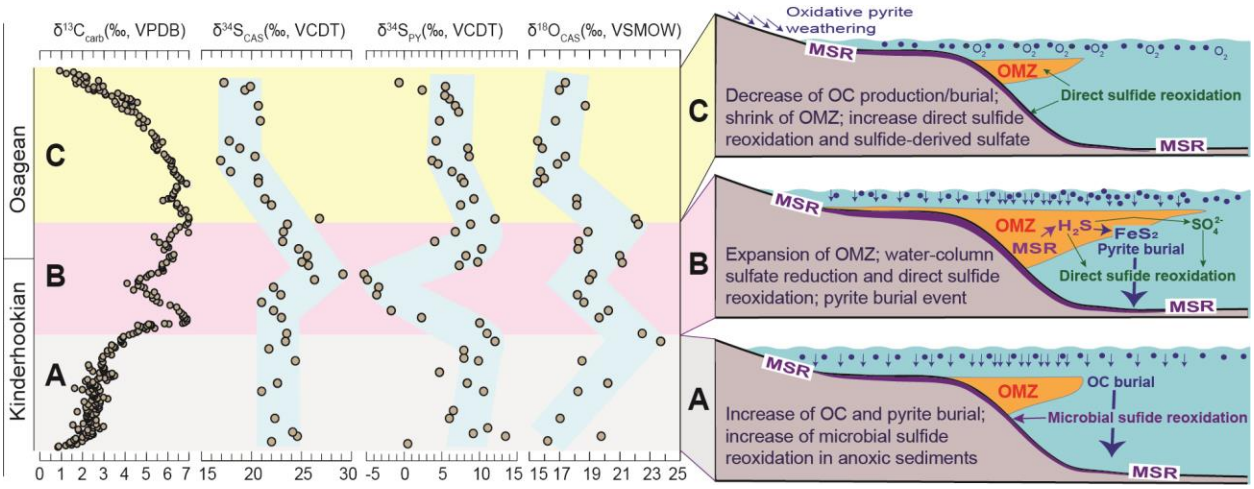

Fig. 10. Schematic diagram summarizing the dynamic sulfur cycle across the K-O $\delta^{13}C$ excursion, based on the $\delta^{13}C$, $\delta^{34}S_{CAS}$, $\delta^{34}S_{PY}$, and $\delta^{18}O_{CAS}$ data from the PR section (Fig. 3), which represent a relatively more complete isotope record. (A) At the rising limb of the K-O $\delta^{13}C$ excursion, pyrite burial certainly increased but had limited effects on the $\delta^{34}S$ of seawater sulfate possibly due to the buffering effect of a large marine sulfate reservoir. In contrast, intensified microbial sulfide reoxidation associated with enhanced organic carbon (OC) burial resulted in a ≥8‰ positive shift in $\delta^{18}O_{CAS}$, in parallel with $\delta^{13}C$. (B) At the peak of the K-O $\delta^{13}C$ excursion, OC production and burial may have reached the maximum and the oxygen minimum zone (OMZ) expanded. Enhanced sulfate reduction, fed by abundantly available OC, happened not only in sediments, but also in water column, resulting in a pyrite burial event and a positive shift in $\delta^{34}S_{CAS}$. Sulfate reduction in the water column also produce ^{13}C-depleted carbon and promote direct sulfide oxidation, resulting in negative $\delta^{13}C$ and $\delta^{18}O_{CAS}$ anomalies. (C) After the peak of the K-O $\delta^{13}C$ excursion, OC production and burial declined and OMZ shrank. Direct sulfide oxidation, plus possibly increased pyrite weathering input, led to coupled negative shifts in both $\delta^{18}O_{CAS}$ and $\delta^{34}S_{CAS}$.

^{13}C-depleted carbon and promoted direct sulfide reoxidation, resulting in negative $\delta^{13}C$ and $\delta^{18}O_{CAS}$ anomalies.

After the peak of the K-O $\delta^{13}C$ excursion, organic carbon production and burial declined and the oxygen minimum zone shrank (Fig. 10C). Oxygen increase, global cooling and sea-level

fall resulted from organic carbon and pyrite burial promoted oxidative pyrite weathering in continents and direct sulfide reoxidation in the ocean, resulting in coupled negative shifts in both $\delta^{18}O_{CAS}$ and $\delta^{34}S_{CAS}$.

6. Conclusion

We report $\delta^{34}S_{CAS}$, $\delta^{34}S_{PY}$, and $\delta^{18}O_{CAS}$ data across the K-O $\delta^{13}C$ excursion from two Early Mississippian sections in the southern Great Basin, western U.S.A. These two sections represent peritidal and outer shelf depositional environments of a west-dipping carbonate platform. The isotope profiles from these sections show similarities in temporal trends but have significant differences near the peak of the K-O $\delta^{13}C$ excursion. The presence of karstic unconformities and exposure surfaces near the $\delta^{13}C$ peak in proximal shallow-water sections suggest that the relatively deeper-water outer shelf section better preserves the carbon, sulfur, and CAS oxygen isotope records.

The sulfur and CAS oxygen isotope data demonstrate a more dynamic sulfur cycle across the K-O $\delta^{13}C$ excursion than previous suggested. At the rising limb of the K-O $\delta^{13}C$ excursion, stable $\delta^{34}S_{CAS}$, $\delta^{34}S_{pyr}$ and $\Delta^{34}S$ suggest that increased pyrite burial associated with organic carbon burial had limited influence on the sulfur isotope change, possibly due to the buffering effect of a large marine sulfate reservoir comparable with or even larger than that of the modern ocean. In contrast, the 8–10‰ increase of $\delta^{18}O_{CAS}$ in parallel with the positive $\delta^{13}C$ shift suggests that enhanced organic carbon burial led to expansion of organic-rich (anoxic) sediments and possibly suboxic environments near water/sediment interface, increasing microbial sulfide reoxidation and $\delta^{18}O$ of resulting sulfate. Near the peak of the K-O $\delta^{13}C$ excursion, a 7‰ positive $\delta^{34}S_{CAS}$ anomaly occurs concomitantly with negative shifts in $\delta^{13}C$, $\delta^{34}S_{PY}$ and $\delta^{18}O_{CAS}$ and increase of $\Delta^{34}S$. These isotope features require the expansion of sulfate reduction and pyrite

burial from predominantly in sediments to ocean water column, in response to the maximum organic carbon production/burial and expansion of the oxygen minimum zone (OMZ) near the $\delta^{13}C$ peak. Mass balance calculation and numerical modeling suggest that the 7‰ positive $\delta^{34}S_{CAS}$ anomaly requires pyrite burial rates 5-10 times higher than that of the modern ocean. The parallel decrease of $\delta^{34}S_{CAS}$ and $\delta^{18}O_{CAS}$ after the K-O $\delta^{13}C$ peak is consistent with the increase of sulfide reoxidation in the ocean and pyrite-derived riverine sulfate input in response to global cooling, sea-level fall, and oxygenation resulted from enhanced organic carbon and pyrite burial.

Table 1. Carbon, oxygen, and sulfur isotopes of measured sections
Section 1 : Pahranagat Range, Alamo (NV), GPS locaton: 37 23' 42.94" N, 115 15' 43.30" W

Strat. Unit	Strat. Height (m)	Sample No.	Lithology	$\delta^{13}C_{carb}$ (‰,VPDB)	$\delta^{18}O_{carb}$ (‰,VPDB)	CAS (ppm)
Joana Limestone	0	PR-65	Wackestone	0.83	-4.39	
Joana Limestone	0.5	PR-65.5	Grainstone	0.87	-4.57	
Joana Limestone	1	PR-66	Wackestone	1.20	-5.23	
Joana Limestone	1.5	PR-66.5	Grainstone	1.48	-4.14	
Joana Limestone	2	PR-67	Grainstone	1.73	-4.93	
Joana Limestone	2.5	PR-67.5	Packstone	1.36	-4.71	
Joana Limestone	3	PR-68	Packstone	1.52	-5.30	
Joana Limestone	3.4	PR-68.4	Packstone	1.41	-5.55	14.0
Joana Limestone	4	PR-69	Grainstone	1.98	-4.17	
Joana Limestone	4.5	PR-69.5	Grainstone	1.63	-5.24	
Joana Limestone	5	PR-70	Grainstone	1.58	-5.63	
Joana Limestone	6	PR-71	Grainstone	1.68	-4.82	
Joana Limestone	6.5	PR-71.5	Grainstone	2.14	-5.53	
Joana Limestone	7	PR-72	Grainstone	1.98	-4.57	
Joana Limestone	7.5	PR-72.5	Wackestone	2.28	-4.54	14.0
Joana Limestone	8	PR-73	Lime mudstone	2.37	-4.83	
Joana Limestone	8.5	PR-73.5	Grainstone	2.18	-5.01	
Joana Limestone	9	PR-74	Grainstone	2.49	-4.68	
Joana Limestone	9.5	PR-74.5	Wackestone	2.44	-4.80	
Joana Limestone	10	PR-75	Packstone	2.14	-4.68	14.8
Joana Limestone	10.5	PR-75.5	Packstone	2.27	-5.03	
Joana Limestone	11	PR-76	Packstone	2.45	-4.69	
Joana Limestone	11.5	PR-76.5	Wackestone	1.81	-4.50	
Joana Limestone	12	PR-77	Wackestone	2.24	-5.33	
Joana Limestone	12.5	PR-77.5	Packstone	1.79	-5.41	
Joana Limestone	13	PR-78	Wackestone	2.80	-3.95	
Joana Limestone	13.5	PR-78.5	Wackestone	2.50	-3.90	
Joana Limestone	14	PR-79	Wackestone	2.68	-4.92	
Joana Limestone	14.5	PR-79.5	Wackestone	2.97	-3.91	
Joana Limestone	15	PR-80	Wackestone	2.50	-4.16	0.0
Joana Limestone	15.5	PR-80.5	Grainstone	1.54	-4.17	
Joana Limestone	16	PR-81	Grainstone	2.63	-4.33	
Joana Limestone	16.5	PR-81.5	Grainstone	2.03	-6.87	
Joana Limestone	17	PR-82	Grainstone	2.34	-5.40	
Joana Limestone	17.5	PR-82.5	Grainstone	2.40	-5.03	
Joana Limestone	18	PR-83	Wackestone	2.31	-4.95	
Joana Limestone	18.5	PR-83.5	Grainstone	0.96	-7.06	
Joana Limestone	19	PR-84	Grainstone	2.63	-7.37	
Joana Limestone	19.5	PR-84.5	Grainstone	2.25	-8.64	
Joana Limestone	20	PR-85	Wackestone	2.24	-5.79	14.0
Joana Limestone	20.5	PR-85.5	Grainstone	2.27	-4.52	
Joana Limestone	21	PR-86	Packstone	2.19	-5.28	
Joana Limestone	21.5	PR-86.5	Grainstone	2.33	-6.24	
Joana Limestone	22	PR-87	Grainstone	2.18	-6.65	
Joana Limestone	22.5	PR-87.5	Wackestone	2.49	-8.23	
Joana Limestone	23	PR-88	Packstone	2.45	-5.60	
Joana Limestone	23.5	PR-88.5	Grainstone	2.22	-5.85	
Joana Limestone	24	PR-89	Grainstone	2.64	-4.64	
Joana Limestone	24.5	PR-89.5	Grainstone	2.21	-4.87	
Joana Limestone	25	PR-90	Grainstone	1.74	-4.87	
Joana Limestone	25.5	PR-90.5	Packstone	2.28	-5.62	
Joana Limestone	26	PR-91	Wackestone	2.19	-5.85	0.0
Joana Limestone	26.5	PR-91.5	Grainstone	2.72	-4.91	
Joana Limestone	27	PR-92	Grainstone	2.57	-4.59	
Joana Limestone	27.6	PR-92.6	Grainstone	2.78	-4.38	

FeS_2 (ppm)	$\delta^{34}S_{CAS}$ (‰, CDT)	$\delta^{34}S_{PY}$ (‰,CDT)	$\Delta^{34}S_{CAS-PY}$	$\delta^{18}O_{CAS}$ (‰,VSMOW)	Age	Conodont zone*
					Kinderhookian	*S. Sandbergi* ?
					Kinderhookian	*S. Sandbergi* ?
					Kinderhookian	*S. Sandbergi* ?
					Kinderhookian	*S. Sandbergi* ?
					Kinderhookian	*S. Sandbergi* ?
					Kinderhookian	*S. Sandbergi* ?
					Kinderhookian	*S. Sandbergi* ?
22.0	22.04	0.47	21.58	16.23	Kinderhookian	*S. Sandbergi* ?
					Kinderhookian	*S. Sandbergi* ?
					Kinderhookian	*S. Sandbergi* ?
					Kinderhookian	*S. Sandbergi* ?
					Kinderhookian	*S. Sandbergi* ?
					Kinderhookian	*S. Sandbergi* ?
					Kinderhookian	*S. Sandbergi* ?
163.7	24.61	13.54	11.07	19.78	Kinderhookian	*S. Sandbergi* ?
					Kinderhookian	*S. Sandbergi* ?
					Kinderhookian	*S. Sandbergi* ?
					Kinderhookian	*S. Sandbergi* ?
					Kinderhookian	*S. Sandbergi* ?
25.0	24.18	9.14	15.04		Kinderhookian	*S. Sandbergi* ?
					Kinderhookian	*S. Sandbergi* ?
					Kinderhookian	*S. Sandbergi* ?
					Kinderhookian	*S. Sandbergi* ?
					Kinderhookian	*S. Sandbergi* ?
					Kinderhookian	*S. Sandbergi* ?
					Kinderhookian	*S. Sandbergi* ?
					Kinderhookian	*S. Sandbergi* ?
					Kinderhookian	*S. Sandbergi* ?
					Kinderhookian	*S. Sandbergi* ?
30.0		11.18			Kinderhookian	*S. Sandbergi* ?
					Kinderhookian	*S. Sandbergi* ?
					Kinderhookian	*S. Sandbergi* ?
					Kinderhookian	*S. Sandbergi* ?
					Kinderhookian	*S. Sandbergi* ?
					Kinderhookian	*S. Sandbergi* ?
					Kinderhookian	*S. Sandbergi* ?
					Kinderhookian	*S. Sandbergi* ?
					Kinderhookian	*S. Sandbergi* ?
					Kinderhookian	*S. Sandbergi* ?
					Kinderhookian	*S. Sandbergi* ?
305.4	22.31	6.06	16.25	17.04	Kinderhookian	*S. Sandbergi* ?
					Kinderhookian	*S. Sandbergi* ?
					Kinderhookian	*S. Sandbergi* ?
					Kinderhookian	*S. Sandbergi* ?
					Kinderhookian	*S. Sandbergi* ?
					Kinderhookian	*S. Sandbergi* ?
					Kinderhookian	*S. Sandbergi* ?
					Kinderhookian	*S. Sandbergi* ?
					Kinderhookian	*S. Sandbergi* ?
					Kinderhookian	*S. Sandbergi* ?
					Kinderhookian	*S. Sandbergi* ?
					Kinderhookian	*S. Sandbergi* ?
					Kinderhookian	*S. Sandbergi* ?
161.1		6.47			Kinderhookian	*S. Sandbergi* ?
					Kinderhookian	*S. Sandbergi* ?
					Kinderhookian	*S. Sandbergi* ?
					Kinderhookian	*S. Sandbergi* ?

Joana Limestone	28	PR-93	Packstone	2.15	-5.61	
Joana Limestone	28.5	PR-93.5	Wackestone	2.41	-5.19	
Joana Limestone	28.5	PR-93.5	Grainstone	2.67	-4.76	
Joana Limestone	29	PR-94	Grainstone	2.75	-5.37	
Joana Limestone	29.5	PR-94.5	Grainstone	2.63	-5.44	
Joana Limestone	30	PR-95	Grainstone	2.26	-5.27	
Joana Limestone	30.5	PR-95.5	Wackestone	2.58	-4.74	
Joana Limestone	31	PR-96	Grainstone	2.81	-4.08	
Joana Limestone	31.6	PR-96.6	Packstone	2.68	-5.34	
Joana Limestone	32	PR-97	Wackestone	2.07	-6.08	
Joana Limestone	32.5	PR-97.5	Grainstone	2.82	-7.13	
Joana Limestone	33	PR-98	Grainstone	2.42	-6.42	
Joana Limestone	33.5	PR-98.5	Wackestone	2.66	-4.65	
Joana Limestone	34	PR-99	Wackestone	3.18	-4.70	
Joana Limestone	34.5	PR-99.5	Wackestone	2.70	-5.31	
Joana Limestone	35	PR-100	Wackestone	2.97	-4.10	
Joana Limestone	35.5	PR-100.5	Packstone	2.51	-5.15	
Joana Limestone	36	PR-101	Packstone	2.57	-5.38	
Joana Limestone	36.5	PR-101.5	Grainstone	2.49	-6.75	
Joana Limestone	37	PR-102	Grainstone	2.45	-5.23	
Joana Limestone	37.5	PR-102.5	Packstone	2.49	-6.37	
Joana Limestone	38	PR-103	Grainstone	2.60	-5.58	
Joana Limestone	38.5	PR-103.5	Grainstone	2.55	-5.65	
Joana Limestone	39	PR-104	Wackestone	2.29	-6.50	36.8
Joana Limestone	39.5	PR-104.5	Grainstone	2.74	-6.54	
Joana Limestone	40	PR-105	Grainstone	2.82	-3.96	
Joana Limestone	40.5	PR-105.5	Grainstone	1.98	-6.23	
Joana Limestone	41	PR-106	Grainstone	2.44	-5.15	
Joana Limestone	41.5	PR-106.5	Packstone	1.62	-5.92	
Joana Limestone	42	PR-107	Grainstone	2.59	-5.27	
Joana Limestone	42.5	PR-107.5	Grainstone	2.73	-6.14	
Joana Limestone	43	PR-108	Grainstone	2.59	-5.54	
Joana Limestone	43.4	PR-108.4	Wackestone	2.33	-5.65	
Joana Limestone	44	PR-109	Grainstone	2.58	-4.92	

					Kinderhookian	*S. Sandbergi* ?
					Kinderhookian	*S. Sandbergi* ?
					Kinderhookian	*S. Sandbergi* ?
					Kinderhookian	*S. Sandbergi* ?
					Kinderhookian	*S. Sandbergi* ?
					Kinderhookian	*S. Sandbergi* ?
					Kinderhookian	Upper *S. crenulata - S. isosticha*
					Kinderhookian	Upper *S. crenulata - S. isosticha*
					Kinderhookian	Upper *S. crenulata - S. isosticha*
					Kinderhookian	Upper *S. crenulata - S. isosticha*
					Kinderhookian	Upper *S. crenulata - S. isosticha*
					Kinderhookian	Upper *S. crenulata - S. isosticha*
					Kinderhookian	Upper *S. crenulata - S. isosticha*
					Kinderhookian	Upper *S. crenulata - S. isosticha*
					Kinderhookian	Upper *S. crenulata - S. isosticha*
					Kinderhookian	Upper *S. crenulata - S. isosticha*
					Kinderhookian	Upper *S. crenulata - S. isosticha*
					Kinderhookian	Upper *S. crenulata - S. isosticha*
					Kinderhookian	Upper *S. crenulata - S. isosticha*
					Kinderhookian	Upper *S. crenulata - S. isosticha*
					Kinderhookian	Upper *S. crenulata - S. isosticha*
					Kinderhookian	Upper *S. crenulata - S. isosticha*
					Kinderhookian	Upper *S. crenulata - S. isosticha*
194.5	21.06	10.57	10.50	18.19	Kinderhookian	Upper *S. crenulata - S. isosticha*
					Kinderhookian	Upper *S. crenulata - S. isosticha*
					Kinderhookian	Upper *S. crenulata - S. isosticha*
					Kinderhookian	Upper *S. crenulata - S. isosticha*
					Kinderhookian	Upper *S. crenulata - S. isosticha*
					Kinderhookian	Upper *S. crenulata - S. isosticha*
					Kinderhookian	Upper *S. crenulata - S. isosticha*
					Kinderhookian	Upper *S. crenulata - S. isosticha*
					Kinderhookian	Upper *S. crenulata - S. isosticha*
					Kinderhookian	Upper *S. crenulata - S. isosticha*
					Kinderhookian	Upper *S. crenulata - S. isosticha*

Joana Limestone	44.5	PR-109.5	Grainstone	2.33	-5.97	
Joana Limestone	45	PR-110	Wackestone	2.46	-5.43	116.2
Joana Limestone	45.5	PR-110.5	Packstone	2.38	-5.56	
Joana Limestone	46	PR-111	Packstone	2.48	-5.91	
Joana Limestone	46.5	PR-111.5	Wackestone	2.13	-9.53	
Joana Limestone	47	PR-112	Wackestone	3.13	-7.21	
Joana Limestone	47.6	PR-112.6	Wackestone	2.23	-7.82	
Joana Limestone	48	PR-113	Wackestone	2.71	-7.96	
Joana Limestone	48.5	PR-113.5	Wackestone	3.04	-6.84	
Joana Limestone	49	PR-114	Wackestone	2.80	-9.89	
Joana Limestone	49.5	PR-114.5	Wackestone	3.29	-4.96	
Joana Limestone	50	PR-115	Wackestone	3.41	-4.00	
Joana Limestone	50.5	PR-115.5	Wackestone	3.50	-4.16	
Joana Limestone	51	PR-116	Wackestone	3.33	-4.05	
Joana Limestone	51.5	PR-116.5	Grainstone	3.26	-3.88	
Joana Limestone	52	PR-117	Grainstone	3.38	-3.55	
Joana Limestone	52.5	PR-117.5	Wackestone	2.79	-4.55	
Joana Limestone	53	PR-118	Wackestone	3.00	-4.42	
Joana Limestone	53.5	PR-118.5	Packstone	2.47	-4.93	
Joana Limestone	54	PR-119	Lime mudstone	2.97	-5.34	0.0
Joana Limestone	55	PR-120	Grainstone	2.96	-4.11	
Joana Limestone	55.5	PR-120.5	Wackestone	3.02	-4.41	
Joana Limestone	56	PR-121	Wackestone	2.32	-5.46	
Joana Limestone	56.3	PR-121.3	Wackestone	2.98	-4.28	
Joana Limestone	57.4	PR-122.4	Grainstone	2.89	-4.95	
Joana Limestone	58	PR-123	Grainstone	2.27	-5.30	
Joana Limestone	58.5	PR-123.5	Grainstone	2.87	-4.80	
Joana Limestone	60	PR-125	Wackestone	2.95	-3.93	11.0
Joana Limestone	62.5	PR-127.5	Grainstone	2.90	-4.89	
Joana Limestone	64	PR-129	Packstone	2.96	-4.69	0.0

					Kinderhookian	Upper *S. crenulata* - *S. isosticha*
253.5	22.63	8.39	14.24	20.24	Kinderhookian	Upper *S. crenulata* - *S. isosticha*
					Kinderhookian	Upper *S. crenulata* - *S. isosticha*
					Kinderhookian	Upper *S. crenulata* - *S. isosticha*
					Kinderhookian	Upper *S. crenulata* - *S. isosticha*
					Kinderhookian	Upper *S. crenulata* - *S. isosticha*
					Kinderhookian	Upper *S. crenulata* - *S. isosticha*
					Kinderhookian	Upper *S. crenulata* - *S. isosticha*
					Kinderhookian	Upper *S. crenulata* - *S. isosticha*
					Kinderhookian	Upper *S. crenulata* - *S. isosticha*
					Kinderhookian	Upper *S. crenulata* - *S. isosticha*
					Kinderhookian	Upper *S. crenulata* - *S. isosticha*
					Kinderhookian	Upper *S. crenulata* - *S. isosticha*
					Kinderhookian	Upper *S. crenulata* - *S. isosticha*
					Kinderhookian	Upper *S. crenulata* - *S. isosticha*
					Kinderhookian	Upper *S. crenulata* - *S. isosticha*
					Kinderhookian	Upper *S. crenulata* - *S. isosticha*
					Kinderhookian	Upper *S. crenulata* - *S. isosticha*
					Kinderhookian	Upper *S. crenulata* - *S. isosticha*
371.6		4.71			Kinderhookian	Upper *S. crenulata* - *S. isosticha*
					Kinderhookian	Upper *S. crenulata* - *S. isosticha*
					Kinderhookian	Upper *S. crenulata* - *S. isosticha*
					Kinderhookian	Upper *S. crenulata* - *S. isosticha*
					Kinderhookian	Upper *S. crenulata* - *S. isosticha*
					Kinderhookian	Upper *S. crenulata* - *S. isosticha*
					Kinderhookian	Upper *S. crenulata* - *S. isosticha*
					Kinderhookian	Upper *S. crenulata* - *S. isosticha*
241.2	24.42	9.91	14.51	18.47	Kinderhookian	Upper *S. crenulata* - *S. isosticha*
					Kinderhookian	Upper *S. crenulata* - *S. isosticha*
435.9		8.04			Kinderhookian	Upper *S. crenulata* - *S. isosticha*

Joana Limestone	65.2	PR-130.2	Grainstone	3.35	-4.35	
Joana Limestone	66.1	PR-131.1	Grainstone	3.16	-4.66	
Joana Limestone	68.1	PR-133.1	Grainstone	3.16	-4.36	
Joana Limestone	69	PR-134	Packstone	3.34	-4.42	25.0
Joana Limestone	70.2	PR-135.2	Grainstone	3.53	-4.48	
Joana Limestone	71	PR-136	Grainstone	3.47	-4.80	
Joana Limestone	72	PR-137	Grainstone	3.37	-5.72	
Joana Limestone	72.9	PR-137.9	Packstone	3.92	-3.26	
Joana Limestone	74.1	PR-139.1	Wackestone	3.80	-3.66	11.0
Joana Limestone	75.1	PR-140.1	Grainstone	3.83	-4.33	
Joana Limestone	76	PR-141	Grainstone	3.79	-4.68	
Joana Limestone	77.3	PR-142.3	Grainstone	3.89	-4.14	
Joana Limestone	78	PR-143	Packstone	3.92	-4.75	
Joana Limestone	79.2	PR-144.2	Packstone	4.18	-3.56	
Joana Limestone	80	PR-145	Wackestone	4.36	-3.49	21.4
Joana Limestone	81.1	PR-146.1	Packstone	4.54	-3.41	
Joana Limestone	82	PR-147	Packstone	4.63	-3.48	
Joana Limestone	83.1	PR-148.1	Wackestone	5.01	-3.23	
Joana Limestone	83.9	PR-148.9	Wackestone	5.39	-3.24	
Joana Limestone	84	PR-149	Wackestone	4.88	-3.70	
Joana Limestone	84.5	PR-149.5	Grainstone	4.90	-4.03	
Joana Limestone	85.2	PR-150.2	Wackestone	4.72	-4.08	
Joana Limestone	85.6	PR-150.6	Wackestone	5.02	-3.22	
Joana Limestone	85.9	PR-150.9	Wackestone	5.24	-3.63	
Joana Limestone	86	PR-151	Wackestone	4.59	-3.30	
Limestone X	86.4	AL-110.4	Lime mudstone	5.23	-4.51	
Limestone X	86.6	AL-110.6	Packstone	5.18	-2.97	
Limestone X	86.8	AL-110.8	Packstone	5.10	-3.61	
Limestone X	87	AL-111	Packstone	6.05	-3.52	
Limestone X	87.2	AL-111.2	Lime mudstone	5.84	-4.56	
Limestone X	87.5	AL-111.5	Lime mudstone	6.70	-3.56	

					Kinderhookian	Upper *S. crenulata - S. isosticha*
					Kinderhookian	Upper *S. crenulata - S. isosticha*
					Kinderhookian	Upper *S. crenulata - S. isosticha*
502.3	21.72	7.91	13.82	15.54	Kinderhookian	Upper *S. crenulata - S. isosticha*
					Kinderhookian	Upper *S. crenulata - S. isosticha*
					Kinderhookian	Upper *S. crenulata - S. isosticha*
					Kinderhookian	Upper *S. crenulata - S. isosticha*
					Kinderhookian	Upper *S. crenulata - S. isosticha*
331.8	23.31	12.10	11.21	23.72	Kinderhookian	Upper *S. crenulata - S. isosticha*
					Kinderhookian	Upper *S. crenulata - S. isosticha*
					Kinderhookian	Upper *S. crenulata - S. isosticha*
					Kinderhookian	Upper *S. crenulata - S. isosticha*
					Kinderhookian	Upper *S. crenulata - S. isosticha*
					Kinderhookian	Upper *S. crenulata - S. isosticha*
56.0	23.46	11.08	12.38	22.46	Kinderhookian	Upper *S. crenulata - S. isosticha*
					Kinderhookian	Upper *S. crenulata - S. isosticha*
					Kinderhookian	Upper *S. crenulata - S. isosticha*
					Kinderhookian	Upper *S. crenulata - S. isosticha*
					Kinderhookian	Upper *S. crenulata - S. isosticha*
					Kinderhookian	Upper *S. crenulata - S. isosticha*
					Kinderhookian	Upper *S. crenulata - S. isosticha*
					Kinderhookian	Upper *S. crenulata - S. isosticha*
					Kinderhookian	Upper *S. crenulata - S. isosticha*
					Kinderhookian	Upper *S. crenulata - S. isosticha*
					Kinderhookian	Upper *S. crenulata - S. isosticha*
					Kinderhookian	Upper *S. crenulata - S. isosticha*
					Kinderhookian	Upper *S. crenulata - S. isosticha*
					Kinderhookian	Upper *S. crenulata - S. isosticha*
					Kinderhookian	Upper *S. crenulata - S. isosticha*
					Kinderhookian	Upper *S. crenulata - S. isosticha*
					Kinderhookian	Upper *S. crenulata - S. isosticha*

Limestone X	88	AL-112	Lime mudstone	6.80	-3.52	0.0
Limestone X	89.1	AL-113.1	Lime mudstone	6.90	-3.48	
Limestone X	90.6	AL-114.6	Wackestone	6.90	-3.72	
Limestone X	91.3	AL-115.3	Lime mudstone	6.80	-3.41	43.1
Limestone X	92.1	AL-116.1	Wackestone	6.70	-3.09	
Limestone X	93.2	AL-117.2	Wackestone	6.75	-3.01	
Limestone X	94.5	AL-118.5	Wackestone	6.64	-3.23	
Limestone X	96	AL-120	Wackestone	6.53	-3.43	115.0
Limestone X	98.8	AL-122.8	Wackestone	6.42	-3.27	
Limestone X	100.2	AL-124.2	Grainstone	6.11	-2.71	
Limestone X	102	AL-126	Wackestone	5.62	-2.85	24.2
Limestone X	103.2	AL-127.2	Wackestone	5.46	-3.35	
Limestone X	105	AL-129	Wackestone	5.29	-3.12	
Limestone X	106.5	AL-130.5	Wackestone	5.48	-1.99	
Limestone X	107.2	AL-131.2	Wackestone	5.25	-2.32	10.0
Limestone X	108.1	AL-132.1	Wackestone	5.01	-2.64	
Limestone X	109.5	AL-133.5	Wackestone	5.37	-2.13	
Limestone X	111	AL-135	Wackestone	4.39	-4.15	
Limestone X	112.5	AL-136.5	Wackestone	4.90	-3.08	
Limestone X	113.5	AL-137.5	Wackestone	4.75	-3.37	206.9
Limestone X	114.1	AL-138.1	Wackestone	4.60	-3.66	
Limestone X	115.7	AL-139.7	Wackestone	4.08	-4.78	
Limestone X	117	AL-141	Wackestone	4.60	-3.31	
Limestone X	117.7	AL-141.7	Lime mudstone	4.65	-3.76	10.0
Limestone X	119.1	AL-143.1	Wackestone	4.70	-4.20	
Limestone X	120.1	AL-144.1	Packstone	5.01	-3.94	
Limestone X	121.7	AL-145.7	Wackestone	5.12	-3.93	14.0
Limestone X	122.5	AL-146.5	Grainstone	5.23	-3.91	
Limestone X	123.2	AL-147.2	Grainstone	5.55	-3.45	
Limestone X	124.5	AL-148.5	Grainstone	5.79	-2.88	
Limestone X	126	AL-150	Grainstone	5.75	-3.87	

71.0		10.10			Kinderhookian	Upper *S. crenulata - S. isosticha*
					Kinderhookian	Upper *S. crenulata - S. isosticha*
					Kinderhookian	Upper *S. crenulata - S. isosticha*
56.0	23.00	2.22	20.77	19.65	Kinderhookian	Upper *S. crenulata - S. isosticha*
					Kinderhookian	Upper *S. crenulata - S. isosticha*
					Kinderhookian	Upper *S. crenulata - S. isosticha*
					Kinderhookian	Upper *S. crenulata - S. isosticha*
747.3	22.23	-1.67	23.90	20.19	Kinderhookian	Upper *S. crenulata - S. isosticha?*
					Kinderhookian	Upper *S. crenulata - S. isosticha?*
					Kinderhookian	Upper *S. crenulata - S. isosticha?*
450.4	21.03			18.61	Kinderhookian	Upper *S. crenulata - S. isosticha?*
					Kinderhookian	Upper *S. crenulata - S. isosticha?*
					Kinderhookian	Upper *S. crenulata - S. isosticha?*
					Kinderhookian	Upper *S. crenulata - S. isosticha?*
202.9	22.98	-3.70	26.69	18.18	Kinderhookian	Upper *S. crenulata - S. isosticha?*
					Kinderhookian	Upper *S. crenulata - S. isosticha?*
					Kinderhookian	Upper *S. crenulata - S. isosticha?*
					Kinderhookian	Upper *S. crenulata - S. isosticha?*
					Kinderhookian	Upper *S. crenulata - S. isosticha?*
365.4	12.21	-3.29	15.51		Kinderhookian	Upper *S. crenulata - S. isosticha?*
					Kinderhookian	Upper *S. crenulata - S. isosticha?*
					Kinderhookian	Upper *S. crenulata - S. isosticha?*
					Kinderhookian	Upper *S. crenulata - S. isosticha?*
197.2	26.32	-12.38	38.71	18.98	Kinderhookian	Upper *S. crenulata - S. isosticha?*
					Kinderhookian	Upper *S. crenulata - S. isosticha?*
					Kinderhookian	Upper *S. crenulata - S. isosticha?*
110.1	29.23	-15.59	44.82	19.18	Kinderhookian	Upper *S. crenulata - S. isosticha?*
					Kinderhookian	Upper *S. crenulata - S. isosticha?*
					Kinderhookian	Upper *S. crenulata - S. isosticha?*
					Kinderhookian	Upper *S. crenulata - S. isosticha?*
					Kinderhookian	Upper *S. crenulata - S. isosticha?*

Limestone X	127	AL-151	Wackestone	5.72	-3.82	
Limestone X	128	AL-152	Packstone	5.73	-2.79	84.8
Limestone X	129.2	AL-153.2	Packstone	5.74	-3.89	
Limestone X	130.5	AL-154.5	Wackestone	5.94	-4.75	10.0
Limestone X	133.1	AL-157.1	Wackestone	6.24	-3.01	
Limestone X	134.5	AL-158.5	Wackestone	6.07	-3.49	
Limestone X	135	AL-159	Wackestone	6.18	-3.38	87.7
Limestone X	136	AL-160	Wackestone	6.28	-3.26	
Limestone X	139.5	AL-163.5	Wackestone	5.83	-3.47	35.6
Limestone X	141.1	AL-165.1	Wackestone	6.04	-3.29	
Limestone X	141.9	AL-165.9	Wackestone	5.96	-3.45	
Limestone X	143.1	AL-167.1	Wackestone	5.89	-6.42	
Limestone X	144.5	AL-168.5	Wackestone	5.61	-3.47	135.5
Limestone X	147.1	AL-171.1	Wackestone	6.08	-3.34	
Limestone X	148.5	AL-172.5	Wackestone	5.37	-4.20	
Limestone X	149.9	AL-173.9	Grainstone	6.18	0.26	
Limestone X	151.6	AL-175.6	Wackestone	6.98	-1.67	85.3
Limestone X	152.9	AL-176.9	Wackestone	6.36	-3.60	
Limestone X	155.5	AL-179.5	Wackestone	6.55	-5.18	
Limestone X	157	AL-181	Wackestone	6.86	-3.93	145.0
Limestone X	158.3	AL-182.3	Wackestone	6.94	-3.92	
Limestone X	159.8	AL-183.8	Wackestone	7.02	-3.91	
Limestone X	161.1	AL-185.1	Lime mudstone	7.00	-3.66	106.2
Limestone X	162.4	AL-186.4	Lime mudstone	6.98	-3.40	
Limestone X	165	AL-189	Lime mudstone	6.63	-4.30	
Limestone X	166.5	AL-190.5	Lime mudstone	6.74	-3.54	
Limestone X	167.5	AL-191.5	Lime mudstone	6.85	-3.55	0.0
Limestone X	169.1	AL-193.1	Wackestone	6.56	-4.29	
Limestone X	170.8	AL-194.8	Wackestone	6.41	-3.68	77.4
Limestone X	172.2	AL-196.2	Wackestone	6.43	-3.05	
Limestone X	174.2	AL-198.2	Wackestone	5.77	-2.63	0.0
Limestone X	175.5	AL-199.5	Lime mudstone	6.02	-3.06	
Limestone X	175.6	AL-199.6	Lime mudstone	6.15	-3.27	38.6
Limestone X	176	AL-200	Lime mudstone	6.21	-3.37	
Limestone X	177.9	AL-201.9	Wackestone	6.27	-3.48	
Limestone X	179	AL-203	Wackestone	6.25	-3.46	
Limestone X	181	AL-205	Lime mudstone	6.35	-1.39	
Limestone X	183	AL-207	Wackestone	6.45	0.69	
Limestone X	184	AL-208	Wackestone	6.41	-1.69	
Limestone X	186.3	AL-210.3	Wackestone	6.88	-2.04	65.8
Limestone X	188.2	AL-212.2	Wackestone	6.64	-2.67	
Limestone X	189.5	AL-213.5	Wackestone	6.60	-2.94	31.7
Limestone X	190.7	AL-214.7	Wackestone	6.50	-3.24	
Limestone X	192.4	AL-216.4	Wackestone	6.39	-3.98	
Limestone X	194.5	AL-218.5	Wackestone	6.27	-3.44	35.0
Limestone X	196.1	AL-220.1	Wackestone	6.29	-2.41	
Limestone X	198.2	AL-222.2	Wackestone	6.15	-2.91	
Limestone X	200	AL-224	Wackestone	6.18	-3.06	51.4
Limestone X	202.2	AL-226.2	Wackestone	6.20	-3.21	
Limestone X	202.5	AL-226.5	Wackestone	6.11	-3.24	100.2
Limestone X	203.5	AL-227.5	Wackestone	6.02	-3.27	
Limestone X	205	AL-229	Lime mudstone	5.92	-3.30	12.0
Limestone X	207	AL-231	Wackestone	5.83	-3.33	
Limestone X	209.7	AL-233.7	Lime mudstone	5.49	-3.36	
Limestone X	210.9	AL-234.9	Lime mudstone	5.50	-3.17	57.1
Limestone X	212.1	AL-236.1	Lime mudstone	5.35	-4.19	
Limestone X	213.2	AL-237.2	Wackestone	5.46	-3.09	

					Kinderhookian	Upper *S. crenulata - S. isosticha?*
185.3	25.58	7.26	18.32	21.22	Kinderhookian	Upper *S. crenulata - S. isosticha?*
					Kinderhookian	Upper *S. crenulata - S. isosticha?*
130.8	25.05	9.82	15.23	15.73	Kinderhookian	Upper *S. crenulata - S. isosticha?*
					Kinderhookian	Upper *S. crenulata - S. isosticha?*
					Kinderhookian	Upper *S. crenulata - S. isosticha?*
165.2	25.59	8.31	17.28	21.06	Osagean	*G. typicus*
					Osagean	*G. typicus*
191.1	24.75	10.37	14.37	18.24	Osagean	*G. typicus*
					Osagean	*G. typicus*
					Osagean	*G. typicus*
					Osagean	*G. typicus*
397.9	23.14	4.09	19.05	18.21	Osagean	*G. typicus*
					Osagean	*G. typicus*
					Osagean	*G. typicus*
					Osagean	*G. typicus*
458.9	23.19	6.79	16.40	18.83	Osagean	*G. typicus*
					Osagean	*G. typicus*
					Osagean	*G. typicus*
310.1	23.67	8.77	14.90	22.24	Osagean	*G. typicus*
					Osagean	*G. typicus*
					Osagean	*G. typicus*
674.1	26.80	12.07	14.73	21.97	Osagean	*G. typicus*
					Osagean	*G. typicus*
					Osagean	*G. typicus*
					Osagean	*G. typicus*
80.0					Osagean	*G. typicus*
					Osagean	*G. typicus*
292.2	22.01	7.54	14.47	18.11	Osagean	*G. typicus*
					Osagean	*G. typicus*
2552.6		9.20			Osagean	*G. typicus*
					Osagean	*G. typicus*
299.0	21.36	15.27	6.09	18.10	Osagean	*G. typicus*
					Osagean	*G. typicus*
					Osagean	*G. typicus*
					Osagean	*G. typicus*
					Osagean	*G. typicus*
					Osagean	*G. typicus*
					Osagean	*G. typicus*
137.7	20.71	7.91	12.80	15.39	Osagean	*G. typicus*
					Osagean	*G. typicus*
943.3	20.72	7.60	13.12	15.85	Osagean	*G. typicus*
					Osagean	*G. typicus*
					Osagean	*G. typicus*
1229.8	17.91	6.42	11.50	15.57	Osagean	*G. typicus*
					Osagean	*G. typicus*
					Osagean	*G. typicus*
878.6		4.56		16.80	Osagean	*G. typicus*
					Osagean	*G. typicus*
1532.7	16.86	3.67	13.19		Osagean	*G. typicus*
					Osagean	*G. typicus*
196.9	20.56	8.73	11.84	17.33	Osagean	*G. typicus*
					Osagean	*G. typicus*
					Osagean	*G. typicus*
1633.5	18.88	8.48	10.40	15.73	Osagean	*G. typicus*
					Osagean	*G. typicus*
					Osagean	*G. typicus*

Limestone X	213.7	AL-237.7	Wackestone	5.61	-2.65	
Limestone X	215.5	AL-239.5	Lime mudstone	5.76	-2.20	164.6
Limestone X	216.9	AL-240.9	Lime mudstone	5.45	-2.93	
Limestone X	218.5	AL-242.5	Wackestone	5.47	-2.89	
Limestone X	220	AL-244	Wackestone	5.36	-2.97	77.0
Limestone X	222	AL-246	Lime mudstone	5.25	-3.04	
Limestone X	225.5	AL-249.5	Lime mudstone	4.87	-3.51	
Limestone X	228.9	AL-252.9	Lime mudstone	4.63	-4.06	
Limestone X	230	AL-254	Lime mudstone	5.03	-3.35	62.8
Limestone X	231.7	AL-255.7	Wackestone	4.85	-3.26	
Limestone X	234	AL-258	Wackestone	4.57	-3.43	
Limestone X	236.7	AL-260.7	Wackestone	4.48	-3.28	
Limestone X	237	AL-261	Wackestone	4.29	-3.28	0.0
Limestone X	237.5	AL-261.5	Wackestone	4.10	-3.29	
Limestone X	239.2	AL-263.2	Lime mudstone	3.85	-3.28	
Limestone X	241	PR2-0	Wackestone	4.33	-3.68	12.0
Limestone X	242	PR2-1	Wackestone	4.00	-3.46	
Limestone X	242.5	AL-266.5	Lime mudstone	3.58	-3.15	
Limestone X	243.5	PR2-2.5	Wackestone	4.57	-2.74	
Limestone X	244	PR2-3	Lime mudstone	4.28	-3.31	
Limestone X	244.3	AL-268.3	Lime mudstone	3.51	-3.98	
Limestone X	245	PR2-4	Lime mudstone	4.31	-3.38	
Limestone X	246	PR2-5	Lime mudstone	4.23	-2.97	0.0
Limestone X	246.5	AL-270.5	Lime mudstone	4.05	-3.06	
Limestone X	247	PR2-6	Wackestone	3.87	-3.15	
Limestone X	248	AL-272	Lime mudstone	3.37	-3.07	0.0
Limestone X	248	PR2-7	Lime mudstone	3.85	-2.82	
Limestone X	249	PR2-8	Wackestone	3.07	-3.81	
Limestone X	249.4	AL-273.4	Wackestone	3.07	-3.60	
Limestone X	250	PR2-9	Lime mudstone	3.66	-3.23	
Limestone X	251	PR2-10	Lime mudstone	3.00	-3.28	0.0
Limestone X	251.8	AL-275.8	Wackestone	2.52	-3.64	97.3
Limestone X	252	PR2-11	Lime mudstone	2.81	-3.09	
Limestone X	253	PR2-12	Wackestone	2.27	-3.41	
Limestone X	253.1	AL-277.1	Wackestone	2.52	-3.43	
Limestone X	254	PR2-13	Wackestone	2.76	-3.46	
Limestone X	254.5	AL-278.5	Lime mudstone	2.52	-4.46	36.7
Limestone X	255	PR2-14	Wackestone	2.96	-3.48	
Limestone X	256.3	AL-280.3	Wackestone	2.04	-4.17	
Limestone X	257	PR2-16	Lime mudstone	1.70	-3.45	24.3
Limestone X	258	AL-282	Lime mudstone	1.82	-4.39	
Limestone X	258	PR2-17	Lime mudstone	2.17	-3.68	
Limestone X	259	PR2-18	Lime mudstone	2.75	-4.17	
Limestone X	260	PR2-19	Lime mudstone	1.65	-4.78	
Limestone X	261	PR2-20	Lime mudstone	2.20	-4.88	0.0
Limestone X	262	PR2-21	Lime mudstone	2.14	-4.18	
Limestone X	263	PR2-22	Wackestone	1.83	-3.37	
Limestone X	264	PR2-23	Wackestone	1.23	-4.56	
Limestone X	265	PR2-24	Wackestone	1.57	-4.41	
Limestone X	266	PR2-25	Wackestone	0.92	-4.93	

					Osagean	*G. typicus*
729.9	17.82	4.28	13.54	15.46	Osagean	*G. typicus*
					Osagean	*G. typicus*
					Osagean	*G. typicus*
150.0	14.51				Osagean	*G. typicus*
					Osagean	*G. typicus*
					Osagean	*G. typicus*
					Osagean	*G. typicus*
623.6	20.88	4.71	16.17	16.73	Osagean	*G. typicus*
					Osagean	*G. typicus*
					Osagean	*G. typicus*
					Osagean	*G. typicus*
204.0		7.33			Osagean	*G. typicus*
					Osagean	*G. typicus*
					Osagean	*G. typicus*
279.7	20.70	6.84	13.86	18.68	Osagean	*G. typicus*
					Osagean	*G. typicus*
					Osagean	*G. typicus*
					Osagean	*G. typicus*
					Osagean	*G. typicus*
					Osagean	*G. typicus*
					Osagean	*G. typicus*
133.5		6.06			Osagean	*G. typicus*
					Osagean	*G. typicus*
					Osagean	*G. typicus*
220.2		5.54			Osagean	*G. typicus*
					Osagean	*G. typicus*
					Osagean	*G. typicus*
					Osagean	*G. typicus*
					Osagean	*G. typicus*
100.0					Osagean	*G. typicus*
368.0	19.37	2.32	17.05	17.06	Osagean	*G. typicus*
					Osagean	*G. typicus*
					Osagean	*G. typicus*
					Osagean	*G. typicus*
					Osagean	*G. typicus*
138.9	19.94	5.49	14.44		Osagean	*G. typicus*
					Osagean	*G. typicus*
					Osagean	*G. typicus*
451.0	17.18	-0.76	17.93	17.38	Osagean	*G. typicus*
					Osagean	*G. typicus*
					Osagean	*G. typicus*
					Osagean	*G. typicus*
					Osagean	*G. typicus*
100.0					Osagean	*G. typicus*
					Osagean	*G. typicus*
					Osagean	*G. typicus*
					Osagean	*G. typicus*
					Osagean	*G. typicus*
					Osagean	*G. typicus*

Section 2: Mountain Home section, Utah (GPS location: 38 35' 43" N, 113 56' 19" W)

Strat. Unit	Strat. Height (m)	Sample No.	Lithology	$\delta^{13}C_{carb}$ (‰,VPDB)	$\delta^{18}O_{carb}$ (‰,VPDB)	CAS (ppm)
Joana Limestone	0	MH-0	Packstone	1.03	-6.91	
Joana Limestone	0.6	MH-0.6	Wackestone	1.30	-5.53	11.0
Joana Limestone	1	MH-1	Packstone	0.93	-6.88	
Joana Limestone	2.2	MH-2.2	Wackestone	1.27	-5.79	36.6
Joana Limestone	3	MH-3	Packstone	0.90	-6.84	
Joana Limestone	4	MH-4	Wackestone	1.63	-6.86	
Joana Limestone	5.1	MH-5.1	Wackestone	1.74	-6.41	30.7
Joana Limestone	6	MH-6	Wackestone	1.87	-6.52	
Joana Limestone	7	MH-7	Grainstone	1.90	-6.50	
Joana Limestone	8.6	MH-8.6	Wackestone	2.18	-6.26	
Joana Limestone	9.3	MH-9.3	Wackestone	2.37	-6.01	
Joana Limestone	10.9	MH-10.9	Packstone	2.12	-7.63	
Joana Limestone	12	MH-12	Grainstone	2.31	-6.99	
Joana Limestone	13.2	MH-13.2	Wackestone	1.98	-6.82	
Joana Limestone	14	MH-14	Wackestone	2.24	-6.72	
Joana Limestone	15.7	MH-15.7	Grainstone	1.44	-7.15	31.0
Joana Limestone	15.8	MH-15.8	Wackestone	1.58	-7.05	
Joana Limestone	16	MH-16	Packstone	1.72	-6.96	
Joana Limestone	17.5	MH-17.5	Wackestone	1.58	-6.95	
Joana Limestone	18.1	MH-18.1	Wackestone	1.51	-6.82	
Joana Limestone	19	MH-19	Wackestone	1.75	-6.73	
Joana Limestone	20.2	MH-20.2	Wackestone	1.45	-7.16	5.0
Joana Limestone	21.3	MH-21.3	Grainstone	1.95	-7.78	
Joana Limestone	22	MH-22	Wackestone	1.33	-7.08	0.0
Joana Limestone	22.9	MH-22.9	Grainstone	1.47	-7.67	
Joana Limestone	24	MH-24	Wackestone	1.09	-7.40	0.0
Joana Limestone	25	MH-25	Grainstone	1.65	-7.75	
Joana Limestone	26	MH-26	Wackestone	2.53	-7.06	

FeS_2 (ppm)	$\delta^{34}S_{CAS}$ (‰, CDT)	$\delta^{34}S_{PY}$ (‰,CDT)	$\Delta^{34}S_{CAS-PY}$	$\delta^{18}O_{CAS}$ (‰,VSMOW)	Age	Conodont zone*
					Kinderhookian	*S. crenulata - isosticha*
89.0	21.18	7.26	13.92	16.17	Kinderhookian	*S. crenulata - isosticha*
					Kinderhookian	*S. crenulata - isosticha*
312.1	20.84	7.96	12.88		Kinderhookian	*S. crenulata - isosticha*
					Kinderhookian	*S. crenulata - isosticha*
					Kinderhookian	*S. crenulata - isosticha*
482.2	9.63	-6.80	16.44	12.66	Kinderhookian	*S. crenulata - isosticha*
					Kinderhookian	*S. crenulata - isosticha*
					Kinderhookian	*S. crenulata - isosticha*
					Kinderhookian	*S. crenulata - isosticha*
					Kinderhookian	*S. crenulata - isosticha*
					Kinderhookian	*S. crenulata - isosticha*
					Kinderhookian	*S. crenulata - isosticha*
					Kinderhookian	*S. crenulata - isosticha*
					Kinderhookian	*S. crenulata - isosticha*
459.4	13.44	-8.90	22.34	11.64	Kinderhookian	*S. crenulata - isosticha*
					Kinderhookian	*S. crenulata - isosticha*
					Kinderhookian	*S. crenulata - isosticha*
					Kinderhookian	*S. crenulata - isosticha*
					Kinderhookian	*S. crenulata - isosticha*
					Kinderhookian	*S. crenulata - isosticha*
48.0	23.36	4.48	18.88	15.84	Kinderhookian	*S. crenulata - isosticha*
					Kinderhookian	*S. crenulata - isosticha*
80.0		10.54			Kinderhookian	*S. crenulata - isosticha*
					Kinderhookian	*S. crenulata - isosticha*
23.0					Kinderhookian	*S. crenulata - isosticha*
					Kinderhookian	*S. crenulata - isosticha*
					Kinderhookian	*S. crenulata - isosticha*

Joana Limestone	27	MH-27	Grainstone	2.06	-6.90	
Joana Limestone	28	MH-28	Wackestone	1.81	-7.28	66.2
Joana Limestone	29	MH-29	Grainstone	1.77	-8.15	
Joana Limestone	30	MH-30	Wackestone	1.70	-8.24	
Joana Limestone	31.2	MH-31.2	Wackestone	1.83	-7.27	0.0
Joana Limestone	32	MH-32	Packstone	1.82	-7.25	
Joana Limestone	33	MH-33	Wackestone	2.71	-6.05	
Joana Limestone	34	MH-34	Wackestone	2.76	-5.69	
Joana Limestone	35	MH-35	Wackestone	2.30	-6.53	0.0
Joana Limestone	37.5	MH-37.5	Grainstone	1.84	-7.37	
Joana Limestone	38	MH-38	Grainstone	1.42	-7.19	
Joana Limestone	39	MH-39	Wackestone	1.62	-5.84	0.0
Joana Limestone	39.5	MH-39.5	Packstone	1.60	-5.28	
Joana Limestone	40.5	MH-40.5	Packstone	1.84	-5.90	
Joana Limestone	41.3	MH-41.3	Wackestone	1.42	-5.69	0.0
Joana Limestone	42	MH-42	Grainstone	1.45	-7.20	
Joana Limestone	42.5	MH-42.5	Wackestone	1.41	-7.26	
Joana Limestone	43	MH-43	Lime mudstone	2.31	-6.26	
Joana Limestone	43.5	MH-43.5	Lime mudstone	3.18	-6.49	
Joana Limestone	44	MH-44	Lime mudstone	2.18	-6.81	
Joana Limestone	44.5	MH-44.5	Lime mudstone	1.85	-6.63	
Joana Limestone	45	MH-45	Lime mudstone	2.04	-6.58	0.0
Joana Limestone	45.6	MH-45.6	Lime mudstone	2.26	-6.64	
Joana Limestone	46	MH-46	Lime mudstone	1.63	-6.38	
Joana Limestone	46.5	MH-46.5	Lime mudstone	2.51	-7.72	
Joana Limestone	47	MH-47	Lime mudstone	2.45	-6.68	
Joana Limestone	48	MH-48	Lime mudstone	2.23	-6.44	
Joana Limestone	48.5	MH-48.5	Lime mudstone	3.16	-7.22	
Joana Limestone	49	MH-49	Lime mudstone	2.39	-5.54	
Joana Limestone	49.9	MH-49.9	Lime mudstone	1.43	-7.31	
Joana Limestone	50.6	MH-50.6	Lime mudstone	2.78	-7.45	

					Kinderhookian	*S. crenulata - isosticha*
30.0	22.17	15.82	6.34	20.93	Kinderhookian	*S. crenulata - isosticha*
					Kinderhookian	*S. crenulata - isosticha*
					Kinderhookian	*S. crenulata - isosticha*
35.0		18.94			Kinderhookian	*S. crenulata - isosticha*
					Kinderhookian	*S. crenulata - isosticha*
					Kinderhookian	*S. crenulata - isosticha*
					Kinderhookian	*S. crenulata - isosticha*
50.4		5.68			Kinderhookian	*S. crenulata - isosticha*
					Kinderhookian	*S. crenulata - isosticha*
					Kinderhookian	*S. crenulata - isosticha*
44.2		10.70			Kinderhookian	*S. crenulata - isosticha*
					Kinderhookian	*S. crenulata - isosticha*
					Kinderhookian	*S. crenulata - isosticha*
44.0					Kinderhookian	*S. crenulata - isosticha*
					Kinderhookian	*S. crenulata - isosticha*
					Kinderhookian	*S. crenulata - isosticha*
					Kinderhookian	*S. crenulata - isosticha*
					Kinderhookian	*S. crenulata - isosticha*
					Kinderhookian	*S. crenulata - isosticha*
184.8		13.20			Kinderhookian	*S. crenulata - isosticha*
					Kinderhookian	*S. crenulata - isosticha*
					Kinderhookian	*S. crenulata - isosticha*
					Kinderhookian	*S. crenulata - isosticha*
					Kinderhookian	*S. crenulata - isosticha*
					Kinderhookian	*S. crenulata - isosticha*
					Kinderhookian	*S. crenulata - isosticha*
					Kinderhookian	*S. crenulata - isosticha*
					Kinderhookian	*S. crenulata - isosticha*

Joana Limestone	51	MH-51	Lime mudstone	2.19	-5.70	
Joana Limestone	51.5	MH-51.5	Lime mudstone	2.82	-6.03	
Joana Limestone	52	MH-52	Lime mudstone	3.05	-6.64	
Joana Limestone	52.6	MH-52.6	Lime mudstone	3.22	-5.94	
Joana Limestone	53	MH-53	Lime mudstone	2.66	-6.30	
Joana Limestone	53.2	MH-53.2	Packstone	2.40	-6.54	461.0
Joana Limestone	53.5	MH-53.5	Grainstone	2.15	-6.78	
Joana Limestone	54.1	MH-54.1	Grainstone	2.41	-6.79	
Joana Limestone	54.2	MH-54.2	Wackestone	3.13	-5.86	
Joana Limestone	54.5	MH-54.5	Grainstone	3.85	-4.92	
Joana Limestone	55	MH-55	Lime mudstone	2.51	-6.56	
Joana Limestone	55.5	MH-55.5	Grainstone	4.17	-5.44	
Joana Limestone	56	MH-56	Grainstone	3.75	-4.07	
Joana Limestone	56.5	MH-56.5	Grainstone	3.76	-4.30	
Joana Limestone	57	MH-57	Grainstone	3.91	-5.18	
Joana Limestone	58	MH-58	Wackestone	4.04	-4.41	322.3
Joana Limestone	58.5	MH-58.5	Grainstone	3.71	-5.27	
Joana Limestone	59.5	MH-59.5	Grainstone	3.41	-5.48	
Joana Limestone	60	MH-60	Packstone	3.29	-4.51	
Joana Limestone	60.1	MH-60.1	Grainstone	3.16	-3.54	56.7
Joana Limestone	61	MH-61	Wackestone	3.76	-3.65	
Joana Limestone	61.5	MH-61.5	Wackestone	3.81	-3.28	
Joana Limestone	62	MH-62	Packstone	4.35	-3.49	0.0
Joana Limestone	62.5	MH-62.5	Wackestone	3.72	-4.39	
Joana Limestone	64	MH-64	Wackestone	4.32	-3.51	136.6
Joana Limestone	64.5	MH-64.5	Wackestone	3.22	-3.59	
Joana Limestone	65	MH-65	Wackestone	4.50	-3.72	
Joana Limestone	65.5	MH-65.5	Packstone	4.59	-3.46	
Joana Limestone	66.1	MH-66.1	Wackestone	4.67	-3.20	0.0
Joana Limestone	66.5	MH-66.5	Wackestone	4.85	-3.18	
Joana Limestone	67	MH-67	Wackestone	3.78	-4.55	

					Kinderhookian	*S. crenulata - isosticha*
					Kinderhookian	*S. crenulata - isosticha*
					Kinderhookian	*S. crenulata - isosticha*
					Kinderhookian	*S. crenulata - isosticha*
					Kinderhookian	*S. crenulata - isosticha*
50.0	22.89	18.06	4.83	18.30	Kinderhookian	*S. crenulata - isosticha*
					Kinderhookian	*S. crenulata - isosticha*
					Kinderhookian	*S. crenulata - isosticha*
					Kinderhookian	*S. crenulata - isosticha*
					Kinderhookian	*S. crenulata - isosticha*
					Kinderhookian	*S. crenulata - isosticha*
					Kinderhookian	*S. crenulata - isosticha*
					Kinderhookian	*S. crenulata - isosticha*
					Kinderhookian	*S. crenulata - isosticha*
					Kinderhookian	*S. crenulata - isosticha*
836.1	23.45	16.50	6.94	25.86	Kinderhookian	*S. crenulata - isosticha*
					Kinderhookian	*S. crenulata - isosticha*
					Kinderhookian	*S. crenulata - isosticha*
				22.30	Kinderhookian	*S. crenulata - isosticha*
173.2	23.16	5.34	17.82		Kinderhookian	*S. crenulata - isosticha*
					Kinderhookian	*S. crenulata - isosticha*
					Kinderhookian	*S. crenulata - isosticha*
100.2		2.48			Kinderhookian	*S. crenulata - isosticha*
					Kinderhookian	*S. crenulata - isosticha*
2047.9	21.26	5.03	16.24	24.47	Kinderhookian	*S. crenulata - isosticha*
					Kinderhookian	*S. crenulata - isosticha*
					Kinderhookian	*S. crenulata - isosticha*
					Kinderhookian	*S. crenulata - isosticha*
57.2		-0.13			Kinderhookian	*S. crenulata - isosticha*
					Kinderhookian	*S. crenulata - isosticha*
					Kinderhookian	*S. crenulata - isosticha*

Joana Limestone	67.5	MH-67.5	Wackestone	3.65	-3.91	
Joana Limestone	68	MH-68	Packstone	3.69	-4.07	
Joana Limestone	68.5	MH-68.5	Packstone	3.93	-3.85	
Joana Limestone	69.5	MH-69.5	Grainstone	4.49	-4.51	
Joana Limestone	69.8	MH-69.8	Grainstone	5.00	-4.25	
Joana Limestone	70.5	MH-70.5	Grainstone	4.72	-4.71	
Joana Limestone	71	MH-71	Grainstone	5.25	-3.75	
Joana Limestone	71.8	MH-71.8	Wackestone	5.07	-4.24	0.0
Joana Limestone	73	MH-73	Grainstone	4.97	-4.08	
Joana Limestone	74.3	MH-74.3	Grainstone	5.19	-4.61	
Joana Limestone	75	MH-75	Wackestone	4.34	-4.47	90.1
Joana Limestone	75.5	MH-75.5	Grainstone	5.20	-4.66	
Joana Limestone	76	MH-76	Packstone	5.50	-3.38	
Joana Limestone	76.5	MH-76.5	Packstone	4.72	-3.29	
Joana Limestone	77.2	MH-77.2	Packstone	3.92	-3.88	
Joana Limestone	77.5	MH-77.5	Wackestone	5.12	-2.60	88.5
Joana Limestone	82	MH-82	Wackestone	4.20	-4.15	0.0
Joana Limestone	82.4	MH-82.4	Wackestone	4.83	-3.94	
Joana Limestone	82.5	MH-82.5	Wackestone	5.46	-3.73	
Joana Limestone	83	MH-83	Wackestone	4.03	-3.69	
Joana Limestone	83.5	MH-83.5	Wackestone	3.89	-3.61	
Joana Limestone	84.5	MH-84.5	Wackestone	3.02	-4.01	
Joana Limestone	84.6	MH-84.6	Wackestone	3.52	-4.30	0.0
Joana Limestone	86	MH-86	Wackestone	4.02	-4.59	0.0
Joana Limestone	88	MH-88	Grainstone	5.25	-3.07	
Joana Limestone	90	MH-90	Packstone	4.01	-4.29	62.1
Joana Limestone	90.5	MH-90.5	Grainstone	3.74	-3.07	
Joana Limestone	92	MH-92	Wackestone	3.97	-3.31	16.2
Joana Limestone	94.1	MH-94.1	Wackestone	4.20	-3.54	
Joana Limestone	95	MH-95	Wackestone	3.73	-3.14	
Joana Limestone	95.5	MH-95.5	Packstone	2.91	-4.78	
Joana Limestone	96.1	MH-96.1	Packstone	2.91	-4.98	
Joana Limestone	96.5	MH-96.5	Wackestone	3.21	-4.90	0.0
Joana Limestone	98	MH-98	Lime mudstone	3.50	-4.82	
Joana Limestone	99.9	MH-99.9	Wackestone	3.65	-3.53	0.0
Joana Limestone	102	MH-102	Grainstone	3.78	-4.16	
Joana Limestone	105	MH-105	Wackestone	3.18	-3.58	60.0
Joana Limestone	107	MH-107	Lime mudstone	2.82	-3.33	0.0
Joana Limestone	107.5	MH-107.5	Grainstone	2.95	-4.05	
Joana Limestone	108	MH-108	Grainstone	3.10	-3.96	
Joana Limestone	108.5	MH-108.5	Grainstone	1.91	-3.48	
Joana Limestone	109	MH-109	Wackestone	1.52	-3.92	15.4
Joana Limestone	111	MH-111	Wackestone	1.61	-5.39	0.0
Joana Limestone	112.4	MH-112.4	Wackestone	1.78	-5.25	
Joana Limestone	112.8	MH-112.8	Wackestone	1.95	-5.12	64.9
Joana Limestone	113.5	MH-113.5	Wackestone	1.78	-5.12	
Joana Limestone	113.6	MH-113.6	Grainstone	1.61	-5.13	
Joana Limestone	113.9	MH-113.9	Grainstone	1.45	-5.13	
Joana Limestone	115	MH-115	Wackestone	1.28	-5.13	0.0
Joana Limestone	117.4	MH-117.4	Grainstone	0.64	-5.78	
Joana Limestone	119.4	MH-119.4	Packstone	0.60	-5.22	0.0
Joana Limestone	121.3	MH-121.3	Packstone	0.23	-5.22	91.0
Joana Limestone	122.9	MH-122.9	Packstone	0.99	-4.68	
Joana Limestone	124.9	MH-124.9	Wackestone	0.86	-4.90	
Joana Limestone	125.5	MH-125.5	Wackestone	0.61	-4.45	
Joana Limestone	126	MH-126	Wackestone	0.99	-4.94	

					Kinderhookian	*S. crenulata - isosticha*
					Kinderhookian	*S. crenulata - isosticha*
					Kinderhookian	*S. crenulata - isosticha*
					Kinderhookian	*S. crenulata - isosticha*
					Kinderhookian	*S. crenulata - isosticha*
					Kinderhookian	*S. crenulata - isosticha*
					Kinderhookian	*S. crenulata - isosticha*
45.0		19.88			Osagean	*G. typicus* ?
					Osagean	*G. typicus* ?
					Osagean	*G. typicus* ?
239.0	22.18	12.58	9.60	21.71	Osagean	*G. typicus* ?
					Osagean	*G. typicus* ?
					Osagean	*G. typicus* ?
					Osagean	*G. typicus* ?
					Osagean	*G. typicus* ?
119.1	20.67	6.38	14.29	20.36	Osagean	*G. typicus* ?
49.6		5.28			Osagean	*G. typicus* ?
					Osagean	*G. typicus*
					Osagean	*G. typicus*
					Osagean	*G. typicus*
					Osagean	*G. typicus*
					Osagean	*G. typicus*
109.8		9.70			Osagean	*G. typicus*
40.9					Osagean	*G. typicus*
					Osagean	*G. typicus*
113.4	20.53	10.25	10.28	20.46	Osagean	*G. typicus*
					Osagean	*G. typicus*
100.0	19.15	7.72	11.44	19.21	Osagean	*G. typicus*
					Osagean	*G. typicus*
					Osagean	*G. typicus*
					Osagean	*G. typicus*
					Osagean	*G. typicus*
147.7		6.28			Osagean	*G. typicus*
					Osagean	*G. typicus*
98.8		8.86			Osagean	*G. typicus*
					Osagean	*G. typicus*
84.4	21.88	9.18	12.70	19.01	Osagean	*G. typicus*
193.9		9.38			Osagean	*G. typicus*
					Osagean	*G. typicus*
					Osagean	*G. typicus*
					Osagean	*G. typicus*
97.7	18.71	1.87	16.84	18.24	Osagean	*G. typicus*
154.6		8.22			Osagean	*G. typicus*
					Osagean	*G. typicus*
248.5	19.87	9.97	9.89	17.85	Osagean	*G. typicus*
					Osagean	*G. typicus*
					Osagean	*G. typicus*
					Osagean	*G. typicus*
141.2		6.36			Osagean	*G. typicus*
					Osagean	*G. typicus*
118.4		1.81			Osagean	*G. typicus*
96.4	20.35	-0.06	20.42	20.04	Osagean	*G. typicus*
					Osagean	*G. typicus*
					Osagean	*G. typicus*
					Osagean	*G. typicus*
					Osagean	*G. typicus*

Joana Limestone	126.5	MH-126.5	Wackestone	1.14	-5.74	
Joana Limestone	127	MH-127	Wackestone	1.90	-5.98	
Joana Limestone	127.5	MH-127.5	Wackestone	1.02	-4.26	
Joana Limestone	127.8	MH-127.8	Wackestone	1.35	-6.32	
Joana Limestone	130.5	MH-130.5	Wackestone	0.41	-4.82	
Joana Limestone	133	MH-133	Wackestone	0.39	-5.11	15.0
Joana Limestone	135	MH-135	Grainstone	0.52	-4.35	
Joana Limestone	137	MH-137	Packstone	0.73	-4.72	
Joana Limestone	138	MH-138	Grainstone	0.65	-5.06	
Joana Limestone	138.5	MH-138.5	Wackestone	0.42	-5.51	
Joana Limestone	139	MH-139	Wackestone	0.52	-5.85	
Joana Limestone	139.5	MH-139.5	Wackestone	1.09	-5.13	
Joana Limestone	140	MH-140	Packstone	0.89	-5.08	
Joana Limestone	140.5	MH-140.5	Packstone	0.68	-6.02	
Joana Limestone	141	MH-141	Wackestone	0.64	-5.65	
Joana Limestone	141.5	MH-141.5	Lime mudstone	0.54	-5.80	
Joana Limestone	142	MH-142	Wackestone	1.41	-5.90	
Joana Limestone	142.5	MH-142.5	Grainstone	0.50	-5.71	
Joana Limestone	143	MH-143	Wackestone	0.21	-5.99	
Joana Limestone	143.5	MH-143.5	Lime mudstone	0.69	-5.79	
Joana Limestone	144	MH-144	Grainstone	0.27	-6.11	
Joana Limestone	144.5	MH-144.5	Grainstone	-0.40	-2.89	
Joana Limestone	145	MH-145	Grainstone	-0.05	-2.93	
Joana Limestone	145.5	MH-145.5	Wackestone	0.54	-5.76	
Joana Limestone	146	MH-146	Wackestone	1.75	-3.74	
Joana Limestone	146.5	MH-146.5	Wackestone	0.93	-5.85	
Joana Limestone	147	MH-147	Wackestone	0.52	-5.65	
Joana Limestone	147.5	MH-147.5	Wackestone	0.38	-5.38	
Joana Limestone	148	MH-148	Wackestone	1.50	-5.00	
Joana Limestone	148.5	MH-148.5	Wackestone	0.54	-5.65	
Joana Limestone	149.5	MH-149.5	Wackestone	1.00	-5.50	
Joana Limestone	150	MH-150	Packstone	1.25	-5.14	
Joana Limestone	150.5	MH-150.5	Wackestone	0.92	-4.61	
Joana Limestone	151	MH-151	Wackestone	0.11	-4.65	
Joana Limestone	151.5	MH-151.5	Wackestone	0.23	-4.41	

* Conodont biostratigraphic data of Pahranagat Range section are mainly from Singler (1987). Biostratigraphic data of the Mountain Home section are mainly from Poole and Sandberg (1991).

					Osagean	*G. typicus*
					Osagean	*G. typicus*
					Osagean	*G. typicus*
					Osagean	*G. typicus*
					Osagean	*G. typicus*
135.5	21.40	5.82	15.58	21.32	Osagean	*G. typicus*
					Osagean	*G. typicus*
					Osagean	*G. typicus*
					Osagean	*G. typicus*
					Osagean	*G. typicus*
					Osagean	*G. typicus*
					Osagean	*G. typicus*
					Osagean	*G. typicus*
					Osagean	*G. typicus*
					Osagean	*G. typicus*
					Osagean	*G. typicus*
					Osagean	*G. typicus*
					Osagean	*G. typicus*
					Osagean	*G. typicus*
					Osagean	*G. typicus*
					Osagean	*G. typicus*
					Osagean	*G. typicus*
					Osagean	*G. typicus*
					Osagean	*G. typicus*
					Osagean	*G. typicus*
					Osagean	*G. typicus*
					Osagean	*G. typicus*
					Osagean	*G. typicus*
					Osagean	*G. typicus*
					Osagean	*G. typicus*
					Osagean	*G. typicus*
					Osagean	*G. typicus*
					Osagean	*G. typicus*
					Osagean	*G. typicus*
					Osagean	*G. typicus*

7. References

Algeo, T., Luo, G., Song, H., Lyons, T., Canfield, D., 2015. Reconstruction of secular variation in seawater sulfate concentrations. Biogeosciences 12, 2131-2151.

Allan, J. and Matthews, R., 1982. Isotope signatures associated with early meteoric diagenesis. Sedimentology 29, 797-817.

Aller, R.C., Madrid, V., Chistoserdov, A., Aller, J.Y., Heilbrun, C., 2010. Unsteady diagenetic processes and sulfur biogeochemistry in tropical deltaic muds: Implications for oceanic isotope cycles and the sedimentary record. Geochimica et Cosmochimica Acta 74, 4671-4692.

Antler, G., Turchyn, A.V., Rennie, V., Herut, B., Sivan, O., 2013. Coupled sulfur and oxygen isotope insight into bacterial sulfate reduction in the natural environment. Geochimica et Cosmochimica Acta 118, 98-117.

Banner, J. L. and Hanson, G. N., 1990. Calculation of simultaneous isotopic and trace element variations during water-rock interaction with applications to carbonate diagenesis. Geochimica et Cosmochimica Acta 54, 3123-3137.

Bao, H., 2006. Purifying Barite for Oxygen Isotope Measurement by Dissolution and Reprecipitation in a Chelating Solution. Analytical Chemistry 78, 304-309.

Beerling, D.J., 2002. Low atmospheric CO2 levels during the Permo- Carboniferous glaciation inferred from fossil lycopsids. Proceedings of the National Academy of Sciences 99, 12567-12571.

Berner, R.A. and Canfield, D.E., 1989. A New Model for Atmospheric Oxygen Over Phanerozoic Time. American Journal of Science 289, 333-361.

Berner, R.A., 2003. The long-term carbon cycle, fossil fuels and atmospheric composition. Nature 426, 323-326.

Berner, R.A., 2006. GEOCARBSULF: a combined model for Phanerozoic atmospheric O 2 and CO 2. Geochimica et Cosmochimica Acta 70, 5653-5664.

Berner, R.A., 2004. *The Phanerozoic Carbon Cycle: CO_2 and O_2*. Oxford University Press, Oxford, 150p.

Böttcher, M.E., Thamdrup, B., Gehre, M., Theune, A., 2005. $^{34}S/^{32}S$ and $^{18}O/^{16}O$ Fractionation during Sulfur Disproportionation by Desulfobulbus propionicus. Geomicrobiology Journal 22, 219-226.

Böttcher, M.E., Thamdrup, B., Vennemann, T.W., 2001. Oxygen and sulfur isotope fractionation during anaerobic bacterial disproportionation of elemental sulfur. Geochimica et Cosmochimica Acta 65, 1601-1609.

Bottrell, S.H., Newton, R.J., 2006. Reconstruction of changes in global sulfur cycling from marine sulfate isotopes. Earth-Science Reviews 75, 59-83.

Bruckschen, P. and Veizer, J., 1997. Oxygen and carbon isotopic composition of Dinantian brachiopods: Paleoenvironmental implications for the Lower Carboniferous of western Europe. Palaeogeography, Palaeoclimatology, Palaeoecology 132, 243-264.

Budai, J.M., Lohmnann, K.C., Wilson, J.L., 1987. Dolomitization of the Madison Group, Wyoming and Utah overthrust belt. American Association of Petroleum Geologist Bulletin 71, 909-924.

Buggisch, W., Joachimski, M.M., Sevastopulo, G., Morrow, J.R., 2008. Mississippian $\delta^{13}C_{carb}$ and conodont apatite $\delta^{18}O$ records − Their relation to the Late Palaeozoic Glaciation. Palaeogeography, Palaeoclimatology, Palaeoecology 268, 273-292.

Canfield, D.E., 2001. Isotope fractionation by natural populations of sulfate-reducing bacteria. Geochimica et Cosmochimica Acta 65, 1117–1124.

Canfield, D.E., Farquhar, J., Zerkle, A.L., 2010. High isotope fractionations during sulfate reduction in a low-sulfate euxinic ocean analog. Geology 38, 415-418.

Canfield, D.E., Raiswell, R., Westrich, J.T., Reaves, C.M., Berner, R.A., 1986. The use of chromium reduction in the analysis of reduced inorganic sulfur on sediments and shales. California Geology 54, 149-155.

Canfield, D.E., Teske, A., 1996. Late Proterozoic rise in atmospheric oxygen concentration inferred from phylogenetic and sulphur-isotope studies. Nature 382, 127-132.

Cooney, M.J., Roschi, E., Marison, I.W., Comminellis, C., von Stockar, U., 1996. Physiologic studies with the sulfate-reducing bacterium Desulfovibrio desulfuricans: Evaluation for use in a biofuel cell. Enzyme and Microbial Technology 18, 358-365.

Derry, L.A., 2010. A burial diagenesis origin for the Ediacaran Shuram-Wonoka carbon isotope anomaly. Earth and Planetary Science Letters 294, 152-162.

Dickens, G.R., O'Neil, J.R., Rea, D.K., Owen, R.M., 1995. Dissociation of oceanic methane hydrate as a cause of the carbon isotope excursion at the end of the Paleocene. Paleoceanography 10, 965-971.

Fielding, C.R., Frank, T.D., Birgenheier, L.P., Rygel, M.C., Jones, A.T., Roberts, J., 2008. Stratigraphic record and facies associations of the late Paleozoic ice age in Eastern Australia (New South Wales and Queensland), in: Fielding, C.R., Frank, T.D., Isbell, J.L. (Eds.), Resolving the Late Paleozoic Ice Age in Time and Space: Geological Society of America Special Paper 441, pp. 41–57.

Fike, D.A., Bradley, A.S., Rose, C.V., 2015. Rethinking the Ancient Sulfur Cycle. Annual Review of Earth and Planetary Sciences 43, 593-622.

Giles, K.A., Dickinson, W.R., 1995. Influence of lithospheric flexure on development of stratigraphic sequences in foreland settings: An example from the Antler foreland, Nevada and Utah, in: Dorobek, S., Ross, G. (Eds.), Stratigraphic Evolution of Foreland Basins. Society for Sedimentary Geology Special Publication 52, pp. 187-211.

Giles, P.S., 2012. Low-latitude Ordovician to Triassic brachiopod habitat temperatures (BHTs) determined from $\delta^{18}O_{[brachiopod\ calcite]}$: A cold hard look at ice-house tropical oceans. Palaeogeography, Palaeoclimatology, Palaeoecology 317-318, 134-152.

Gill, B.C., Lyons, T.W., Frank, T.D., 2008. Behavior of carbonate-associated sulfate during meteoric diagenesis and implications for the sulfur isotope paleoproxy. Geochimica et Cosmochimica Acta 72, 4699-4711.

Gill, B.C., Lyons, T.W., Saltzman, M.R., 2007. Parallel, high-resolution carbon and sulfur isotope records of the evolving Paleozoic marine sulfur reservoir. Palaeogeography, Palaeoclimatology, Palaeoecology 256, 156-173.

Gill, B.C., Lyons, T.W., Young, S.A., Kump, L.R., Knoll, A.H., Saltzman, M.R., 2011. Geochemical evidence for widespread euxinia in the Later Cambrian ocean. Nature 469, 80-83.

Gomes, M.L., Hurtgen, M.T., 2015. Sulfur isotope fractionation in modern euxinic systems: Implications for paleoenvironmental reconstructions of paired sulfate-sulfide isotope records. Geochimica et Cosmochimica Acta 157, 39-55.

Grossman, E.L., Yancey, T.E., Jones, T.E., Bruckschen, P., Chuvashov, B., Mazzullo, S.J., Mii, H.-s., 2008. Glaciation, aridification, and carbon sequestration in the Permo-Carboniferous: The isotopic record from low latitudes. Palaeogeography, Palaeoclimatology, Palaeoecology 268, 222-233.

Grossman, E.L., 2012. Chapter 10, Oxygen isotope stratigraphy, in: Gradstein, F.M., Ogg, J.G., Schmitz, M., Ogg, G. (Eds.), Geological time Scale 2012. Elsevier, pp. 181-206.

Habicht, K.S., Gade, M., Thamdrup, B., Berg, P., Canfield, D.E., 2002. Calibration of sulfate levels in the Archean Ocean. Science 298, 2372-2374.

Habicht, K.S., Canfield, D.E., 2001. Isotope fractionation by sulfate-reducing natural populations and the isotopic composition of sulfide in marine sediments. Geology 29, 555-558.

Halevy, I., Peters, S.E., Fischer, W.W., 2012. Sulfate Burial Constraints on the Phanerozoic Sulfur Cycle. Science 337, 331-334.

Hance, L., Devuyst, F.-X., and Poty, E., 2002. Sequence stratigraphy of the Belgium Lower Carboniferous—Tentative correlation with the British Isles, in: Hills, L.V., Henderson, C.M., and Bamber, E.W., (Eds.), Carboniferous and Permian of the World: Canadian Society of Petroleum Geologists Memoir 19, pp. 41–51.

Haq, B.U. and Al-Qahtani, A.M., 2005. Phanerozoic cycles of sea-level change on the Arabian Platform. Geoarabia 10, 127-160.

Isaacson, P., Hladil, J., Shen, J., Kalvoda, J., Grader, G., 1999. Late Devonian (Famennian) glaciation in South America and marine offlap on other continents. Abhandlungen-Geologischen Bundesanstalt 54, 239-258.

Isbell, J.L., Miller, M.F., Wolfe, K.L., Lenaker, P.A., 2003. Timing of late Paleozoic glaciation in Gondwana: was glaciation responsible for the development of northern hemisphere cyclothems?, in: Chan, M.A., Archer, A.W. (Eds.), Extreme depositional environments: mega end members in geologic time: Geological Society of America Special Paper 370, pp. 5–24.

Isbell, J.L., Henry, L.C., Gulbranson, E.L., Limarino, C.O., Fraiser, M.L., Koch, Z.J., Ciccioli, P.L., Dineen, A.A., 2012. Glacial paradoxes during the late Paleozoic ice age: Evaluating the equilibrium line altitude as a control on glaciation. Gondwana Research 22, 1-19.

Jacobsen, S.B. and Kaufman, A.J., 1999. The Sr, C and O isotopic evolution of Neoproterozoic seawater. Chemical Geology 161, 37-57.

Jones, D.S., Fike, D.A., 2013. Dynamic sulfur and carbon cycling through the end-Ordovician extinction revealed by paired sulfate-pyrite $\delta^{34}S$. Earth and Planetary Science Letters 363, 144-155.

Kah, L.C., Lyons, T.W., Frank, T.D., 2004. Low marine sulphate and protracted oxygenation of the Proterozoic biosphere. Nature 431, 834-838.

Kalvoda, J., 1989. Tournaisian events in Moravia (Czechoslovakia) and their significance. Courier Forschungsinstitut Senckenberg 117, 353–358.

Kalvoda, J., 2002, Late Devonian–Early Carboniferous Foraminiferal Fauna: Zonations, Evolutionary Events, Paleobiogeography and Tectonic Implications. Brno, Czech Republic, Folia, Geologia 39, Masaryk University, 213 p.

Kammer, T.W., Matchen, D.L., 2008, Evidence for eustasy at the Kinderhookian-Osagean (Mississippian) boundary in the United States: Response to late Tournaisian glaciation?, in: Fielding, C.R., Frank, T.D., and Isbell, J.L., (Eds.), Resolving the Late Paleozoic Ice Age in Time and Space: Geological Society of America Special Paper 441, pp. 261–274.

Kampschulte, A., Bruckschen, P., Strauss, H., 2001. The sulphur isotopic composition of trace sulphates in Carboniferous brachiopods: implications for coeval seawater, correlation with other geochemical cycles and isotope stratigraphy. Chemical Geology 175, 149-173.

Kampschulte, A., Strauss, H., 2004. The sulfur isotopic evolution of Phanerozoic seawater based on the analysis of structurally substituted sulfate in carbonates. Chemical Geology 204, 255-286.

Katz, D.A., Buoniconti, M.R., Montañez, I.P., Swart, P.K., Eberli, G.P., Smith, L.B., 2007. Timing and local perturbations to the carbon pool in the lower Mississippian Madison Limestone, Montana and Wyoming. Palaeogeography, Palaeoclimatology, Palaeoecology 256, 231-253.

Kaufman, A.J., Hayes, J.M., Knoll, A.H., Germs, G.J.B., 1991. Isotopic compositions of carbonates and organic carbon from upper Proterozoic successions in Namibia; stratigraphic variation and the effects of diagenesis and metamorphism. Precambrian Research 49, 301-327.

Kaufman, A.J., Knoll, A.H., 1995. Neoproterozoic variations in the C-isotopic composition of seawater; stratigraphic and biogeochemical implications. Precambrian Research 73, 27-49.

Lane, H.R., Brenckle, P.L., 2005. Type Mississippian subdivisions and biostratigraphic succession, in: Heckel, P.H. (Eds.), Stratigraphy and biostratigraphy of the Mississippian subsystem (Carboniferous System) in its type region, the Mississippi River Valley of

Illinois, Missouri and Iowa. Champaign, Illinois, Illinois State Geological Survey, Guidebook 34, International Union of Geological Sciences Subcommission on Carboniferous Stratigraphy, Guidebook for Field Conference, St. Louis, Missouri, 8–13 September 2001, pp. 83-107.

Leavitt, W.D., Halevy, I., Bradley, A.S., Johnston, D.T., 2013. Influence of sulfate reduction rates on the Phanerozoic sulfur isotope record. Proceedings of the National Academy of Sciences of the United States of America 110, 11244-11249.

Lloyd, R.M., 1968. Oxygen isotope behavior in the Sulfate-Water System. Journal of Geophysical Research 73, 6099-6110.

Lyons, T.W., Walter, L.M., Gellatly, A.M., Martini, A.M., Blake, R.E., 2004. Sites of anomalous organic remineralization in the carbonate sediments of South Florida, U.S.A.: The sulfur cycle and carbonate-associated sulfate, in: Amend, J., Edwards, K., W, L.T. (Eds.), Sulfur Biogeochemistry-Past and Present. Geological Society of America Special Paper 379, pp. 161-176.

Marenco, P.J., Corsetti, F.A., Kaufman, A.J., Bottjer, D.J., 2008. Environmental and diagenetic variations in carbonate associated sulfate: An investigation of CAS in the Lower Triassic of the western USA. Geochimica et Cosmochimica Acta 72, 1570-1582.

Marenco, P.J., Marenco, K.N., Lubitz, R.L., Niu, D., 2013. Contrasting long-term global and short-term local redox proxies during the Great Ordovician Biodiversification Event: A case study from Fossil Mountain, Utah, USA. Palaeogeography, Palaeoclimatology, Palaeoecology 377, 45-51.

Markovic, S., Paytan, A., Li, H., Wortmann, U.G., 2016. A revised seawater sulfate oxygen isotope record for the last 4 Myr. Geochimica et Cosmochimica Acta 175, 239-251.

Mii, H.S., Grossman, E.L., Yancey, T.E., 1999. Carboniferous isotope stratigraphies of North America: Implications for Carboniferous paleoceanography and Mississippian glaciation. Geological Society of America Bulletin 111, 960-973.

Montañez, I.P., Poulsen, C.J., 2013. The Late Paleozoic Ice Age: An Evolving Paradigm. Annual Review of Earth and Planetary Sciences 41, 629-656.

Oehlert, A.M., Swart, P.K., 2014. Interpreting carbonate and organic carbon isotope covariance in the sedimentary record. Nature Communications 5, 4672.

Oleszkiewicz, J.A., Marstaller, T., McCartney, D.M., 1989. Effects of pH on sulfide toxicity to anaerobic processes. Environmental Technology Letters 10, 815-822.

Owens, J.D., Gill, B.C., Jenkyns, H.C., Bates, S.M., Severmann, S., Kuypers, M.M.M., Woodfine, R.G., Lyons, T.W., 2013. Sulfur isotopes track the global extent and dynamics of euxinia during Cretaceous Oceanic Anoxic Event 2. Proceedings of the National Academy of Sciences 110, 18407-18412.

Peng, Y., Xiao, S., Bao, Huiming, Pratt, M.L., Kaufman, A.J., Jiang, G., Boyd, D., Wang, Q., Zhou, C., 2014. Widespread contamination of carbonate-associated sulfate by present-day secondary atmospheric sulfate: evidence from triple oxygen isotopes. Geology 42, 815-818.

Poole, F.G., Sandberg, C.A., 1991. Mississippian paleogeography and conodont biostratigraphy of the western United States, in: Cooper, J.D., Stevens, G.H. (Eds.), Paleozoic Paleogeography of the Western United States. Pacific Section, Society of Economic Paleontologists and Mineralogists Special Publication 42, pp. 109–124.

Qie, W.K., Zhang, X.H., Du, Y., Zhang, Y., 2011. Lower Carboniferous carbon isotope stratigraphy in South China: Implications for the Late Paleozoic glaciation. Science in China - Series D 54, 84-92.

Raab, M. and Spiro, B., 1991. Sulfur isotopic variations during seawater evaporation with fractional crystallization. Chemical Geology 86, 323-333.

Raiswell, R., Berner, R.A., 1986. Pyrite and organic matter in Phanerozoic normal marine shales. Geochimica et Cosmochimica Acta 50, 1967-1976.

Reis, M.A.M., Almeida, J.S., Lemos, P.C., Carrondo, M.J.T., 1992. Effect of hydrogen sulfide on growth of sulfate reducing bacteria. Biotechnology and Bioengineering 40, 593-600.

Rennie, V., Turchyn, A.V., 2014. The preservation of $\delta^{34}S_{SO4}$ and $\delta^{18}O_{SO4}$ in carbonate-associated sulfate during marine diagenesis: a 25 Myr test case using marine sediments. Earth and Planetary Science Letters 395, 13-23.

Ross, C.A., Ross, J.R.P., 1985. Late Paleozoic Depositional Sequences are Synchronous and Worldwide. Geology 13, 194-197.

Saltzman, M.R., 2002. Carbon and oxygen isotope stratigraphy of the Lower Mississippian (Kinderhookian-lower Osagean), western United States: Implications for seawater chemistry and glaciation. Geological Society of America Bulletin 114, 96-108.

Saltzman, M.R., 2003a. Organic Carbon Burial and Phosphogenesis in the Antler Foreland Basin: An Out-of-Phase Relationship During the Lower Mississippian. Journal of Sedimentary Research 73, 844-855.

Saltzman, M.R., 2003b. Late Paleozoic ice age; oceanic gateway or pCO_2? Geology 31, 151-154.

Saltzman, M.R., 2003. Organic carbon burial and phosphogenesis in the Antler foreland basin: an out-of-phase relationship during the Lower Mississippian. Journal of Sedimentary Research 73, 844-855.

Saltzman, M.R., Gonzalez, L.A., Lohmann, K.C., 2000. Earliest Carboniferous cooling step triggered by the Antler Orogeny? Geology 28, 347-350.

Saltzman, M.R., Groessens, E., Zhuravlev, A.V., 2004. Carbon cycle models based on extreme changes in $\delta^{13}C$: an example from the lower Mississippian. Palaeogeography, Palaeoclimatology, Palaeoecology 213, 359-377.

Schobben, M., Stebbins, A., Ghaderi, A., Strauss, H., Korn, D., Korte, C., 2015. Flourishing ocean drives the end-Permian marine mass extinction. Proceedings of the National Academy of Sciences of the United States of America 112, 10298-10303.

Sim, M.S., Bosak, T., Ono, S., 2011. Large Sulfur Isotope Fractionation Does Not Require Disproportionation. Science 333, 74-77.

Sim, M.S., Ono, S., Hurtgen, M.T., 2015. Sulfur isotope evidence for low and fluctuating sulfate levels in the Late Devonian ocean and the potential link with the mass extinction event. Earth and Planetary Science Letters 419, 52-62.

Singler, C.S., 1987. Carbonate petrology and conodont biostratigraphy of a Mississippian carbonate unit, East Pahranagat Range, Lincoln County, Nevada [M.S. thesis]. Pullman, Washington State University, 107 p.

Smith, M.T., Dickinson, W.R., Gehrels, G.E., 1993. Contractional nature of Devonian-Mississippian Antler tectonism along the North American continental margin. Geology 21, 21-24.

Speed, R., Sleep, N., 1982. Antler orogeny and foreland basin: A model. Geological Society of America Bulletin 93, 815-828.

Strauss, H., 1997. The isotopic composition of sedimentary sulfur through time. Palaeogeography, Palaeoclimatology, Palaeoecology 132, 97-118.

Swart, P.K., 2008. Global synchronous changes in the carbon isotopic composition of carbonate sediments unrelated to changes in the global carbon cycle. Proceedings of the National Academy of Sciences of the United States of America 105, 13741-13745.

Swart, P.K., 2015. The geochemistry of carbonate diagenesis: The past, present and future. Sedimentology 62, 1233-1304.

Swennen, R., Bless, M.J., Bouckaert, J., Razina, T.P., Simakov, K.V., 1986. Evaluation of transgression-regression events in the Upper Famennian-Tournaisian strata of the southeastern Omolon area (NE-Siberia, USSR). Annales De La Société Géologique De Belgique 109, 237-248.

Turchyn, A.V., Schrag, D.P., 2004. Oxygen Isotope Constraints on the Sulfur Cycle over the Past 10 Million Years. Science 303, 2004-2007.

Turchyn, A.V., Schrag, D.P., 2006. Cenozoic evolution of the sulfur cycle: Insight from oxygen isotopes in marine sulfate. Earth and Planetary Science Letters 241, 763-779.

Turchyn, A.V., Schrag, D.P., Coccioni, R., Montanari, A., 2009. Stable isotope analysis of the Cretaceous sulfur cycle. Earth and Planetary Science Letters 285, 115-123.

Wing, B.A., Halevy, I., 2014. Intracellular metabolite levels shape sulfur isotope fractionation during microbial sulfate respiration. Proceedings of the National Academy of Sciences of the United States of America 111, 18116-18125.

Wortmann, U.G., Paytan, A., 2012. Rapid Variability of Seawater Chemistry Over the Past 130 Million Years. Science 337, 334-336.

Wotte, T., Shields-Zhou, G.A., Strauss, H., 2012. Carbonate-associated sulfate: Experimental comparisons of common extraction methods and recommendations toward a standard analytical protocol. Chemical Geology 326–327, 132-144.

Yao, L., Qie, W., Luo, G., Liu, J., Algeo, T.J., Bai, X., Yang, B., Wang, X., 2015. The TICE event: Perturbation of carbon-nitrogen cycles during the mid-Tournaisian (Early Carboniferous) greenhouse-icehouse transition. Chemical Geology 401, 1-14.

Chapter 3

Paired carbonate-organic carbon and nitrogen isotope variations in Lower Mississippian strata of the southern Great Basin, western United States

Abstract

The Early Mississippian K–O (Kinderhookian-Osagean) $\delta^{13}C$ excursion or TICE (mid-Tournaisian carbon isotope excursion) is one of the most prominent positive carbon isotope excursions of the Phanerozoic. Recent studies raise uncertainties about the representative magnitude of this $\delta^{13}C$ excursion (3‰ to ≥6‰ in South China, ≤5‰ in Europe, and ≥7‰ in North America) and the 3‰ unidirectional increase in nitrogen isotopes across the $\delta^{13}C$ excursion, which is unanticipated considering the amount of organic carbon burial required to form the $\delta^{13}C$ excursion and its resultant oxygen increase and global cooling. To address these issues, we have conducted paired carbonate carbon ($\delta^{13}C_{carb}$), organic carbon ($\delta^{13}C_{org}$) and nitrogen ($\delta^{15}N$) isotope analyses across the K-O interval in two well-exposed sections of the southern Great Basin, western U.S.A. In the outer shelf section where no exposure surface is present, both $\delta^{13}C_{carb}$ and $\delta^{13}C_{org}$ show double spikes with peak values up to 7‰ and a negative shift down to 4‰ between the peaks. In the shallower-water section where two karstic disconformities are observed, $\delta^{13}C_{org}$ shows similar double spikes but $\delta^{13}C_{carb}$ displays only a single peak with the highest value of 5.5‰. The missing $\delta^{13}C_{carb}$ spike is caused by diagenetic alteration below a karstic disconformity that lowered $\delta^{13}C_{carb}$ but not $\delta^{13}C_{org}$ values, resulting in smaller magnitude of the $\delta^{13}C_{carb}$ excursion. These features suggest that the 7‰ magnitude and the double spikes are more representative of the K-O $\delta^{13}C$ excursion. The smaller magnitude of

the K-O $\delta^{13}C_{carb}$ excursion in some sections of the Great Basin and the TICE in other sections globally may have been overprinted with local environmental and/or diagenetic signal, which needs to be clarified in future research.

The $\delta^{15}N$ across the K-O $\delta^{13}C$ excursion in the outer shelf section is decoupled from $\delta^{13}C$, with the majority of $\delta^{15}N$ values around 4±1‰ that do not show any obvious temporal trend and a few low values down to 1–2‰ at the peak of the $\delta^{13}C$ excursion. In contrast, $\delta^{15}N$ values in the shallow-water section is coupled with the K-O $\delta^{13}C$ excursion, with a 3‰ positive shift from 4‰ to 7‰ at the rising limb of the $\delta^{13}C$ excursion and a negative shift from 7‰ to 1–2‰ at the falling limb of the $\delta^{13}C$ excursion. Considering the sensitivity of $\delta^{15}N$ to redox conditions of the depositional environments, the coupled $\delta^{13}C$–$\delta^{15}N$ pattern from the shallow-water section may better represent the isotope signature of the oceanic nitrate (NO_3^-) reservoir, while the decoupled $\delta^{13}C$–$\delta^{15}N$ in the deeper-water section records local N-biochemical cycling in periodically developed suboxic-euxinic environments. The increase of $\delta^{15}N$ toward the peak of the K-O $\delta^{13}C$ excursion is consistent with the expansion of the oxygen minimum zone (OMZ) in the ocean that may have promoted water-column denitrification and ^{15}N-enrichment in the marine nitrate (NO_3^-) reservoir. The decrease of $\delta^{15}N$ at the falling limb of the K-O $\delta^{13}C$ excursion may record the shrink of the OMZ and decrease of water-column denitrification in response to more oxygenated and cooler oceans. Collectively, the $\delta^{15}N$ variations documented from the K-O interval are consistent with the climate and ocean redox changes anticipated from a major perturbation of the global carbon cycle.

Key words: Organic carbon isotopes, nitrogen isotopes, Kinderhookian-Osagean, Early Mississippian, Great Basin

1. Introduction

The Lower Mississippian strata host one of the largest positive carbon isotope ($\delta^{13}C$) excursions of the Phanerozoic. This $\delta^{13}C$ excursion, informally referred to as the K-O (Kinderhookian–Osagean) $\delta^{13}C$ excursion in North America (Saltzman et al., 2002) or TICE (mid-Tournaisian carbon isotope excursion; Yao et al., 2015) in other global places, strides across the *Siphondella isosticha* and *Gnathodus typicus* conodont zones around ca. 352 Ma and has a duration of 2–4 million years (Saltzman et al., 2004; Buggisch et al., 2008; Yao et al., 2015). The K-O $\delta^{13}C$ excursion has been documented from many sections globally, mostly through carbonate carbon isotope ($\delta^{13}C_{carb}$) analyses, but the shape and magnitude of this excursion vary significantly. In North America, the K-O $\delta^{13}C_{carb}$ excursion has a magnitude of ≥7‰ and in many sections a secondary 2–3‰ negative shift is present at the peak of the excursion, making a "double spike" appearance (e.g., Mii et al., 1999; Saltzman, 2002, 2003; Saltzman et al., 2000, 2004; Katz et al., 2007; Buggisch et al., 2008). In Europe and Russia, the amplitude of the TICE is about 5.5‰ and the double spikes are present in some sections but are less apparent (Saltzman et al., 2004; Buggisch et al., 2008). In South China, the magnitude of the TICE varies from 3‰ to ≥6‰ in two sections but the low stratigraphic resolution of $\delta^{13}C_{carb}$ data are insufficient to show the double spikes.

The varying magnitudes of the K-O $\delta^{13}C_{carb}$ excursion or TICE raise uncertainties on the representative seawater isotope signature across the K-O interval. Saltzman et al. (2004) argued that the higher magnitude (≥7‰) of the K-O $\delta^{13}C$ excursion in North America may have overprinted with signature from local carbon cycling in a broad epeiric sea and suggested that the magnitude of 5.5‰ from the European sections is more representative of the global seawater signature. However, later organic carbon isotope ($\delta^{13}C_{org}$) analyses in some European sections

(Buggisch et al., 2008) indicated that the positive $\delta^{13}C_{org}$ shift across the K-O interval has an amplitude of ≥6.5‰. The small magnitude of the TICE (~3‰) in one of the South China sections is interpreted as resulting from meteoric alteration and stratigraphic truncation (Yao et al., 2015), which suggests that the larger (≥6‰) magnitude is more representative of the TICE. In North America, the 7‰ magnitude of the K-O $\delta^{13}C_{carb}$ excursion is not present in all measured sections; there are sections that have peak $\delta^{13}C_{carb}$ values of ≤5‰ (e.g., Koch et al., 2014). Further evaluation on the completeness and representativeness of the K-O $\delta^{13}C_{carb}$ excursion is still needed.

The K-O $\delta^{13}C_{carb}$ excursion, even with a magnitude of 5‰, requires significant amount of organic carbon burial (≥7.5×10^{19} g carbon; Saltzman et al., 2004) that would result in decrease of atmospheric CO_2, increase of oxygen, global cooling, and sea-level fall (Mii et al., 1999; Saltzman, 2000, 2002; Buggisch et al., 2008). Because at higher partial pressure of atmospheric O_2 (pO_2), marine phytoplankton may increase isotopic discrimination for ^{12}C (Berner, 2000; Beerling et al., 2002; Saltzman et al., 2013), it is anticipated that the carbonate-organic isotope fractionation or $\Delta^{13}C$ ($\Delta^{13}C = \delta^{13}C_{carb} - \delta^{13}C_{org}$) across the K-O $\delta^{13}C$ excursion would increase. Some $\delta^{13}C_{org}$ data across K-O interval have been reported (Buggisch et al., 2008), but the general lack of stratigraphically continuous, paired $\delta^{13}C_{carb} - \delta^{13}C_{org}$ data makes it difficult to test this prediction.

The increase of oxygen and global cooling resulting from organic carbon burial may cause ocean redox changes that impact the nitrogen (N) biogeochemical cycling in the ocean. Nitrogen fixation and denitrification are the major source and sink of bioavailable nitrogen in the ocean, respectively (DeVries et al., 2012). Nitrogen fixation provides bioavailable nitrogen to the ocean and its nitrogen isotope ($\delta^{15}N$) value is close to that of atmospheric N_2 ($\delta^{15}N \approx 0$‰;

Junium and Arthur, 2007). Denitrification, a bacterial reduction of nitrate, reduces nitrogen species in sediments and water column where oxygen is nearly absent and results in higher $\delta^{15}N$ values of the seawater nitrate reservoir ($\delta^{15}N \approx +5‰$ in the modern ocean)(Algeo et al., 2014; Ader et al., 2016; Stüeken et al., 2016). Evidence from the Quaternary (e.g., Altabet et al., 1995; Deutsch et al., 2004), Pleistocene (e.g., Liu et al., 2005; Robinson et al., 2014) and Late Carboniferous (Algeo et al., 2008; Algeo et al., 2012) has shown that high $\delta^{15}N$ values indicative of enhanced water-column denitrification are commonly associated with interglacial stages, while low $\delta^{15}N$ values are found during glacial periods. In this context, lower $\delta^{15}N$ values are anticipated during the late stage of the K-O $\delta^{13}C_{carb}$ excursion when enhanced organic carbon burial led to cooling and oxygen increase. In contrast to this expectation, recent $\delta^{15}N$ data from South China reveal a 3‰ unidirectional increase in $\delta^{15}N$ across the K-O $\delta^{13}C_{carb}$ excursion (Yao et al., 2015). The increase of $\delta^{15}N$ has been interpreted as recording the long-term change in the locus of marine denitrification from continental shelf sediments to continent margin OMZ when sea-level falls during glaciation (Algeo et al., 2014; Yao et al., 2015). The South China data, however, are faithfully seen in a single section and require confirmation from other successions globally.

To better constrain the shape and magnitude of the K-O $\delta^{13}C_{carb}$ excursion and understand the interactions between carbon and nitrogen cycles, in this study we have generated paired $\delta^{13}C_{carb}$, $\delta^{13}C_{org}$ and $\delta^{15}N$ data from the K-O interval in two well-exposed sections in the southern Great Basin, western U.S.A (Fig. 1). We also compare the $\delta^{13}C_{carb}$ and $\delta^{15}N$ data with those available from South China, which was paleogeographically located at the similar low latitude (Fig. 1A). These data are used to evaluate the potential changes in the nitrogen cycle in response to global cooling and oxygenation resulted from a major carbon cycle perturbation.

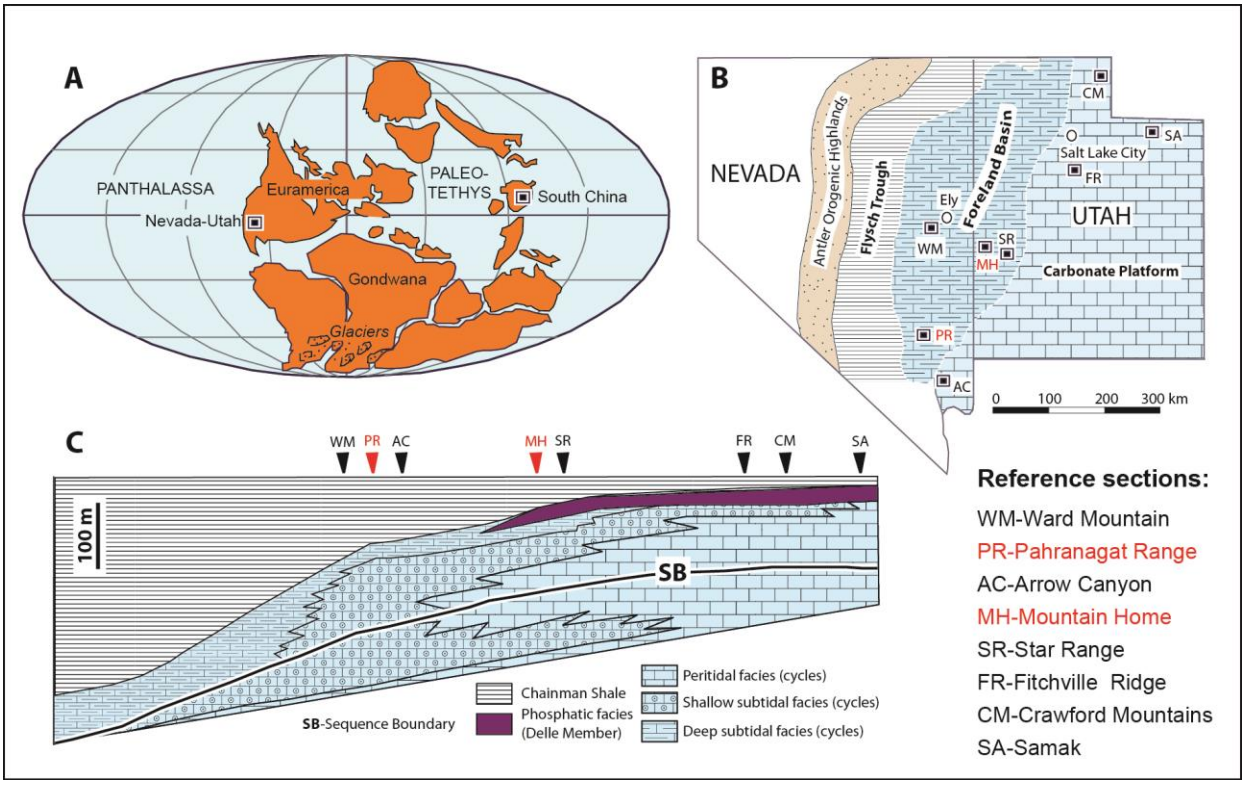

Fig. 1. Paleogeographic location of the measured sections. (A) Paleogeographic location of the southern Great Basin and South China during the Early Mississippian (after Scotese and McKerrow, 1990; Saltzman et al., 2004). (B) Early Mississippian paleogeography of the southern Great Basin (Nevada and Utah) in western U.S. showing a few representative sections including Pahranagat Range (PR) and Mountain Home (MH) (after Stevens et al., 1991; Saltzman et al., 2004). (C) Schematic cross section from eastern Nevada to northeastern Utah showing the facies changes in a west-dipping Early Mississippian carbonate platform and the approximate location of a few representative sections including PR and MH (after Giles, 1996).

2. Geological setting and stratigraphic sections

This study focuses on two Early Mississippian sections (Fig. 1) at the southern Pahranagat Range (PR) near Alamo, Nevada (GPS: N37º23′35.7″, W115º16′5.4″) and the Mountain Home (MH) Range of western Utah (GPS: N38º35′44.7″, W113º56′19.5″). The PR and MH sections were paleogeographically located in distal and proximal ramp settings of a

west-facing carbonate ramp, respectively, in the craton side of the Antler foreland basin (Fig. 1B and C; Stevens et al., 1991; Giles, 1996; Saltzman et al., 2004). The Antler foreland basin was developed over the early Paleozoic passive margin of western North America during the Antler orogeny (Late Devonian–Mississippian), when the Roberts Mountains allochthon thrust over the west-facing continental margin (Speed and Sleep, 1982; Smith et al., 1993; Giles and Dickinson, 1995; Giles, 1996).

Upper Devonian to Lower Mississippian strata in the PR section are well-exposed in the eastern side of an overturned syncline, which include, in ascending order, the Guilmette Formation, Pilot Shale, Joana Limestone, and Chainman Shale (Fig. 2A). The Lower Mississippian Joana Limestone unconformably overlies the Late Devonian Pilot Shale and was used as a single unit between Pilot Shale and Chainman Shale (Fig. 2A; Reso, 1963; Jayko, 2007), but it was later divided into the Joana Limestone and Limestone X (Fig. 2B; Single, 1987; Saltzman, 2002). In this later division, the Joana Limestone refers to the cliff-forming crinoid-rich grainstone and packstone, while the Limestone X consists mainly of lime mudstone and wackestone, with subordinate packstone and grainstone interbeds (Fig. 3). In the original description of Singler (1987), the Limestone X includes 4 members (Members A–D). In our measured section (Figs. 2 and 3), the Joana Limestone is 86 m thick and the Limestone X is 186 m thick. The K-O (Kinderhookian-Osagean) boundary defined by conodont zones *Siphonodella isosticha* and *Gnathodus typicus* (Singler, 1987) is located in the lower Limestone X, about 60 m above the Limestone X and Joana Limestone boundary. The contact between the Limestone X and its overlying Chainman Shale is not exposed in the measured section, although sparse siltstone, mudstone, and silty limestone outcrops of the Chainman shale can be found when tracing around the axis of the syncline (Fig. 2). Previous studies have reported $\delta^{13}C_{carb}$ (Saltzman

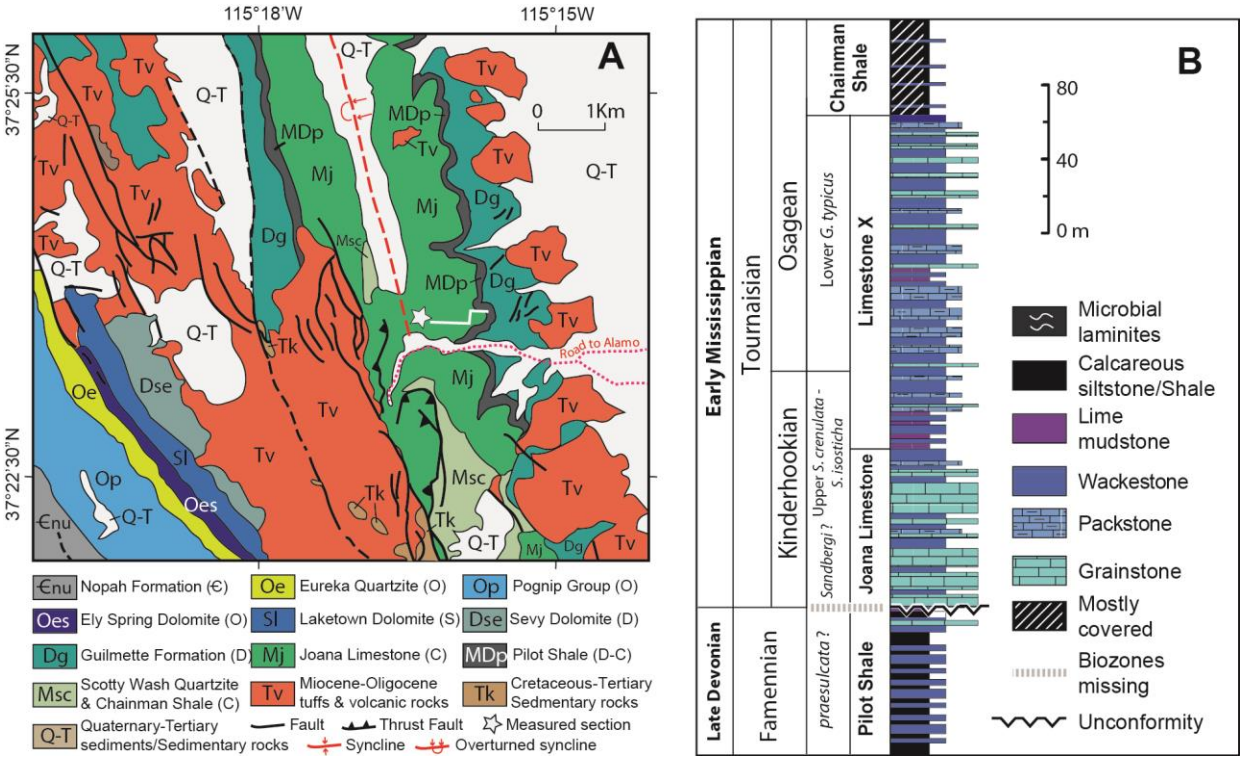

Fig. 2. Location and stratigraphy of the southern Pahranagat Range (PR) section near Alamo, Nevada. (A) Simplified geological map showing the measured section (modified from Jayko, 2007; USGS Scientific Investigations Map 2904). (B) Litho- and biostratigraphy of the PR section. The contact between the Joana Limestone and Pilot Shale is an unconformity with possibly one or two conodont biozones missing (Poole and Sandberg, 1991). The contact between Limestone X and its overlying Chainman Shale is not exposed in this locality, although sparse outcrops of the Chainman shale can be found when tracing northward. The conodont biozones are from Singler (1987), but after careful correlation and lateral tracing, we think that the lithostratigraphic boundary between the Joana Limestone and Limestone X should be higher than what was described in Singler (1987).

et al., 2000; Saltzman, 2002) and $\delta^{13}C_{org}$ (Buggisch et al., 2008) data from this section, but in those studies isotope analyses did not cover the uppermost part of the Limestone X and the $\delta^{13}C_{carb}$ and $\delta^{13}C_{org}$ did not return back to pre-excursion values.

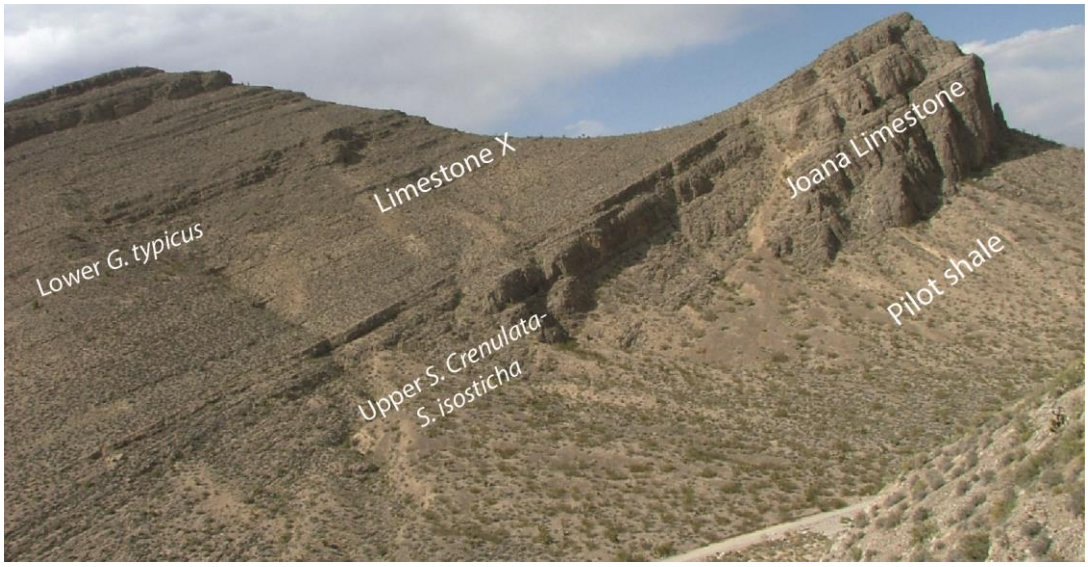

Fig. 3. Field photograph showing the measured PR section near Alamo, Nevada, with the stratigraphic units and conodont biozones (Singler, 1987) marked.

Upper Devonian to Lower Mississippian strata in the MH section includes the Middle Member and West Range Limestone Member of the Guilmette Formation, Pilot Shale, Joana Limestone, and Chainman Formation (Fig. 4A; Hintze and Davis, 2002). The Middle Member of the Guilmette Formation in this locality is sandstone dominated and is sometimes named as the Cove Fort Quartzite (e.g., Giles et al., 1999). The Lower Mississippian Joana Limestone in this section is 152 m thick (Fig. 4B), covering the upper *Siphonodella crenulata–Siphonodella isosticha* (Kinderhookian) and lower *Gnathodus typicus* (Osagean) conodont zones (Poole and Sandberg, 1991), but it is uncertain if the Devonian-Carboniferous boundary is located within the underlying Pilot Shale (Giles and Dickinson, 1995; Giles, 1996). The lower part (0–60 m) of the Joana Limestone consists mainly of packstone and grainstone, with wackestone, lime mudstone, and microbial limestone interbeds. Dissolution cavities and reworked karst breccias are observed at 40 m and 60 m, indicating subaerial exposure and potential erosion. The upper part (60–152 m) of the Joana Limestone shows decrease of grainstone and increase of wackestone and lime

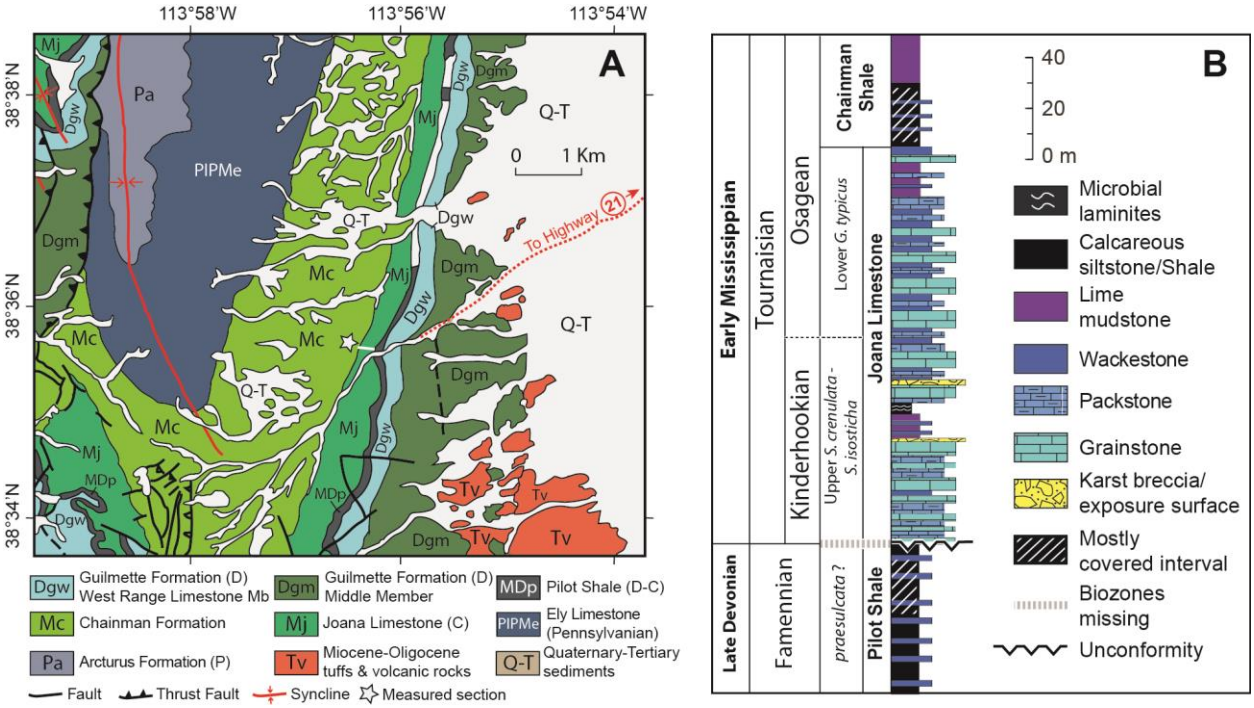

Fig. 4. Location and stratigraphy of the Mountain Home (MH) section, about 55 miles northwest of Milford, Utah. (A) Simplified geological map showing the measured section (Modified from Hintze and Davis, 2002; Utah Geological Survey Map 182). (B) Litho- and biostratigraphy of the MH section. In this section, the amount of time missing at the contact between the Joana Limestone and Pilot Shale may be 1–3 conodont zones (Poole and Sandberg, 1991; Giles, 1996), but it requires further bio- and chemostratigraphic study to confirm. Except for the lowermost few meters of the Chainman Shale that is covered, the Joana Limestone and its overlying strata are very well exposed.

mudstone, indicating a shift toward deeper-water depositional environments (Giles, 1996). Except for the lowermost few meters of the Chainman Shale that is covered, the Joana Limestone and its overlying strata are very well exposed in this section.

In the PR section, the grainstone- and packstone-dominated Joana Limestone was mostly likely deposited in shallow subtidal environments above the fairweather wave base (Giles, 1996), while the lime mudstone- and wackestone-dominated Limestone X suggests deposition from

deep subtidal to basin environments below storm wave base. In the MH section, the low part of the Joana Limestone (0–60 m) is dominated by packstone and grainstone with dissolution cavities and reworked carbonate breccias seen in some intervals, suggesting shallow subtidal to intertidal depositional environments. The upper part of the Joana Limestone (60–152 m) consists of unevenly interbedded wackestone, lime mudstone, and packestone/grainstone, with cross bedding occasionally preserved in the latter, suggesting alternating deep and shallow subtidal environments (Giles, 1996).

3. Sampling and analytical methods

Samples were collected in an average spacing of ≤ 1 m. After cutting and cleaning, sample powders were drilled from the fresh and dark portion of the samples for $\delta^{13}C_{carb}$, $\delta^{18}O_{carb}$, and $\delta^{13}C_{org}$ analyses. For $\delta^{13}C_{carb}$ and $\delta^{18}O_{carb}$ analyses, about 200 μg of sample powders were reacted with orthophosphoric acid for 10 min at 70°C in a Kiel device coupled with Finnigan Delta Plus dual-inlet mass spectrometer. Isotopic results are reported as standard δ notation as per mil (‰) deviations from Vienna-Pee Dee belemnite (VPDB). For both C and O isotopes, multiple measurements of NBS-19 (National bureau of Standards-19) and an internal standard determined the precision better than 0.05‰. Analyses were carried out at the Las Vegas Isotope Science (LVIS) Laboratory at University of Nevada Las Vegas (UNLV).

Organic carbon isotope analyses were performed by decarbonation of about 40 mg of sample powders placed in a silver capsule using acid fumigation method (Harris et al., 2001). A drop of 10% HCL was used to ensure the complete removal of carbonates from the sample. Decarbonated residues in each silver capsule were rinsed with DI water three times in isolated beakers to remove HCL and dried at 100°C. After drying, samples were wrapped in tin capsules and stored in refrigerator before analyses. Elemental analyzer coupled with a Delta plus XP mass

spectrometer was used to analyze organic carbon isotopes and the results were reported as standard δ notation as per mil (‰) deviations from VPDB. Precision determined by acetanilide standards was better than 0.2‰ for $\delta^{13}C_{org}$ and 0.1% for TOC (Jiang et al., 2012). To double check the reproducibility, some samples were prepared using the traditional decarbonation method that use 6–10 g of samples (see below). Portion of the samples were analyzed in the UNLV LVIS lab and the other portion was analyzed at the Oxy-Anion Stable Isotope Consortium (OASIC) at the Louisiana State University (LSU).

For nitrogen isotope analyses, clean samples were crushed into powders using a shatterbox. About 6 to 10 g of sample powers were decarbonated in a 100 ml glass tube using 10% HCL. To confirm complete removal of carbonates, HCL was added to the reaction tube multiple times until there is no reaction. The carbonate-free residues were dried and 20–90 mg was wrapped in tin capsules. Nitrogen isotopes were analyzed using Elemental Analyzer connected to Delta plus XP mass spectrometer in the OASIC at LSU and the results are reported as standard δ notation as per mil (‰) deviations from atmospheric N_2 (‰, Air). For each sample, we run two to three times using different amount of sample powders. The first run is used to determine the amount of N in each sample and the sample size. After adjusting the sample size, we run samples a second time and pre-adjust the peak to perfect match of the sample size (we put the samples that have similar N contents in the same run). We run some samples a third time or even a fourth time until results are reproducible at the differences between multiple runs are ≤0.2‰ for $\delta^{15}N$ and ≤0.08% for total nitrogen (TN). Uncertainties determined by duplicates of acetanilide are better than 0.1‰ for $\delta^{15}N$ and 0.08% for total nitrogen (TN).

4. Results

4.1. Carbon isotope profiles

The isotope results are reported in Table 1 and Figs. 5–7. Both $\delta^{13}C_{carb}$ and $\delta^{13}C_{org}$ values of the PR section show a broad positive excursion with double peaks (Fig. 5). The $\delta^{13}C_{carb}$ values of the Joana Limestone increase upward to a peak of 6.9‰, followed by a brief negative shift down to 4.1‰, which again gradually increase up to 7.0‰ and fall back to an average value of ~1‰ at the top of the Limestone X. The $\delta^{13}C_{org}$ values show a similar pattern, rising from –29.5‰ to –24.5‰ in the Joana Limestone, followed by a negative shift down to –27.1‰ in the lower part of Limestone X and an increase back to –23.7‰, which fall back again to –29.5‰ at the top of the Limestone X. The carbonate and organic carbon isotope difference or fractionation $\Delta\delta^{13}C$ ($\Delta\delta^{13}C = \delta^{13}C_{carb} - \delta^{13}C_{org}$) of the PR section increases from 29.8‰ to 32.9‰ in the Joana Limestone and remain at 31±1‰ through the majority of the Limestone X. The $\delta^{13}C_{carb}$ trends are similar to those reported in Saltzman (2002) from the same section but are more complete especially for the uppermost part of the Limestone X. The $\delta^{13}C_{org}$ has the range of values similar to that of Buggisch et al. (2008), but the current data are much less scattered and stratigraphically more complete.

In the MH section, $\delta^{13}C_{carb}$ values of the Joana Limestone increase up section from 0.3‰ to the peak value of 5.5‰ and return back to 0.2‰ (Fig. 6). The uppermost 15 m of the Joana Limestone, below the Joana Limestone and Chainman Shale contact, $\delta^{13}C_{carb}$ values show a slight increase to 1±0.5‰. Intriguingly, like in the PR section, the $\delta^{13}C_{org}$ values in the MH section also show a positive excursion with double peaks: increasing upward from –29.6‰ to peak values of –23.6‰ and –24.7‰, with a negative shift down to –27.4‰ between the two peaks. The $\delta^{13}C_{org}$ returns back to –29.8‰ in the upper part of the Joana Limestone and a slight increase (~1‰) at the top. The $\Delta\delta^{13}C$ values in the MH section are mostly within 30±1‰, except

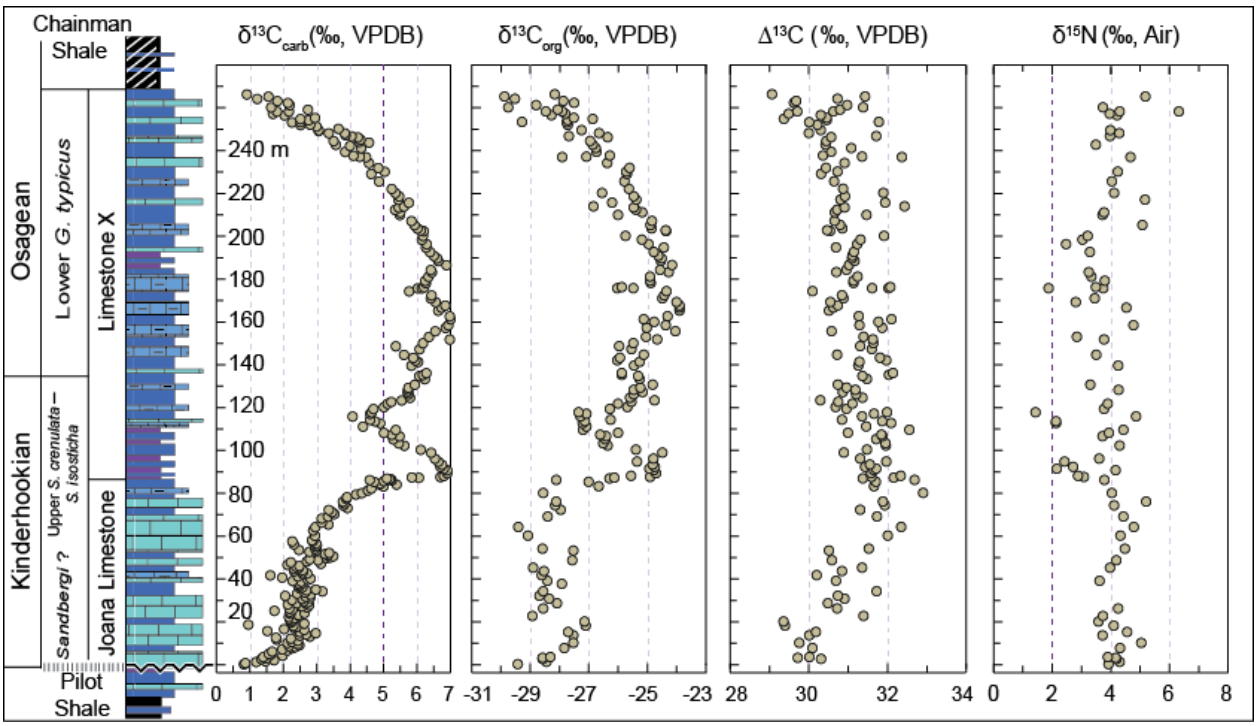

Fig. 5. Carbonate carbon ($\delta^{13}C_{carb}$), organic carbon ($\delta^{13}C_{org}$), carbonate and organic carbon isotope difference ($\Delta^{13}C = \delta^{13}C_{carb} - \delta^{13}C_{org}$) and nitrogen isotope ($\delta^{15}N$) variations of the Kinderhookian-Osagean (K-O) strata from the PR section. The covariation of $\delta^{13}C_{carb}$ and $\delta^{13}C_{org}$ supports that the temporal isotope trends are well preserved. The $\Delta^{13}C$ shows a 1–2‰ increase toward the peak of the K-O $\delta^{13}C$ excursion. Most of the $\delta^{15}N$ values are 4±1‰, similar to that of the modern ocean sediments, except for a few low values down to ~2‰ at the peak of the K-O $\delta^{13}C$ excursion. Interestingly, in this section $\delta^{15}N_{org}$ does not change with $\delta^{13}C_{carb}$ and $\delta^{13}C_{org}$. Particularly, at the falling limb of the $\delta^{13}C$ excursion, $\delta^{15}N$ shows a 2‰ increase, similar to those documented from correlative units in South China (Yao et al., 2015).

for the interval of 40–60 m between the two karstic disconformities where $\Delta\delta^{13}C$ values display a negative shift down to 25‰ (Fig. 6).

Both PR and MH sections exhibit broad positive $\delta^{13}C_{carb}$ and $\delta^{13}C_{org}$ excursions, with the exception of the $\delta^{13}C_{carb}$ profile in the MH section that only records single $\delta^{13}C_{carb}$ peak instead of two, as seen in its $\delta^{13}C_{org}$ profile and in both $\delta^{13}C_{carb}$ and $\delta^{13}C_{org}$ profiles of the PR section.

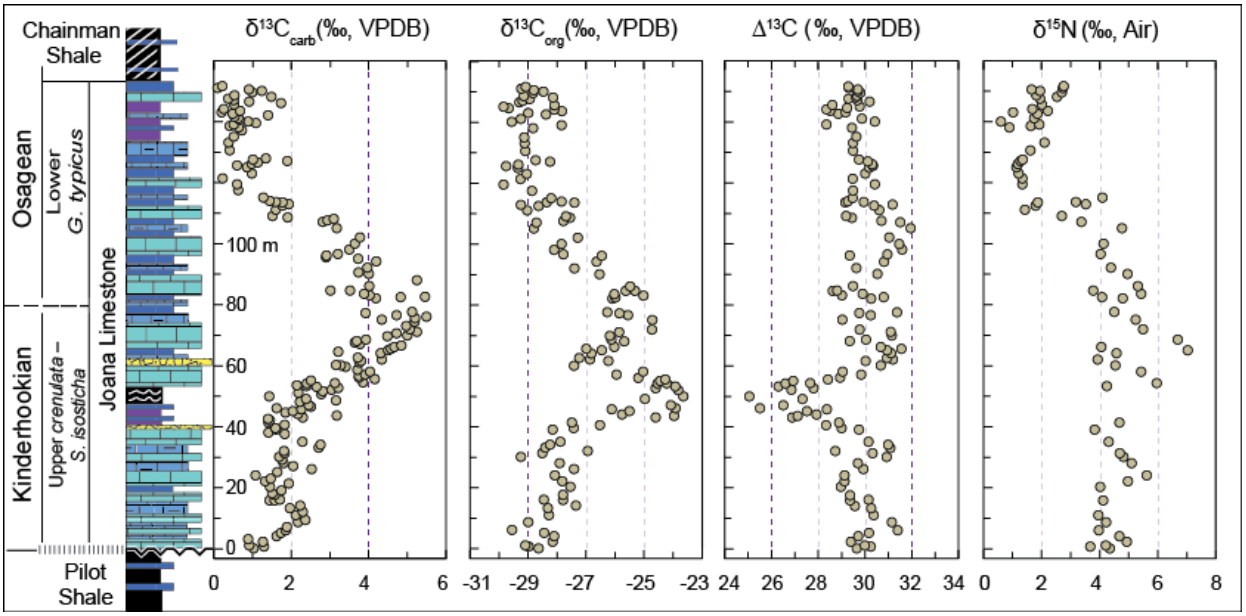

Fig. 6. The $\delta^{13}C_{carb}$, $\delta^{13}C_{org}$, $\Delta^{13}C$, and $\delta^{15}N$ variations of the Kinderhookian-Osagean (K-O) strata from the MH section. In general, $\delta^{13}C_{carb}$ and $\delta^{13}C_{org}$ covary. However, at the interval of 40-60 m, which is bounded by two exposure surfaces, $\delta^{13}C_{org}$ shows an obvious positive shift similar to that of the PR section, while $\delta^{13}C_{carb}$ does not display the same magnitude of variation. We suspect that the absence of a $\delta^{13}C_{carb}$ peak comparable with $\delta^{13}C_{org}$ is due to diagenetic alteration below a karstic disconformity at 60 m, which may have had more significant impact on $\delta^{13}C_{carb}$. Most of the $\Delta^{13}C$ values are within 30±1.5‰, except for the interval of 40-60 m where a negative shift is caused by lower $\delta^{13}C_{carb}$ values. In contrast to the PR section, $\delta^{15}N$ is coupled with $\delta^{13}C_{carb}$ and $\delta^{13}C_{org}$, showing a 3‰ increase from 4‰ to 7‰ at the rising limb of the $\delta^{13}C$ excursion and 5–6‰ decrease from 7‰ to ~2‰ at the falling limb of the $\delta^{13}C$ excursion.

The decoupled $\delta^{13}C_{carb}$ and $\delta^{13}C_{org}$ at the interval of 40–60 m in the MH section is most likely resulted from diagenetic alteration of either $\delta^{13}C_{carb}$ or $\delta^{13}C_{org}$, which will be elaborated in the later discussion section.

4.2. Nitrogen isotope profiles

In the PR section, $\delta^{15}N$ values are decoupled from $\delta^{13}C_{carb}$ and $\delta^{13}C_{org}$ and do not show any obvious temporal trend (Fig. 5). Most of the $\delta^{15}N$ values are around 4±1‰ throughout the K-

O $\delta^{13}C$ excursion, but a few data points are down to 2‰ at the peak of the $\delta^{13}C$ excursion. In contrast, $\delta^{15}N$ values in the MH section show a 3‰ increase toward the peak of the K-O $\delta^{13}C$ excursion, followed by a decrease from 7‰ to 1.3‰ at the falling limb of the $\delta^{13}C$ excursion (Fig. 6). A slight $\delta^{15}N$ increase from 1.3‰ to 2.7‰ occurs the upmost 15 m of the Joana Limestone, coincident with the 1–1.5‰ increase of $\delta^{13}C_{carb}$ and $\delta^{13}C_{org}$.

5. Discussions

5.1. Covarying $\delta^{13}C_{carb}$ and $\delta^{13}C_{org}$ and their implications

The covariance of $\delta^{13}C_{carb}$ and $\delta^{13}C_{org}$ from the PR and MH sections provide strong evidence for the preservation of primary or near primary isotope signature because most secondary diagenetic processes would not shift both $\delta^{13}C_{carb}$ and $\delta^{13}C_{org}$ towards the same direction at comparable magnitudes (Knoll et al., 1986; Johnston et al., 2012). Exceptions may include repeatedly exposed carbonate platforms where meteoric alteration caused negative shift in $\delta^{13}C_{carb}$ and terrestrial organic matter contributed to lower $\delta^{13}C_{org}$ values (Oehlert and Swart, 2014), but so far this is a localized phenomenon documented from a single drill core; its representativeness for regionally or globally correlatable negative $\delta^{13}C$ 'excursions' still needs to be confirmed. In the PR section, a strong correlation ($R^2 = 0.83$; Fig. 7A) between $\delta^{13}C_{carb}$ and $\delta^{13}C_{org}$ is present for all the samples throughout the section, independent of lithology and TOC contents (Table 1). Particularly, both $\delta^{13}C_{carb}$ and $\delta^{13}C_{org}$ show double peaks with a comparable 3‰ negative shift in between. This negative shift occurs in laminated, fine-grained lime mudstone and wackestone that were most likely deposited in deep subtidal environments below fairweather wave base instead of periodically exposed tidal flat or carbonate bank (cf. Oehlert and Swart, 2014). There is a weak $\delta^{13}C_{carb}$–$\delta^{18}O_{carb}$ correlation ($R^2 = 0.4$; Fig. 7E) in the PR section, but a large portion of this correlation may be related to the 2‰ increase in $\delta^{18}O$ towards

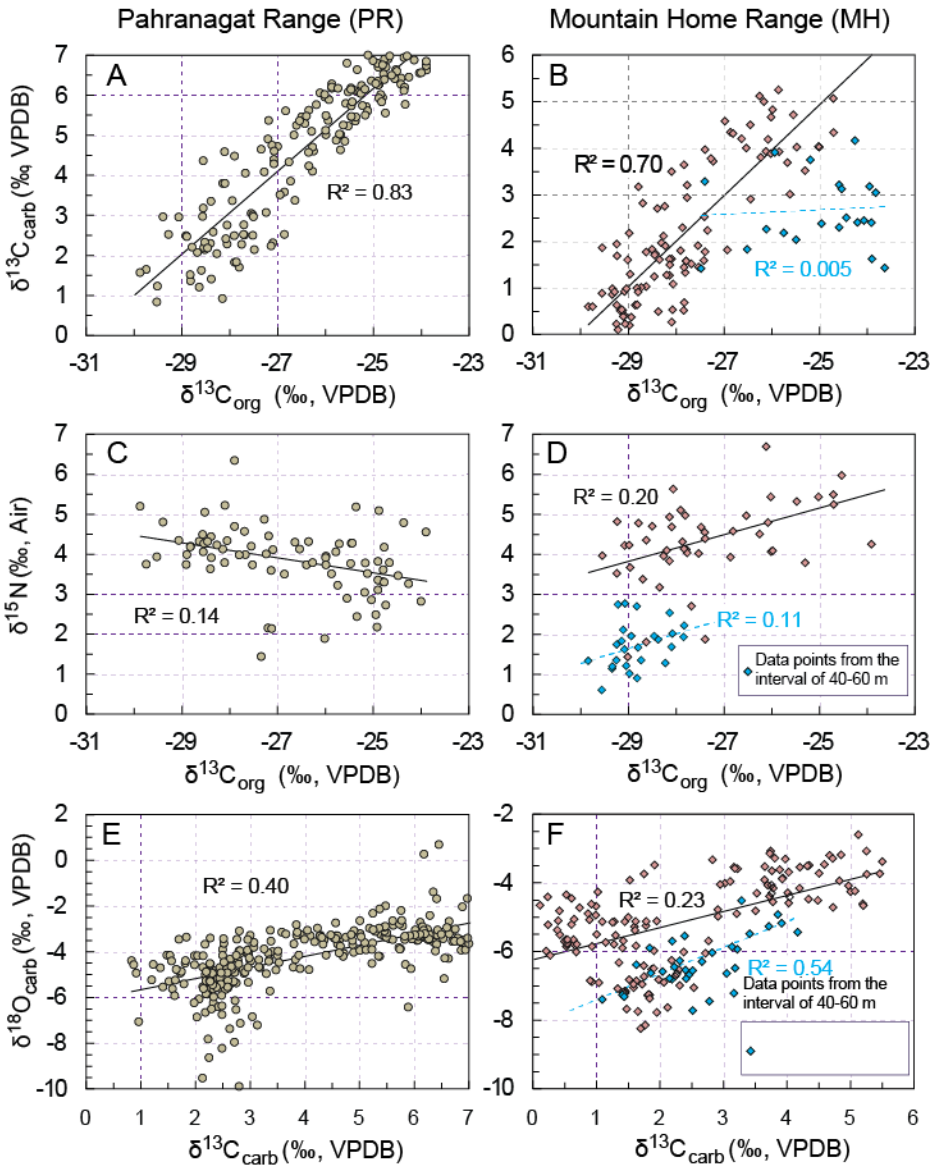

Fig. 7. Cross plots of carbon, oxygen, and nitrogen isotopes. (A) Cross plot of $\delta^{13}C_{carb}$–$\delta^{13}C_{org}$ data from the PR section showing a positive correlation (R^2 = 0.83). (B) Cross plot of $\delta^{13}C_{carb}$–$\delta^{13}C_{org}$ data from the MH section showing a positive correlation (R^2 = 0.70) except for the data from the interval of 40-60 m (R^2 = 0.005). (C) Cross plot of $\delta^{15}N$–$\delta^{13}C_{org}$ data from the PR section. (D) Cross plot of $\delta^{15}N$–$\delta^{13}C_{org}$ data from the MH section. In both sections $\delta^{15}N$ and $\delta^{13}C_{org}$ data do not show a positive correlation. (E) Cross plot of $\delta^{13}C_{carb}$–$\delta^{18}O_{carb}$ data from the PR section showing a very weak correlation (R^2 = 0.40). (F) Cross plot of $\delta^{13}C_{carb}$–$\delta^{18}O_{carb}$ data from the MH section. The interval of 40-60 m shows a positive correlation (R^2 = 0.54), while the rest of the data do not have an obvious correlation (R^2 = 0.23).

the $\delta^{13}C$ peak in response to global cooling (Mii et al., 1999; Saltzman et al., 2000; Saltzman, 2002; Buggsich et al., 2008). All these features suggest that both $\delta^{13}C_{carb}$ and $\delta^{13}C_{org}$ values record isotopic signatures derived from the same DIC (dissolved inorganic carbon) reservoir in the ocean, from which organic matter is synthesized with a kinetic fractionation of ~30±1‰ associated with carbon fixation.

The majority of $\delta^{13}C_{carb}$ and $\delta^{13}C_{org}$ from the MH section also show a strong covariance (R^2 = 0.70), except for the disconformity-bounded interval of 40–60 m that does not display $\delta^{13}C_{carb}$ and $\delta^{13}C_{org}$ covariation (R^2 = 0.005; Fig. 7B). This interval also show considerable $\delta^{13}C_{carb}$–$\delta^{18}O_{carb}$ covariation (R^2 = 0.54; Fig. 7F). Although both $\delta^{13}C_{carb}$ and $\delta^{13}C_{org}$ could be modified during diagenesis, the magnitude of $\delta^{13}C_{org}$ alteration during meteoric and burial diagenesis by addition of bacterial biomass or terrestrial organic matter, organic matter degradation, thermal maturation, and methanogenesis is commonly within the range of 1–3‰ (e.g., Peters et al., 1981; Hatcher et al., 1983; Lehmann et al., 2002; Hayes et al., 1999; Hill et al., 2003; Jiang et al., 2012). In contrast, meteoric and burial diagenetic alteration on $\delta^{13}C_{carb}$ may be much more significant, depending on the fluid-rock ratios and duration (e.g., da Silva and Boulvain, 2008; Knauth and Kennedy, 2009; Derry, 2010; Swart, 2008, 2015). Considering the low TOC contents (< 0.1%; Table 1) and the 7‰ positive shift in $\delta^{13}C_{org}$ that is comparable with that of the PR section (Fig. 8), it is more likely that the lack of covariance at 40–60 m is caused by meteoric alteration of $\delta^{13}C_{carb}$ underneath a karstic disconformity.

Correlation between the PR and MH sections suggests that the 7‰ magnitude and the double spikes are more representative of the K-O $\delta^{13}C$ excursion (Fig. 8). In the PR section, both $\delta^{13}C_{carb}$ and $\delta^{13}C_{org}$ show double spikes with peak values up to 7‰ and a negative shift down to 4‰ between the peaks. In the MH section, $\delta^{13}C_{org}$ shows similar double spikes but $\delta^{13}C_{carb}$

displays only a single peak with the highest value of 5.5‰. The missing $\delta^{13}C_{carb}$ spike is most likely caused by meteoric diagenetic alteration below a karstic disconformity that lowered $\delta^{13}C_{carb}$ but not $\delta^{13}C_{org}$ values, resulting in smaller magnitude of the $\delta^{13}C_{carb}$ excursion. The negative $\delta^{13}C_{carb}$ shift at the peak of the K-O $\delta^{13}C$ excursion appears in many successions globally, including the Samaria Mountain section in Idaho (Saltzman, 2002), Clark Fork Canyon and Sheep Mountain sections in Wyoming (Saltzman, 2003; Katz et al., 2007), Fitchville Ridge section in central Utah (Saltzman, 2003), and sections in the Dinant Basin of Belgium and Northern Urals of Russia (Saltzman et al., 2004). The lack of this negative $\delta^{13}C$ shift in some sections is likely due to incomplete stratigraphic records and/or meteoric diagenetic alteration of $\delta^{13}C_{carb}$ near exposure surfaces/unconformities in shallow-water sections, such as in the MH section (Fig. 8). The K-O $\delta^{13}C$ excursion is stratigraphically "self-destructive": increase of organic carbon burial would result in global cooling and sea-level fall and form exposure surfaces/unconformities in shallow-water carbonate platforms. Unconformities and exposure surfaces are indeed present at or near the peak the K-O $\delta^{13}C$ excursion in the Great Basin area (e.g., Fig. 8), across the entire United States (Lane and Brenckle, 2005; Kammer and Matchen, 2008), and in South China (Yao et al., 2015; Jiang, unpublished data). Therefore, only at relatively deep-water sections the complete isotope records are preserved. In this context, the $\delta^{13}C_{carb}$ and $\delta^{13}C_{org}$ pattern seen in the PR section (Figs. 5 and 8) may be more representative of the K-O $\delta^{13}C$ excursion in western North America, and potentially the TICE in other successions globally. The smaller magnitude of the K-O $\delta^{13}C_{carb}$ excursion or TICE may have been overprinted with local environmental and/or diagenetic signal, which needs to be clarified in future research.

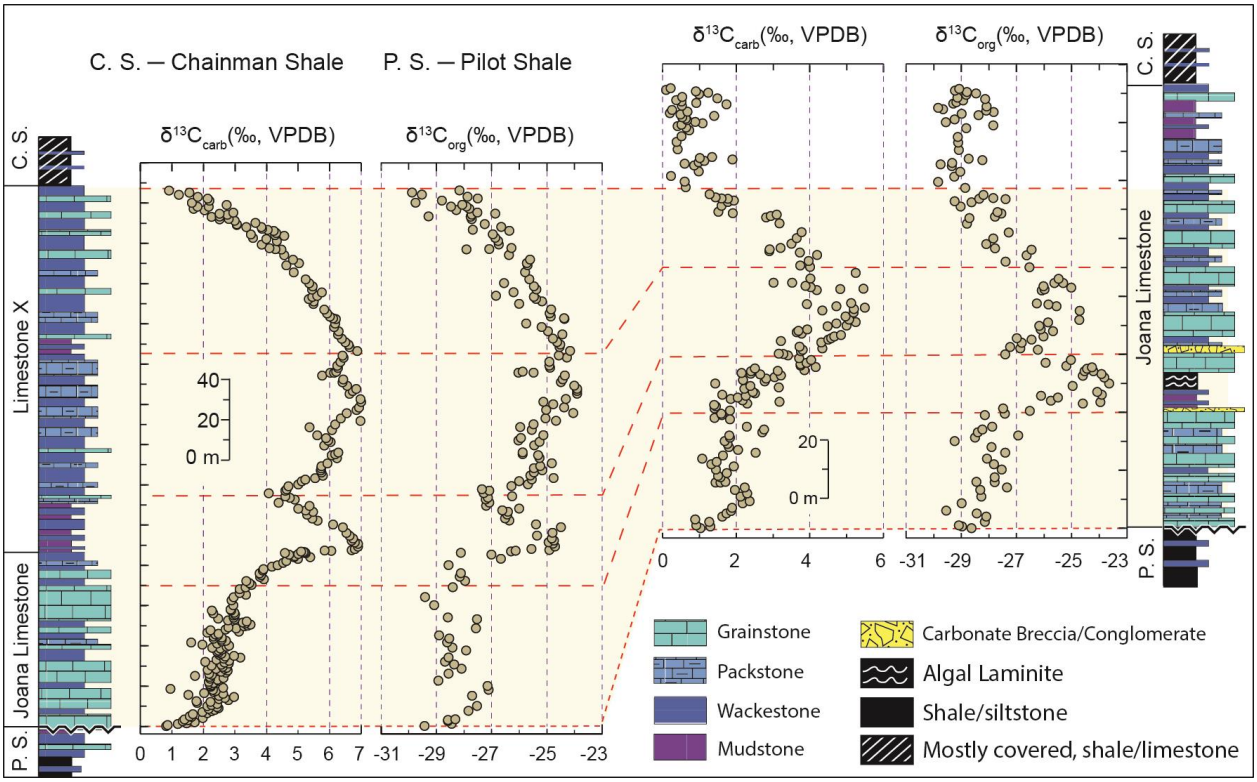

Fig. 8. Correlation of the K-O $\delta^{13}C$ excursion between PR and MH sections. The secondary negative $\delta^{13}C_{carb}$ shift at the peak of the K-O $\delta^{13}C$ excursion observed in the PR section is missing at the MH section, but the $\delta^{13}C_{org}$ shows identical patterns in both sections. It suggests that the $\delta^{13}C_{carb}$ values from the interval of 40-60 m in the MH section, have been altered, possibly due to meteoric diagenesis associated with the karstic disconformity at 60 m. The presence of $\delta^{13}C_{carb}$–$\delta^{18}O_{carb}$ covariation (R^2 = 0.54; Fig. 7F) and lack of $\delta^{13}C_{carb}$–$\delta^{13}C_{org}$ correlation (R^2 = 0.005; Fig. 7B) in this interval also suggest altered $\delta^{13}C_{carb}$ values.

5.2. Temporal changes in carbon isotope fractionation

The temporal changes in carbon isotope fractionation have been used to estimate the atmospheric O_2 level in geological history (e.g., Berner, 2000; Beerling et al., 2002; Saltzman et al., 2013). Laboratory experiments demonstrated that at higher partial pressure of atmospheric O_2 (pO_2), vascular land plants, bryophytes, and marine phytoplanktons preferentially uptake ^{12}C, resulting in high carbon isotope fractionation (Beerling et al., 2002; Fletcher et al., 2006). In the

PR section, $\Delta^{13}C$ values show a 2‰ increase toward the peak of the K-O $\delta^{13}C$ excursion (Fig. 5). The magnitude of $\Delta^{13}C$ increase is similar to that of the $\Delta^{13}C$ variations documented across the late Cambrian SPICE (Steptoean Positive Carbon Isotope Excursion) event (Saltzman et al., 2013), implying significant increase in atmospheric O_2 resulted from enhanced organic carbon and pyrite burial. However, in the MH section, $\Delta^{13}C$ values do not show temporal changes across the K-O $\delta^{13}C$ excursion, except for the 4‰ decrease at the interval of 40–60 m that is closely related to the missing of the $\delta^{13}C_{carb}$ peak. Ideally, shallow-water sections above fairweather wave base should be the best locality to record the $\Delta^{13}C$ change if atmospheric O_2 had an impact on the photosynthetic isotopic discrimination because at the shallow mixing zone, seawater O_2 concentration would be in equilibrium with atmospheric O_2. Since $\Delta^{13}C$ values can be influenced by a variety of processes including concentrations of aqueous CO_2 ($[CO_2]_{aq}$) in seawater, productivity and growth rate, cellular volume to surface area (V/S) ratios (e.g., Hayes et al., 1999), the ecosystem of primary producers (e.g., Raven et al., 2002), and carbon cycling by heterotrophs and chemoautotrophs in specific depositional environments (e.g., Hayes et al., 1999; Jiang et al., 2012), the validity of using $\Delta^{13}C$ change as paleo-O_2 proxy needs to be cautious. The ideal scenario to use $\Delta^{13}C$ for pO_2 estimation might be data from shallow-water sections (above fairweather wave base) without significant temporal changes in depositional environments and without frequent subaerial exposures, which requires further exploration for the K-O interval.

5.3. Nitrogen isotope variations and implications

Nitrogen (N) is a macronutrient for organisms and its availability in the ocean exerts a major control on the primary productivity (e.g., Falkowski, 1997; Canfield et al., 2010). Nitrogen isotopes of organic matter in sedimentary rocks ($\delta^{15}N$) serves as an important tool for

investigating the N-biogeochemical cycles in modern and ancient environments (e.g., Godfrey and Falkowski, 2009; Algeo et al., 2014; Ader et al., 2016; Stüeken et al., 2016). In the modern ocean, the primary source of bioavailable N is from biological nitrogen fixation, during which N-fixing bacteria (e.g., diazotrophy) convert atmospheric N_2 to ammonium (NH_4^+). Nitrogen fixation ($N_2 \rightarrow NH_4^+$) has limited isotope fractionation so that ammonium has $\delta^{15}N$ values (–2‰ to 1‰) close to that of atmospheric N_2 ($\delta^{15}N \approx 0$‰). In oxygenated oceans, fixed nitrogen (NH_4^+) are quantitatively oxidized to nitrate (NO_3^-) without significant isotope changes (Ader et al., 2016). A portion of the nitrate (NO_3^-) reservoir in the ocean, however, is lost during denitrification ($NO_3^- \rightarrow NO_2^- \rightarrow N_2$) and less commonly anammox ($NH_4^+ \rightarrow NO_2^- \rightarrow N_2$), at or near the oxygen minimum zone (OMZ) and in sediments. This denitrification process releases N_2 that has $\delta^{15}N$ values up to 28‰ lower than its parent NO_3^-, resulting in higher $\delta^{15}N$ values in the oceanic nitrate pool ($\delta^{15}N \approx 5$‰ in the modern ocean), from which photosynthetic organisms take N to form organic matter. In this context, $\delta^{15}N$ from organic matter is considered recording the N isotope values of the seawater nitrate pool (e.g., Algeo et al., 2014; Ader et al., 2016).

Since denitrification in sediments is nearly quantitative and causes limited isotope change (0–3‰; Stüeken et al., 2016), water-column denitrification at or near the OMZ exerts the first order control on the $\delta^{15}N$ of the seawater nitrate pool. In oxygenated oceans like the modern in which a stable nitrate pool is developed (for Precambrian anoxic and stratified oceans, see reviews in Stüeken et al., 2016 and Ader et al., 2016), higher water-column denitrification or expansion of the OMZ would result in heavier $\delta^{15}N$ values, while more oxygenated ocean with contracted OMZ would have lower $\delta^{15}N$ values (e.g., Quan and Falkowski, 2009). Numerous studies have indicated that the Early Mississippian oceans are well-oxygenated (e.g., Berner and Canfield, 1989; Kampschulte et al., 2001, 2004; Gill et al., 2007) and it is anticipated that N-

biochemcial cycling would be similar to that of the modern ocean. In general, the majority of the $\delta^{15}N$ data from the PR and MH sections and those from the South China section (Yao e al., 2015) are in the range of 3‰ to 5‰ (Fig. 9), consistent with aerobic N cycling in oxygenated oceans (Stüeken et al., 2016).

The different temporal $\delta^{15}N$ trends between the PR and MH sections (Fig. 9), however, invoke two alternative interpretations. In the PR section, $\delta^{15}N_{org}$ values are mostly 4±1‰ and do not show obvious temporal change across the majority of the K-O $\delta^{13}C_{carb}$ excursion but a slight increase at the end of the excursion. This is similar to the $\delta^{15}N$ profile documented from the Malanbian section in South China (Fig. 9). In contrast, $\delta^{15}N$ values from the MH sections show a 3‰ increase toward the peak of the K-O $\delta^{13}C_{carb}$ excursion and a 5‰ decrease at the falling limb of the K-O $\delta^{13}C_{carb}$ excursion. If the $\delta^{15}N$ trend of the PR and Malanbian sections are more representative of the isotope change of the marine nitrate pool, the increase of $\delta^{15}N$ associated with the K-O $\delta^{13}C_{carb}$ excursion marks the onset of a multimillion-year change in N-isotopes to the $\delta^{15}N$ plateau of the Late Paleozoic ice age, which have been linked to a long-term shift in the locus of denitrification from continental-shelf sediments to continent-margin oxygen-minimum zones (Algeo et al., 2014; Yao et al., 2015). In this case, the $\delta^{15}N$ trend recorded in the MH section, particularly the 5‰ decrease in $\delta^{15}N$ during the late stage of the C-isotope excursion, reflects locally intensified nitrogen fixation in restricted environments that are possibly isolated from the open ocean. Alternatively, the $\delta^{15}N$ trends from the MH section are more representative of the isotope change of the marine nitrate pool. In this case, the increase of $\delta^{15}N$ at the rising limb of the $\delta^{13}C_{carb}$ excursion record the expansion of the OMZ in response to enhanced organic carbon production and burial, while the decrease of $\delta^{15}N$ at the falling limb of the $\delta^{13}C_{carb}$ excursion reflects more oxygenated oceans and shrink of the OMZ after maximum organic

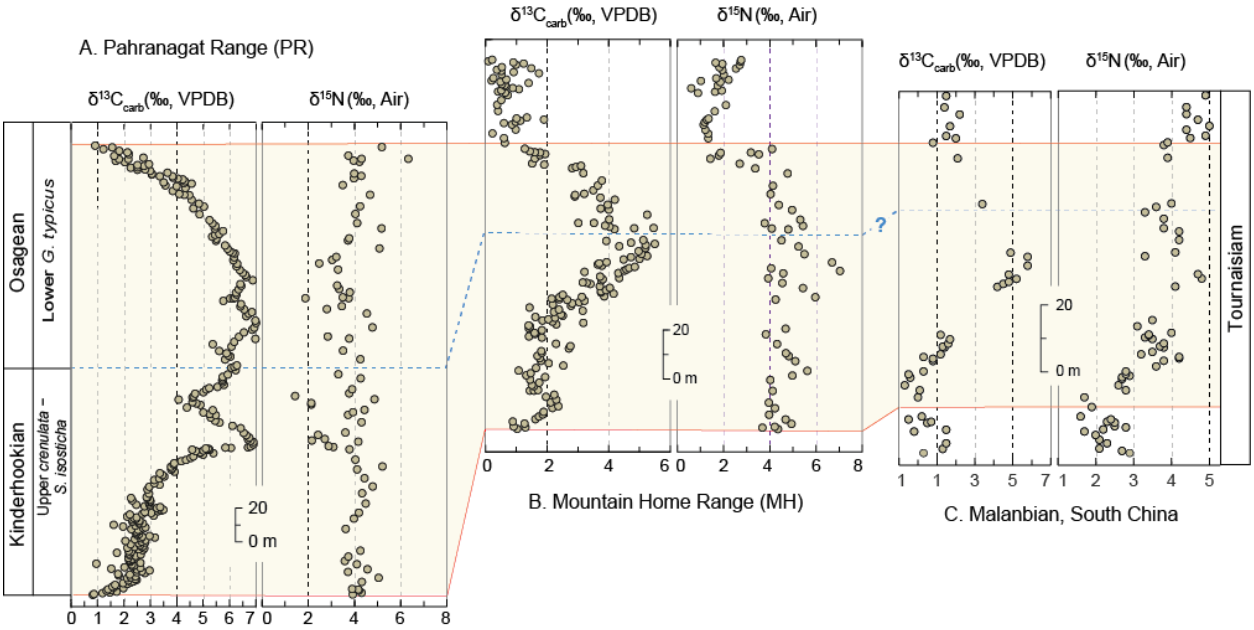

Fig. 9. Correlation of $\delta^{13}C_{carb}$ and $\delta^{15}N$ profiles of the PR and MH sections with those from the Malanbian section in South China (Yao et al., 2015). The $\delta^{15}N$ data from the MH section show coupled $\delta^{13}C$ and $\delta^{15}N$, while in both the PR and the Malanbian sections, $\delta^{15}N$ values do not show a negative shift after the peak of the K-O $\delta^{13}C$ excursion. With the available data, it is uncertain which pattern (the MH section or the PR and Malanbian sections) is more representative of the K-O $\delta^{15}N_{org}$ signature, although the coupled $\delta^{13}C_{carb}$ and $\delta^{15}N$ observed from the MH section better explains potentially more oxygenated oceans after the prominent K-O $\delta^{13}C$ excursion.

carbon production and burial. In this interpretation, the high $\delta^{15}N$ values from the PR and Malanbian sections may record local ^{15}N-enrichments close to margins of the OMZ in deeper-water environments (e.g., the PR section) or restricted proximal environments (e.g., Malanbian section).

The current data are insufficient to discriminate these alternative interpretations. The long-term shift in the locus of sediments vs. water column denitrification has support from the compiled data of the entire Phanerozoic (Algeo et al., 2004), but the temporal resolution is multi-

million years. The second interpretation is more consistent with the N-isotope variations of Quaternary (e.g., Altabet et al., 1995; Deutsch et al., 2004), Pleistocene (e.g., Liu et al., 2005; Robinson et al., 2014) and Late Carboniferous (Algeo et al., 2008; Algeo et al., 2012) glacial-interglacial cycles. A more comprehensive study with broader temporal and spatial coverage is needed to clarify the uncertainties.

6. Conclusions

Paired carbonate and organic carbon isotope analyses across the K-O interval reveal strong covariance of $\delta^{13}C_{carb}$–$\delta^{13}C_{org}$ data and confirm the primary origin of the K-O $\delta^{13}C$ excursion. Stratigraphic and isotopic correlations between the deep and shallow-water sections suggest that the 7‰ magnitude and double spikes are more representative of the K-O $\delta^{13}C_{carb}$ excursion. The smaller magnitude of the K-O $\delta^{13}C_{carb}$ excursion in some sections of the Great Basin and the TICE in other sections globally may have been overprinted with local environmental and/or diagenetic signal, which needs to be clarified in future research. The temporal $\Delta^{13}C$ variations differ between shallow- and deep-water sections and therefore using $\Delta^{13}C$ as a paelo-pO_2 proxy needs to be cautious. The different $\delta^{15}N$ trends across the K-O $\delta^{13}C$ excursion invoke two alternative interpretations. If the coupled $\delta^{13}C$-$\delta^{15}N$ from the shallow-water sections are more representative of the isotope signature of the marine nitrate pool, the $\delta^{15}N$ record reflects the expansion and shrink of the oxygen-minimum zone and water-column denitrification in response to changes in organic carbon production and burial. If the decoupled $\delta^{13}C$-$\delta^{15}N$ from the deep-water section is more representative of the seawater signature, the $\delta^{15}N$ record may mark the onset of a long-term shift in the locus of denitrification from continental-shelf sediments to continent-margin oxygen-minimum zones. Confirming these interpretations

requires a more comprehensive study with broader temporal and spatial coverage of the Lower Mississippian strata in western U.S.A. and in other places globally.

Table 1. Carbon, oxygen and nitrogen isotope data from measured Early Mississippian sections in the Great Basin, western USA

Section 1 : Pahranagat Range, Alamo (NV), GPS locaton: 37 23' 42.94" N, 115 15' 43.30" W

Strat. Unit	Height (m)	Sample No.	Lithology	$\delta^{13}C_{carb}$ (‰,VPDB)	$\delta^{18}O_{carb}$ (‰,VPDB)	TOC (w%)
Joana Limestone	0	PR-65	Wackestone	0.83	-4.39	0.03
Joana Limestone	0.5	PR-65.5	Grainstone	0.87	-4.57	
Joana Limestone	1	PR-66	Wackestone	1.20	-5.23	0.05
Joana Limestone	1.5	PR-66.5	Grainstone	1.48	-4.14	
Joana Limestone	2	PR-67	Grainstone	1.73	-4.93	
Joana Limestone	2.5	PR-67.5	Packstone	1.36	-4.71	0.04
Joana Limestone	3	PR-68	Packstone	1.52	-5.30	0.03
Joana Limestone	3.4	PR-68.4	Packstone	1.41	-9.55	0.03
Joana Limestone	4	PR-69	Grainstone	1.98	-4.17	
Joana Limestone	4.5	PR-69.5	Grainstone	1.63	-5.24	
Joana Limestone	5	PR-70	Grainstone	1.58	-5.63	
Joana Limestone	6	PR-71	Grainstone	1.68	-4.82	
Joana Limestone	6.5	PR-71.5	Grainstone	2.14	-5.53	
Joana Limestone	7	PR-72	Grainstone	1.98	-4.57	
Joana Limestone	7.5	PR-72.5	Wackestone	2.28	-4.54	0.03
Joana Limestone	8	PR-73	Lime mudstone	2.37	-4.83	
Joana Limestone	8.5	PR-73.5	Grainstone	2.18	-5.01	
Joana Limestone	9	PR-74	Grainstone	2.49	-4.68	
Joana Limestone	9.5	PR-74.5	Wackestone	2.44	-4.80	
Joana Limestone	10	PR-75	Packstone	2.14	-4.68	0.01
Joana Limestone	10.5	PR-75.5	Packstone	2.27	-5.03	
Joana Limestone	11	PR-76	Packstone	2.45	-4.69	
Joana Limestone	11.5	PR-76.5	Wackestone	1.81	-4.50	
Joana Limestone	12	PR-77	Wackestone	2.24	-5.33	
Joana Limestone	12.5	PR-77.5	Packstone	1.79	-5.41	
Joana Limestone	13	PR-78	Wackestone	2.80	-3.95	
Joana Limestone	13.5	PR-78.5	Wackestone	2.50	-3.90	0.03
Joana Limestone	14	PR-79	Wackestone	2.68	-4.92	
Joana Limestone	14.5	PR-79.5	Wackestone	2.97	-3.91	
Joana Limestone	15	PR-80	Wackestone	2.50	-4.16	0.03
Joana Limestone	15.5	PR-80.5	Grainstone	1.54	-4.17	
Joana Limestone	16	PR-81	Grainstone	2.63	-4.33	
Joana Limestone	16.5	PR-81.5	Grainstone	2.03	-6.87	
Joana Limestone	17	PR-82	Grainstone	2.34	-5.40	
Joana Limestone	17.5	PR-82.5	Grainstone	2.40	-5.03	
Joana Limestone	18	PR-83	Wackestone	2.31	-4.95	0.02
Joana Limestone	18.5	PR-83.5	Grainstone	0.96	-7.06	
Joana Limestone	19	PR-84	Grainstone	2.63	-7.37	
Joana Limestone	19.5	PR-84.5	Grainstone	2.25	-8.64	
Joana Limestone	20	PR-85	Wackestone	2.24	-5.79	0.03
Joana Limestone	20.5	PR-85.5	Grainstone	2.27	-4.52	
Joana Limestone	21	PR-86	Packstone	2.19	-5.28	
Joana Limestone	21.5	PR-86.5	Grainstone	2.33	-6.24	
Joana Limestone	22	PR-87	Grainstone	2.18	-6.65	
Joana Limestone	22.5	PR-87.5	Wackestone	2.49	-8.23	0.03
Joana Limestone	23	PR-88	Packstone	2.45	-5.60	
Joana Limestone	23.5	PR-88.5	Grainstone	2.22	-5.85	
Joana Limestone	24	PR-89	Grainstone	2.64	-4.64	
Joana Limestone	24.5	PR-89.5	Grainstone	2.21	-4.87	
Joana Limestone	25	PR-90	Grainstone	1.74	-4.87	
Joana Limestone	25.5	PR-90.5	Packstone	2.28	-5.62	
Joana Limestone	26	PR-91	Wackestone	2.19	-5.85	0.03
Joana Limestone	26.5	PR-91.5	Grainstone	2.72	-4.91	
Joana Limestone	27	PR-92	Grainstone	2.57	-4.59	
Joana Limestone	27.6	PR-92.6	Grainstone	2.78	-4.38	

$\delta^{13}C_{org}$ (‰,VPDB)	TN (%w)	$\delta^{15}N_{org}$ (‰, air)	$\Delta\delta^{13}C$	Age	Conodont zone*
-29.52	0.011	3.93	30.35	Kinderhookian	*S. Sandbergi* ?
				Kinderhookian	*S. Sandbergi* ?
-28.64	0.024	4.32	29.84	Kinderhookian	*S. Sandbergi* ?
				Kinderhookian	*S. Sandbergi* ?
				Kinderhookian	*S. Sandbergi* ?
-28.82	0.050	4.20	30.18	Kinderhookian	*S. Sandbergi* ?
-28.61	0.020	4.18	30.13	Kinderhookian	*S. Sandbergi* ?
-28.38	0.013	3.91	29.79	Kinderhookian	*S. Sandbergi* ?
				Kinderhookian	*S. Sandbergi* ?
				Kinderhookian	*S. Sandbergi* ?
				Kinderhookian	*S. Sandbergi* ?
				Kinderhookian	*S. Sandbergi* ?
				Kinderhookian	*S. Sandbergi* ?
				Kinderhookian	*S. Sandbergi* ?
-28.05	0.010	4.34	30.33	Kinderhookian	*S. Sandbergi* ?
				Kinderhookian	*S. Sandbergi* ?
				Kinderhookian	*S. Sandbergi* ?
				Kinderhookian	*S. Sandbergi* ?
				Kinderhookian	*S. Sandbergi* ?
-28.52	0.013	5.05	30.66	Kinderhookian	*S. Sandbergi* ?
				Kinderhookian	*S. Sandbergi* ?
				Kinderhookian	*S. Sandbergi* ?
				Kinderhookian	*S. Sandbergi* ?
				Kinderhookian	*S. Sandbergi* ?
				Kinderhookian	*S. Sandbergi* ?
				Kinderhookian	*S. Sandbergi* ?
-27.52	0.009	3.73	30.02	Kinderhookian	*S. Sandbergi* ?
				Kinderhookian	*S. Sandbergi* ?
				Kinderhookian	*S. Sandbergi* ?
-27.69	0.008	4.57	30.19	Kinderhookian	*S. Sandbergi* ?
				Kinderhookian	*S. Sandbergi* ?
				Kinderhookian	*S. Sandbergi* ?
				Kinderhookian	*S. Sandbergi* ?
				Kinderhookian	*S. Sandbergi* ?
				Kinderhookian	*S. Sandbergi* ?
-27.10	0.007	4.11	29.41	Kinderhookian	*S. Sandbergi* ?
				Kinderhookian	*S. Sandbergi* ?
				Kinderhookian	*S. Sandbergi* ?
				Kinderhookian	*S. Sandbergi* ?
-27.14	0.005	3.60	29.37	Kinderhookian	*S. Sandbergi* ?
				Kinderhookian	*S. Sandbergi* ?
				Kinderhookian	*S. Sandbergi* ?
				Kinderhookian	*S. Sandbergi* ?
				Kinderhookian	*S. Sandbergi* ?
-28.91	0.006	3.74	31.40	Kinderhookian	*S. Sandbergi* ?
				Kinderhookian	*S. Sandbergi* ?
				Kinderhookian	*S. Sandbergi* ?
				Kinderhookian	*S. Sandbergi* ?
				Kinderhookian	*S. Sandbergi* ?
				Kinderhookian	*S. Sandbergi* ?
				Kinderhookian	*S. Sandbergi* ?
-28.54	0.002	4.27	30.73	Kinderhookian	*S. Sandbergi* ?
				Kinderhookian	*S. Sandbergi* ?
				Kinderhookian	*S. Sandbergi* ?
				Kinderhookian	*S. Sandbergi* ?

Joana Limestone	28	PR-93	Packstone	2.15	-5.61	
Joana Limestone	28.5	PR-93.5	Wackestone	2.41	-5.19	0.03
Joana Limestone	28.5	PR-93.5	Grainstone	2.67	-4.76	
Joana Limestone	29	PR-94	Grainstone	2.75	-5.37	
Joana Limestone	29.5	PR-94.5	Grainstone	2.63	-5.44	
Joana Limestone	30	PR-95	Grainstone	2.26	-5.27	
Joana Limestone	30.5	PR-95.5	Wackestone	2.58	-4.74	0.03
Joana Limestone	31	PR-96	Grainstone	2.81	-4.08	
Joana Limestone	31.6	PR-96.6	Packstone	2.68	-5.34	
Joana Limestone	32	PR-97	Wackestone	2.07	-6.08	0.05
Joana Limestone	32.5	PR-97.5	Grainstone	2.82	-7.13	
Joana Limestone	33	PR-98	Grainstone	2.42	-6.42	
Joana Limestone	33.5	PR-98.5	Wackestone	2.66	-4.65	
Joana Limestone	34	PR-99	Wackestone	3.18	-4.70	0.06
Joana Limestone	34.5	PR-99.5	Wackestone	2.70	-5.31	
Joana Limestone	35	PR-100	Wackestone	2.97	-4.10	0.02
Joana Limestone	35.5	PR-100.5	Packstone	2.51	-5.15	
Joana Limestone	36	PR-101	Packstone	2.57	-5.38	
Joana Limestone	36.5	PR-101.5	Grainstone	2.49	-6.75	
Joana Limestone	37	PR-102	Grainstone	2.45	-5.23	
Joana Limestone	37.5	PR-102.5	Packstone	2.49	-6.37	0.11
Joana Limestone	38	PR-103	Grainstone	2.60	-5.58	
Joana Limestone	38.5	PR-103.5	Grainstone	2.55	-5.65	
Joana Limestone	39	PR-104	Wackestone	2.29	-6.50	0.04
Joana Limestone	39.5	PR-104.5	Grainstone	2.74	-6.54	
Joana Limestone	40	PR-105	Grainstone	2.82	-3.96	
Joana Limestone	40.5	PR-105.5	Grainstone	1.98	-6.23	
Joana Limestone	41	PR-106	Grainstone	2.44	-5.15	
Joana Limestone	41.5	PR-106.5	Packstone	1.62	-5.92	0.08
Joana Limestone	42	PR-107	Grainstone	2.59	-5.27	
Joana Limestone	42.5	PR-107.5	Grainstone	2.73	-6.14	
Joana Limestone	43	PR-108	Grainstone	2.59	-5.54	
Joana Limestone	43.4	PR-108.4	Wackestone	2.33	-5.65	0.03
Joana Limestone	44	PR-109	Grainstone	2.58	-4.92	

				Kinderhookian	*S. Sandbergi* ?
-28.08	0.001		30.49	Kinderhookian	*S. Sandbergi* ?
				Kinderhookian	*S. Sandbergi* ?
				Kinderhookian	*S. Sandbergi* ?
				Kinderhookian	*S. Sandbergi* ?
				Kinderhookian	*S. Sandbergi* ?
-28.34	0.002		30.92	Kinderhookian	Upper *S. crenulata* - *S. isosticha*
				Kinderhookian	Upper *S. crenulata* - *S. isosticha*
				Kinderhookian	Upper *S. crenulata* - *S. isosticha*
-28.68	0.002		30.75	Kinderhookian	Upper *S. crenulata* - *S. isosticha*
				Kinderhookian	Upper *S. crenulata* - *S. isosticha*
				Kinderhookian	Upper *S. crenulata* - *S. isosticha*
				Kinderhookian	Upper *S. crenulata* - *S. isosticha*
-28.55	0.002		31.73	Kinderhookian	Upper *S. crenulata* - *S. isosticha*
				Kinderhookian	Upper *S. crenulata* - *S. isosticha*
	0.001			Kinderhookian	Upper *S. crenulata* - *S. isosticha*
				Kinderhookian	Upper *S. crenulata* - *S. isosticha*
				Kinderhookian	Upper *S. crenulata* - *S. isosticha*
				Kinderhookian	Upper *S. crenulata* - *S. isosticha*
				Kinderhookian	Upper *S. crenulata* - *S. isosticha*
-27.91	0.006			Kinderhookian	Upper *S. crenulata* - *S. isosticha*
				Kinderhookian	Upper *S. crenulata* - *S. isosticha*
				Kinderhookian	Upper *S. crenulata* - *S. isosticha*
-28.41	0.002	3.63	30.70	Kinderhookian	Upper *S. crenulata* - *S. isosticha*
				Kinderhookian	Upper *S. crenulata* - *S. isosticha*
				Kinderhookian	Upper *S. crenulata* - *S. isosticha*
				Kinderhookian	Upper *S. crenulata* - *S. isosticha*
				Kinderhookian	Upper *S. crenulata* - *S. isosticha*
-28.59	0.006		30.21	Kinderhookian	Upper *S. crenulata* - *S. isosticha*
				Kinderhookian	Upper *S. crenulata* - *S. isosticha*
				Kinderhookian	Upper *S. crenulata* - *S. isosticha*
				Kinderhookian	Upper *S. crenulata* - *S. isosticha*
-28.52	0.003		30.85	Kinderhookian	Upper *S. crenulata* - *S. isosticha*
				Kinderhookian	Upper *S. crenulata* - *S. isosticha*

Joana Limestone	44.5	PR-109.5	Grainstone	2.33	-5.97	
Joana Limestone	45	PR-110	Wackestone	2.46	-5.43	0.02
Joana Limestone	45.5	PR-110.5	Packstone	2.38	-5.56	
Joana Limestone	46	PR-111	Packstone	2.48	-5.91	
Joana Limestone	46.5	PR-111.5	Wackestone	2.13	-9.53	
Joana Limestone	47	PR-112	Wackestone	3.13	-7.21	0.03
Joana Limestone	47.6	PR-112.6	Wackestone	2.23	-7.82	
Joana Limestone	48	PR-113	Wackestone	2.71	-7.96	
Joana Limestone	48.5	PR-113.5	Wackestone	3.04	-6.84	0.06
Joana Limestone	49	PR-114	Wackestone	2.80	-9.89	
Joana Limestone	49.5	PR-114.5	Wackestone	3.29	-4.96	
Joana Limestone	50	PR-115	Wackestone	3.41	-4.00	
Joana Limestone	50.5	PR-115.5	Wackestone	3.50	-4.16	
Joana Limestone	51	PR-116	Wackestone	3.33	-4.05	
Joana Limestone	51.5	PR-116.5	Grainstone	3.26	-3.88	
Joana Limestone	52	PR-117	Grainstone	3.38	-3.55	
Joana Limestone	52.5	PR-117.5	Wackestone	2.79	-4.55	0.03
Joana Limestone	53	PR-118	Wackestone	3.00	-4.42	0.09
Joana Limestone	53.5	PR-118.5	Packstone	2.47	-4.93	
Joana Limestone	54	PR-119	Lime mudstone	2.97	-5.34	0.06
Joana Limestone	55	PR-120	Grainstone	2.96	-4.11	
Joana Limestone	55.5	PR-120.5	Wackestone	3.02	-4.41	
Joana Limestone	56	PR-121	Wackestone	2.32	-5.46	
Joana Limestone	56.3	PR-121.3	Wackestone	2.98	-4.28	0.01
Joana Limestone	57.4	PR-122.4	Grainstone	2.89	-4.95	
Joana Limestone	57.5	PR-122.5	Grainstone	2.27	-5.30	
Joana Limestone	58	PR-123	Grainstone	2.87	-4.80	
Joana Limestone	60	PR-125	Wackestone	2.95	-3.93	0.02
Joana Limestone	62.5	PR-127.5	Grainstone	2.90	-4.89	
Joana Limestone	64	PR-129	Packstone	2.96	-4.69	0.01
Joana Limestone	65.2	PR-130.2	Grainstone	3.35	-4.35	

				Kinderhookian	Upper *S. crenulata* - *S. isosticha*
-28.90	0.002	3.99	31.36	Kinderhookian	Upper *S. crenulata* - *S. isosticha*
				Kinderhookian	Upper *S. crenulata* - *S. isosticha*
				Kinderhookian	Upper *S. crenulata* - *S. isosticha*
				Kinderhookian	Upper *S. crenulata* - *S. isosticha*
	0.002			Kinderhookian	Upper *S. crenulata* - *S. isosticha*
				Kinderhookian	Upper *S. crenulata* - *S. isosticha*
				Kinderhookian	Upper *S. crenulata* - *S. isosticha*
-27.55	0.003	4.20	30.59	Kinderhookian	Upper *S. crenulata* - *S. isosticha*
				Kinderhookian	Upper *S. crenulata* - *S. isosticha*
				Kinderhookian	Upper *S. crenulata* - *S. isosticha*
				Kinderhookian	Upper *S. crenulata* - *S. isosticha*
				Kinderhookian	Upper *S. crenulata* - *S. isosticha*
				Kinderhookian	Upper *S. crenulata* - *S. isosticha*
				Kinderhookian	Upper *S. crenulata* - *S. isosticha*
				Kinderhookian	Upper *S. crenulata* - *S. isosticha*
	0.001			Kinderhookian	Upper *S. crenulata* - *S. isosticha*
-27.52	0.004		30.52	Kinderhookian	Upper *S. crenulata* - *S. isosticha*
				Kinderhookian	Upper *S. crenulata* - *S. isosticha*
-28.57	0.003	4.49	31.53	Kinderhookian	Upper *S. crenulata* - *S. isosticha*
				Kinderhookian	Upper *S. crenulata* - *S. isosticha*
				Kinderhookian	Upper *S. crenulata* - *S. isosticha*
				Kinderhookian	Upper *S. crenulata* - *S. isosticha*
	0.000			Kinderhookian	Upper *S. crenulata* - *S. isosticha*
				Kinderhookian	Upper *S. crenulata* - *S. isosticha*
				Kinderhookian	Upper *S. crenulata* - *S. isosticha*
				Kinderhookian	Upper *S. crenulata* - *S. isosticha*
-29.07	0.001	4.34	32.02	Kinderhookian	Upper *S. crenulata* - *S. isosticha*
				Kinderhookian	Upper *S. crenulata* - *S. isosticha*
-29.40	0.002	4.80	32.36	Kinderhookian	Upper *S. crenulata* - *S. isosticha*
				Kinderhookian	Upper *S. crenulata* - *S. isosticha*

Joana Limestone	66.1	PR-131.1	Grainstone	3.16	-4.66	0.01
Joana Limestone	68.1	PR-133.1	Grainstone	3.16	-4.36	
Joana Limestone	69	PR-134	Packstone	3.34	-4.42	0.01
Joana Limestone	70.2	PR-135.2	Grainstone	3.53	-4.48	
Joana Limestone	71	PR-136	Grainstone	3.47	-4.80	0.01
Joana Limestone	72	PR-137	Grainstone	3.37	-5.72	0.03
Joana Limestone	72.9	PR-137.9	Packstone	3.92	-3.26	
Joana Limestone	74.1	PR-139.1	Wackestone	3.80	-3.66	0.02
Joana Limestone	75.1	PR-140.1	Grainstone	3.83	-4.33	
Joana Limestone	76	PR-141	Grainstone	3.79	-4.68	0.02
Joana Limestone	77.3	PR-142.3	Grainstone	3.89	-4.14	
Joana Limestone	78	PR-143	Packstone	3.92	-4.75	0.02
Joana Limestone	79.2	PR-144.2	Packstone	4.18	-3.56	
Joana Limestone	80	PR-145	Wackestone	4.36	-3.49	0.03
Joana Limestone	81.1	PR-146.1	Packstone	4.54	-3.41	
Joana Limestone	82	PR-147	Packstone	4.63	-3.48	
Joana Limestone	83.1	PR-148.1	Wackestone	5.01	-3.23	0.15
Joana Limestone	83.9	PR-148.9	Wackestone	5.39	-3.24	
Joana Limestone	84	PR-149	Wackestone	4.88	-3.70	
Joana Limestone	84.5	PR-149.5	Grainstone	4.90	-4.03	
Joana Limestone	85.2	PR-150.2	Wackestone	4.72	-4.08	0.09
Joana Limestone	85.6	PR-150.6	Wackestone	5.02	-3.22	
Joana Limestone	85.9	PR-150.9	Wackestone	5.24	-3.63	
Joana Limestone	86	PR-151	Wackestone	4.59	-3.30	0.06
Limestone X	86.4	AL-110.4	Lime mudstone	5.23	-4.51	
Limestone X	86.6	AL-110.6	Packstone	5.18	-2.97	
Limestone X	86.8	AL-110.8	Packstone	5.10	-3.61	0.09
Limestone X	87	AL-111	Packstone	6.05	-3.52	0.08
Limestone X	87.2	AL-111.2	Lime mudstone	5.84	-4.56	
Limestone X	87.5	AL-111.5	Lime mudstone	6.70	-3.56	0.21
Limestone X	88	AL-112	Lime mudstone	6.80	-3.52	0.06

	0.000			Kinderhookian	Upper *S. crenulata* - *S. isosticha*
				Kinderhookian	Upper *S. crenulata* - *S. isosticha*
-28.40	0.002	4.44	31.74	Kinderhookian	Upper *S. crenulata* - *S. isosticha*
				Kinderhookian	Upper *S. crenulata* - *S. isosticha*
	0.000			Kinderhookian	Upper *S. crenulata* - *S. isosticha*
-27.95	0.002		31.31	Kinderhookian	Upper *S. crenulata* - *S. isosticha*
				Kinderhookian	Upper *S. crenulata* - *S. isosticha*
-28.15	0.001	4.13	31.94	Kinderhookian	Upper *S. crenulata* - *S. isosticha*
				Kinderhookian	Upper *S. crenulata* - *S. isosticha*
-28.10	0.001	5.22	31.89	Kinderhookian	Upper *S. crenulata* - *S. isosticha*
				Kinderhookian	Upper *S. crenulata* - *S. isosticha*
	0.001			Kinderhookian	Upper *S. crenulata* - *S. isosticha*
				Kinderhookian	Upper *S. crenulata* - *S. isosticha*
-28.56	0.002	4.06	32.91	Kinderhookian	Upper *S. crenulata* - *S. isosticha*
				Kinderhookian	Upper *S. crenulata* - *S. isosticha*
				Kinderhookian	Upper *S. crenulata* - *S. isosticha*
-26.66	0.007		31.66	Kinderhookian	Upper *S. crenulata* - *S. isosticha*
				Kinderhookian	Upper *S. crenulata* - *S. isosticha*
				Kinderhookian	Upper *S. crenulata* - *S. isosticha*
				Kinderhookian	Upper *S. crenulata* - *S. isosticha*
-27.00	0.006		31.72	Kinderhookian	Upper *S. crenulata* - *S. isosticha*
				Kinderhookian	Upper *S. crenulata* - *S. isosticha*
				Kinderhookian	Upper *S. crenulata* - *S. isosticha*
-28.11	0.006	3.79	32.70	Kinderhookian	Upper *S. crenulata* - *S. isosticha*
				Kinderhookian	Upper *S. crenulata* - *S. isosticha*
				Kinderhookian	Upper *S. crenulata* - *S. isosticha*
-26.32			31.42	Kinderhookian	Upper *S. crenulata* - *S. isosticha*
-26.12	0.006		32.17	Kinderhookian	Upper *S. crenulata* - *S. isosticha*
				Kinderhookian	Upper *S. crenulata* - *S. isosticha*
-24.90	0.018	3.10	31.60	Kinderhookian	Upper *S. crenulata* - *S. isosticha*
-25.55	0.005	2.90	32.35	Kinderhookian	Upper *S. crenulata* - *S. isosticha*

Limestone X	89.1	AL-113.1	Lime mudstone	6.90	-3.48	0.15
Limestone X	90.6	AL-114.6	Wackestone	6.90	-3.72	0.15
Limestone X	91.3	AL-115.3	Lime mudstone	6.80	-3.41	0.11
Limestone X	92.1	AL-116.1	Wackestone	6.70	-3.09	0.15
Limestone X	93.2	AL-117.2	Wackestone	6.75	-3.01	0.13
Limestone X	94.5	AL-118.5	Wackestone	6.64	-3.23	0.15
Limestone X	96	AL-120	Wackestone	6.53	-3.43	0.15
Limestone X	98.8	AL-122.8	Wackestone	6.42	-3.27	0.13
Limestone X	100.2	AL-124.2	Grainstone	6.11	-2.71	0.07
Limestone X	102	AL-126	Wackestone	5.62	-2.85	0.14
Limestone X	103.2	AL-127.2	Wackestone	5.46	-3.35	0.17
Limestone X	105	AL-129	Wackestone	5.29	-3.12	0.13
Limestone X	106.5	AL-130.5	Wackestone	5.48	-1.99	0.10
Limestone X	107.2	AL-131.2	Wackestone	5.25	-2.32	0.01
Limestone X	108.1	AL-132.1	Wackestone	5.01	-2.64	0.26
Limestone X	109.5	AL-133.5	Wackestone	5.37	-2.13	0.20
Limestone X	111	AL-135.1	Wackestone	4.39	-4.15	0.17
Limestone X	112.5	AL-136.5	Wackestone	4.90	-3.08	0.20
Limestone X	113.5	AL-137.5	Wackestone	4.75	-3.37	0.15
Limestone X	114.1	AL-138.1	Wackestone	4.60	-3.66	0.08
Limestone X	115.7	AL-139.7	Wackestone	4.08	-4.78	0.09
Limestone X	117	AL-141	Wackestone	4.60	-3.31	0.07
Limestone X	117.7	AL-141.7	Lime mudstone	4.65	-3.76	0.15
Limestone X	119.1	AL-143.1	Wackestone	4.70	-4.20	0.11
Limestone X	120.1	AL-144.1	Packstone	5.01	-3.94	0.10
Limestone X	121.7	AL-145.7	Wackestone	5.12	-3.93	0.04
Limestone X	122.5	AL-146.5	Grainstone	5.23	-3.91	0.08
Limestone X	123.2	AL-147.2	Grainstone	5.55	-3.45	0.09
Limestone X	124.5	AL-148.5	Grainstone	5.79	-2.88	0.10
Limestone X	126	AL-150	Grainstone	5.75	-3.87	0.13
Limestone X	127	AL-151	Wackestone	5.72	-3.82	0.09

-24.69			31.59	Kinderhookian	Upper *S. crenulata* - *S. isosticha*
-24.77	0.009	4.17	31.67	Kinderhookian	Upper *S. crenulata* - *S. isosticha*
-24.92	0.010	2.17	31.72	Kinderhookian	Upper *S. crenulata* - *S. isosticha*
-24.74	0.008	2.73	31.44	Kinderhookian	Upper *S. crenulata* - *S. isosticha*
-24.81			31.56	Kinderhookian	Upper *S. crenulata* - *S. isosticha*
-25.34	0.009	2.44	31.98	Kinderhookian	Upper *S. crenulata* - *S. isosticha*
-24.79	0.009	3.61	31.32	Kinderhookian	Upper *S. crenulata* - *S. isosticha?*
-24.48	0.006		30.90	Kinderhookian	Upper *S. crenulata* - *S. isosticha?*
-25.38	0.004		31.49	Kinderhookian	Upper *S. crenulata* - *S. isosticha?*
-26.35	0.001	4.32	31.97	Kinderhookian	Upper *S. crenulata* - *S. isosticha?*
-26.50			31.96	Kinderhookian	Upper *S. crenulata* - *S. isosticha?*
-26.43	0.007		31.72	Kinderhookian	Upper *S. crenulata* - *S. isosticha?*
-26.40	0.010	3.73	31.88	Kinderhookian	Upper *S. crenulata* - *S. isosticha?*
-26.61	0.001		31.85	Kinderhookian	Upper *S. crenulata* - *S. isosticha?*
-25.99	0.012	3.95	31.00	Kinderhookian	Upper *S. crenulata* - *S. isosticha?*
-27.19	0.008	4.45	32.56	Kinderhookian	Upper *S. crenulata* - *S. isosticha?*
-27.08			31.47	Kinderhookian	Upper *S. crenulata* - *S. isosticha?*
-27.20	0.009	2.15	32.10	Kinderhookian	Upper *S. crenulata* - *S. isosticha?*
-27.12	0.008	2.14	31.87	Kinderhookian	Upper *S. crenulata* - *S. isosticha?*
-26.25	0.005		30.85	Kinderhookian	Upper *S. crenulata* - *S. isosticha?*
-27.31	0.046	4.87	31.39	Kinderhookian	Upper *S. crenulata* - *S. isosticha?*
-27.07	0.006		31.67	Kinderhookian	Upper *S. crenulata* - *S. isosticha?*
-27.35	0.009	1.44	32.00	Kinderhookian	Upper *S. crenulata* - *S. isosticha?*
-26.27	0.012	3.79	30.97	Kinderhookian	Upper *S. crenulata* - *S. isosticha?*
-25.68			30.69	Kinderhookian	Upper *S. crenulata* - *S. isosticha?*
-26.00	0.002	3.91	31.12	Kinderhookian	Upper *S. crenulata* - *S. isosticha?*
-25.53	0.007		30.76	Kinderhookian	Upper *S. crenulata* - *S. isosticha?*
-24.75			30.30	Kinderhookian	Upper *S. crenulata* - *S. isosticha?*
-25.58	0.006		31.37	Kinderhookian	Upper *S. crenulata* - *S. isosticha?*
-25.46	0.005		31.21	Kinderhookian	Upper *S. crenulata* - *S. isosticha?*
-25.15			30.87	Kinderhookian	Upper *S. crenulata* - *S. isosticha?*

Limestone X	128	AL-152	Packstone	5.73	-2.79	0.10
Limestone X	129.2	AL-153.2	Packstone	5.74	-3.89	0.13
Limestone X	130.5	AL-154.5	Wackestone	5.94	-4.75	0.08
Limestone X	133.1	AL-157.1	Wackestone	6.24	-3.01	0.25
Limestone X	134.5	AL-158.5	Wackestone	6.07	-3.49	0.07
Limestone X	135	AL-159	Wackestone	6.18	-3.38	0.480
Limestone X	136	AL-160	Wackestone	6.28	-3.26	0.46
Limestone X	139.5	AL-163.5	Wackestone	5.83	-3.47	0.12
Limestone X	141.1	AL-165.1	Wackestone	6.04	-3.29	0.12
Limestone X	141.9	AL-165.9	Wackestone	5.96	-3.45	0.21
Limestone X	143.1	AL-167.1	Wackestone	5.89	-6.42	0.10
Limestone X	144.5	AL-168.5	Wackestone	5.61	-3.47	0.17
Limestone X	147.1	AL-171.1	Wackestone	6.08	-3.34	0.15
Limestone X	148.5	AL-172.5	Wackestone	5.37	-4.20	0.14
Limestone X	149.9	AL-173.9	Grainstone	6.18	0.26	0.11
Limestone X	151.6	AL-175.6	Wackestone	6.98	-1.67	0.14
Limestone X	152.9	AL-176.9	Wackestone	6.36	-3.60	0.17
Limestone X	155.5	AL-179.5	Wackestone	6.55	-5.18	0.11
Limestone X	157	AL-181	Wackestone	6.86	-3.93	0.16
Limestone X	158.3	AL-182.3	Wackestone	6.94	-3.92	0.13
Limestone X	159.8	AL-183.8	Wackestone	7.02	-3.91	0.05
Limestone X	161.1	AL-185.1	Lime mudstone	7.00	-3.66	0.03
Limestone X	162.4	AL-186.4	Lime mudstone	6.98	-3.40	0.07
Limestone X	165	AL-189	Lime mudstone	6.63	-4.30	0.07
Limestone X	166.5	AL-190.5	Lime mudstone	6.74	-3.54	0.08
Limestone X	167.5	AL-191.5	Lime mudstone	6.85	-3.55	0.08
Limestone X	169.1	AL-193.1	Wackestone	6.56	-4.29	0.11
Limestone X	170.8	AL-194.8	Wackestone	6.41	-3.68	0.11
Limestone X	172.2	AL-196.2	Wackestone	6.43	-3.05	0.08
Limestone X	174.2	AL-198.2	Wackestone	5.77	-2.63	0.04
Limestone X	175.5	AL-199.5	Lime mudstone	6.02	-3.06	0.10
Limestone X	175.6	AL-199.6	Lime mudstone	6.15	-3.27	0.07
Limestone X	176	AL-200	Lime mudstone	6.21	-3.37	0.06
Limestone X	177.9	AL-201.9	Wackestone	6.27	-3.48	0.12
Limestone X	179	AL-203	Wackestone	6.25	-3.46	0.11
Limestone X	181	AL-205	Lime mudstone	6.35	-1.39	0.10
Limestone X	183	AL-207	Wackestone	6.45	0.69	0.08
Limestone X	184	AL-208.2	Wackestone	6.41	-1.69	0.12
Limestone X	186.3	AL-210.3	Wackestone	6.88	-2.04	0.08
Limestone X	188.2	AL-212.2	Wackestone	6.64	-2.67	0.10
Limestone X	189.5	AL-213.5	Wackestone	6.60	-2.94	0.07
Limestone X	190.7	AL-214.7	Wackestone	6.50	-3.24	0.09
Limestone X	192.4	AL-216.4	Wackestone	6.39	-3.98	0.07
Limestone X	194.5	AL-218.5	Wackestone	6.27	-3.44	0.06
Limestone X	196.1	AL-220.1	Wackestone	6.29	-2.41	0.09
Limestone X	198.2	AL-222.2	Wackestone	6.15	-2.91	0.09
Limestone X	200	AL-224	Wackestone	6.18	-3.06	0.10
Limestone X	202.2	AL-226.2	Wackestone	6.20	-3.21	0.06
Limestone X	202.5	AL-226.5	Wackestone	6.11	-3.24	0.061
Limestone X	203.5	AL-227.5	Wackestone	6.02	-3.27	0.07
Limestone X	205	AL-229	Lime mudstone	5.92	-3.30	0.11
Limestone X	207	AL-231	Wackestone	5.83	-3.33	0.11
Limestone X	209.7	AL-233.7	Lime mudstone	5.49	-3.36	0.11
Limestone X	210.9	AL-234.9	Lime mudstone	5.50	-3.17	0.10
Limestone X	212.1	AL-236.1	Lime mudstone	5.35	-4.19	0.09
Limestone X	213.2	AL-237.2	Wackestone	5.46	-3.09	0.04
Limestone X	213.7	AL-237.7	Wackestone	5.61	-2.65	0.10
Limestone X	215.5	AL-239.5	Lime mudstone	5.76	-2.20	0.04

-25.46	0.006	4.27	31.19	Kinderhookian	Upper *S. crenulata* - *S. isosticha?*
-25.23			30.97	Kinderhookian	Upper *S. crenulata* - *S. isosticha?*
-24.81	0.006	3.31	30.75	Kinderhookian	Upper *S. crenulata* - *S. isosticha?*
-25.25			31.49	Kinderhookian	Upper *S. crenulata* - *S. isosticha?*
-25.30	0.003		31.37	Kinderhookian	Upper *S. crenulata* - *S. isosticha?*
-25.87	0.023		32.04	Osagean	*G. typicus*
-25.64	0.006		31.92	Osagean	*G. typicus*
-25.44	0.006	4.27	31.27	Osagean	*G. typicus*
-25.26	0.006		31.30	Osagean	*G. typicus*
-26.02			31.98	Osagean	*G. typicus*
-25.93	0.006		31.82	Osagean	*G. typicus*
-25.12	0.005	3.52	30.73	Osagean	*G. typicus*
-25.53			31.61	Osagean	*G. typicus*
-25.95			31.32	Osagean	*G. typicus*
-25.47	0.003		31.65	Osagean	*G. typicus*
-24.66	0.005	3.79	31.64	Osagean	*G. typicus*
-25.04	0.009	2.86	31.40	Osagean	*G. typicus*
-24.12	0.005		30.67	Osagean	*G. typicus*
-25.01	0.004		31.87	Osagean	*G. typicus*
-24.36	0.009	4.79	31.30	Osagean	*G. typicus*
-24.46	0.002		31.48	Osagean	*G. typicus*
-25.11	0.001		32.11	Osagean	*G. typicus*
-24.30	0.002		31.28	Osagean	*G. typicus*
-23.67	0.005		30.30	Osagean	*G. typicus*
-23.90	0.008	4.55	30.64	Osagean	*G. typicus*
-23.90	0.003		30.75	Osagean	*G. typicus*
-24.00	0.007	2.82	30.56	Osagean	*G. typicus*
-24.48	0.008	3.46	30.89	Osagean	*G. typicus*
-24.42	0.004		30.85	Osagean	*G. typicus*
-24.34	0.007		30.11	Osagean	*G. typicus*
-26.02	0.008	1.89	32.04	Osagean	*G. typicus*
-25.47	0.009	3.76	31.61	Osagean	*G. typicus*
-25.87	0.006	3.51	32.08	Osagean	*G. typicus*
-24.88	0.007		31.15	Osagean	*G. typicus*
-24.90	0.017	3.81	31.15	Osagean	*G. typicus*
-24.90	0.009	3.35	31.25	Osagean	*G. typicus*
-24.26	0.009	3.26	30.71	Osagean	*G. typicus*
-24.56			30.97	Osagean	*G. typicus*
-24.15	0.006		31.03	Osagean	*G. typicus*
-24.53			31.17	Osagean	*G. typicus*
-24.51	0.008		31.11	Osagean	*G. typicus*
-24.62			31.12	Osagean	*G. typicus*
-24.77	0.009	3.30	31.16	Osagean	*G. typicus*
-24.43	0.004		30.70	Osagean	*G. typicus*
-24.95	0.007	2.48	31.24	Osagean	*G. typicus*
-25.18	0.007	3.04	31.33	Osagean	*G. typicus*
-25.74	0.011	3.22	31.92	Osagean	*G. typicus*
-24.35	0.003		30.55	Osagean	*G. typicus*
-24.36	0.003		30.47	Osagean	*G. typicus*
-24.85	0.005		30.86	Osagean	*G. typicus*
-24.89	0.013	5.09	30.81	Osagean	*G. typicus*
-24.75			30.58	Osagean	*G. typicus*
-25.99	0.008	3.73	31.48	Osagean	*G. typicus*
-25.17	0.006	3.78	30.67	Osagean	*G. typicus*
-25.38			30.73	Osagean	*G. typicus*
-25.46			30.92	Osagean	*G. typicus*
-26.83	0.005		32.44	Osagean	*G. typicus*
-26.19	0.005		31.95	Osagean	*G. typicus*

Limestone X	216.9	AL-240.9	Lime mudstone	5.45	-2.93	0.158
Limestone X	218.5	AL-242.5	Wackestone	5.47	-2.89	0.03
Limestone X	220	AL-244	Wackestone	5.36	-2.97	0.05
Limestone X	222	AL-246	Lime mudstone	5.25	-3.04	0.06
Limestone X	225.5	AL-249.5	Lime mudstone	4.87	-3.51	0.08
Limestone X	228.9	AL-252.9	Lime mudstone	4.63	-4.06	0.08
Limestone X	230	AL-254	Lime mudstone	5.03	-3.35	0.07
Limestone X	231.7	AL-255.7	Wackestone	4.85	-3.26	0.05
Limestone X	234	AL-258	Wackestone	4.57	-3.43	0.07
Limestone X	236.7	AL-260.7	Wackestone	4.48	-3.28	0.04
Limestone X	237	AL-261	Wackestone	4.29	-3.28	0.08
Limestone X	237.5	AL-261.5	Wackestone	4.10	-3.29	0.05
Limestone X	239.2	AL-263.2	Lime mudstone	3.85	-3.28	0.06
Limestone X	241	PR2-0	Wackestone	4.33	-3.68	0.046
Limestone X	242	PR2-1	Wackestone	4.00	-3.46	
Limestone X	242.5	AL-266.5	Lime mudstone	3.58	-3.15	0.06
Limestone X	243.5	PR2_2.5	Wackestone	4.57	-2.74	
Limestone X	244	PR2-3	Lime mudstone	4.28	-3.31	
Limestone X	244.3	AL-268.3	Lime mudstone	3.51	-3.98	0.06
Limestone X	245	PR2-4	Lime mudstone	4.31	-3.38	
Limestone X	246	PR2-5	Lime mudstone	4.23	-2.97	0.05
Limestone X	246.5	AL-270.5	Lime mudstone	4.05	-3.06	0.06
Limestone X	247	PR2-6	Wackestone	3.87	-3.15	
Limestone X	248	AL-272	Lime mudstone	3.37	-3.07	0.05
Limestone X	248	PR2-7	Lime mudstone	3.85	-2.82	
Limestone X	249	PR2-8	Wackestone	3.07	-3.81	
Limestone X	249.4	AL-273.4	Wackestone	3.07	-3.60	0.08
Limestone X	250	PR2-9	Lime mudstone	3.66	-3.23	
Limestone X	251	PR2-10	Lime mudstone	3.00	-3.28	
Limestone X	251.8	AL-275.8	Wackestone	2.52	-3.64	0.06
Limestone X	252	PR2-11	Lime mudstone	2.81	-3.09	
Limestone X	253	PR2-12	Wackestone	2.27	-3.41	0.08
Limestone X	253.1	AL-277.1	Wackestone	2.52	-3.43	0.09
Limestone X	254	PR2-13	Wackestone	2.76	-3.46	0.11
Limestone X	254.5	AL-278.5	Lime mudstone	2.52	-4.46	0.04
Limestone X	255	PR2-14	Wackestone	2.96	-3.48	0.08
Limestone X	256.3	AL-280.3	Wackestone	2.04	-4.17	0.07
Limestone X	257	PR2-16	Lime mudstone	1.70	-3.45	0.11
Limestone X	258	AL-282	Lime mudstone	1.82	-4.39	0.191
Limestone X	258	PR2-17	Lime mudstone	2.17	-3.68	0.11
Limestone X	259	PR2-18	Lime mudstone	2.75	-4.17	0.08
Limestone X	260	PR2-19	Lime mudstone	1.65	-4.78	0.11
Limestone X	261	PR2-20	Lime mudstone	2.20	-4.88	0.06
Limestone X	262	PR2-21	Lime mudstone	2.14	-4.18	0.10
Limestone X	263	PR2-22	Wackestone	1.83	-3.37	0.06
Limestone X	264	PR2-23	Wackestone	1.23	-4.56	0.19
Limestone X	265	PR2-24	Wackestone	1.57	-4.41	0.25
Limestone X	266	PR2-25	Wackestone	0.92	-4.93	0.09

-25.36	0.028	5.18	30.82	Osagean	*G. typicus*
-25.46			30.93	Osagean	*G. typicus*
-26.54	0.011	4.12	31.90	Osagean	*G. typicus*
-25.63			30.88	Osagean	*G. typicus*
-25.78	0.009	4.05	30.65	Osagean	*G. typicus*
-25.69			30.32	Osagean	*G. typicus*
-25.71	0.006	4.26	30.74	Osagean	*G. typicus*
-25.60	0.002		30.45	Osagean	*G. typicus*
-26.36	0.005		30.92	Osagean	*G. typicus*
-27.90	0.003	4.69	32.38	Osagean	*G. typicus*
-27.08	0.004		31.37	Osagean	*G. typicus*
-26.27			30.37	Osagean	*G. typicus*
-26.73	0.003		30.58	Osagean	*G. typicus*
-26.76	0.005		31.09	Osagean	*G. typicus*
				Osagean	*G. typicus*
-26.86	0.009	3.50	30.44	Osagean	*G. typicus*
				Osagean	*G. typicus*
				Osagean	*G. typicus*
-26.95			30.46	Osagean	*G. typicus*
				Osagean	*G. typicus*
-26.35			30.58	Osagean	*G. typicus*
-27.67	0.008	3.98	31.72	Osagean	*G. typicus*
				Osagean	*G. typicus*
-26.64	0.014	4.30	30.01	Osagean	*G. typicus*
				Osagean	*G. typicus*
				Osagean	*G. typicus*
-27.24	0.010	4.00	30.31	Osagean	*G. typicus*
				Osagean	*G. typicus*
				Osagean	*G. typicus*
-27.71	0.005		30.23	Osagean	*G. typicus*
				Osagean	*G. typicus*
-27.75	0.007		30.02	Osagean	*G. typicus*
-29.28	0.006		31.79	Osagean	*G. typicus*
-27.70	0.009		30.47	Osagean	*G. typicus*
-26.86	0.003		29.38	Osagean	*G. typicus*
-27.51	0.008		30.47	Osagean	*G. typicus*
-28.27	0.010	4.23	30.31	Osagean	*G. typicus*
-27.80	0.015	3.98	29.50	Osagean	*G. typicus*
-27.90	0.030	6.34	29.72	Osagean	*G. typicus*
-28.47	0.012	4.31	30.64	Osagean	*G. typicus*
-28.06	0.006		30.80	Osagean	*G. typicus*
-29.74	0.010	3.75	31.39	Osagean	*G. typicus*
-28.79	0.003		30.99	Osagean	*G. typicus*
-27.49	0.006		29.63	Osagean	*G. typicus*
-27.86	0.004		29.69	Osagean	*G. typicus*
-29.51	0.007		30.74	Osagean	*G. typicus*
-29.87	0.045	5.19	31.44	Osagean	*G. typicus*
-28.15	0.040		29.07	Osagean	*G. typicus*

Section 2: Mountain Home section, Utah (GPS location: 38 35' 43" N, 113 56' 19" W)

Strat. Unit	Height (m)	Sample No.	Lithology	$\delta^{13}C_{carb}$ (‰,VPDB)	$\delta^{18}O_{carb}$ (‰,VPDB)	TOC (w%)
Joana Limestone	0	MH-0	Packstone	1.03	-6.91	0.04
Joana Limestone	0.6	MH-0.6	Wackestone	1.30	-5.53	0.02
Joana Limestone	1	MH-1	Packstone	0.93	-6.88	0.05
Joana Limestone	2.2	MH-2.2	Wackestone	1.27	-5.79	0.01
Joana Limestone	3	MH-3	Packstone	0.90	-6.84	0.01
Joana Limestone	4	MH-4	Wackestone	1.63	-6.86	0.06
Joana Limestone	5.1	MH-5.1	Wackestone	1.74	-6.41	0.04
Joana Limestone	6	MH-6	Wackestone	1.87	-6.52	0.11
Joana Limestone	7	MH-7	Grainstone	1.90	-6.50	0.23
Joana Limestone	8.6	MH-8.6	Wackestone	2.18	-6.26	0.04
Joana Limestone	9.3	MH-9.3	Wackestone	2.37	-6.01	0.03
Joana Limestone	10.9	MH-10.9	Packstone	2.12	-7.63	0.02
Joana Limestone	12	MH-12	Grainstone	2.31	-6.99	
Joana Limestone	13.2	MH-13.2	Wackestone	1.98	-6.82	0.02
Joana Limestone	14	MH-14	Wackestone	2.24	-6.72	0.03
Joana Limestone	15.7	MH-15.7	Grainstone	1.44	-7.15	0.09
Joana Limestone	15.8	MH-15.8	Wackestone	1.58	-7.05	0.09
Joana Limestone	16	MH-16	Packstone	1.72	-6.96	0.07
Joana Limestone	17.5	MH-17.5	Wackestone	1.58	-6.95	0.03
Joana Limestone	18.1	MH-18.1	Wackestone	1.51	-6.82	0.02
Joana Limestone	19	MH-19	Wackestone	1.75	-6.73	0.44
Joana Limestone	20.2	MH-20.2	Wackestone	1.45	-7.16	0.02
Joana Limestone	21.3	MH-21.3	Grainstone	1.95	-7.78	
Joana Limestone	22	MH-22	Wackestone	1.33	-7.08	0.14
Joana Limestone	22.9	MH-22.9	Grainstone	1.47	-7.67	0.01
Joana Limestone	24	MH-24	Wackestone	1.09	-7.40	0.02
Joana Limestone	25	MH-25	Grainstone	1.65	-7.75	0.10
Joana Limestone	26	MH-26	Wackestone	2.53	-7.06	0.02

$\delta^{13}C_{org}$ (‰,VPDB)	TN (%w)	$\delta^{15}N_{org}$ (‰, air)	$\Delta\delta^{13}C$	Age	Conodont zone*
-28.63	0.004	4.35	29.66	Kinderhookian	*S. crenulata - isosticha*
-28.97	0.001	3.68	30.27	Kinderhookian	*S. crenulata - isosticha*
-29.08	0.004	4.22	30.01	Kinderhookian	*S. crenulata - isosticha*
-28.14	0.001	4.94	29.41	Kinderhookian	*S. crenulata - isosticha*
	0.000			Kinderhookian	*S. crenulata - isosticha*
-28.10	0.004	4.69	29.72	Kinderhookian	*S. crenulata - isosticha*
-28.44	0.001		30.18	Kinderhookian	*S. crenulata - isosticha*
-29.55	0.002	3.97	31.41	Kinderhookian	*S. crenulata - isosticha*
	0.001			Kinderhookian	*S. crenulata - isosticha*
-28.99	0.002	4.23	31.17	Kinderhookian	*S. crenulata - isosticha*
	0.000			Kinderhookian	*S. crenulata - isosticha*
-28.26	0.003	3.96	30.38	Kinderhookian	*S. crenulata - isosticha*
				Kinderhookian	*S. crenulata - isosticha*
-28.31	0.001		30.28	Kinderhookian	*S. crenulata - isosticha*
-27.34	0.001		29.58	Kinderhookian	*S. crenulata - isosticha*
	0.001			Kinderhookian	*S. crenulata - isosticha*
-27.79	0.004	4.12	29.37	Kinderhookian	*S. crenulata - isosticha*
-28.45	0.003		30.17	Kinderhookian	*S. crenulata - isosticha*
-27.79	0.002		29.37	Kinderhookian	*S. crenulata - isosticha*
	0.000			Kinderhookian	*S. crenulata - isosticha*
	0.000			Kinderhookian	*S. crenulata - isosticha*
-27.53	0.002	4.02	28.98	Kinderhookian	*S. crenulata - isosticha*
				Kinderhookian	*S. crenulata - isosticha*
-27.81	0.012	4.97	29.15	Kinderhookian	*S. crenulata - isosticha*
	0.000			Kinderhookian	*S. crenulata - isosticha*
-28.06	0.006	5.63	29.15	Kinderhookian	*S. crenulata - isosticha*
	0.000			Kinderhookian	*S. crenulata - isosticha*
-27.41	0.002		29.94	Kinderhookian	*S. crenulata - isosticha*

Joana Limestone	27	MH-27	Grainstone	2.06	-6.90	
Joana Limestone	28	MH-28	Wackestone	1.81	-7.28	0.02
Joana Limestone	29	MH-29	Grainstone	1.77	-8.15	0.02
Joana Limestone	30	MH-30	Wackestone	1.70	-8.24	0.08
Joana Limestone	31.2	MH-31.2	Wackestone	1.83	-7.27	0.06
Joana Limestone	32	MH-32	Packstone	1.82	-7.25	0.02
Joana Limestone	33	MH-33	Wackestone	2.71	-6.05	0.07
Joana Limestone	34	MH-34	Wackestone	2.76	-5.69	0.10
Joana Limestone	35	MH-35	Wackestone	2.30	-6.53	0.02
Joana Limestone	37.5	MH-37.5	Grainstone	1.84	-7.37	0.01
Joana Limestone	38	MH-38	Grainstone	1.42	-7.19	0.02
Joana Limestone	39	MH-39	Wackestone	1.62	-5.84	0.05
Joana Limestone	39.5	MH-39.5	Packstone	1.60	-5.28	0.02
Joana Limestone	40.5	MH-40.5	Packstone	1.84	-5.90	0.02
Joana Limestone	41.3	MH-41.3	Wackestone	1.42	-5.69	0.04
Joana Limestone	42	MH-42	Grainstone	1.45	-7.20	0.00
Joana Limestone	42.5	MH-42.5	Wackestone	1.41	-7.26	
Joana Limestone	43	MH-43	Lime mudstone	2.31	-6.26	0.03
Joana Limestone	43.5	MH-43.5	Lime mudstone	3.18	-6.49	0.07
Joana Limestone	44	MH-44	Lime mudstone	2.18	-6.81	0.07
Joana Limestone	44.5	MH-44.5	Lime mudstone	1.85	-6.63	
Joana Limestone	45	MH-45	Lime mudstone	2.04	-6.58	0.05
Joana Limestone	45.6	MH-45.6	Lime mudstone	2.26	-6.64	0.04
Joana Limestone	46	MH-46	Lime mudstone	1.63	-6.38	0.04
Joana Limestone	46.5	MH-46.5	Lime mudstone	2.51	-7.72	
Joana Limestone	47	MH-47	Lime mudstone	2.45	-6.68	0.04
Joana Limestone	48	MH-48	Lime mudstone	2.23	-6.44	
Joana Limestone	48.5	MH-48.5	Lime mudstone	3.16	-7.22	
Joana Limestone	49	MH-49	Lime mudstone	2.39	-5.54	0.05
Joana Limestone	49.9	MH-49.9	Lime mudstone	1.43	-7.31	0.03
Joana Limestone	50.6	MH-50.6	Lime mudstone	2.78	-7.45	0.04

				Kinderhookian	*S. crenulata - isosticha*
-27.91	0.001	5.10	29.71	Kinderhookian	*S. crenulata - isosticha*
	0.000			Kinderhookian	*S. crenulata - isosticha*
-29.24	0.009	4.82	30.93	Kinderhookian	*S. crenulata - isosticha*
-28.50	0.007	4.70	30.34	Kinderhookian	*S. crenulata - isosticha*
-26.93	0.001		28.75	Kinderhookian	*S. crenulata - isosticha*
-28.39	0.002		31.11	Kinderhookian	*S. crenulata - isosticha*
-28.24	0.002		31.00	Kinderhookian	*S. crenulata - isosticha*
-27.87	0.002	4.32	30.17	Kinderhookian	*S. crenulata - isosticha*
	0.000			Kinderhookian	*S. crenulata - isosticha*
	0.002			Kinderhookian	*S. crenulata - isosticha*
-28.14	0.006	3.84	29.76	Kinderhookian	*S. crenulata - isosticha*
-27.42	0.001		29.02	Kinderhookian	*S. crenulata - isosticha*
-26.52	0.001		28.35	Kinderhookian	*S. crenulata - isosticha*
-27.48	0.007	4.68	28.90	Kinderhookian	*S. crenulata - isosticha*
	0.000			Kinderhookian	*S. crenulata - isosticha*
				Kinderhookian	*S. crenulata - isosticha*
-24.59	0.001		26.90	Kinderhookian	*S. crenulata - isosticha*
-23.95	0.003		27.13	Kinderhookian	*S. crenulata - isosticha*
-25.75	0.002		27.93	Kinderhookian	*S. crenulata - isosticha*
				Kinderhookian	*S. crenulata - isosticha*
-25.49	0.002		27.53	Kinderhookian	*S. crenulata - isosticha*
-26.11	0.002		28.37	Kinderhookian	*S. crenulata - isosticha*
-23.90	0.003		25.53	Kinderhookian	*S. crenulata - isosticha*
				Kinderhookian	*S. crenulata - isosticha*
-24.07	0.002		26.52	Kinderhookian	*S. crenulata - isosticha*
				Kinderhookian	*S. crenulata - isosticha*
				Kinderhookian	*S. crenulata - isosticha*
-24.96	0.001		27.35	Kinderhookian	*S. crenulata - isosticha*
-23.63	0.002		25.07	Kinderhookian	*S. crenulata - isosticha*
	0.004			Kinderhookian	*S. crenulata - isosticha*

Joana Limestone	51	MH-51	Lime mudstone	2.19	-5.70	0.06
Joana Limestone	51.5	MH-51.5	Lime mudstone	2.82	-6.03	
Joana Limestone	52	MH-52	Lime mudstone	3.05	-6.64	0.04
Joana Limestone	52.6	MH-52.6	Lime mudstone	3.22	-5.94	0.03
Joana Limestone	53	MH-53	Lime mudstone	2.66	-6.30	0.01
Joana Limestone	53.2	MH-53.2	Packstone	2.40	-6.54	0.04
Joana Limestone	53.5	MH-53.5	Grainstone	2.15	-6.78	0.02
Joana Limestone	54.1	MH-54.1	Grainstone	2.41	-6.79	0.02
Joana Limestone	54.2	MH-54.2	Wackestone	3.13	-5.86	0.05
Joana Limestone	54.5	MH-54.5	Grainstone	3.85	-4.92	
Joana Limestone	55	MH-55	Lime mudstone	2.51	-6.56	0.03
Joana Limestone	55.5	MH-55.5	Grainstone	4.17	-5.44	0.05
Joana Limestone	56	MH-56	Grainstone	3.75	-4.07	0.06
Joana Limestone	56.5	MH-56.5	Grainstone	3.76	-4.30	
Joana Limestone	57	MH-57	Grainstone	3.91	-5.18	0.04
Joana Limestone	58	MH-58	Wackestone	4.04	-4.41	0.05
Joana Limestone	58.5	MH-58.5	Grainstone	3.71	-5.27	
Joana Limestone	59.5	MH-59.5	Grainstone	3.41	-5.48	
Joana Limestone	60	MH-60	Packstone	3.29	-4.51	0.07
Joana Limestone	60.1	MH-60.1	Grainstone	3.16	-3.54	0.01
Joana Limestone	61	MH-61	Wackestone	3.76	-3.65	
Joana Limestone	61.5	MH-61.5	Wackestone	3.81	-3.28	0.04
Joana Limestone	62	MH-62	Packstone	4.35	-3.49	0.03
Joana Limestone	62.5	MH-62.5	Wackestone	3.72	-4.39	0.05
Joana Limestone	64	MH-64	Wackestone	4.32	-3.51	0.03
Joana Limestone	64.5	MH-64.5	Wackestone	3.22	-3.59	
Joana Limestone	65	MH-65	Wackestone	4.50	-3.72	0.09
Joana Limestone	65.5	MH-65.5	Packstone	4.59	-3.46	0.02
Joana Limestone	66.1	MH-66.1	Wackestone	4.67	-3.20	0.06
Joana Limestone	66.5	MH-66.5	Wackestone	4.85	-3.18	0.01
Joana Limestone	67	MH-67	Wackestone	3.78	-4.55	0.01

	0.001			Kinderhookian	*S. crenulata - isosticha*
				Kinderhookian	*S. crenulata - isosticha*
-23.82	0.002		26.87	Kinderhookian	*S. crenulata - isosticha*
-24.59	0.001		27.81	Kinderhookian	*S. crenulata - isosticha*
	0.000			Kinderhookian	*S. crenulata - isosticha*
-23.91	0.002	4.26	26.31	Kinderhookian	*S. crenulata - isosticha*
	0.000			Kinderhookian	*S. crenulata - isosticha*
-24.21	0.001		26.62	Kinderhookian	*S. crenulata - isosticha*
-24.53	0.002	5.97	27.66	Kinderhookian	*S. crenulata - isosticha*
				Kinderhookian	*S. crenulata - isosticha*
-24.44	0.003		26.95	Kinderhookian	*S. crenulata - isosticha*
-24.26	0.012		28.43	Kinderhookian	*S. crenulata - isosticha*
-25.19	0.008		28.95	Kinderhookian	*S. crenulata - isosticha*
				Kinderhookian	*S. crenulata - isosticha*
-25.93	0.003		29.85	Kinderhookian	*S. crenulata - isosticha*
-25.02	0.002	5.44	29.06	Kinderhookian	*S. crenulata - isosticha*
				Kinderhookian	*S. crenulata - isosticha*
				Kinderhookian	*S. crenulata - isosticha*
-27.40	0.009	4.54	30.69	Kinderhookian	*S. crenulata - isosticha*
	0.000			Kinderhookian	*S. crenulata - isosticha*
				Kinderhookian	*S. crenulata - isosticha*
-26.23	0.004		30.03	Kinderhookian	*S. crenulata - isosticha*
-26.86	0.008	3.93	31.21	Kinderhookian	*S. crenulata - isosticha*
-27.23	0.003		30.95	Kinderhookian	*S. crenulata - isosticha*
-26.81	0.001	4.58	31.13	Kinderhookian	*S. crenulata - isosticha*
				Kinderhookian	*S. crenulata - isosticha*
-26.45	0.009	7.04	30.95	Kinderhookian	*S. crenulata - isosticha*
-26.98	0.001		31.57	Kinderhookian	*S. crenulata - isosticha*
-26.02	0.005	4.07	30.69	Kinderhookian	*S. crenulata - isosticha*
	0.000			Kinderhookian	*S. crenulata - isosticha*
	0.000			Kinderhookian	*S. crenulata - isosticha*

Joana Limestone	67.5	MH-67.5	Wackestone	3.65	-3.91	
Joana Limestone	68	MH-68	Packstone	3.69	-4.07	0.05
Joana Limestone	68.5	MH-68.5	Packstone	3.93	-3.85	0.05
Joana Limestone	69.5	MH-69.5	Grainstone	4.49	-4.51	
Joana Limestone	69.8	MH-69.8	Grainstone	5.00	-4.25	0.04
Joana Limestone	70.5	MH-70.5	Grainstone	4.72	-4.71	0.03
Joana Limestone	71	MH-71	Grainstone	5.25	-3.75	0.04
Joana Limestone	71.8	MH-71.8	Wackestone	5.07	-4.24	0.06
Joana Limestone	73	MH-73	Grainstone	4.97	-4.08	
Joana Limestone	74.3	MH-74.3	Grainstone	5.19	-4.61	0.06
Joana Limestone	75	MH-75	Wackestone	4.34	-4.47	0.07
Joana Limestone	75.5	MH-75.5	Grainstone	5.20	-4.66	0.02
Joana Limestone	76	MH-76	Packstone	5.50	-3.38	
Joana Limestone	76.5	MH-76.5	Packstone	4.72	-3.29	0.03
Joana Limestone	77.2	MH-77.2	Packstone	3.92	-3.88	0.02
Joana Limestone	77.5	MH-77.5	Wackestone	5.12	-2.60	0.05
Joana Limestone	82	MH-82	Wackestone	4.20	-4.15	0.05
Joana Limestone	82.4	MH-82.4	Wackestone	4.83	-3.94	0.03
Joana Limestone	82.5	MH-82.5	Wackestone	5.46	-3.73	
Joana Limestone	83	MH-83	Wackestone	4.03	-3.69	0.02
Joana Limestone	83.5	MH-83.5	Wackestone	3.89	-3.61	0.04
Joana Limestone	84.5	MH-84.5	Wackestone	3.02	-4.01	0.04
Joana Limestone	84.6	MH-84.6	Wackestone	3.52	-4.30	0.03
Joana Limestone	86	MH-86	Wackestone	4.02	-4.59	0.03
Joana Limestone	88	MH-88	Grainstone	5.25	-3.07	0.30
Joana Limestone	90	MH-90	Packstone	4.01	-4.29	0.03
Joana Limestone	90.5	MH-90.5	Grainstone	3.74	-3.07	
Joana Limestone	92	MH-92	Wackestone	2.25	-4.36	0.02
Joana Limestone	94.1	MH-94.1	Wackestone	4.20	-3.54	0.02
Joana Limestone	95	MH-95	Wackestone	3.73	-3.14	
Joana Limestone	95.5	MH-95.5	Packstone	2.91	-4.78	
Joana Limestone	96.1	MH-96.1	Packstone	2.91	-4.98	0.01
Joana Limestone	96.5	MH-96.5	Wackestone	3.21	-4.90	0.02
Joana Limestone	98	MH-98	Lime mudstone	3.50	-4.82	0.02
Joana Limestone	99.9	MH-99.9	Wackestone	3.65	-3.53	0.06
Joana Limestone	102	MH-102	Grainstone	3.78	-4.16	0.02
Joana Limestone	105	MH-105	Wackestone	3.18	-3.58	0.02
Joana Limestone	107	MH-107	Lime mudstone	2.82	-3.33	0.04
Joana Limestone	107.5	MH-107.5	Grainstone	2.95	-4.05	0.03
Joana Limestone	108	MH-108	Grainstone	3.10	-3.96	
Joana Limestone	108.5	MH-108.5	Grainstone	1.91	-3.48	0.04
Joana Limestone	109	MH-109	Wackestone	1.52	-3.92	0.01
Joana Limestone	111	MH-111	Wackestone	1.61	-5.39	0.02
Joana Limestone	112.4	MH-112.4	Wackestone	1.78	-5.25	0.03
Joana Limestone	112.8	MH-112.8	Wackestone	1.95	-5.12	0.01
Joana Limestone	113.5	MH-113.5	Wackestone	1.78	-5.12	0.09
Joana Limestone	113.6	MH-113.6	Grainstone	1.61	-5.13	0.01
Joana Limestone	113.9	MH-113.9	Grainstone	1.45	-5.13	0.03
Joana Limestone	115	MH-115	Wackestone	1.28	-5.13	0.03
Joana Limestone	117.4	MH-117.4	Grainstone	0.64	-5.78	0.02
Joana Limestone	119.4	MH-119.4	Packstone	0.60	-5.22	0.03
Joana Limestone	121.3	MH-121.3	Packstone	0.23	-5.22	0.02
Joana Limestone	122.9	MH-122.9	Packstone	0.99	-4.68	0.04
Joana Limestone	124.9	MH-124.9	Wackestone	0.86	-4.90	0.04
Joana Limestone	125.5	MH-125.5	Wackestone	0.61	-4.45	0.01
Joana Limestone	126	MH-126	Wackestone	0.99	-4.94	0.08

				Kinderhookian	*S. crenulata - isosticha*
-25.67	0.001		29.36	Kinderhookian	*S. crenulata - isosticha*
-26.12	0.004	6.69	30.05	Kinderhookian	*S. crenulata - isosticha*
				Kinderhookian	*S. crenulata - isosticha*
-26.16	0.002		31.17	Kinderhookian	*S. crenulata - isosticha*
	0.000			Kinderhookian	*S. crenulata - isosticha*
-25.86	0.002		31.11	Kinderhookian	*S. crenulata - isosticha*
-24.71	0.008	5.49	29.78	Osagean	*G. typicus*?
				Osagean	*G. typicus*?
	0.001			Osagean	*G. typicus*?
-24.71	0.008	5.25	29.05	Osagean	*G. typicus*?
	0.000			Osagean	*G. typicus*?
				Osagean	*G. typicus*?
-25.55	0.002		30.27	Osagean	*G. typicus*?
-25.84	0.002		29.77	Osagean	*G. typicus*?
-26.25	0.003	4.51	31.38	Osagean	*G. typicus*?
-26.08	0.007	4.79	30.28	Osagean	*G. typicus*?
-25.98	0.002	4.09	30.81	Osagean	*G. typicus*
				Osagean	*G. typicus*
-25.01	0.001		29.03	Osagean	*G. typicus*
-26.02	0.004	5.44	29.91	Osagean	*G. typicus*
-25.62	0.003		28.64	Osagean	*G. typicus*
-25.30	0.001	3.79	28.82	Osagean	*G. typicus*
-25.47	0.001	5.32	29.50	Osagean	*G. typicus*
	0.002			Osagean	*G. typicus*
-26.53	0.002	4.96	30.54	Osagean	*G. typicus*
				Osagean	*G. typicus*
-27.40	0.001	4.39	29.65	Osagean	*G. typicus*
-26.63	0.002		30.84	Osagean	*G. typicus*
				Osagean	*G. typicus*
				Osagean	*G. typicus*
-26.44	0.001		29.36	Osagean	*G. typicus*
-27.77	0.001	4.04	30.98	Osagean	*G. typicus*
-28.10	0.001		31.60	Osagean	*G. typicus*
-27.83	0.007	4.14	31.48	Osagean	*G. typicus*
-27.27	0.002		31.05	Osagean	*G. typicus*
-28.79	0.002	4.78	31.97	Osagean	*G. typicus*
-28.70	0.007	3.38	31.52	Osagean	*G. typicus*
-27.77	0.002		30.71	Osagean	*G. typicus*
				Osagean	*G. typicus*
-27.54	0.003		29.45	Osagean	*G. typicus*
-27.68	0.001	2.70	29.20	Osagean	*G. typicus*
-29.02	0.001	1.44	30.63	Osagean	*G. typicus*
-28.63	0.002	1.80	30.41	Osagean	*G. typicus*
-29.24	0.001	3.52	31.19	Osagean	*G. typicus*
-27.39	0.009	1.88	29.17	Osagean	*G. typicus*
-28.35	0.001	3.18	29.96	Osagean	*G. typicus*
-27.84	0.002		29.29	Osagean	*G. typicus*
-28.20	0.003	4.10	29.48	Osagean	*G. typicus*
-28.86	0.002		29.50	Osagean	*G. typicus*
-29.84	0.003	1.34	30.44	Osagean	*G. typicus*
-29.25	0.014	1.35	29.48	Osagean	*G. typicus*
-29.04	0.010	1.21	30.03	Osagean	*G. typicus*
-29.34	0.051	1.14	30.21	Osagean	*G. typicus*
-29.75	0.002		30.36	Osagean	*G. typicus*
-29.33	0.010	1.20	30.32	Osagean	*G. typicus*

Joana Limestone	126.5	MH-126.5	Wackestone	1.14	-5.74	
Joana Limestone	127	MH-127	Wackestone	1.90	-5.98	0.06
Joana Limestone	127.5	MH-127.5	Wackestone	1.02	-4.26	0.04
Joana Limestone	127.8	MH-127.8	Wackestone	1.35	-6.32	
Joana Limestone	130.5	MH-130.5	Wackestone	0.41	-4.82	0.04
Joana Limestone	133	MH-133	Wackestone	0.39	-5.11	0.02
Joana Limestone	135	MH-135	Grainstone	0.52	-4.35	0.04
Joana Limestone	137	MH-137	Packstone	0.73	-4.72	
Joana Limestone	138	MH-138	Grainstone	0.65	-5.06	0.05
Joana Limestone	138.5	MH-138.5	Wackestone	0.42	-5.51	0.22
Joana Limestone	139	MH-139	Wackestone	0.52	-5.85	0.05
Joana Limestone	139.5	MH-139.5	Wackestone	1.09	-5.13	
Joana Limestone	140	MH-140	Packstone	0.89	-5.08	0.06
Joana Limestone	140.5	MH-140.5	Packstone	0.68	-6.02	0.02
Joana Limestone	141	MH-141	Wackestone	0.64	-5.65	0.04
Joana Limestone	141.5	MH-141.5	Lime mudstone	0.54	-5.80	
Joana Limestone	142	MH-142	Wackestone	1.41	-5.90	
Joana Limestone	142.5	MH-142.5	Grainstone	0.50	-5.71	0.04
Joana Limestone	143	MH-143	Wackestone	0.21	-5.99	0.04
Joana Limestone	143.5	MH-143.5	Lime mudstone	0.69	-5.79	0.02
Joana Limestone	144	MH-144	Grainstone	0.27	-6.11	0.25
Joana Limestone	144.5	MH-144.5	Grainstone	-0.40	-2.89	0.04
Joana Limestone	145	MH-145	Grainstone	-0.05	-2.93	0.04
Joana Limestone	145.5	MH-145.5	Wackestone	0.54	-5.76	0.01
Joana Limestone	146	MH-146	Wackestone	1.75	-3.74	
Joana Limestone	146.5	MH-146.5	Wackestone	0.93	-5.85	0.04
Joana Limestone	147	MH-147	Wackestone	0.52	-5.65	0.03
Joana Limestone	147.5	MH-147.5	Wackestone	0.38	-5.38	0.02
Joana Limestone	148	MH-148	Wackestone	1.50	-5.00	0.05
Joana Limestone	148.5	MH-148.5	Wackestone	0.54	-5.65	0.02
Joana Limestone	149.5	MH-149.5	Wackestone	1.00	-5.50	0.03
Joana Limestone	150	MH-150	Packstone	1.25	-5.14	0.01
Joana Limestone	150.5	MH-150.5	Wackestone	0.92	-4.61	0.04
Joana Limestone	151	MH-151	Wackestone	0.11	-4.65	0.04
Joana Limestone	151.5	MH-151.5	Wackestone	0.23	-4.41	0.03

* Conodont biostratigraphic data of Pahranagat Range section are mainly from Singler (1987). Biostratigraphic data of the Mountain Home section are mainly from Poole and Sandberg (1991).

				Osagean	*G. typicus*
-28.23	0.009	1.28	30.13	Osagean	*G. typicus*
-28.73	0.040	1.35	29.75	Osagean	*G. typicus*
				Osagean	*G. typicus*
-29.08	0.023	1.62	29.50	Osagean	*G. typicus*
-29.11	0.001	2.11	29.50	Osagean	*G. typicus*
-29.12	0.003		29.64	Osagean	*G. typicus*
				Osagean	*G. typicus*
-28.81	0.004	0.90	29.46	Osagean	*G. typicus*
	0.009	1.63	0.42	Osagean	*G. typicus*
-27.84	0.024	1.93	28.37	Osagean	*G. typicus*
				Osagean	*G. typicus*
-29.55	0.010	0.61	30.44	Osagean	*G. typicus*
	0.001			Osagean	*G. typicus*
-29.24	0.017	1.75	29.88	Osagean	*G. typicus*
				Osagean	*G. typicus*
				Osagean	*G. typicus*
-28.38	0.013	1.87	28.87	Osagean	*G. typicus*
-28.98	0.010	1.02	29.18	Osagean	*G. typicus*
-27.83	0.009	2.22	28.52	Osagean	*G. typicus*
-28.10	0.016	1.68	28.37	Osagean	*G. typicus*
-29.66	0.002		29.26	Osagean	*G. typicus*
-29.84	0.001		29.79	Osagean	*G. typicus*
-28.08	0.002	2.02	28.61	Osagean	*G. typicus*
				Osagean	*G. typicus*
-29.29	0.003		30.22	Osagean	*G. typicus*
-29.17	0.002		29.69	Osagean	*G. typicus*
-28.94	0.006	1.96	29.32	Osagean	*G. typicus*
-28.13	0.032	2.53	29.63	Osagean	*G. typicus*
-29.14	0.008	1.83	29.68	Osagean	*G. typicus*
-28.82	0.013	2.70	29.82	Osagean	*G. typicus*
-28.46	0.015	1.95	29.71	Osagean	*G. typicus*
-28.80	0.024	1.67	29.71	Osagean	*G. typicus*
-29.22	0.038	2.74	29.33	Osagean	*G. typicus*
-29.07	0.021	2.77	29.30	Osagean	*G. typicus*

7. References

Ader, M., Thomazo, C., Sansjofre, P., Busigny, V., Papineau, D., Laffont, R., Cartigny, P., Halverson, G.P., 2016. Interpretation of the nitrogen isotopic composition of Precambrian sedimentary rocks: Assumptions and perspectives. Chemical Geology 429, 93-110.

Algeo, T. J., Rowe, H., Hower, J. C., Schwark, L., Hermann, A. and Heckel, P. H., 2008. Oceanic denitrification during Late Carboniferous glacial-interglacial cycles. Nature Geoscience, 1, 709–714.

Algeo, T. J., Henderson, C. M., Ellwood, B., Rowe, H., Elswick, E., Bates, S., Lyons, T., Hower, J. C., Smith, C., Maynard, J. B., Hays, L. E., Summons, R. E., Fulton, J., and Freeman, K. H., 2012. Evidence for a diachronous Late Permian marine crisis from the Canadian Arctic region. Geological Society of America Bulletin 124, 1424–1448.

Algeo, T.J., Meyers, P.A., Robinson, R.S., Rowe, H., Jiang, G.Q., 2014. Icehouse-greenhouse variations in marine denitrification. Biogeosciences 11, 1273-1295.

Altabet, M.A., Francois, R., Murray, D.W., Prell, W.L., 1995. Climate-related variations in denitrification in the Arabian Sea from sediment $^{15}N/^{14}N$ ratios. Nature 373, 506-509.

Beerling, D.J., 2002. Low atmospheric CO2 levels during the Permo- Carboniferous glaciation inferred from fossil lycopsids. Proceedings of the National Academy of Sciences 99, 12567-12571.

Berner, R.A. and Canfield, D.E., 1989. A New Model for Atmospheric Oxygen Over Phanerozoic Time. American Journal of Science 289, 333-361.

Berner, R.A., Petsch, S.T., Lake, J.A., Beerling, D.J., Popp, B.N., Lane, R.S., Laws, E.A., Westley, M.B., Cassar, N., Woodward, F.I., Quick, W.P., 2000. Isotope Fractionation and Atmospheric Oxygen: Implications for Phanerozoic O2 Evolution. Science 287, 1630-1633.

Buggisch, W., Joachimski, M.M., Sevastopulo, G., Morrow, J.R., 2008. Mississippian $\delta^{13}C_{carb}$ and conodont apatite $\delta^{18}O$ records− Their relation to the Late Palaeozoic Glaciation. Palaeogeography, Palaeoclimatology, Palaeoecology 268, 273-292.

Canfield, D.E., Glazer, A.N., Falkowski, P.G., 2010. The Evolution and Future of Earth's Nitrogen Cycle. Science 330, 192-196.

da Silva, A., Boulvain, F., 2008. Carbon isotope lateral variability in a Middle Frasnian carbonate platform (Belgium): Significance of facies, diagenesis and sea-level history. Palaeogeography, Palaeoclimatology, Palaeoecology 269, 189-204.

Derry, L.A., 2010. A burial diagenesis origin for the Ediacaran Shuram-Wonoka carbon isotope anomaly. Earth and Planetary Science Letters 294, 152-162.

Deutsch, C., Sigman, D.M., Thunell, R.C., Meckler, A.N., Haug, G.H., 2004. Isotopic constraints on glacial/interglacial changes in the oceanic nitrogen budget. Global Biogeochemical Cycles 18, 1-22.

DeVries, T., Deutsch, C., Primeau, F., Chang, B., and Devol, A., 2012. Global rates of water-column denitrification derived from nitrogen gas measurements. Nature Geoscience 5, 547–550.

Falkowski, P.G., 1997. Evolution of the nitrogen cycle and its influence on the biological sequestration of CO2 in the ocean. Nature 387, 272-275.

Fletcher, B.J., Brentnall, S.J., Quick, W.P., Beerling, D.J., 2006. BRYOCARB: A process-based model of thallose liverwort carbon isotope fractionation in response to CO2, O2, light and temperature. Geochimica et Cosmochimica Acta 70, 5676-5691.

Giles, K.A., 1996. Tectonically forced retrogradation of the lower Mississippian Joana Limestone, Nevada and Utah, in: Longman, M.W., Sonnenfeld, M.D. (Eds), Paleozoic systems of the Rocky Mountain region. Rocky Mountain Section, Society for Sedimentary Geology, pp. 145-164.

Giles, K.A., Bocko, M., Lawton, T.F., 1999. Stacked Late Devonian lowstand shorelines and their relation to tectonic subsidence at the Cordilleran Hingeline, western Utah. Journal of Sedimentary Research 69, 1181-1190.

Giles, K.A., Dickinson, W.R., 1995. Influence of lithospheric flexure on development of stratigraphic sequences in foreland settings: An example from the Antler foreland, Nevada and Utah, in: Dorobek, S., Ross, G. (Eds.), Stratigraphic Evolution of Foreland Basins. Society for Sedimentary Geology Special Publication 52, pp. 187-211.

Gill, B.C., Lyons, T.W., Saltzman, M.R., 2007. Parallel, high-resolution carbon and sulfur isotope records of the evolving Paleozoic marine sulfur reservoir. Palaeogeography, Palaeoclimatology, Palaeoecology 256, 156-173.

Godfrey, L.V., Falkowski, P.G., 2009. The cycling and redox state of nitrogen in the Archaean ocean. Nature Geoscience 2, 725-729.

Harris, D., Horwath, W.R., van Kessel, C., 2001. Acid fumigation of soils to remove carbonates prior to total organic carbon or Carbon-13 isotopic analysis. Soil Science Society of America Journal 65, 1853-1856.

Hatcher, P.G., Spiker, E.C., Szeverenyi, N.M., Maciel, G.E., 1983. Selective preservation and origin of petroleum-forming aquatic kerogen. Nature 305, 498-501.

Hayes, J.M., Strauss, H., Kaufman, A.J., 1999. The abundance of ^{13}C in marine organic matter and isotopic fractionation in the global biogeochemical cycle of carbon during the past 800 Ma. Chemical Geology 161, 103-125.

Hill, R.J., Tang, Y., Kaplan, I.R., 2003. Insights into oil cracking based on laboratory experiments. Organic Geochemistry 34, 1651-1672.

Hintze, L.F., Davis, F.D., 2002. Geologic map of the Wah Wah mountains north 30’ x 60’ quadrangle and part of the Garrison 30’ x 60’ quadrangle, southwest Millard County and part of Beaver County, Utah. Utah Geological Survey Map 182.

Jayko, A.S., 2007. Geologic Map of the Pahranagat Range 30' × 60' Quadrangle, Lincoln and Nye Counties, Nevada. United States Geologcial Survey, Scientific Investigations Map 2904.

Jiang, G., Wang, X., Shi, X., Xiao, S., Zhang, S., Dong, J., 2012. The origin of decoupled carbonate and organic carbon isotope signatures in the early Cambrian (ca. 542-520 Ma) Yangtze platform. Earth and Planetary Science Letters 317-318, 96-110.

Johnston, D.T., Macdonald, F.A., Gill, B.C., Hoffman, P.F., Schrag, D.P., 2012. Uncovering the Neoproterozoic carbon cycle. Nature 483, 320-324.

Junium, C.K., Arthur, M.A., 2007. Nitrogen cycling during the Cretaceous, Cenomanian-Turonian Oceanic Anoxic Event II. Geochemistry, Geophysics, Geosystems 8, 1-18.

Kammer, T.W., Matchen, D.L., 2008, Evidence for eustasy at the Kinderhookian-Osagean (Mississippian) boundary in the United States: Response to late Tournaisian glaciation?, in: Fielding, C.R., Frank, T.D., and Isbell, J.L., (Eds.), Resolving the Late Paleozoic Ice Age in Time and Space: Geological Society of America Special Paper 441, pp. 261–274.

Kampschulte, A., Bruckschen, P., Strauss, H., 2001. The sulphur isotopic composition of trace sulphates in Carboniferous brachiopods: implications for coeval seawater, correlation with other geochemical cycles and isotope stratigraphy. Chemical Geology 175, 149-173.

Kampschulte, A., Strauss, H., 2004. The sulfur isotopic evolution of Phanerozoic seawater based on the analysis of structurally substituted sulfate in carbonates. Chemical Geology 204, 255-286.

Katz, D.A., Buoniconti, M.R., Montañez, I.P., Swart, P.K., Eberli, G.P., Smith, L.B., 2007. Timing and local perturbations to the carbon pool in the lower Mississippian Madison Limestone, Montana and Wyoming. Palaeogeography, Palaeoclimatology, Palaeoecology 256, 231-253.

Knauth, L.P., Kennedy, M.J., 2009. The late Precambrian greening of the Earth. Nature 460, 728-732.

Knoll, A.H., Hayes, J.M., Kaufman, A.J., Swett, K., Lambert, I.B., 1986. Secular variation in carbon isotope ratios from upper Proterozoic successions of Svalbard and East Greenland. Nature 321, 832-838.

Koch, J.T., Frank, T.D., Bulling, T.P., 2014. Stable-isotope chemostratigraphy as a tool to correlate complex Mississippian marine carbonate facies of the Anadarko shelf, Oklahoma and Kansas. American Association of Petroleum Geologists Bulletin 98, 1071-1090.

Lane, H.R., Brenckle, P.L., 2005. Type Mississippian subdivisions and biostratigraphic succession, in: Heckel, P.H. (Eds.), Stratigraphy and biostratigraphy of the Mississippian subsystem (Carboniferous System) in its type region, the Mississippi River Valley of Illinois, Missouri and Iowa. Champaign, Illinois, Illinois State Geological Survey, Guidebook 34, International Union of Geological Sciences Subcommission on Carboniferous Stratigraphy, Guidebook for Field Conference, St. Louis, Missouri, 8–13 September 2001, pp. 83-107.

Lehmann, M.F., Bernasconi, S.M., Barbieri, A., McKenzie, J.A., 2002. Preservation of organic matter and alteration of its carbon and nitrogen isotope composition during simulated and in situ early sedimentary diagenesis. Geochimica et Cosmochimica Acta 66, 3573-3584.

Liu, Z., Altabet, M.A., Herbert, T.D., 2005. Glacial-interglacial modulation of eastern tropical North Pacific denitrification over the last 1.8-Myr. Geophysical Research Letters 32, 1-4.

Mii, H.S., Grossman, E.L., Yancey, T.E., 1999. Carboniferous isotope stratigraphies of North America: Implications for Carboniferous paleoceanography and Mississippian glaciation. Geological Society of America Bulletin 111, 960-973.

Oehlert, A.M., Swart, P.K., 2014. Interpreting carbonate and organic carbon isotope covariance in the sedimentary record. Nature Communications 5, 4672.

Peters, K.E., Rohrback, B.G., Kaplan, I.R., 1981. Carbon and hydrogen stable isotope variations in kerogen during laboratory simulated thermal maturaltion. American Association of Petroleum Geologists Bulletin 65, 501-508.

Poole, F.G., Sandberg, C.A., 1991. Mississippian paleogeography and conodont biostratigraphy of the western United States, in: Cooper, J.D., Stevens, G.H. (Eds.), Paleozoic Paleogeography of the Western United States. Pacific Section, Society of Economic Paleontologists and Mineralogists Special Publication 42, pp. 109–124.

Quan, T.M., Falkowski, P.G., 2009. Redox control of N:P ratios in aquatic ecosystems. Geobiology 7, 124-139.

Raven, J.A., Johnston, A.M., Kubler, J.E., Korb, R.E., McInroy, S.G., Handley, L.L., Scrimgeor, C.M., Walker, D.I., Beardall, J., Vanderklift, M., Frederiksen, J., Dunton, K.H., 2002. Mechanistic interpretation of carbon isotope discrimination by marine macroalgae and seagrasses. Functional Plant Biology 29, 355-378.

Reso, A., 1963. Composite Columnar Section of Exposed Paleozoic and Cenozoic Rocks in the Pahranagat Range, Lincoln County, Nevada. Geological Society of America Bulletin 74, 901-918.

Robinson, R.S., Etourneau, J., Martinez, P.M., Schneider, R., 2014. Expansion of pelagic denitrification during early Pleistocene cooling. Earth and Planetary Science Letters 389, 52-61.

Saltzman, M.R., 2002. Carbon and oxygen isotope stratigraphy of the Lower Mississippian (Kinderhookian-lower Osagean), western United States: Implications for seawater chemistry and glaciation. Geological Society of America Bulletin 114, 96-108.

Saltzman, M.R., 2003. Organic Carbon Burial and Phosphogenesis in the Antler Foreland Basin: An Out-of-Phase Relationship During the Lower Mississippian. Journal of Sedimentary Research 73, 844-855.

Saltzman, M.R., Gonzalez, L.A., Lohmann, K.C., 2000. Earliest Carboniferous cooling step triggered by the Antler Orogeny? Geology 28, 347-350.

Saltzman, M.R., Groessens, E., Zhuravlev, A.V., 2004. Carbon cycle models based on extreme changes in $\delta^{13}C$: an example from the lower Mississippian. Palaeogeography, Palaeoclimatology, Palaeoecology 213, 359-377.

Saltzman, M.R., Sedlacek, A.R.C., 2013. Chemostratigraphy indicates a relatively complete Late Permian to Early Triassic sequence in the western United States. Geology 41, 399-402.

Singler, C.S., 1987. Carbonate petrology and conodont biostratigraphy of a Mississippian carbonate unit, East Pahranagat Range, Lincoln County, Nevada [M.S. thesis]. Pullman, Washington State University, 107 p.

Smith, M.T., Dickinson, W.R., Gehrels, G.E., 1993. Contractional nature of Devonian-Mississippian Antler tectonism along the North American continental margin. Geology 21, 21-24.

Speed, R., Sleep, N., 1982. Antler orogeny and foreland basin: A model. Geological Society of America Bulletin 93, 815-828.

Stevens, C.H., Stone, P., Belasky, P., 1991. Paleogeography and structural significance of an Upper Mississippian facies boundary in southern Nevada and east-central California. Geological Society of America Bulletin 103, 876-885.

Stüeken, E.E., Kipp, M.A., Koehler, M.C., Buick, R., 2016. The evolution of Earth's biogeochemical nitrogen cycle. Earth-Science Reviews 160, 220-239.

Swart, P.K., 2008. Global synchronous changes in the carbon isotopic composition of carbonate sediments unrelated to changes in the global carbon cycle. Proceedings of the National Academy of Sciences of the United States of America 105, 13741-13745.

Swart, P.K., 2015. The geochemistry of carbonate diagenesis: The past, present and future. Sedimentology 62, 1233-1304.

Yao, L., Qie, W., Luo, G., Liu, J., Algeo, T.J., Bai, X., Yang, B., Wang, X., 2015. The TICE event: Perturbation of carbon-nitrogen cycles during the mid-Tournaisian (Early Carboniferous) greenhouse-icehouse transition. Chemical Geology 401, 1-14.

Chapter 4

The origin of unusually low $\delta^{18}O$ values in Early Mississippian carbonates of the southern Great Basin, western United States

Abstract

Oxygen isotopes ($\delta^{18}O$) of diagenetically modified rocks record the chemistry of interacting fluids. This study documents unusually low $\delta^{18}O$ values (down to –34‰, VPDB) in Early Mississippian carbonates from Nevada and Utah. In addition to carbon and oxygen isotope analyses, three block samples from ^{18}O-depleted intervals of the Star Range (SR) and Pahranagat Range (PR) sections are analyzed at macro- to micro-scales for fluid inclusion, major and trace elements, and rare earth elements (REEs) to understand the origin and processes involved during carbonate diagenesis. Calcite veins from the PR section have $\delta^{18}O$ values of –16‰ to –23‰ (VPDB), which are ~8‰ (VPDB) lower than those obtained from its highly fractured host rock (wackestone). These calcite veins were precipitated from fluids that had $\delta^{18}O$ values as high as –7‰ (SMOW) at a minimum homonization temperature of 105°C to 110°C. Samples from the SR section are collected along karstic unconformities and they show different textures and variable $\delta^{18}O$ values. In a wackestone sample that is dissected by veins, both the veins and the host rock have undistinguishable low $\delta^{18}O$ values of –22‰ to –34‰ (VPDB). In a conglomeratic sample, carbonate clasts have low $\delta^{18}O$ values (down to –30‰, VPDB) and the hosting matrix has higher $\delta^{18}O$ values of ≥ –11‰ (VPDB). These differences require the mixing of two different types of fluids. With the temperature information obtained from fluid inclusions, themodynamic modeling suggests that ^{18}O-depleted carbonates from the SR section are altered from diagenetic fluids with $\delta^{18}O$ of ≤ –15‰ (SMOW) at a minimum homonization temperature of ~200°C. Lack

of positive Eu anomaly in the REEs and the low salinity content in fluid inclusions suggest that diagenetic fluids were originated from freshwater. The REEs and fluid inclusion data from the PR section samples suggest that the low $\delta^{18}O$ values from fractured wackestones were derived from deeply charged meteoric water alteration with geothermal temperatures up to 150°C. Samples along the unconformities from the SR section might have been altered by glacial melt water with $\delta^{18}O$ values ≤ –15‰ (SMOW), supporting glacial advance to low latitude during the Early Mississippian.

1. Introduction

Carbonate minerals record the fluid chemistry from which it is precipitated; however its chemistry is prone to change when it is in contact with physically and chemically distinct fluids during diagenesis. This diagenetic feature in carbonates may be important to trace the origin of secondary fluids (Simmons and Christenson, 1994; Gianelli et al., 1997; Cai et al., 2008; Jaguin et al., 2014; Franchi et al., 2015). However, diagenetically altered carbonates by secondary fluids often record mixed signal and their geochemical variations depend on water to rock ratios involved during diagenesis (Jacobsen and Kaufman, 1999). The temperature of diagenetic fluid and the rock type it passes through add additional complexity to diagenetically precipitated minerals (Mathieu et al., 2015; Jakubowicz et al., 2015).

Oxygen isotopes ($\delta^{18}O$) from carbonate minerals have been widely used to track the source of fluids, which may provide information for paleoclimate and paleoenvironment (Zhao and Zheng, 2010; Herwartz et al., 2015). Significantly depleted $\delta^{18}O$ values, down to –27‰ (VPDB), from Precambrian carbonates in South China were interpreted as having formed from glacial melt waters (Zhao and Zheng, 2015; Bindeman and Serebryakov, 2011). In contrast, similar unusually low $\delta^{18}O$ values from Mississippian carbonates were interpreted as having

been formed by hydrothermal fluids originated from meteoric water (Katz et al., 2006). In this respect, only $\delta^{18}O$ value is insufficient or inconclusive to determine if a carbonate mineral record a primary or secondary signal. When marine carbonates are altered by ^{18}O-depleted meteoric waters, water-rock interaction may drive the $\delta^{18}O$ value of fluids progressively less negative. Therefore, the lowest $\delta^{18}O$ value recorded by altered rocks may represent the $\delta^{18}O$ value close to or higher than that of the meteoric water. Moreover, if the water is heated to >350°C, the water-rock fractionation is minimum and the precipitated mineral may preserve the $\delta^{18}O$ value of its original fluid (Criss and Taylor, 1986; Bindeman and Serebryakov, 2011; Herwartz et al., 2015). This paper describes two types of diagenetically altered Early Mississippian carbonates and their isotope signatures from the southern Great Basin of western United States: one type relates to alteration by meteoric water circulation into the depth through fractures, and the other type involves earlier meteoric and later deep burial diagenetic alteration at elevated geothermal temperatures.

Fluid inclusions and REE+Y patterns of the Early Mississippian carbonates may help understanding the origin of remarkably low $\delta^{18}O$ values. Some fluid inclusion and strontium isotope data from Early Mississippian diagenetic carbonates were previously reported by Katz et al. (2006). Based on the high temperature estimated from fluid inclusions and highly radiogenic strontium isotope values, the low $\delta^{18}O$ values, down to –26.5‰ (VPDB) in carbonate cements, were interpreted to have formed from meteoric water circulation through the basement rocks where it was heated up and migrated vertically through fault systems. However, similar records of $\delta^{18}O$ and strontium isotopes from Ediacaran carbonates have been interpreted as the glacial meltwater signatures (Zhao et al., 2009; Zhao and Zheng, 2010; Wang et al., 2014). The preservation of glacial meltwater argument was based on the REE+Y pattern and the absence of

Europium (Eu) anomaly which negates the hydrothermal origin. This study reports more depleted $\delta^{18}O$ values from the Mississippian carbonates, down to –34‰, in addition to Katz et al. (2006), which may suggest that the formation of unusually low $\delta^{18}O$ values during the Early Mississippian represent a widespread regional phenomenon. In addition to $\delta^{13}C$ and $\delta^{18}O$ analyses, fluid inclusions and REE+Y patterns from block samples are used to understand the origin of depleted $\delta^{18}O$ values and to track the isotope composition of diagenetic fluids.

2. Geological setting

During Early Mississippian North America was straddled near paleo-equator (Blakey, 2007) and its western margin is characterized by a westward facing carbonate ramp (Sando, 1976; Poole and Sandberg, 1991; Giles, 1996). The Lower Mississippian carbonate strata was deposited in a west-facing carbonate ramp in the continental side of the Antler foreland basin, which was formed by the Antler orogeny that modified the structural and depositional framework of the early Paleozoic system of the western North America (Poole and Sandberg, 1991). The Antler foreland basin was developed when Roberts Mountains allochthon thrust eastward over the passive margin in the western North America (Speed and Sleep, 1982) and formed a contractional belt extending over 2300 km from southern California to British Columbia in the north (Smith et al., 1993).

This study focuses on Early Mississippian carbonates of the Monte Cristo Limestone at Star Range (SR), Utah , and the Joana Limestone at the southern Pahranagat Range (PR) near Alamo, Nevada (Fig. 1 and 2). The Monte Cristo Limestone unconformably overlies the Late Devonian rocks at 50 m marker. The boundary unconformity records significant stratigraphic gap spanning Late Devonian through Early Mississippian (Poole and Sandberg, 1991; Giles and Dickinson, 1995). The base of the Monte Cristo Limestone at 50 to 55 m markers, above the

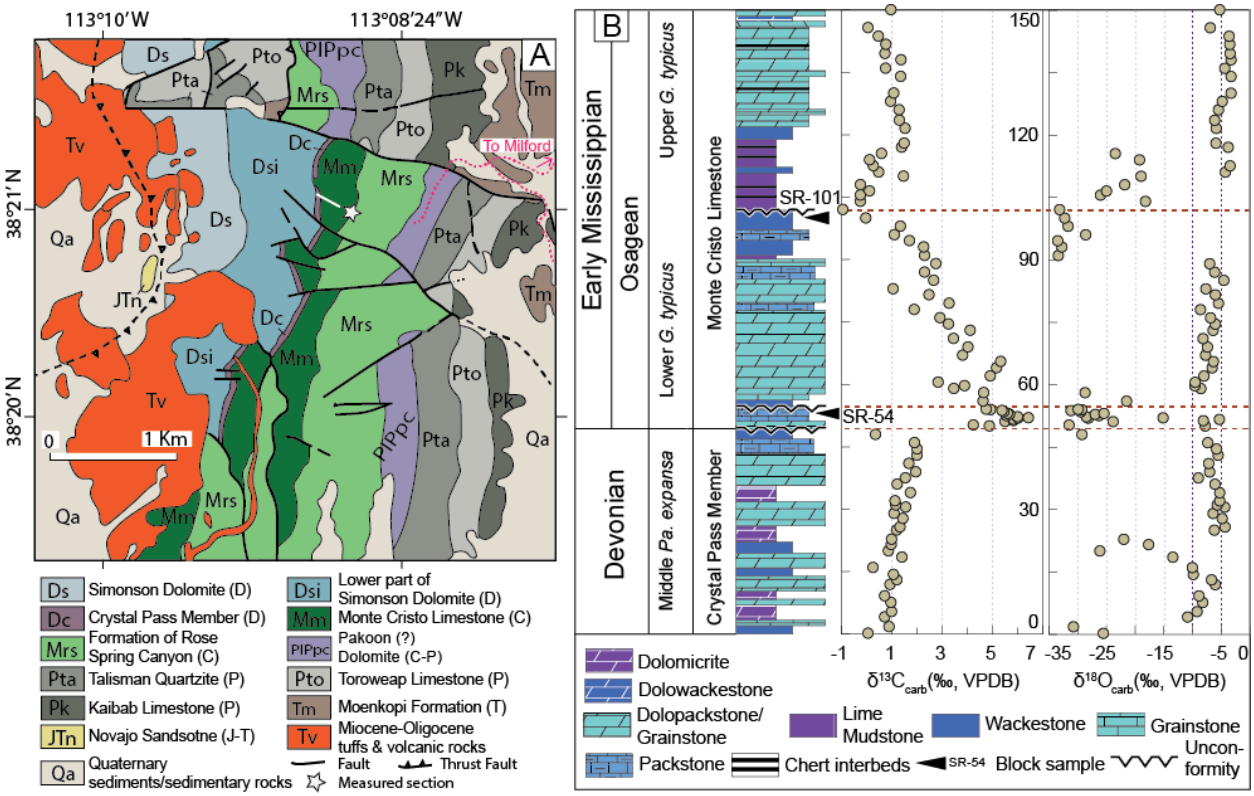

Fig. 1. Location and stratigraphy of the Star Range (SR) section, Utah. (A) Simplified geological map showing the measured section (modified from Best et al., 1989; USGS Scientific Investigations Map). (B) Litho-, Bio-, and chemostratigraphy of $\delta^{13}C_{carb}$ and $\delta^{18}O_{carb}$ of the SR section. Biostratigarphy are based on Poole and Sandberg (1991) and Giles and Dickinson (1995). The contact between Crystal Pass Member and Monte Cristo Limestone separates Devonian and Mississippian rocks and represents a major unconformity with four to five conodont biozones missing (Poole and Sandberg, 1991). The $\delta^{13}C_{carb}$ shows an abrupt positive shift across this contact. Also, highly depleted $\delta^{18}O_{carb}$ values are associated with exposure surfaces.

unconformity is characterized by dark gray oolitic dolograinstone which is overlain by dark gray, thin to medium bedded oolitic packstone with thin bioclastic peloidal grainstone layers. The top of the oolitic packstone contains conglomeratic layers that are representative of lag deposits along an exposure surface. These rock units are followed by dark gray, thinly bedded

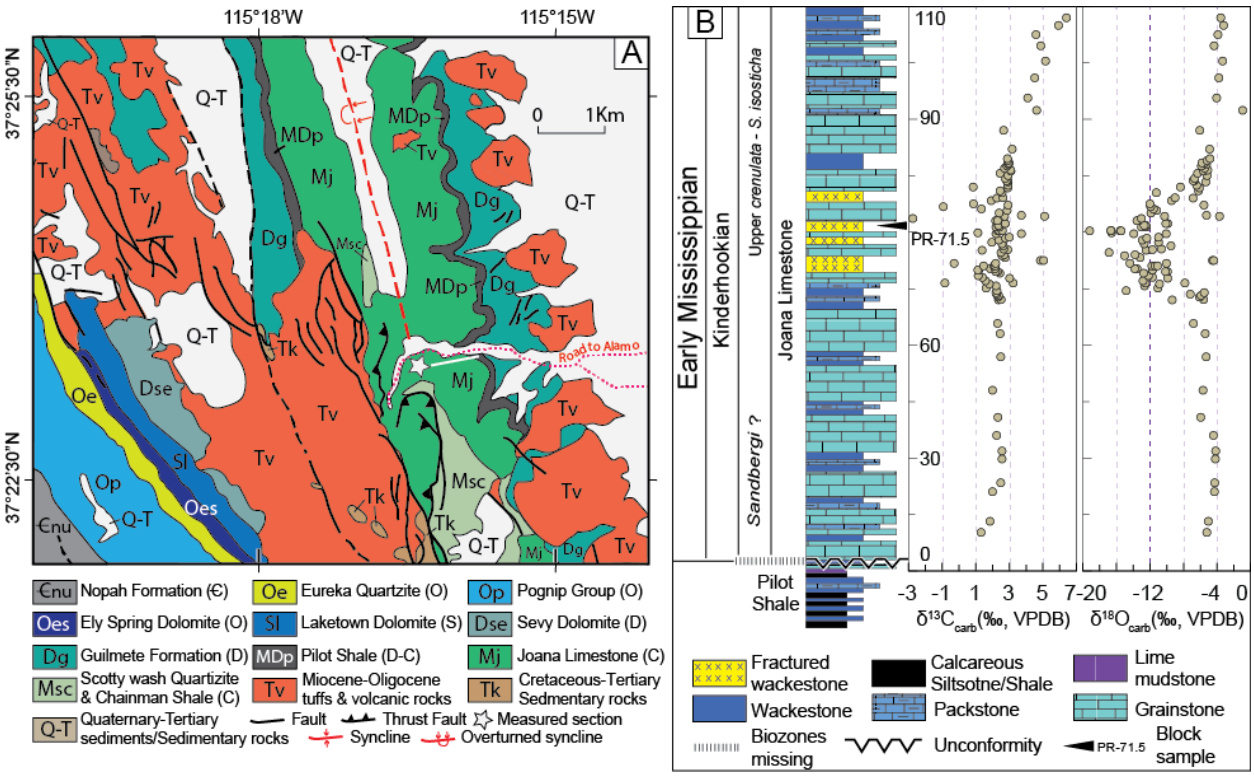

Fig. 2. Location and stratigraphy of the southern Pahranagat Range (PR) section, about 7 miles northwest of Alamo, Nevada. (A) Simplified geological map showing the PR section (modified from Jayko, 2007; USGS Scientific Investigations Map 2904). (B) Litho-, Bio-, and chemostratigraphy of $\delta^{13}C_{carb}$ and $\delta^{18}O_{carb}$ of the PR section. Notice that the section is measured in the southern side of the valley and the Joana Limestone is partially deformed in this locality. The contact between Joana Limestone and Pilot Shale is an unconformity with one or two conodont biozones missing. The conodont biozones are based on Poole and Sandberg (1991). The $\delta^{13}C_{carb}$ and $\delta^{18}O_{carb}$ values beyond the 58-83 m interval are taken from Henry (2011). Note that the low $\delta^{18}O_{carb}$ values are from highly fractured wackestones that are stratigraphically discontinuous in the field, i.e., it is not present in the northern side of the valley.

wackestone/packstone and cross-bedded oolitic dolograinstone and packstone with interbeds of bioclastic layers, which grade into intervals of dark gray bioclastic wackestone with laterally discontinuous, thin bioclastic packstone beds. The top of this interval, at 102 m marker, is an unconformity, which is overlain by dark gray, thin to medium bedded mudstone and chert layers.

This fine-grained mudstone interval (Fig. 1B) is possibly equivalent to the Delle Phosphate Member of the Deseret Limestone (Giles and Dickinson, 1995). Above this interval, the rest of the Monte Cristo Limestone consists of thin to medium beds of micritic dolostone and bioclastic oolitic dolograinstone/packstone. Based on conodont biostratigraphy, the Monte Cristo Limestone is an Osagean in age within Lower to Upper *Typicus* conodont zones (Poole and Sandberg, 1991). The abrupt changes in $\delta^{13}C_{carb}$ at the base and the middle of the Monte Cristo Limestone are consistent with field evidence for exposure and erosion at these horizons (Fig. 1B).

The Joana Limestone of the PR section represents the distal ramp deposits and is composed of massive beds of crinoidal oolitic grainstone at the base, coral bioherm dominated thick fossiliferous grainstone in the middle and medium to thick beds of bioclastic grainstone and packstone with corals and large crinoid fragments at the upper portion (Fig. 2). Different from the section measured for N- and S-isotopes, for this study the section is measured from the southern side of the valley (Fig. 2A) where portion of the Joana Limestone is structurally deformed and some stratigraphic repetition is present. The interval of 60–80 m contains highly fractured wackestone between grainstones, which are cemented by late stage calcite veins. The upper portion also contained numerous discontinuous bands of chert nodules. Thin to medium bedded bioclastic wackestone/packstone between thick to massive beds of grainstone/packstone is common in the succession. The base of the Joana Limestone unconformable overlies the Pilot Shale with one or more conodont zones missing. Based on conodont biostratigraphy, the Joana Limestone is the Early Mississippian (Kinderhookina-Osagean) in age (Poole and Sandberg, 1991). This study focuses on intervals that have unusually negative $\delta^{18}O$ values of the Monte Cristo Limestone in Star Range and Joana Limestone in southern Pahranagat Range.

3. Samples and methods

In addition to stratigraphic samples that document the general trends of $\delta^{13}C$ and $\delta^{18}O$ (Figs. 1B and 2B), three block samples are collected for macro- and micro-scale isotope and geochemical analyses. Stratigraphic samples were collected at the spacing of 1 to 2 m and their $\delta^{13}C$ and $\delta^{18}O$ (Table 1A) serve as chemostratigraphic profiles for regional correlation. For the PR section, parts of the $\delta^{13}C$ data are taken from Henry (2011). Block samples were collected only from oxygen isotope depleted horizons and are analyzed for $\delta^{13}C$, $\delta^{18}O$, fluid inclusion, petrography, rare earth elements (REEs), trace elements, and major elements. For block samples, $\delta^{13}C$ and $\delta^{18}O$ are reported in Table 1B, element data in Table 2 and fluid inclusion data in Table 3.

For $\delta^{13}C$ and $\delta^{18}O$ analyses, carbonate powders are micro-drilled from polished and cleaned surfaces. About 200 μg of carbonate powders were reacted with orthophosphoric acid for 10 minutes at 70°C in a Kiel device coupled with Finnigan Delta Plus dual-inlet mass spectrometer. Isotope data was reported in δ notation in per mil relative to VPDB standard. Uncertainties were monitored by the duplicate analyses of laboratory standards calibrated to NBS-19, which are better than 0.1‰ for both $\delta^{13}C$ and $\delta^{18}O$.

For REE+Y and major and trace element analyses, 22–50 mg of carbonate powders micro-drilled from polished block samples were leached in 0.5 M distilled acetic acid at room temperature. After centrifuging, the supernatant solution was separated, dried, and the diluted in 2% nitric acid (HNO_3) to 50 ml. REE+Y and elemental concentrations are analyzed with an Agilent 7700 ICP-MS (Inductively Coupled Plasma Mass Spectrometer) at the University of Nevada Las Vegas. All analyses are within the USEPA Method 6020A limits. The REE values are normalized to Post Archean Australian Shale (PAAS; Nance and Taylor, 1976). La, Ce, Eu

and Gd anomalies were calculated based on methods described by Bau and Dulski (1996), Webb and Kamber (2000) and Lawrence et al. (2006): La/La* =$(La/(3Pr-2Nd))_{SN}$, Ce/Ce* = $(Ce/(Pr*(Pr/Nd))_{SN}$, Eu/Eu* = $(Eu/(0.67Sm + 0.33Tb))_{SN}$, Gd/Gd* = $(Gd/0.33Sm + 0.67Tb))_{SN}$, where $_{SN}$ is the shale normalized values.

Fluid inclusion analyses were performed for calcite veins in the Block samples. Altogether six thick section samples were analyzed under transmitted and reflected light using Nikon Optiphot and Olympus BX60 polarized light microscopes. In order to collect homogenization temperature and salinities from fluid inclusions, heating and freezing experiments were performed on a Linkam THMSG 600 heating and freezing stage attached to an Olympus BX60 petrographic microscope, which is controlled by Linkys32 software. Ice melting temperature (Tm_{ice}) and homogenization temperatures were collected following the methods described by Goldstein and Reynolds (1994). Tm_{ice} values are used to calculate salinity of the fluid inclusions following Goldstein and Reynolds (1994): Salinity (NaCl wt.%) = $0.00 + 1.78 (Tm_{ice}) – 0.0442 (Tm_{ice})^2 + 0.000557 (Tm_{ice})^3$.

4. Results

4.1. Carbon and Oxygen Isotopes

The $\delta^{13}C$ and $\delta^{18}O$ data are given in Table 1A and 1B and are shown graphically in Figs. 1–5. The $\delta^{13}C$ values in the SR section remain between 0–2‰ as the baseline values with a remarkable positive shift up to 4.9‰ at 50 m in the section that is correlated with K-O (Kinderhookian-Osagean) $\delta^{13}C$ excursion. The abrupt shift in $\delta^{13}C$ records a major unconformity spanning Late Devonian through Early Mississippian that cut off the rising limb of the K-O $\delta^{13}C$ excursion (Figs. 1 and 3). The $\delta^{18}O$ values show large variations with baseline values between –5‰ and –9‰ and significantly low values down to –33.4‰ that are repeatedly recorded at three

intervals of the measured section. Interestingly, the 25 m interval between 91 to 115.5 m has the majority of $\delta^{18}O$ values ≤ – 18‰ (Fig. 1B), a pattern very similar to those documented from the Ediacaran Doushantuo Formation in South China (Zhao and Zhen, 2009; Wang et al., 2014). The block samples from these anomalous horizons at 54 m and 101 m record $\delta^{18}O$ values from –11.03 to –34‰. Sample SR-54 show conglomeratic texture, in which $\delta^{18}O$ values of peloiodal grainstone clasts (–25.5 to –31.3‰) are 5–10‰ lower than those of matrix (– 18.8 to –28.5‰) and corals (–11.3 to –24.8‰) (Fig. 5). Sample SR-101 is dissected by calcite veins and both the veins and host rock (wallrock) record similar range of $\delta^{18}O$ values (–22.1 to –34‰). In comparison, the fractured block sample from the PR section shows that $\delta^{18}O$ values of calcite veins (–16.3 to –22.8‰) are 8‰ lower than those of the wallrock (–7.8 to –13.6‰).

4.2. Mineralogy and major element composition

Major element contents are reported from different facies in the block samples (Table 2). In all samples, wallrocks are composed of wackestone or grainstone and veins and cements are characterized by blocky calcite (Fig. 6, A-H). Block samples from SR show similar range of major element concentration between different facies; Mg (858-9054 ppm), Al (24-460 ppm), Ca (119893-377099 ppm), Mn (20-274 ppm), Fe (102-484 ppm), Sr (167-503 ppm) and Mg/Ca ratio (0.01-0.02). However, PR-71.5 sample from the PR section show that wallrock (wackestone) contain a significantly low concentration of Mg (1841-2180 ppm), Al (41-65 ppm) and Fe (86-115 ppm) relative to calcite veins.

4.3. Trace elements and REE geochemistry

Trace elements and PAAS-normalized REE concentration are reported in Table 2 and are shown in Figs. 7 and 8. Matrix and calcite veins from the block samples contain high concentrations of La, Nd and Y with the majority of other REEs contents below 1 ppm and low

P, high Zn and Mo concentrations. Collectively, the shale-normalized REE patterns indicate slightly enriched MREE (i.e., Sm, Eu, Gd and Tb) and HREE (i.e, Dy, Ho, Er, Tm, Yb and Lu) compared to LREE (i.e., La, Ce, Pr and Nd). Total REE contents in block samples range between 0.5 to 17.9 ppm, in which high REE contents (>6 ppm) are associated with the high P and Zn contents (>180 ppm). Samples from both calcite veins and wallrock show a wide range of Y/Ho ratios varying from 63.9 and 135.7, with two significantly high outlier values (>562) from samples SR-101_S1 and PR-71.5_V13. Ce and Gd anomalies are all positive and range from 0.32 to 1.57 and 1.5 to 10.5, respectively. SR samples mostly show positive Ce anomalies while the PR sample demonstrate mostly negative Ce anomaly (Fig. 9). Both SR and PR samples indicate absence of Eu anomaly.

Interestingly, both calcite veins and wallrock carbonate record similar REE+Y patterns with higher ∑REE concentrations in the wallrock (i.e., wackestone or grainstone). Generally, studies have shown that REE fractionation varies accordingly with different facies, for instance, higher ∑REE content in micrite (Feng et al., 2009; Franchi et al., 2015; Jakubowicz et al., 2015).

4.4. Fluid inclusion

Results of fluid inclusion analyses are reported in Table 3 and Fig. 11. Fluid inclusion analyses were performed mostly in sample SR-101. Sample PR-71.5 contained very few numbers of measurable fluid inclusions. The calcite vein from SR-101 records a narrow range of homonization temperature (150–175°C). Close to the fluid inclusion sampling points, the oxygen isotope values of the calcite vein are –32.8 and –33.9‰. The salinity, expressed in weight percent of NaCl, corresponding to the fluid inclusions are < 1.5%. A fluid inclusion from PR-71.5-P1 records the homonization temperature range of 105°C to 110°C and 8% salinity, with the corresponding $\delta^{18}O$ value of –20.9‰. The minimum homonization temperature records from

these two samples correspond to the most depleted $\delta^{18}O$ values and suggest that the temperature range may reflect the lower limit in each sample.

5. Discussion

5.1. Physico-chemical signature of diagenetic fluid

Minimum temperature of mineral precipitation can be recorded by the fluid inclusion enclosed during the mineral formation and has been used to explore temperature conditions of the original fluid (Goldstein and Reynolds, 1994; Simmons and Christenson, 1994; Jaguin et al., 2014). However, secondary fluid inclusion may give significantly different and wide range of temperature record and cannot provide reliable temperature information. Primary fluid inclusion is the one associated with the crystal growth line and provide a narrow range of temperature and salinity data from different fluid inclusion associations (Goldstein and Reynolds, 1994). Calcite veins from SR and PR record a narrow range of homonization temperature (105°C to 175°C) and salinity (< 1.5% to 8%), which indicates the preservation of primary fluid inclusions. Moreover, these records are consistent with previous temperature records of diagenetic carbonates from Early Mississippian carbonates in western USA (Katz et al., 2006).

REEs have been used to define fluid composition from various sources (Bau et al., 2010; Zhao et al., 2009; Franchi et al., 2015; Mathieu et al., 2015), especially because REEs in carbonates preserve original composition during diagenesis (Webb and Kamber, 2000, Nothdurft et al., 2004). Modern seawater has a characteristic feature of REE pattern, with the strong LREE depletion and HREE enrichment (Fig. 10). Similar patterns have been documented from ancient carbonates, suggesting that ancient seawater particularly post-Devonian oceans, had modern like REE patterns (Webb and Kamber, 2000, Nothdurft et al., 2004; Shields and Webb, 2004; Wallace et al., 2017).

Modification by surficial freshwater and/or geothermal/hydrothermal fluids of unknown composition, could have affected REE concentration and its patterns within SR and PR samples. Importantly, the high temperature records from SR and PR samples suggest that diagenetic alteration may have been occurred with interactions from geothermal or hydrothermal fluids. The diagenesis at elevated temperature may result in REE patterns in the precipitating minerals similar to that of interacting fluid (Hopf, 1993; Middleton et al., 2014; Mathieu et al., 2015; Jakubowicz et al., 2015). Besides the diagenetic records of REE in carbonates, it can be largely influenced by even a small percentage (<1%) of siliciclastic and/or Fe-Mn-oxyhydroxides contamination (Murray et al., 1991; Nothdurft et al., 2004). There is no correlation between ∑REE and Al, Fe, or Mn (Fig. 7C) in the SR and PR samples, suggesting that any such contamination is insignificant and the REEs of these samples record their diagenetic fluid chemistry. However, SR-101 sample record moderate correlation ($R^2 = 0.66$) between ∑REE and Al (Fig. 7C), suggesting that the diagenetic fluid could have been reacted with terrestrial siliciclastics.

5.2. Temperature constraints on carbon and oxygen isotopes

Because oxygen isotope fractionation between calcite and water depends on temperature (Epstein et al, 1953), oxygen isotope in precipitating carbonates is sensitive to the temperature of diagenetic fluid (Epstein and Mayeda, 1953; Herwatz et al., 2015). Extremely low $\delta^{18}O$ (≤ – 30‰) has been reported in the rocks from either very cold environment, e.g., modern central Antartica (Faure et al., 1988) or from high temperature associated with geothermal or hydrothermal alteration (Simmons and Christenson, 1994; Bindeman and Serebryakov, 2011). Moreover, water/rock ratio is also important during diagenesis, which may significantly alter carbon and oxygen isotope composition of rocks (Jacobsen and Kaufman, 1999).

Carbonate Samples from the SR section preserve very low oxygen isotope values down to –34‰ (Fig. 3, 4 and 5, Table 1A and 1B). These carbonates (or calcite mineral) could have been formed at higher latitude (above 60 degrees latitude) where $\delta^{18}O$ of meteoric water is < –15‰ (Bowen and Wilkinson, 2002). However, North America was in the equatorial position during Early Mississippian which negates the conditions of higher latitude meteoric water source. If the calcite is precipitated from present sea water ($\delta^{18}O_w$ = 0‰), the measured low oxygen isotope value can only be achieved at unrealistically high temperature (i.e., >>1000°C). Moreover, the same low $\delta^{18}O$ calcite formed from Modern equatorial meteoric water ($\delta^{18}O_w$ = –5‰) would require a precipitating temperature of ~580°C (O'Neil et al., 1969). This is only possible when the meteoric water is heated by geothermal or hydrothermal processes.

Fluid inclusions measured from the SR and PR samples show that the minimum homonization temperature of the diagenetic fluid ranges from 105°C to 175°C. Because the presence of Eu anomaly originated from hydrothermal fluid requires a temperature of above 200°C (Bau, 1991), the absence of Eu anomaly in REE patterns (Fig. 8) in SR and PR samples has constrained the maximum possible diagenetic fluid temperature below 200°C and negates the hydrothermal origin of the diagenetic fluid.

The temperature range (105°C to 200°C) of the diagenetic fluid cannot modify the modern equatorial meteoric water composition ($\delta^{18}O_w$ = –5‰) to precipitate calcite with $\delta^{18}O$ value of –34‰. It implies that the $\delta^{18}O$ of the precipitating fluid has to be significantly lower than the Modern equatorial meteoric water. Katz et al. (2006) has reported low $\delta^{18}O$ in late stage calcite, down to –26.5‰, and its minimum homonization temperature of ~140°C from fluid inclusion in the Early Mississippian carbonates of the Madison Formation. With their more radiogenic strontium isotope ratios, they have suggested that the diagenetic fluid could have been

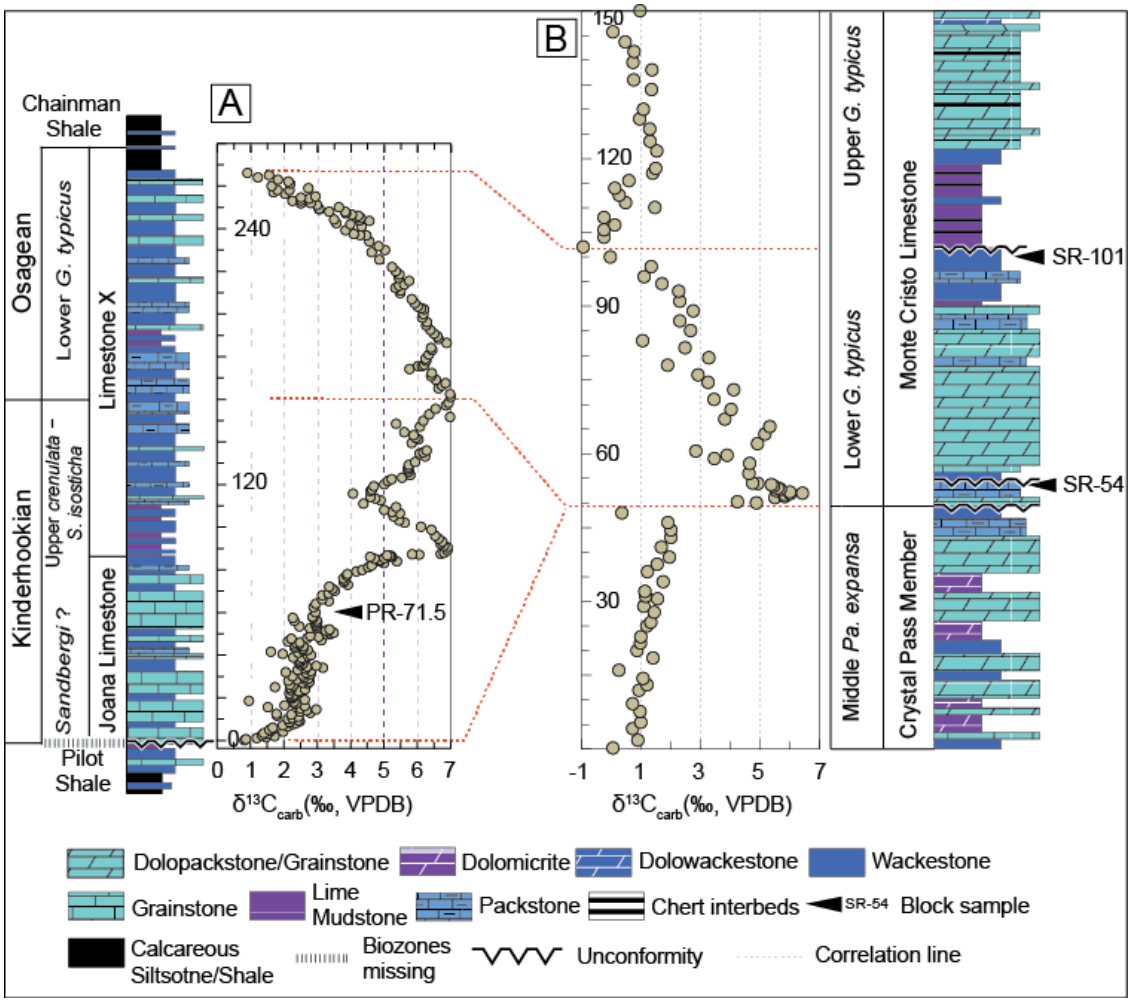

Fig. 3. Correlation between SR and PR sections using biostratigraphy and $\delta^{13}C_{carb}$ chemostratigraphy. In SR section, the contact between Crystal Pass Member and Monte Cristo Limestone is a major unconformity that cut off the rising half of the K-O $\delta^{13}C$ excursion (the Kinderhookian strata are entirely missing here). Biostratigarphy for SR are from Poole and Sandberg (1991) and Giles and Dickinson (1995), and for PR it is based on Singler (1987) and Poole and Sandberg (1991).

originated from meteoric water with $\delta^{18}O$ values as low as –10.5‰, which interacted with felsic-rich basement rocks, gained elevated geothermal temperature, migrated vertically through fault system and altered the carbonates in Madison Formation. Under this condition, diagenesis of the

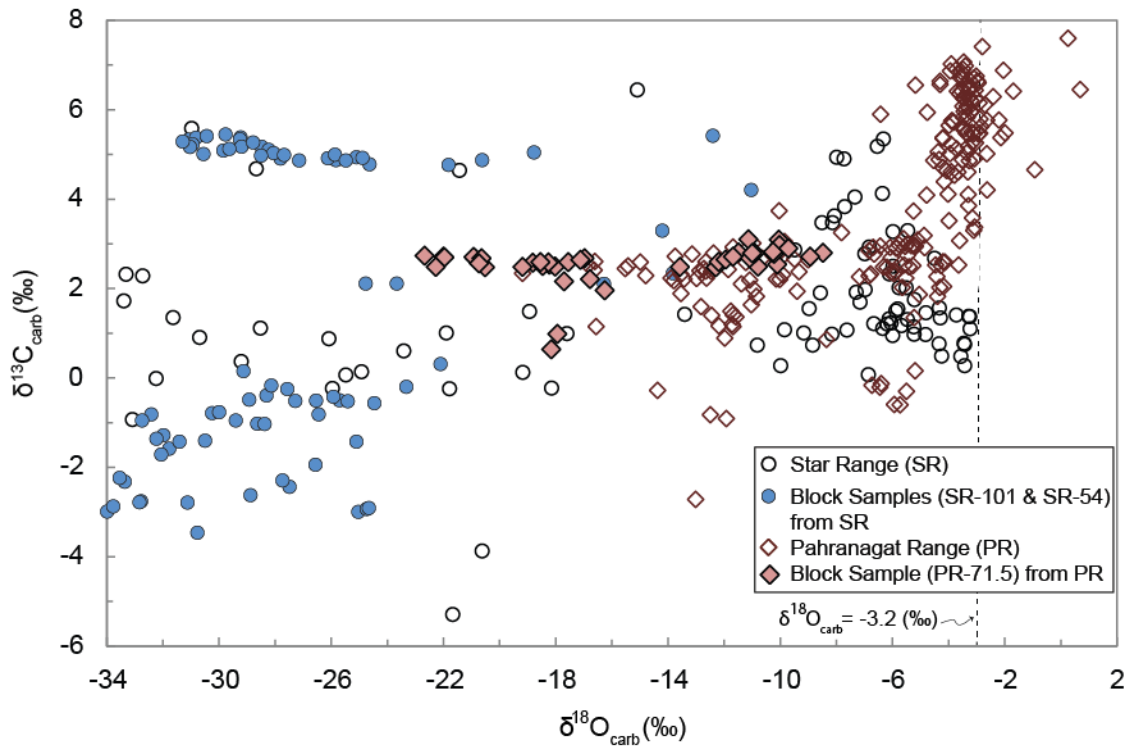

Fig. 4. Distribution of $\delta^{13}C_{carb}$ and $\delta^{18}O_{carb}$ from SR and PR sections. Data from the SR section including those from the block samples show remarkably low $\delta^{18}O$ values down to –34‰. The dashed line marks $\delta^{18}O$ values of –3.2‰ that is the background value of these sections or the closest to primary $\delta^{18}O$ values.

SR samples requires the meteoric water or fresh water composition significantly lower than –10.5‰ in order to archive the $\delta^{18}O$ values of –34‰ in SR samples. Alternatively, the fresh water (i.e., the meteoric water or glacial melt water) with $\delta^{18}O$ values <–10.5‰ could have modified the SR samples below the unconformity (exposure surface) and later subjected to further modification at higher burial temperature of ≤ 200°C when these rocks attained significant buried depth.

Because seawater and magmatic hydrothermal/metamorphic fluids have salinity 3.5% and >20%, respectively (Epstein and Mayada, 1953; Li et al., 2016), the low salinity (< 1.5 wt. %) measured from the fluid inclusion in SR-101 negates these water sources. Instead, it suggests

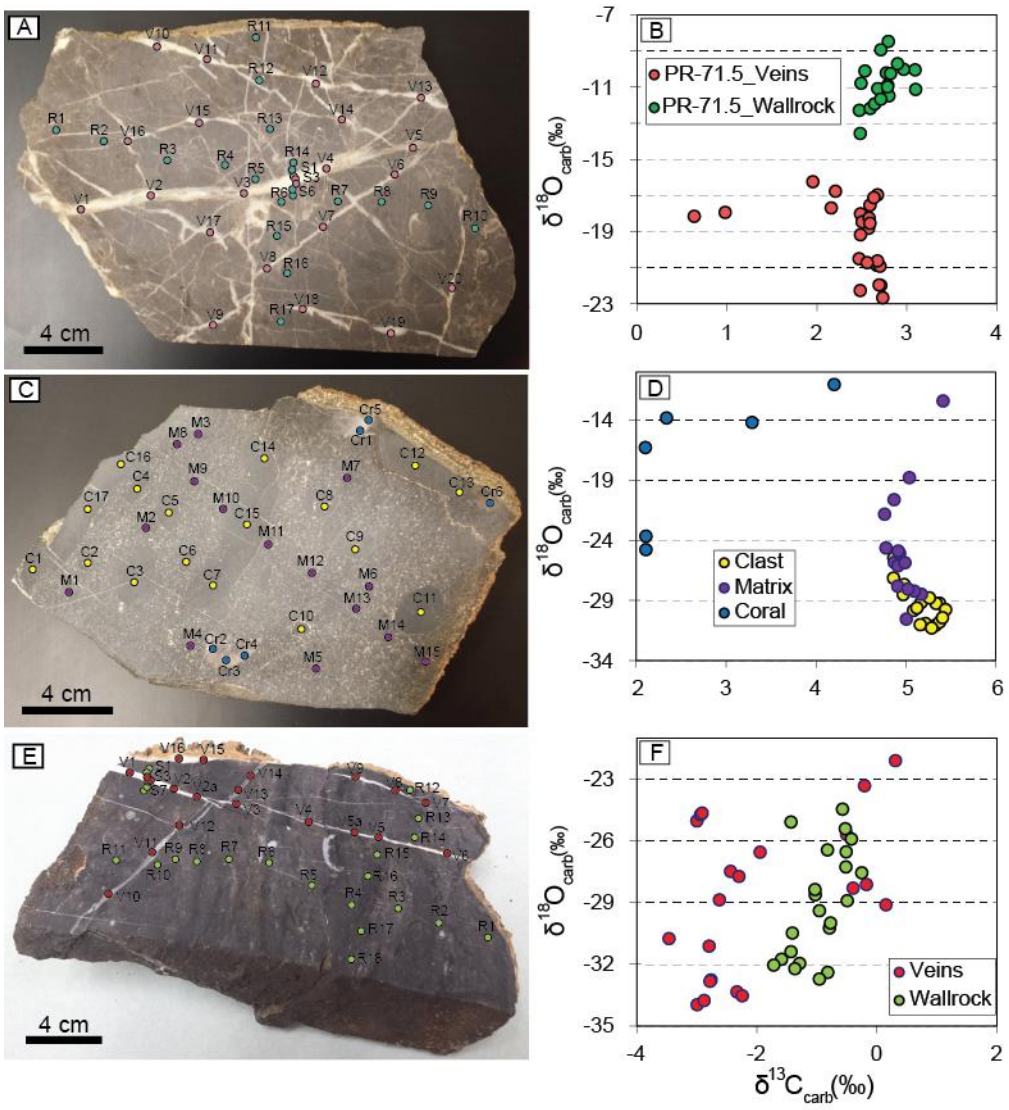

Fig. 5. Block samples and their corresponding cross plots of $\delta^{13}C_{carb}$–$\delta^{18}O_{carb}$ values. (A) A block sample (PR-71.5) from the PR section is a wackestone containing calcite veins. (B) Cross plot of $\delta^{13}C_{carb}$–$\delta^{18}O_{carb}$ from PR-71.5 showing that $\delta^{18}O_{carb}$ values in calcite veins are 8‰ lower than those of the wallrock. (C) A block sample (SR-54) from the SR section at 54 m showing conglomeratic texture consisting of peloidal grainstone clasts and matrix/cement. (D) Cross plot of $\delta^{13}C_{carb}$–$\delta^{18}O_{carb}$ from SR-54 showing unusually low $\delta^{18}O_{carb}$ values in clasts, down to –34‰. (E) A block sample (SR-101) from the SR section at 101 m containing calcite veins. (F) Cross plot of $\delta^{13}C_{carb}$–$\delta^{18}O_{carb}$ from SR-101 showing comparable $\delta^{18}O_{carb}$ values in wallrock and calcite veins. The $\delta^{13}C_{carb}$ values in all block samples are less variable than $\delta^{18}O_{carb}$ values.

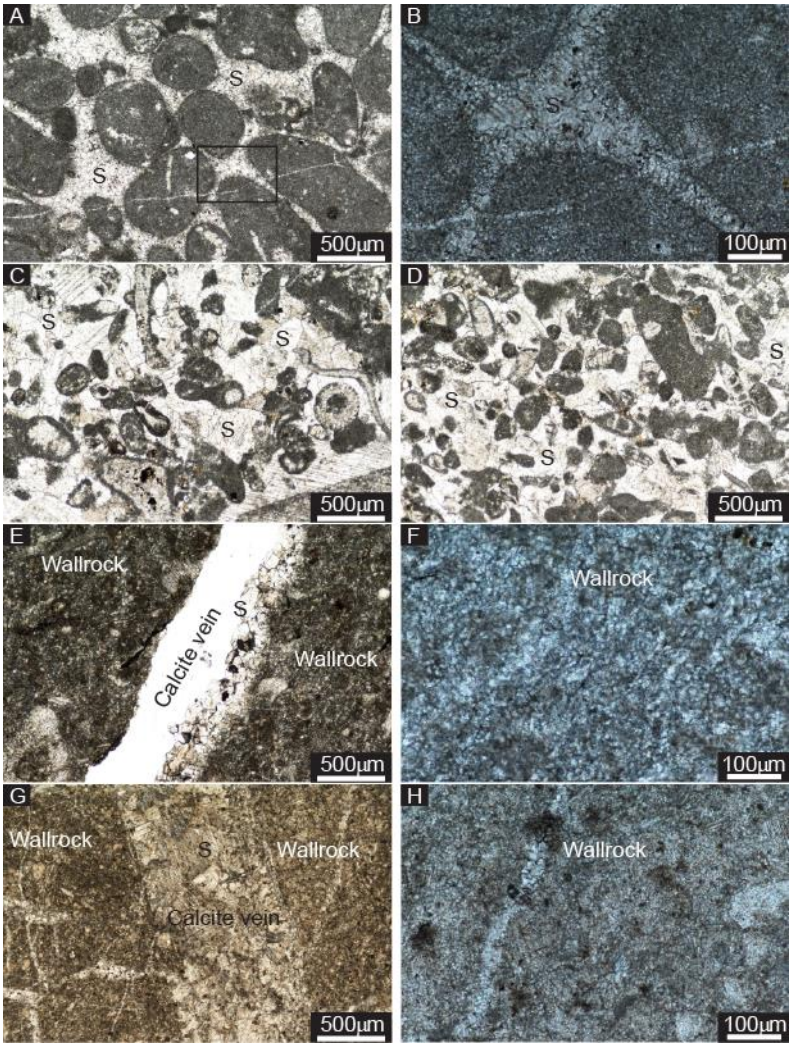

Fig 6. Microphotographs from SR and PR block samples. (A) A peloidal grainstone clast from SR-54 showing rounded to sub-rounded peloids encased in secondary calcite cement (S). (B) Secondary calcite between peloids showing recrystallization features. This figure is zoomed from the rectangle area in (A). (C) and (D) Matrix at different areas of SR-54 showing recrystallized peloids with their original relics preserved, which are cemented by blocky calcite. (E) Calcite vein in SR-101 showing coarser grains away from the edge of the wallrock (wackestone). (F) Wallrock in SR-101 showing recrystallization. (G) Calcite vein in PR-71.5 showing coarse crystals but there is no change in grain size from the edge of the wallrock (wackestone) as seen in (E). (H) Wallrock in PR-71.5 showing recrystallization features. More homogeneous crystal sizes in the wall rock of PR-71.5 show lesser degree of recrystallization than in SR-101.

that the low $\delta^{18}O$ in SR and PR samples could have been originated from freshwaters. Then, the salinity value of 8% from PR-71.5 could have been derived from freshwater partially interacted with evaporites as it has significantly high salinity (i.e., > 20%, Katz et al., 2006).

To understand the possible $\delta^{18}O$ values of the diagenetic fluid and diagenetic process involved in SR and PR samples, we conducted a simple modeling using minimum homonization temperatures and their associated $\delta^{18}O$ values from calcite veins. Results suggest that the $\delta^{18}O$ values for the digenetic fluids ($\delta^{18}O_w$) would range from –7 to ≤ –15‰ for PR and SR samples, respectively (Fig. 11A). Such $\delta^{18}O_w$ values support the fresh water origin of the diagenetic fluids. Further, the model estimates the ranges of water/rock ratios and temperatures required to alter the SR and PR samples.

Considering that the high $\delta^{18}O$ values of Early Mississippian carbonates are unaltered, the initial $\delta^{18}O_r$ value for the unaltered carbonates is taken as –3.2‰ (Fig. 4 and 11). Likewise, the initial $\delta^{18}O_w$ is considered as –15‰ for SR-101. Then, to get the measured range of $\delta^{18}O$ values (–22.1‰ to –33.9‰) of SR-101, the water/rock ratio requires to be higher than ten with the possible temperature range of 50–200°C (Gray shade in Fig. 11E). Therefore, under such a condition, veins and wallrock in SR-101 has similar range of low $\delta^{18}O$ values.

The SR-54-Clasts record $\delta^{18}O$ values from –25.5 to –31.3‰ (Fig. 5, C and D) that is within the range found in SR-101. However, SR-54-Matrix contains a mixture of broken fragments from wallrock (i.e., SR-54-Clasts) and calcite cement (Fig. 6, C and D), which show wide range of $\delta^{18}O$ values from –11.0‰ to –28.5‰. This suggests that low $\delta^{18}O$ values (i.e., –28.5‰) are possibly from broken fragments of wallrock while higher $\delta^{18}O$ values (i.e., –11.03‰) are from late stage calcite cement, showing two distinct sources of $\delta^{18}O$ values. The high $\delta^{18}O$ values in the late stage calcite may be the result of mixing of original diagenetic fluid

with low $\delta^{18}O$ broken fragments of wallrock. Then, the original $\delta^{18}O$ value of the diagenetic fluid that precipitates the late stage calcite may be higher than –11.03‰.

Calcite veins from the PR sample show $\delta^{18}O$ value from –16.3‰ to –22.7‰ that are 8‰ lower than its wallrock carbonates (–8.5 to –13.6‰), suggesting that the calcite vein have been precipitated from chemically distinct diagenetic fluid with $\delta^{18}O$ value of –7‰ (Fig. 11, A and B), which is close to the present equatorial meteoric water composition (Bowen and Wilkinson, 2002). The calcite vein shows a homonization temperature between 105°C and 110°C that corresponds to the $\delta^{18}O$ value of –20.9‰, suggesting that the lowest $\delta^{18}O$ values of –22.7‰ from the same vein may have the temperature above 110°C and possibly below 150°C (Gray shade, Fig. 11B). Therefore, the diagenetic fluid with a temperature range of 50–150°C and the water/rock ratios > 5 (Fig. 11B) is required to get $\delta^{18}O$ values in the calcite veins from PR-71.5. Similarly, the wallrock of PR-71.5 could have been altered by the diagenetic fluid with $\delta^{18}O$ value of –7‰ within the same temperature range but lower water/rock ratios (i.e., <1) (Fig. 11B). This suggest that the initial wallrock $\delta^{18}O$ composition of –3.2‰ in the PR-71.5 sample has been modified to much lower $\delta^{18}O$ values down to –13.6‰.

5.3. Trace elements and REE patterns

Both calcite veins and wallrock (Fig. 6) display similar REE patterns in SR and PR samples (Fig. 8). Provided that the petrographic evidence of strong dissolution and recrystallization of the wallrock (Fig. 6; B, C, D and F), the original signature of the carbonates would have been overprinted by incipient diagenesis resulting homogeneous REE patterns.

Interestingly, these REE patterns do not mimic either seawater REE pattern or hydrothermal water and modern deep water (Fig. 11). Generally, the PAAS normalized REE+Y patterns of modern seawater is characterized by a strong LREE depletion, positive La and Gd

anomalies, negative Ce anomaly and super chondritic Y/Ho ratio (Bau, 1996; Webb and Kamber, 2000; Oliver and Boyet, 2006). However, hydrothermal fluids have pronounced Eu enrichments (Bau, 1991). Therefore, REE+Y patterns from SR and PR samples represent the freshwater composition. Moreover, the presence of positive La and Gd anomalies (Table 2A) and super chondritic Y/Ho ratio may suggest the mixing between seawater and the freshwater.

SR and PR samples have high ∑REE concentrations in the wackestone/peloidal grainstone facies of the wallrock, with some exception in the calcite veins. The ∑REE in peloidal grainstone clasts from SR-54 is significantly higher (6–18 ppm) than the matrix and/or cements (<6 ppm). Similarly, micrite from samples SR-101 and PR-71.5 show higher ∑REE content than calcite vein (Table 2A). Similar ∑REE enrichment in micrite have been observed in both seep-related and non-seep environments of carbonate precipitation (Feng et al., 2009; Jakubowicz et al., 2015).

∑REE from the samples show good correlation with P and Zn concentration (Fig. 7, A and B) and indicate that both of them are derived from geothermal fluid. Although phosphates incorporate REE disproportionally (German and Elderfield, 1990; Reynard et al., 1999), the correlation between ∑REE and P for PR-71.5 sample (Fig. 7C) has no influence on REE pattern in the sample. Moreover, the REE patterns from PR-71.5 do not match with the pattern derived from laboratory experiments under the influence of phosphate coprecipitation (Byrne et al., 1996).

***5.3.1. Cerium anolmaly*:** Cerium anomaly in rocks has been used to define oxic or anoxic conditions of deposition. Ce is insoluble in oxic water and forms Ce^{4+} ions which are removed from the solution by Fe-oxyhydroxides, leaving a negative Ce anomaly in the seawater (Derry

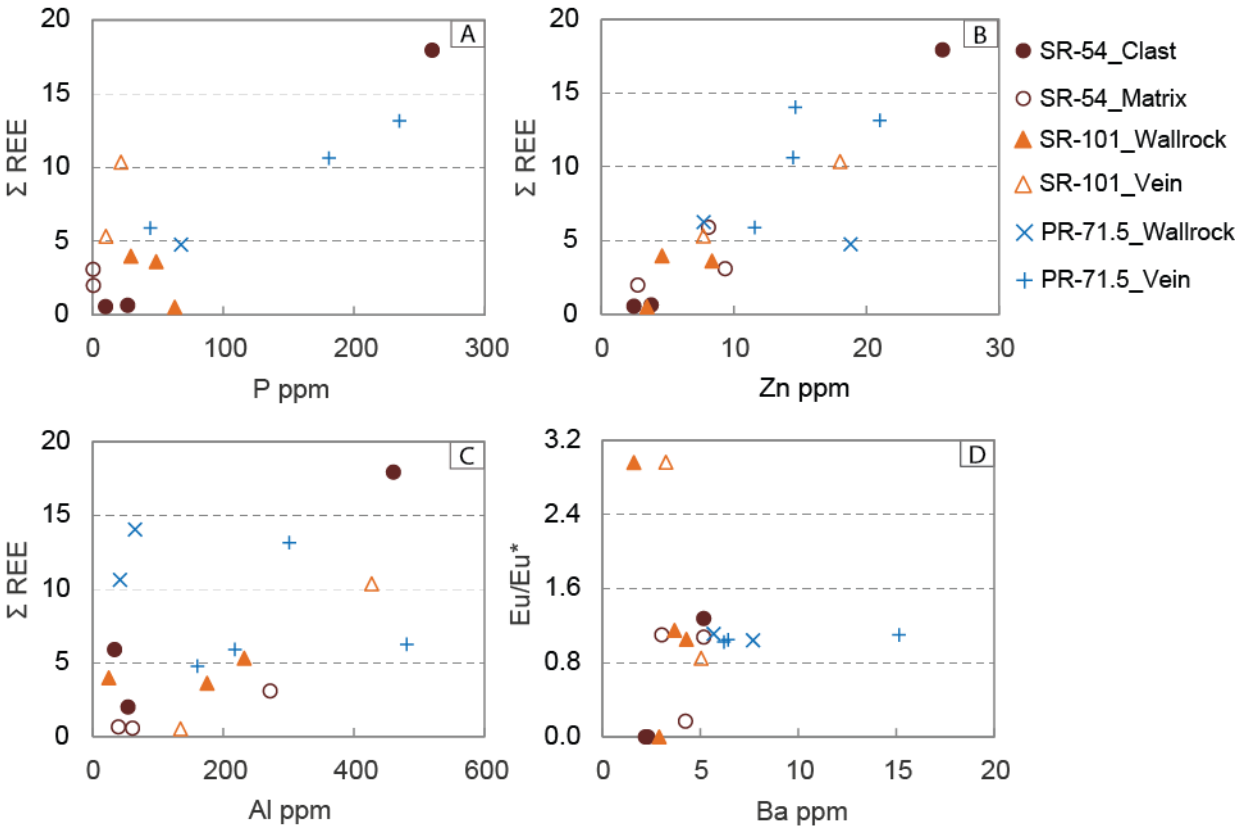

Fig. 7. Plots of P, Zn, Al and Ba contents versus ∑REE and Eu/Eu*. (A) Crossplot of ∑REE−P values. Data from SR samples do not show ∑REE−P correlation but those from the PR sample display strong correlation (R^2 = 0.95). This correlation does not change the REE pattern in PR-71.5, suggesting that P content does not affect REEs in this sample. (B) Crossplot of ∑REE−Zn values showing a good correlation (R^2 = 0.76). (C) Crossplot of ∑REE−Al values. Only the data from SR-101 show moderate correlation (R^2 = 0.66) suggesting that diagenetic fluid may have interacted with silicilastic components. (D) Crossplot of ∑REE−Ba values showing that none of the data from SR and PR has ∑REE−Ba correlation, suggesting that the diagenetic fluid is not from a hydrothermal source.

and Jacobsen, 1990). Positive Ce anomaly indicates anoxic depositions and is common in seep-derived limestones (Feng et al., 2010; Rongemaille et al., 2011). SR and PR samples show

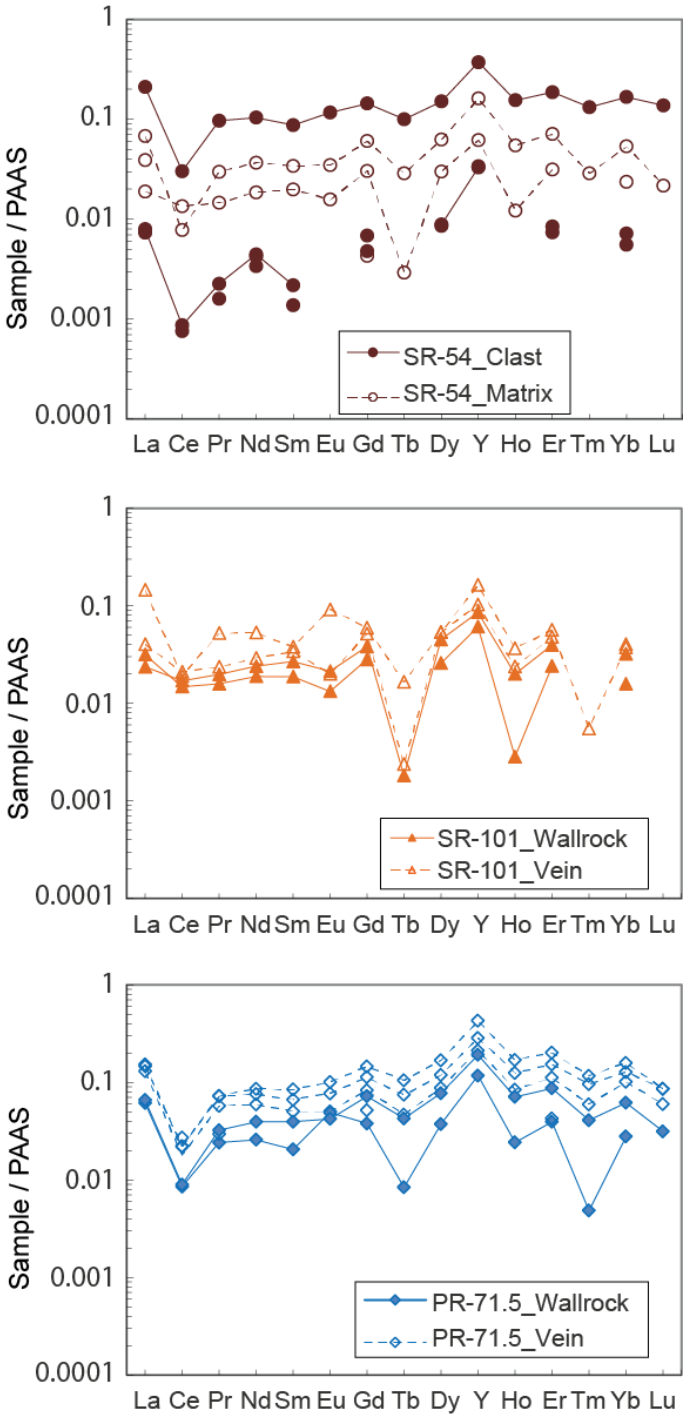

Fig. 8. PAAS normalized REE patterns from SR and PR block samples. All samples including wall rock, veins and matrix show similar REE patterns. These REE patterns are different from seawater and hydrothermal fluids, suggesting that these samples could have been altered by surficial waters.

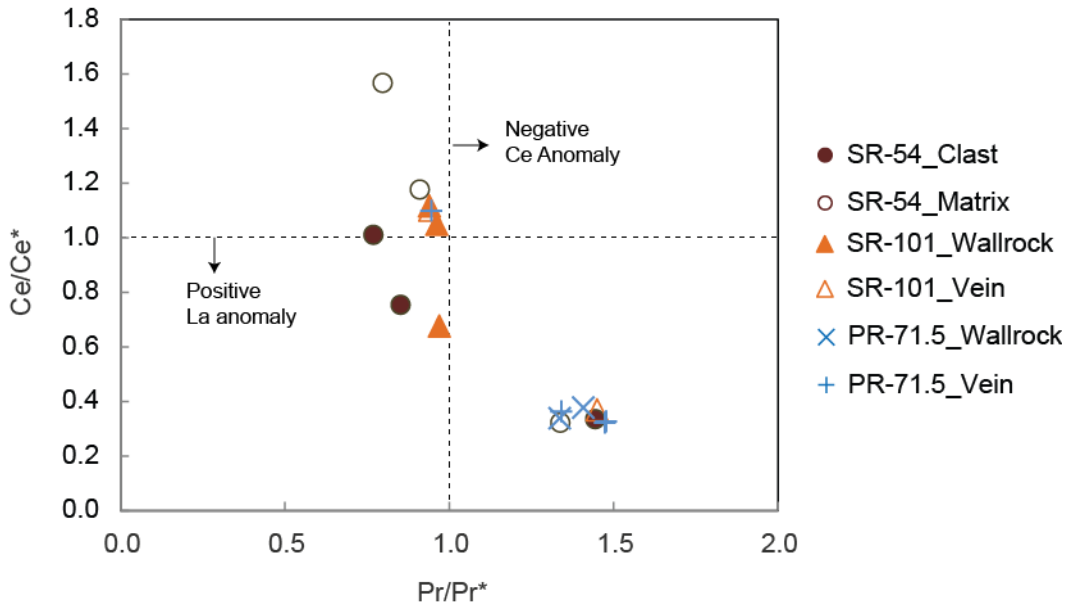

Fig. 9. Diagram showing determination of Ce and La anomalies (after Bau et al., 1997). Most SR samples show positive Ce anomaly, while PR samples have mostly negative Ce anomaly, suggesting two different diagenetic processes.

variable Ce anomalies (Fig. 9), among which most of the data from PR-71.5 show negative Ce anomaly, suggesting that there is an influence from oxic diagenetic fluid in shallower diagenetic environment. On the other hand, most of the data from SR samples show positive Ce anomaly, suggesting that these samples could have been recrystallized in anoxic conditions at depth.

***5.3.2. Europium anomaly*:** Positive europium (Eu) anomaly is the characteristics of highly reducing environment and/or hydrothermal fluid with temperature >200°C (Sverjensky, 1984; Bau, 1991; Bau et al., 2010; Allen and Seyfried, 2005). SR and PR samples do not show Eu anomaly and suggest that calcite precipitating temperature could be <200°C, providing an upper limit of the precipitating temperature (Fig. 8). This suggests neither hydrothermal origin nor strongly reducing conditions has occurred. Moreover, the Eu anomaly does not correlate with Ba (Fig. 7D) which also negates the hydrothermal origin for the diagenetic fluid.

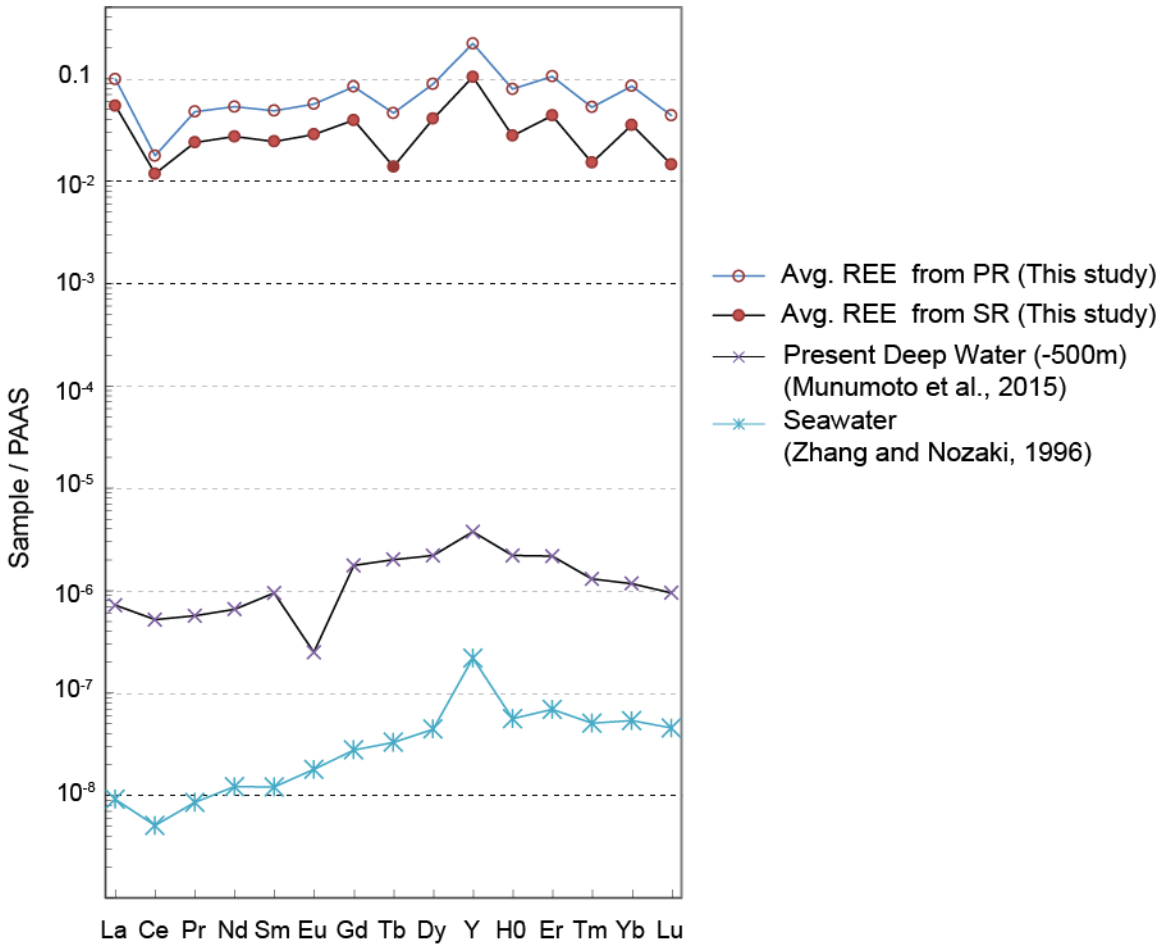

Fig. 10. Comparison of PAAS normalized REE abundances with that of modern seawater. REE values from SR and PR samples are averaged to their single pattern. Modern deep water are the average of 4 analyses from Munemoto et al. (2015) and modern seawater are from Zhang and Nozaki, (1996). REE patterns from this study are more flat than those of modern surface and deep waters, suggesting dominantly meteoric water influence.

5.4. Origin of diagenetic fluid and its climate implication

Studies have demonstrated that climate signal could have been preserved in the diagenetically altered rocks, especially by hyrothermal alteration (Blattner et al., 1997; Dallai et al., 2001; Bindeman and Serebryakov, 2011; Herwartz et al., 2015). Late Paleozoic climate shows significantly cooling and glaciation which has been imprinted in sedimentary sequences

(Fielding et al., 2008) and geochemical records (Buggisch et al., 2008). Soreghan et al. (2008) records sedimentary evidence of equatorial glaciation, i.e., glacial valley and diamictites, in the western Pangea during Permo-Carboniferous. Although the initiation of Carboniferous glaciation is speculative, the anomalous carbon and oxygen isotope records during Early Mississippian suggest that a significant cooling and glaciation could have been occurred during this time (Mii et al., 1999; Buggisch et al., 2008). If this is true, it is possible that the evidence of glaciation may have imprinted the geochemical records in the diagenetic environment. As mentioned earlier, Katz et al. (2006) has documented a significantly low $\delta^{18}O$ value down to –26.5‰ from Early Mississippian carbonates from Western US with a precipitating temperature of ~140°C and has suggested that the diagenetic fluid could have been originated from meteoric water circulation through depth. Similarly, Mathieu et al. (2015) showed the diagenetic imprint of Late Devonian meteoric waters in the Neoproterozoic and Cambro-Ordovician carbonates and also suggested that the meteoric waters interacted with phosphatic rock. These records indicate that the $\delta^{18}O$ values in diagenetic carbonates may have an implication to trace the source of diagenetic fluid during Late Paleozoic. If freshwater diagenesis had occurred below an unconformity and produced significantly low $\delta^{18}O$ value in sediments or rock, it would have recorded the climate signal from the time when the unconformity (exposure surface) was developed.

The SR-71.5 sample is precipitated from the diagenetic fluid with $\delta^{18}O$ composition of –7‰. We suggest that this diagenetic fluid would have been originated from meteoric water since its $\delta^{18}O$ composition is similar to present tropical meteoric waters (Bowen and Wilkinson, 2002). The minimum homonization temperature of 105–110°C recorded in calcite veins from PR-71.5 suggests that the meteoric water would have been heated at depth, migrated vertically by fault

and/or fractures and altered the PR sample. Because diagenesis occurred at moderate temperature, it produced large difference in $\delta^{18}O$ values between calcite veins and wallrock. Similar diagenetic patterns under similar temperature conditions have been recorded in diagenetic carbonates in Madison Formation (Katz et al., 2006).

The $\delta^{18}O$ values in SR samples are very low, down to –34‰. The REE patterns with no Eu anomaly and fluid inclusions with low salinity values suggest that the low $\delta^{18}O$ values are dominantly originated from freshwaters. The $\delta^{18}O$ values of the freshwater required to alter SR samples would be ≤ –15‰, which is only observed at high latitude (≥50° latitude) in modern meteoric water (Bowen and Wilkinson, 2002). Given that the North American continent was at the equatorial position during Early Mississippian, $\delta^{18}O$ value of –15‰ in this location would be possible only under glacial conditions since hydrothermal alteration was not supported by geochemical evidence mentioned earlier. The low $\delta^{18}O$ values in SR-101 and SR-54 samples have been documented close to or below the unconformity (Fig. 1B), suggesting that these low $\delta^{18}O$ values would have been preserved at the same time when the unconformities were developed. Under these conditions, it implies that glacial advance might have reached the low latitude during the Early Mississippian.

A study on meteoric diagenesis of Late Paleozoic and Mesozoic limestones suggests that altered $\delta^{18}O$ values below ancient exposure surfaces are more homogeneous and can be very low (Allan and Matthews, 1982). The SR-101 carbonates below the exposure surface would have modified by the glacial melt water with $\delta^{18}O$ values of –15‰ and subsequently calcite is precipitated in open cracks at karstic surface as calcite veins. The carbonates would have been buried to a sufficient depth, attained the geothermal temperature close to 200°C and

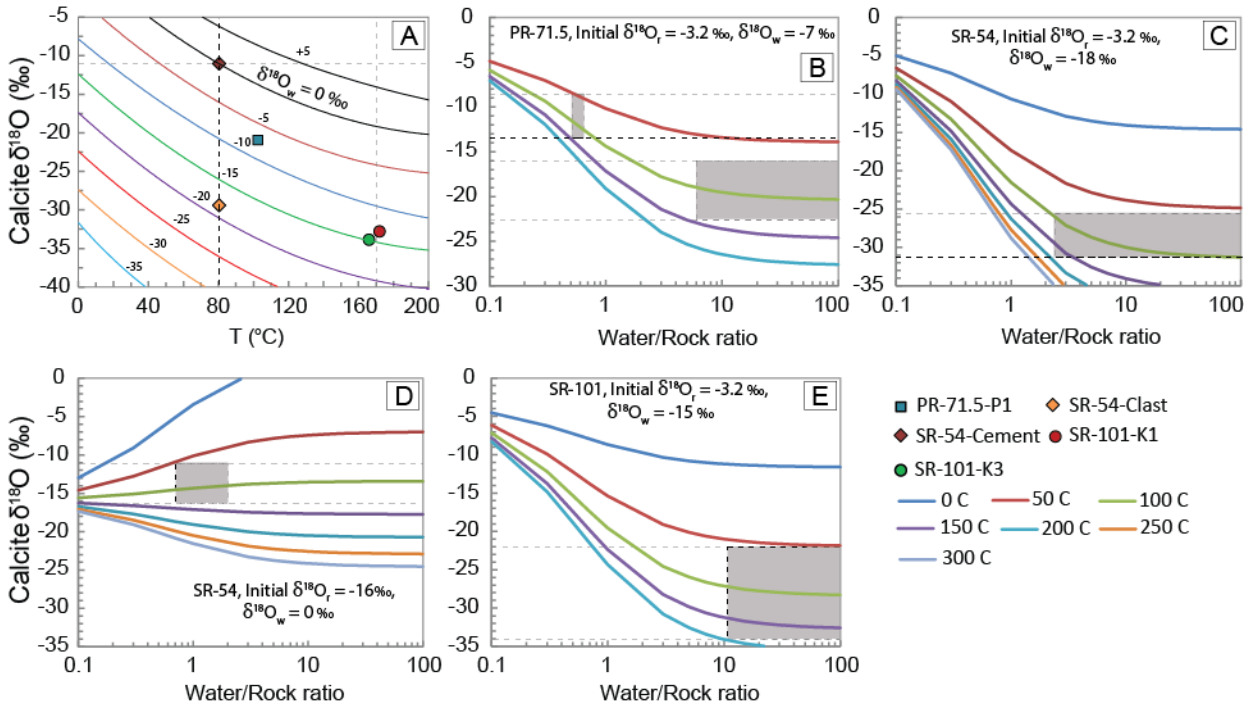

Fig. 11. Modeling results using $\delta^{18}O$ values and homonization temperatures from fluid inclusions (after, Jacobsen and Kaufman, 1999). (A) Prediction of $\delta^{18}O$ values of the diagenetic fluid; ≤ –15‰ for SR samples and –7‰ for PR-71.5. The lines with different colors indicate $\delta^{18}O$ values (VSMOW) of waters from which calcite precipitates at different temperature (after, O' Neil et al., 1969). (B) Determination of water/rock ratio for PR-71.5, considering an initial $\delta^{18}O_r$ value of –3.2‰ for the sample and diagenetic fluid $\delta^{18}O_w$ composition of –7‰. Higher water/rock ratio is required at the temperature range of 50–200°C to get the very low $\delta^{18}O$ values in calcite veins. (C), (D), (E) and (F) Prediction of water/rock ratio for SR-101 and SR-54 at different initial rock and fluid compositions (see text for details). Both samples show that higher water/rock ratio is required at the temperature range of 50–200°C to get the very low $\delta^{18}O$ values in calcite veins and/or wallrock.

recrystallized. The final recrystallization may have involved high water/rock ratio (>10) and the meteorically altered $\delta^{18}O$ values further decreases from –22.1 to –34‰ (Fig. 11E).

The diagenetic pattern in SR-54 is unique. Clasts (or wallrock) are very low in $\delta^{18}O$, as low as –31.3‰, lower than that of the matrix which is as high as –11.0‰, opposite to the pattern

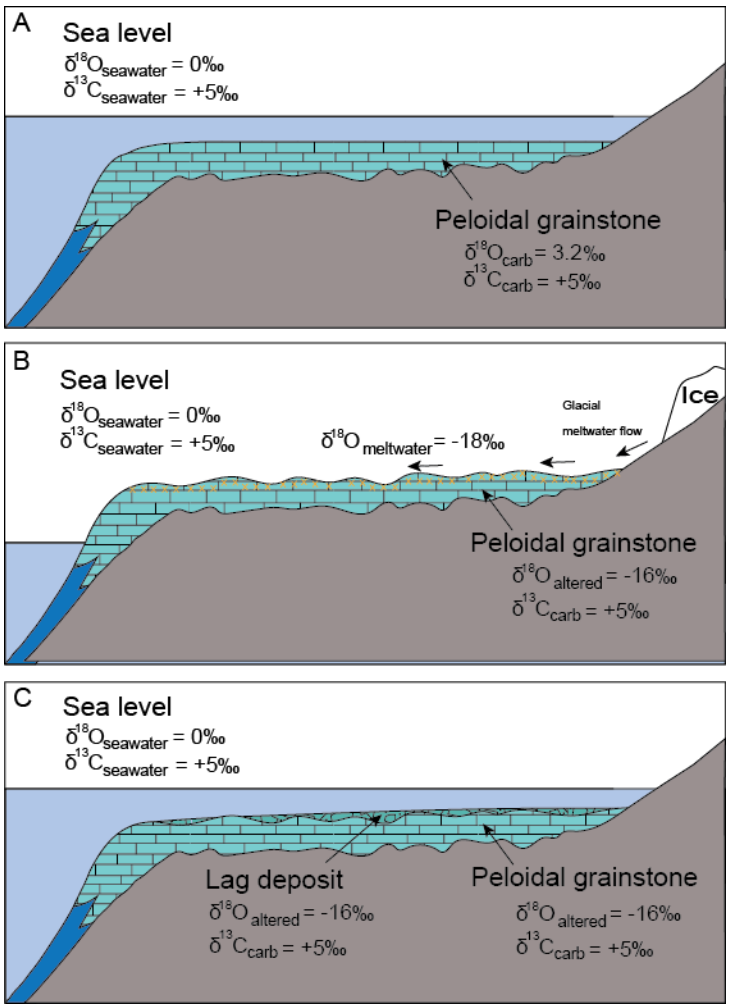

Fig. 12. A simple model showing the diagenetic processes for SR-54, which requires two different fluids, glacial meltwater and seawater. (A) Peloidal grainstone/packstone was deposited from shallow-water shelf environments. These rocks overlie the major unconformity between Devonian and Mississippian rocks. (B) The Early Mississippian glaciation would have lowered the sea level and the peloidal grainstone/packstone was exposed to subarieal weathering and alteration by glacial meltwater with $\delta^{18}O$ composition of –18‰. Below the exposure surface these rocks were altered to homogeneous $\delta^{18}O$ values of –18‰ in the vadose zone (Allan and Matthews, 1982) and brecciated. (C) Subsequent sea-level rise and transgression rework on previously exposed breccias, forming lag deposits along the exposure surface. After deep burial, isotopically mixed surface rock recrystallized at high burial temperature ≤200°C and altered the rock to very low $\delta^{18}O$ values down to –34‰. The temperature information is taken from fluid inclusions in SR-101.

seen in SR-101 and PR-71.5. Two processes would have involved in the SR-54 diagenesis: the alteration of marine carbonates below the unconformity by glacial melt water and subsequent modification by seawater (Fig. 12). Physical evidence of exposure and karstic breccia at this horizon supports this interpretation (Fig. 1B). However, it also requires further modification at burial temperature of ≤200°C. The maximum burial temperature that can alter seawater $\delta^{18}O$ value of 0‰ to –11.0 (i.e., the highest $\delta^{18}O$ value in SR-54) is ~80°C. With this burial temperature, the lowest $\delta^{18}O$ values of –31.3‰ in SR-54 can be achieved with initial glacial meltwater $\delta^{18}O$ value of –18‰ (Fig. 11A). Therefore, we assume that initial peloidal grainstone with $\delta^{18}O$ value of –3.2‰ could have been altered by glacial meltwater with $\delta^{18}O$ value of –18‰ (Figs. 11C; 12B). Then, it would have been further modified by seawater with $\delta^{18}O$ value of 0‰ (Fig. 11D; 12C). Subsequent burial at a higher depth with burial temperature between 50–200°C further modifies the $\delta^{18}O$ towards lower values.

6. Conclusion

Unusually low $\delta^{18}O$ values down to –34‰ (VPDB) are found in the Early Mississippian carbonates from the SR and PR sections. The REE, trace element, and fluid inclusion analyses of these isotopically light carbonates demonstrate that different digenetic fluids and processes have involved during the diagenesis. REE patterns are unlike seawater and hydrothermal fluids and their salinity of < 1.5 wt.% for SR samples suggest that freshwater was the dominant sources of diagenetic fluids. Moreover, the precipitating temperature range of 50°C-200°C for the SR and PR samples suggest that these samples may have been modified under geothermal conditions when they are buried to the sufficient depth.

Different diagenetic processes may have involved in SR and PR samples that produce different diagenetic patterns. Calcite veins from the fractured PR sample (PR-71.5) show $\delta^{18}O$

values as low as –22.7‰, which is ~8‰ lower than that of its wallrock. This diagenetic pattern and its minimum homogenization temperature of 105–110°C suggest that the PR-71.5 sample was altered by a fluid sourced from meteoric water with $\delta^{18}O$ value of –7‰ (VSMOW) which percolate down along fractures to greater depth, heated up by geothermal heat and migrated upward through the fault system. However, SR samples were initially altered at the exposure surfaces by glacial melt water with $\delta^{18}O$ value of ≤ –15‰ (VSMOW). Diagenetic pattern in SR-54, i.e., clasts are very low in $\delta^{18}O$ in compare to its matrix, suggesting that it has been further exposed to seawater diagenesis. Then, these SR samples are buried to the greater depth and recrystallized under geothermal temperature range of 50°C - 200°C. These different diagenetic processes and patterns in SR-101 and SR-54 samples leave very low $\delta^{18}O$ values down to –34‰. The SR samples preserve unique isotope signature of glacial meltwater, which suggests glacial advance to low latitude during the Early Mississippian.

Table 1A. Carbon and oxygen isotope data from the Early Mississippian carbonate succession in Star Range, Utah (GPS location: N 38 20' 53.6", W 113 08' 53")

Stratigraphic unit	Sample No.	Strat. Height (m)	Lithology	$\delta^{13}C$ (‰, VPDB)	$\delta^{18}O$ (‰,VPDB)	Conodont Zone	Notice
Crystal Pass Member	SR-0.15	0.15	Grainstone	0.07	-25.47	*Middle Pa. expansa*	Devonian
Crystal Pass Member	SR-1.8	1.8	Grainstone	0.90	-30.68	*Middle Pa. expansa*	Devonian
Crystal Pass Member	SR-4.15	4.15	Dolo-grainstone	0.73	-10.81	*Middle Pa. expansa*	Devonian
Crystal Pass Member	SR-5.4	5.4	Dolo-grainstone	1.00	-9.16	*Middle Pa. expansa*	Devonian
Crystal Pass Member	SR-7.6	7.6	Dolo-grainstone	0.97	-8.15	*Middle Pa. expansa*	Devonian
Crystal Pass Member	SR-9.2	9.2	Dolo-grainstone	0.73	-8.83	*Middle Pa. expansa*	Devonian
Crystal Pass Member	SR-11.9	11.9	Dolo-grainstone	0.94	-5.98	*Middle Pa. expansa*	Devonian
Crystal Pass Member	SR-13	13	Dolo-grainstone	1.21	-6.66	*Middle Pa. expansa*	Devonian
Crystal Pass Member	SR-14.3	14.3	Dolo-grainstone	1.07	-9.84	*Middle Pa. expansa*	Devonian
Crystal Pass Member	SR-16	16	Dolo-grainstone	0.27	-9.98	*Middle Pa. expansa*	Devonian
Crystal Pass Member	SR-18.5	18.5	Grainstone	1.42	-13.40	*Middle Pa. expansa*	Devonian
Crystal Pass Member	SR-20	20	Grainstone	0.87	-26.07	*Middle Pa. expansa*	Devonian
Crystal Pass Member	SR-21.5	21.5	Grainstone	0.99	-17.60	*Middle Pa. expansa*	Devonian
Crystal Pass Member	SR-22.8	22.8	Grainstone	1.00	-21.90	*Middle Pa. expansa*	Devonian
Crystal Pass Member	SR-25	25	Dolo-grainstone	1.21	-6.18	*Middle Pa. expansa*	Devonian
Crystal Pass Member	SR-25.7	25.7	Dolo-grainstone	1.34	-4.29	*Middle Pa. expansa*	Devonian
Crystal Pass Member	SR-27.8	27.8	Dolo-grainstone	1.45	-4.80	*Middle Pa. expansa*	Devonian
Crystal Pass Member	SR-29	29	Dolo-grainstone	1.10	-6.35	*Middle Pa. expansa*	Devonian
Crystal Pass Member	SR-30.5	30.5	Dolo-grainstone	1.56	-4.32	*Middle Pa. expansa*	Devonian
Crystal Pass Member	SR-31	31	Dolo-grainstone	1.17	-5.67	*Middle Pa. expansa*	Devonian
Crystal Pass Member	SR-32	32	Dolo-wackestone	1.14	-5.23	*Middle Pa. expansa*	Devonian
Crystal Pass Member	SR-34	34	Dolo-wackestone	1.75	-5.22	*Middle Pa. expansa*	Devonian
Crystal Pass Member	SR-36	36	Dolo-grainstone	1.22	-6.05	*Middle Pa. expansa*	Devonian
Crystal Pass Member	SR-37.5	37.5	Dolo-grainstone	1.55	-8.97	*Middle Pa. expansa*	Devonian
Crystal Pass Member	SR-39	39	Dolo-grainstone	1.97	-6.97	*Middle Pa. expansa*	Devonian
Crystal Pass Member	SR-41	41	Dolo-grainstone	1.69	-7.15	*Middle Pa. expansa*	Devonian
Crystal Pass Member	SR-43	43	Dolo-grainstone	2.01	-5.51	*Middle Pa. expansa*	Devonian
Crystal Pass Member	SR-44.5	44.5	Dolo-grainstone	2.02	-5.76	*Middle Pa. expansa*	Devonian
Crystal Pass Member	SR-46	46	Dolo-grainstone	1.91	-7.28	*Middle Pa. expansa*	Devonian
Crystal Pass Member	SR-48	48	Wackestone	0.37	-29.20	*Middle Pa. expansa*	Devonian
Monte Cristo Limestone	SR-50	50	Dolo-grainstone	4.90	-7.72	*Lower typicus*	Osagean
Monte Cristo Limestone	SR-50.2	50.2	Wackestone	4.26	-31.42	*Lower typicus*	Osagean
Monte Cristo Limestone	SR-51.1	51.1	Wackestone	5.51	-23.79	*Lower typicus*	Osagean
Monte Cristo Limestone	SR-51.3	51.3	Wackestone	5.84	-8.09	*Lower typicus*	Osagean
Monte Cristo Limestone	SR-51.6	51.6	Grainstone	5.85	-5.29	*Lower typicus*	Osagean
Monte Cristo Limestone	SR-51.9	51.9	Grainstone	6.03	-28.13	*Lower typicus*	Osagean
Monte Cristo Limestone	SR-52	52	Grainstone	6.44	-15.08	*Lower typicus*	Osagean
Monte Cristo Limestone	SR-52.2	52.2	Grainstone	6.02	-28.43	*Lower typicus*	Osagean
Monte Cristo Limestone	SR-52.5	52.5	Grainstone	5.57	-26.25	*Lower typicus*	Osagean
Monte Cristo Limestone	SR-52.8	52.8	Grainstone	5.70	-26.89	*Lower typicus*	Osagean
Monte Cristo Limestone	SR-53	53	Grainstone	5.60	-25.36	*Lower typicus*	Osagean
Monte Cristo Limestone	SR-53.4	53.4	Grainstone	5.47	-29.43	*Lower typicus*	Osagean
Monte Cristo Limestone	SR-53.7	53.7	Grainstone	5.39	-31.13	*Lower typicus*	Osagean

Monte Cristo Limestone	SR-53.9	53.9	Grainstone	4.94	-29.26	*Lower typicus*	Osagean
Monte Cristo Limestone	SR-54	54	Grainstone	4.77	-29.88	*Lower typicus*	Osagean
Monte Cristo Limestone	SR-56	56	Grainstone	4.64	-21.43	*Lower typicus*	Osagean
Monte Cristo Limestone	SR-58	58	Grainstone	4.67	-28.66	*Lower typicus*	Osagean
Monte Cristo Limestone	SR-59	59	Dolo-grainstone	3.47	-8.51	*Lower typicus*	Osagean
Monte Cristo Limestone	SR-59.7	59.7	Dolo-grainstone	3.91	-9.56	*Lower typicus*	Osagean
Monte Cristo Limestone	SR-60.5	60.5	Dolo-grainstone	2.86	-9.47	*Lower typicus*	Osagean
Monte Cristo Limestone	SR-62	62	Dolo-grainstone	4.93	-7.98	*Lower typicus*	Osagean
Monte Cristo Limestone	SR-64	64	Dolo-grainstone	5.18	-6.53	*Lower typicus*	Osagean
Monte Cristo Limestone	SR-65.5	65.5	Dolo-grainstone	5.34	-6.31	*Lower typicus*	Osagean
Monte Cristo Limestone	SR-67	67	Dolo-grainstone	3.83	-7.69	*Lower typicus*	Osagean
Monte Cristo Limestone	SR-69	69	Dolo-grainstone	4.04	-7.34	*Lower typicus*	Osagean
Monte Cristo Limestone	SR-71	71	Dolo-grainstone	3.47	-8.13	*Lower typicus*	Osagean
Monte Cristo Limestone	SR-73	73	Dolo-grainstone	4.12	-6.36	*Lower typicus*	Osagean
Monte Cristo Limestone	SR-74.5	74.5	Dolo-grainstone	3.27	-5.97	*Lower typicus*	Osagean
Monte Cristo Limestone	SR-76	76	Dolo-grainstone	2.92	-6.82	*Lower typicus*	Osagean
Monte Cristo Limestone	SR-78	78	Dolo-grainstone	1.90	-8.57	*Lower typicus*	Osagean
Monte Cristo Limestone	SR-79.5	79.5	Dolo-grainstone	3.29	-5.45	*Lower typicus*	Osagean
Monte Cristo Limestone	SR-81.5	81.5	Dolo-grainstone	2.49	-5.98	*Lower typicus*	Osagean
Monte Cristo Limestone	SR-83	83	Dolo-grainstone	1.06	-7.62	*Lower typicus*	Osagean
Monte Cristo Limestone	SR-85	85	Dolo-grainstone	2.67	-4.49	*Lower typicus*	Osagean
Monte Cristo Limestone	SR-87	87	Dolo-grainstone	2.32	-6.11	*Lower typicus*	Osagean
Monte Cristo Limestone	SR-89	89	Dolo-grainstone	2.77	-6.98	*Lower typicus*	Osagean
Monte Cristo Limestone	SR-91	91	Wackestone	2.32	-33.30	*Lower typicus*	Osagean
Monte Cristo Limestone	SR-93	93	Wackestone	2.28	-32.71	*Lower typicus*	Osagean
Monte Cristo Limestone	SR-94.5	94.5	Wackestone	1.72	-33.39	*Lower typicus*	Osagean
Monte Cristo Limestone	SR-96	96	Grainstone	1.11	-28.52	*Lower typicus*	Osagean
Monte Cristo Limestone	SR-98	98	Wackestone	1.35	-31.62	*?*	Osagean
Monte Cristo Limestone	SR-100	100	Wackestone	-0.02	-32.23	*?*	Osagean
Monte Cristo Limestone	SR-102	102	Wackestone	-0.94	-33.08	*?*	Osagean
Monte Cristo Limestone	SR-104	104	Wackestone	-0.23	-18.14	*?*	Osagean
Monte Cristo Limestone	SR-105.5	105.5	Wackestone	-0.24	-25.95	*?*	Osagean
Monte Cristo Limestone	SR-106.5	106.5	Wackestone	0.13	-24.91	*?*	Osagean
Monte Cristo Limestone	SR-108	108	Wackestone	-0.24	-21.77	*Upper typicus*	Osagean
Monte Cristo Limestone	SR-110	110	Wackestone	1.48	-18.92	*Upper typicus*	Osagean
Monte Cristo Limestone	SR-111	111	Dolo-wackestone	0.49	-4.25	*Upper typicus*	Osagean
Monte Cristo Limestone	SR-112.5	112.5	Dolo-wackestone	0.27	-3.43	*Upper typicus*	Osagean
Monte Cristo Limestone	SR-114	114	Packstone	0.12	-19.17	*Upper typicus*	Osagean
Monte Cristo Limestone	SR-115.5	115.5	Packstone	0.60	-23.41	*Upper typicus*	Osagean
Monte Cristo Limestone	SR-117	117	Dolo-grainstone	1.40	-3.72	*Upper typicus*	Osagean
Monte Cristo Limestone	SR-118	118	Dolo-grainstone	1.50	-5.87	*Upper typicus*	Osagean
Monte Cristo Limestone	SR-121.5	121.5	Dolo-grainstone	1.54	-5.81	*Upper typicus*	Osagean
Monte Cristo Limestone	SR-123.5	123.5	Dolo-grainstone	1.32	-6.11	*Upper typicus*	Osagean
Monte Cristo Limestone	SR-126	126	Dolo-grainstone	1.30	-5.46	*Upper typicus*	Osagean
Monte Cristo Limestone	SR-128	128	Dolo-grainstone	0.97	-4.81	*Upper typicus*	Osagean
Monte Cristo Limestone	SR-130	130	Dolo-wackestone	1.09	-3.23	*Upper typicus*	Osagean
Monte Cristo Limestone	SR-134	134	Dolo-grainstone	1.37	-3.24	*Upper typicus*	Osagean
Monte Cristo Limestone	SR-136	136	Dolo-grainstone	0.76	-4.34	*Upper typicus*	Osagean
Monte Cristo Limestone	SR-138	138	Dolo-grainstone	1.37	-3.28	*Upper typicus*	Osagean

Monte Cristo Limestone	SR-139.5	139.5	Dolo-grainstone	0.74	-3.43	*Upper typicus*	Osagean
Monte Cristo Limestone	SR-141.7	141.7	Dolo-grainstone	0.77	-3.44	*Upper typicus*	Osagean
Monte Cristo Limestone	SR-143.7	143.7	Dolo-grainstone	0.48	-3.56	*Upper typicus*	Osagean
Monte Cristo Limestone	SR-145.7	145.7	Dolo-grainstone	0.07	-6.85	*Upper typicus*	Osagean
Monte Cristo Limestone	SR-150	150	Dolo-micrite	0.973	-5.222	*Upper typicus*	Osagean

Table 1B. Carbon and oxygen isotope data from the Early Mississippian carbonate succession in Pahranagat Range, Nevada (GPS locaton: 37 23' 42.94" N, 115 15' 43.30" W)

Stratigraphic unit	Sample No.	Strat. Height (m)	Lithology	$\delta^{13}C$ (‰, VPDB)	$\delta^{18}O$ (‰,VPDB)	Conodont Zone	Notice
Pilot Shale	AL - 0.3	0.30	Shaley Lime-Mudston	-0.21	-6.45		Devonian
Pilot Shale	AL - 1.4	1.40	Shaley Lime-Mudston	-0.17	-6.73		Devonian
Pilot Shale	AL - 2.05	2.05	Wackestone	-0.13	-6.40		Devonian
Pilot Shale	AL - 6.0	6.00	Grainstone	-0.60	-5.93		Devonian
Pilot Shale	AL - 7.1	7.10	Grainstone	0.15	-5.19		Devonian
Pilot Shale	AL - 8.1	8.10	Wackestone	-0.60	-5.73		Devonian
Pilot Shale	AL - 9	9.00	Wackestone	-0.30	-5.50		Devonian
Joana Limestone	AL - 16.8	16.80	Grainstone	1.34	-5.22		Early Mississippian
Joana Limestone	AL - 18.8	18.80	Grainstone	1.86	-5.04		Early Mississippian
Joana Limestone	AL - 24	24.00	Packstone	2.02	-4.31		Early Mississippian
Joana Limestone	AL - 25.6	25.60	Grainstone	2.51	-4.27		Early Mississippian
Joana Limestone	AL - 29.8	29.80	Grainstone	2.59	-4.19		Early Mississippian
Joana Limestone	AL - 31.2	31.20	Grainstone	2.59	-4.13		Early Mississippian
Joana Limestone	AL - 34	34.00	Grainstone	2.26	-4.41		Early Mississippian
Joana Limestone	AL - 37.2	37.20	Grainstone	2.33	-5.94	*S. isosticha*	Early Mississippian
Joana Limestone	AL - 42	42.00	Grainstone	2.02	-5.65	*S. isosticha*	Early Mississippian
Joana Limestone	AL - 47.9	47.90	Packstone	2.51	-5.27	*S. isosticha*	Early Mississippian
Joana Limestone	AL - 52	52.00	Grainstone	2.48	-5.40	*S. isosticha*	Early Mississippian
Joana Limestone	AL - 53.8	53.80	Grainstone	2.32	-6.78	*S. isosticha*	Early Mississippian
Joana Limestone	Al_58	58	Wackestone	2.37	-9.33	*S. isosticha*	Early Mississippian
Joana Limestone	AL - 58.05	58.05	Grainstone	2.53	-5.57	*S. isosticha*	Early Mississippian
Joana Limestone	Al_58.5	58.5	Wackestone	2.36	-6.06	*S. isosticha*	Early Mississippian
Joana Limestone	Al_58.8	58.8	Wackestone	2.38	-5.88	*S. isosticha*	Early Mississippian
Joana Limestone	Al_59	59	Wackestone	2.26	-7.17	*S. isosticha*	Early Mississippian
Joana Limestone	Al_59.3	59.3	Wackestone	2.23	-5.52	*S. isosticha*	Early Mississippian
Joana Limestone	Al_59.6	59.6	Wackestone	2.29	-14.79	*S. isosticha*	Early Mississippian
Joana Limestone	Al_60.1	60.1	Wackestone	1.64	-11.02	*S. isosticha*	Early Mississippian
Joana Limestone	Al_60.5	60.5	Wackestone	2.23	-12.62	*S. isosticha*	Early Mississippian
Joana Limestone	Al_60.8	60.8	Wackestone	1.82	-10.84	*S. isosticha*	Early Mississippian
Joana Limestone	AL - 61	61.00	Packstone	3.25	-7.81	*S. isosticha*	Early Mississippian
Joana Limestone	Al_61	61	Wackestone	-0.83	-12.49	*S. isosticha*	Early Mississippian
Joana Limestone	Al_61.4	61.4	Wackestone	1.59	-12.81	*S. isosticha*	Early Mississippian
Joana Limestone	Al_61.8	61.8	Wackestone	3.05	-9.84	*S. isosticha*	Early Mississippian
Joana Limestone	Al_62	62	Wackestone	1.41	-11.67	*S. isosticha*	Early Mississippian
Joana Limestone	Al_62.3	62.3	Wackestone	1.16	-12.18	*S. isosticha*	Early Mississippian
Joana Limestone	Al_62.7	62.7	Wackestone	2.45	-12.71	*S. isosticha*	Early Mississippian
Joana Limestone	Al_63	63	Wackestone	2.31	-9.91	*S. isosticha*	Early Mississippian
Joana Limestone	AL63	63	Wackestone	2.21	-10.14	*S. isosticha*	Early Mississippian
Joana Limestone	Al_63.3	63.3	Wackestone	1.20	-11.72	*S. isosticha*	Early Mississippian
Joana Limestone	AL63.3	63.3	Wackestone	1.15	-11.67	*S. isosticha*	Early Mississippian
Joana Limestone	Al_63.5	63.5	Wackestone	1.89	-13.53	*S. isosticha*	Early Mississippian
Joana Limestone	AL63.5	63.5	Wackestone	2.17	-13.78	*S. isosticha*	Early Mississippian
Joana Limestone	AL - 64	64.00	Grainstone	1.49	-11.76	*S. isosticha*	Early Mississippian

Joana Limestone	Al_64	64	Wackestone	2.10	-11.38	*S. isosticha*	Early Mississippian
Joana Limestone	AL64	64	Wackestone	2.18	-11.08	*S. isosticha*	Early Mississippian
Joana Limestone	Al_64.5	64.5	Wackestone	2.20	-10.01	*S. isosticha*	Early Mississippian
Joana Limestone	AL64.5	64.5	Wackestone	-0.28	-14.37	*S. isosticha*	Early Mississippian
Joana Limestone	Al_65	65	Wackestone	4.86	-4.53	*S. isosticha*	Early Mississippian
Joana Limestone	AL65	65	Wackestone	5.05	-4.37	*S. isosticha*	Early Mississippian
Joana Limestone	AL65.5	65.5	Wackestone	2.76	-13.14	*S. isosticha*	Early Mississippian
Joana Limestone	AL65.8	65.8	Wackestone	2.59	-14.99	*S. isosticha*	Early Mississippian
Joana Limestone	AL66	66	Wackestone	2.72	-13.74	*S. isosticha*	Early Mississippian
Joana Limestone	AL66.4	66.4	Wackestone	2.52	-16.84	*S. isosticha*	Early Mississippian
Joana Limestone	AL66.8	66.8	Wackestone	1.40	-12.44	*S. isosticha*	Early Mississippian
Joana Limestone	AL - 66.9	66.90	Grainstone	2.92	-11.68	*S. isosticha*	Early Mississippian
Joana Limestone	AL67	67	Wackestone	2.68	-10.63	*S. isosticha*	Early Mississippian
Joana Limestone	AL67.6	67.6	Wackestone	2.65	-9.49	*S. isosticha*	Early Mississippian
Joana Limestone	AL67.9	67.9	Wackestone	2.59	-12.65	*S. isosticha*	Early Mississippian
Joana Limestone	AL68.2	68.2	Wackestone	1.98	-10.94	*S. isosticha*	Early Mississippian
Joana Limestone	AL68.6	68.6	Wackestone	2.40	-12.87	*S. isosticha*	Early Mississippian
Joana Limestone	AL68.9	68.9	Wackestone	2.79	-12.37	*S. isosticha*	Early Mississippian
Joana Limestone	AL69.1	69.1	Wackestone	3.01	-10.97	*S. isosticha*	Early Mississippian
Joana Limestone	Al_69.7	69.7	Wackestone	2.23	-13.89	*S. isosticha*	Early Mississippian
Joana Limestone	AL69.7	69.7	Wackestone	3.74	-10.03	*S. isosticha*	Early Mississippian
Joana Limestone	AL69.9	69.9	Wackestone	1.14	-16.55	*S. isosticha*	Early Mississippian
Joana Limestone	AL - 70.2	70.20	Packstone	2.34	-19.18	*S. isosticha*	Early Mississippian
Joana Limestone	Al_70.2	70.2	Wackestone	2.45	-15.52	*S. isosticha*	Early Mississippian
Joana Limestone	AL70.2	70.2	Wackestone	2.50	-15.42	*S. isosticha*	Early Mississippian
Joana Limestone	Al_70.3	70.3	Wackestone	2.41	-16.63	*S. isosticha*	Early Mississippian
Joana Limestone	AL70.3	70.3	Wackestone	2.60	-16.61	*S. isosticha*	Early Mississippian
Joana Limestone	Al_70.9	70.9	Wackestone	2.22	-12.98	*S. isosticha*	Early Mississippian
Joana Limestone	AL70.9	70.9	Wackestone	2.43	-12.40	*S. isosticha*	Early Mississippian
Joana Limestone	Al_71.2	71.2	Wackestone	2.38	-12.45	*S. isosticha*	Early Mississippian
Joana Limestone	AL71.2	71.2	Wackestone	2.38	-12.64	*S. isosticha*	Early Mississippian
Joana Limestone	Al_71.5	71.5	Wackestone	2.74	-9.87	*S. isosticha*	Early Mississippian
Joana Limestone	AL71.5	71.5	Wackestone	2.76	-10.09	*S. isosticha*	Early Mississippian
Joana Limestone	Al_72	72	Wackestone	2.21	-13.42	*S. isosticha*	Early Mississippian
Joana Limestone	AL72	72	Wackestone	2.32	-13.54	*S. isosticha*	Early Mississippian
Joana Limestone	AL72.4	72.4	Wackestone	-2.72	-13.01	*S. isosticha*	Early Mississippian
Joana Limestone	AL - 72.8	72.80	Wackestone	2.74	-10.25	*S. isosticha*	Early Mississippian
Joana Limestone	Al_72.8	72.8	Wackestone	5.12	-3.71	*S. isosticha*	Early Mississippian
Joana Limestone	Al_73	73	Wackestone	3.73	-5.25	*S. isosticha*	Early Mississippian
Joana Limestone	Al_73.4	73.4	Wackestone	2.42	-11.84	*S. isosticha*	Early Mississippian
Joana Limestone	Al_73.8	73.8	Wackestone	2.88	-11.19	*S. isosticha*	Early Mississippian
Joana Limestone	Al_74.1	74.1	Wackestone	1.36	-11.57	*S. isosticha*	Early Mississippian
Joana Limestone	Al_74.5	74.5	Wackestone	-0.91	-11.91	*S. isosticha*	Early Mississippian
Joana Limestone	Al_74.8	74.8	Wackestone	2.94	-5.54	*S. isosticha*	Early Mississippian
Joana Limestone	Al_75	75	Wackestone	0.89	-11.97	*S. isosticha*	Early Mississippian
Joana Limestone	Al_75.6	75.6	Wackestone	1.94	-9.39	*S. isosticha*	Early Mississippian
Joana Limestone	Al_76	76	Wackestone	2.28	-6.84	*S. isosticha*	Early Mississippian
Joana Limestone	AL - 76.1	76.10	Wackestone	2.64	-9.00	*S. isosticha*	Early Mississippian
Joana Limestone	AL_77	77	Wackestone	2.58	-11.22	*S. isosticha*	Early Mississippian

Joana Limestone	AL_77.3	77.3	Wackestone	2.48	-6.19	*S. isosticha*	Early Mississippian
Joana Limestone	Al_77.8	77.8	Wackestone	2.92	-6.08	*S. isosticha*	Early Mississippian
Joana Limestone	Al_78.0	78	Wackestone	0.86	-8.34	*S. isosticha*	Early Mississippian
Joana Limestone	Al_78.3	78.3	Wackestone	2.95	-6.43	*S. isosticha*	Early Mississippian
Joana Limestone	Al_78.9	78.9	Wackestone	2.95	-5.32	*S. isosticha*	Early Mississippian
Joana Limestone	Al_79.1	79.1	Wackestone	2.91	-6.68	*S. isosticha*	Early Mississippian
Joana Limestone	Al_79.1	79.1	Wackestone	2.85	-6.83	*S. isosticha*	Early Mississippian
Joana Limestone	Al_79.5	79.5	Wackestone	2.77	-6.65	*S. isosticha*	Early Mississippian
Joana Limestone	Al_80.0	80	Wackestone	2.93	-5.19	*S. isosticha*	Early Mississippian
Joana Limestone	Al_80.4	80.4	Wackestone	2.48	-6.32	*S. isosticha*	Early Mississippian
Joana Limestone	Al_80.8	80.8	Wackestone	3.11	-5.59	*S. isosticha*	Early Mississippian
Joana Limestone	Al_81.0	81	Wackestone	3.09	-5.09	*S. isosticha*	Early Mississippian
Joana Limestone	Al_81.3	81.3	Wackestone	2.74	-5.46	*S. isosticha*	Early Mississippian
Joana Limestone	Al_81.7	81.7	Wackestone	2.89	-5.86	*S. isosticha*	Early Mississippian
Joana Limestone	Al_82.0	82	Wackestone	2.97	-5.24	*S. isosticha*	Early Mississippian
Joana Limestone	AL - 82.2	82.20	Wackestone	2.99	-5.47	*S. isosticha*	Early Mississippian
Joana Limestone	Al_82.3	82.3	Wackestone	2.98	-5.77	*S. isosticha*	Early Mississippian
Joana Limestone	AL_82.7	82.7	Wackestone	2.95	-5.18	*S. isosticha*	Early Mississippian
Joana Limestone	Al_83.0	83	Wackestone	2.91	-4.84	*S. isosticha*	Early Mississippian
Joana Limestone	AL - 84.7	84.70	Packstone	3.18	-4.87	*S. isosticha*	Early Mississippian
Joana Limestone	AL - 88	88.00	Packstone	2.68	-6.04	*S. isosticha*	Early Mississippian
Joana Limestone	AL - 91.6	91.60	Packstone	4.65	-0.92	*S. isosticha*	Early Mississippian
Joana Limestone	AL - 93.8	93.80	Packstone	4.11	-4.02	*S. isosticha*	Early Mississippian
Joana Limestone	AL - 97.3	97.30	Wackestone	4.53	-3.78	*S. isosticha*	Early Mississippian
Joana Limestone	AL - 100.3	100.30	Wackestone	5.18	-3.30	*S. isosticha*	Early Mississippian
Joana Limestone	AL - 103	103.00	Wackestone	4.88	-4.33	*S. isosticha*	Early Mississippian
Joana Limestone	AL - 105	105.00	Wackestone	4.61	-3.90	*S. isosticha*	Early Mississippian
Joana Limestone	AL - 106.6	106.60	Wackestone	5.95	-3.22	*S. isosticha*	Early Mississippian
Joana Limestone	AL - 108	108.00	Wackestone	6.42	-3.54	*S. isosticha*	Early Mississippian

Note: Parts of the data has been taken from Henry (2011)

Table 1C. Carbon and oxygen isotope data from block samples from Early Mississippian carbonates.
Section 1: Star Range section, Utah (GPS location: N 38 20' 53.6", W 113 08' 53")

Stratigraphic unit	Sample No.	Points on the Block	Strat. Height, m	Lithology	$\delta^{13}C$ (‰,VPDB)	$\delta^{18}O$(‰, VPDB)	Notice
Monte Cristo Limestone	SR54	SR54-Cr1	54	Coral	2.11	-24.76	Osagean
Monte Cristo Limestone	SR54	SR54-Cr2	54	Coral	2.10	-16.27	Osagean
Monte Cristo Limestone	SR54	SR-54_Cr3	54	Coral	2.34	-13.82	Osagean
Monte Cristo Limestone	SR54	SR-54_Cr4	54	Coral	3.29	-14.19	Osagean
Monte Cristo Limestone	SR54	SR-54_Cr5	54	Coral	2.11	-23.66	Osagean
Monte Cristo Limestone	SR54	SR-54_Cr6	54	Coral	4.20	-11.03	Osagean
Monte Cristo Limestone	SR54	SR54-M1	54	Matrix	4.91	-27.80	Osagean
Monte Cristo Limestone	SR54	SR54-M2	54	Matrix	4.78	-24.63	Osagean
Monte Cristo Limestone	SR54	SR54-M3	54	Matrix	4.87	-25.83	Osagean
Monte Cristo Limestone	SR54	SR54-M4	54	Matrix	4.91	-26.11	Osagean
Monte Cristo Limestone	SR54	SR54-M5	54	Matrix	4.87	-20.62	Osagean
Monte Cristo Limestone	SR54	SR54-M6	54	Matrix	4.93	-25.10	Osagean
Monte Cristo Limestone	SR54	SR54-M7	54	Matrix	4.92	-24.88	Osagean
Monte Cristo Limestone	SR54	SR-54_M8	54	Matrix	5.0	-25.9	Osagean
Monte Cristo Limestone	SR54	SR-54_M9	54	Matrix	5.2	-28.5	Osagean
Monte Cristo Limestone	SR54	SR-54_M10	54	Matrix	5.0	-30.5	Osagean
Monte Cristo Limestone	SR54	SR-54_M11	54	Matrix	5.1	-28.2	Osagean
Monte Cristo Limestone	SR54	SR-54_M12	54	Matrix	5.0	-28.0	Osagean
Monte Cristo Limestone	SR54	SR-54_M13	54	Matrix	5.0	-18.8	Osagean
Monte Cristo Limestone	SR54	SR-54_M14	54	Matrix	5.42	-12.39	Osagean
Monte Cristo Limestone	SR54	SR-54_M15	54	Matrix	4.76	-21.81	Osagean
Monte Cristo Limestone	SR54	SR54-C1	54	Peloidal grainstone clast	4.86	-25.47	Osagean
Monte Cristo Limestone	SR54	SR54-C2	54	Peloidal grainstone clast	5.33	-31.07	Osagean
Monte Cristo Limestone	SR54	SR54-C3	54	Peloidal grainstone clast	5.37	-30.81	Osagean
Monte Cristo Limestone	SR54	SR54-C4	54	Peloidal grainstone clast	4.97	-28.50	Osagean
Monte Cristo Limestone	SR54	SR54-C5	54	Peloidal grainstone clast	5.22	-30.93	Osagean
Monte Cristo Limestone	SR54	SR54-C6	54	Peloidal grainstone clast	5.37	-29.22	Osagean
Monte Cristo Limestone	SR54	SR54-C7	54	Peloidal grainstone clast	5.09	-29.84	Osagean
Monte Cristo Limestone	SR54	SR54-C8	54	Peloidal grainstone clast	5.16	-31.02	Osagean
Monte Cristo Limestone	SR54	SR54-C9	54	Peloidal grainstone clast	5.34	-29.25	Osagean
Monte Cristo Limestone	SR54	SR54-C10	54	Peloidal grainstone clast	5.17	-29.19	Osagean
Monte Cristo Limestone	SR54	SR54-C11	54	Peloidal grainstone clast	5.26	-28.77	Osagean
Monte Cristo Limestone	SR54	SR54-C12	54	Peloidal grainstone clast	5.44	-29.76	Osagean
Monte Cristo Limestone	SR54	SR-54_C13	54	Peloidal grainstone clast	5.41	-30.43	Osagean
Monte Cristo Limestone	SR54	SR-54_C14	54	Peloidal grainstone clast	5.29	-31.28	Osagean
Monte Cristo Limestone	SR54	SR-54_C15	54	Peloidal grainstone clast	5.12	-29.62	Osagean
Monte Cristo Limestone	SR54	SR-54_C16	54	Peloidal grainstone clast	4.98	-27.68	Osagean
Monte Cristo Limestone	SR54	SR-54_C17	54	Peloidal grainstone clast	4.86	-27.14	Osagean
Monte Cristo Limestone	SR-101	SR-101_V1	101	Calcite vein	-3.0	-25.0	Osagean
Monte Cristo Limestone	SR-101	SR-101_V2	101	Calcite vein	-2.8	-32.8	Osagean
Monte Cristo Limestone	SR-101	SR-101_V2a	101	Calcite vein	-2.33	-33.35	Osagean
Monte Cristo Limestone	SR-101	SR-101_V3	101	Calcite vein	-3.5	-30.8	Osagean
Monte Cristo Limestone	SR-101	SR-101_V4	101	Calcite vein	-2.8	-31.1	Osagean

Monte Cristo Limestone	SR-101	SR-101_V5	101	Calcite vein	-3.0	-34.0	Osagean
Monte Cristo Limestone	SR-101	SR-101_V5a	101	Calcite vein	-2.88	-33.77	Osagean
Monte Cristo Limestone	SR-101	SR-101_V6	101	Calcite vein	-1.9	-26.6	Osagean
Monte Cristo Limestone	SR-101	SR-101_V7	101	Calcite vein	-2.4	-27.5	Osagean
Monte Cristo Limestone	SR-101	SR-101_V8	101	Calcite vein	0.1	-29.1	Osagean
Monte Cristo Limestone	SR-101	SR-101_V9	101	Calcite vein	-2.2	-33.5	Osagean
Monte Cristo Limestone	SR-101	SR-101_V10	101	Calcite vein	-0.4	-28.3	Osagean
Monte Cristo Limestone	SR-101	SR-101_V11	101	Calcite vein	-0.2	-28.1	Osagean
Monte Cristo Limestone	SR-101	SR-101_V12	101	Calcite vein	0.3	-22.1	Osagean
Monte Cristo Limestone	SR-101	SR-101_V13	101	Calcite vein	-0.5	-25.7	Osagean
Monte Cristo Limestone	SR-101	SR-101_V14	101	Calcite vein	-0.2	-23.3	Osagean
Monte Cristo Limestone	SR-101	SR-101_V15	101	Calcite vein	-2.3	-27.7	Osagean
Monte Cristo Limestone	SR-101	SR-101_V16	101	Calcite vein	-2.9	-24.7	Osagean
Monte Cristo Limestone	SR-101	SR-101_R1	101	Wallrock	-0.3	-27.6	Osagean
Monte Cristo Limestone	SR-101	SR-101_R2	101	Wallrock	-1.4	-25.1	Osagean
Monte Cristo Limestone	SR-101	SR-101_R3	101	Wallrock	-0.5	-27.3	Osagean
Monte Cristo Limestone	SR-101	SR-101_R4	101	Wallrock	-1.0	-28.6	Osagean
Monte Cristo Limestone	SR-101	SR-101_R5	101	Wallrock	-0.43	-25.92	Osagean
Monte Cristo Limestone	SR-101	SR-101_R6	101	Wallrock	-0.51	-26.53	Osagean
Monte Cristo Limestone	SR-101	SR-101_R7	101	Wallrock	-1.03	-28.37	Osagean
Monte Cristo Limestone	SR-101	SR-101_R8	101	Wallrock	-0.82	-26.44	Osagean
Monte Cristo Limestone	SR-101	SR-101_R9	101	Wallrock	-0.6	-24.5	Osagean
Monte Cristo Limestone	SR-101	SR-101_R10	101	Wallrock	-0.8	-30.2	Osagean
Monte Cristo Limestone	SR-101	SR-101_R11	101	Wallrock	-0.8	-30.0	Osagean
Monte Cristo Limestone	SR-101	SR-101_R12	101	Wallrock	-1.6	-31.8	Osagean
Monte Cristo Limestone	SR-101	SR-101_R13	101	Wallrock	-1.3	-32.0	Osagean
Monte Cristo Limestone	SR-101	SR-101_R14	101	Wallrock	-1.4	-30.5	Osagean
Monte Cristo Limestone	SR-101	SR-101_R15	101	Wallrock	-1.7	-32.0	Osagean
Monte Cristo Limestone	SR-101	SR-101_R16	101	Wallrock	-1.0	-29.4	Osagean
Monte Cristo Limestone	SR-101	SR-101_R17	101	Wallrock	-0.5	-28.9	Osagean
Monte Cristo Limestone	SR-101	SR-101_R18	101	Wallrock	-0.5	-25.4	Osagean
Monte Cristo Limestone	SR-101	SR-101_S1	101	Wallrock	-1.43	-31.40	Osagean
Monte Cristo Limestone	SR-101	SR-101_S2	101	Wallrock	-1.37	-32.22	Osagean
Monte Cristo Limestone	SR-101	SR-101_S3	101	Calcite vein	-2.91	-24.65	Osagean
Monte Cristo Limestone	SR-101	SR-101_S4	101	Calcite vein	-2.63	-28.87	Osagean
Monte Cristo Limestone	SR-101	SR-101_S5	101	Calcite vein	-2.78	-32.83	Osagean
Monte Cristo Limestone	SR-101	SR-101_S6	101	Wallrock	-0.82	-32.41	Osagean
Monte Cristo Limestone	SR-101	SR-101_S7	101	Wallrock	-0.96	-32.73	Osagean

Section 2: Pahranagat Range section, Nevada (GPS location: N 37 23.4', W 115 15.9')

Stratigraphic unit	Sample No.	Points on the Block	Strat. Height, m	Lithology	$\delta^{13}C$ (‰,VPDB)	$\delta^{18}O$(‰, VPDB)	Notice
Joana Limestone	PR-71.5	PR-71.5_V1	71.5	Calcite Vein	2.67	-20.87	Kinderhookian
Joana Limestone	PR-71.5	PR-71.5_V2	71.5	Calcite Vein	2.70	-20.92	Kinderhookian
Joana Limestone	PR-71.5	PR-71.5_V3	71.5	Calcite Vein	2.71	-21.99	Kinderhookian
Joana Limestone	PR-71.5	PR-71.5_V4	71.5	Calcite Vein	2.73	-22.67	Kinderhookian
Joana Limestone	PR-71.5	PR-71.5_V5	71.5	Calcite Vein	2.47	-20.51	Kinderhookian
Joana Limestone	PR-71.5	PR-71.5_V6	71.5	Calcite Vein	2.16	-17.70	Kinderhookian
Joana Limestone	PR-71.5	PR-71.5_V7	71.5	Calcite Vein	2.53	-18.22	Kinderhookian
Joana Limestone	PR-71.5	PR-71.5_V8	71.5	Calcite Vein	2.49	-18.01	Kinderhookian
Joana Limestone	PR-71.5	PR-71.5_V9	71.5	Calcite Vein	2.21	-16.77	Kinderhookian
Joana Limestone	PR-71.5	PR-71.5_V10	71.5	Calcite Vein	0.63	-18.16	Kinderhookian
Joana Limestone	PR-71.5	PR-71.5_V11	71.5	Calcite Vein	0.98	-17.94	Kinderhookian
Joana Limestone	PR-71.5	PR-71.5_V12	71.5	Calcite Vein	2.58	-18.82	Kinderhookian
Joana Limestone	PR-71.5	PR-71.5_V13	71.5	Calcite Vein	2.50	-18.46	Kinderhookian
Joana Limestone	PR-71.5	PR-71.5_V14	71.5	Calcite Vein	2.58	-18.26	Kinderhookian
Joana Limestone	PR-71.5	PR-71.5_V15	71.5	Calcite Vein	2.59	-18.55	Kinderhookian
Joana Limestone	PR-71.5	PR-71.5_V16	71.5	Calcite Vein	2.59	-17.55	Kinderhookian
Joana Limestone	PR-71.5	PR-71.5_V17	71.5	Calcite Vein	1.96	-16.25	Kinderhookian
Joana Limestone	PR-71.5	PR-71.5_V18	71.5	Calcite Vein	2.67	-16.97	Kinderhookian
Joana Limestone	PR-71.5	PR-71.5_V19	71.5	Calcite Vein	2.63	-17.12	Kinderhookian
Joana Limestone	PR-71.5	PR-71.5_V20	71.5	Calcite Vein	2.48	-19.18	Kinderhookian
Joana Limestone	PR-71.5	PR-71.5_R1	71.5	Wallrock	2.49	-10.79	Kinderhookian
Joana Limestone	PR-71.5	PR-71.5_R2	71.5	Wallrock	3.09	-10.05	Kinderhookian
Joana Limestone	PR-71.5	PR-71.5_R3	71.5	Wallrock	3.10	-11.13	Kinderhookian
Joana Limestone	PR-71.5	PR-71.5_R4	71.5	Wallrock	2.80	-11.48	Kinderhookian
Joana Limestone	PR-71.5	PR-71.5_R5	71.5	Wallrock	2.79	-10.90	Kinderhookian
Joana Limestone	PR-71.5	PR-71.5_R6	71.5	Wallrock	2.47	-12.29	Kinderhookian
Joana Limestone	PR-71.5	PR-71.5_R7	71.5	Wallrock	2.59	-12.18	Kinderhookian
Joana Limestone	PR-71.5	PR-71.5_R8	71.5	Wallrock	2.53	-10.10	Kinderhookian
Joana Limestone	PR-71.5	PR-71.5_R9	71.5	Wallrock	2.80	-8.47	Kinderhookian
Joana Limestone	PR-71.5	PR-71.5_R10	71.5	Wallrock	2.71	-8.93	Kinderhookian
Joana Limestone	PR-71.5	PR-71.5_R11	71.5	Wallrock	2.97	-10.02	Kinderhookian
Joana Limestone	PR-71.5	PR-71.5_R12	71.5	Wallrock	2.77	-10.22	Kinderhookian
Joana Limestone	PR-71.5	PR-71.5_R13	71.5	Wallrock	2.64	-11.94	Kinderhookian
Joana Limestone	PR-71.5	PR-71.5_R14	71.5	Wallrock	2.68	-11.08	Kinderhookian
Joana Limestone	PR-71.5	PR-71.5_R15	71.5	Wallrock	2.79	-10.99	Kinderhookian
Joana Limestone	PR-71.5	PR-71.5_R16	71.5	Wallrock	2.82	-10.25	Kinderhookian
Joana Limestone	PR-71.5	PR-71.5_R17	71.5	Wallrock	2.90	-9.70	Kinderhookian
Joana Limestone	PR-71.5	PR-71.5_S1	71.5	Wallrock	2.71	-11.67	Kinderhookian
Joana Limestone	PR-71.5	PR-71.5_S2	71.5	Calcite Vein	2.67	-20.64	Kinderhookian
Joana Limestone	PR-71.5	PR-71.5_S3	71.5	Calcite Vein	2.69	-21.97	Kinderhookian
Joana Limestone	PR-71.5	PR-71.5_S4	71.5	Calcite Vein	2.48	-22.27	Kinderhookian
Joana Limestone	PR-71.5	PR-71.5_S5	71.5	Calcite Vein	2.56	-20.73	Kinderhookian
Joana Limestone	PR-71.5	PR-71.5_S6	71.5	Wallrock	2.48	-13.57	Kinderhookian

Table 2A. REE contents of calcite veins and bulk rocks from Early Mississippian carbonates

Sample No.	Mineral/rock	Sc	La	Ce	Pr	Nd	Sm	Eu	Gd	Tb	Dy	Y	Ho	Er	Tm	Yb
SR-54_M4	Matrix	0.57	0.72	1.08	0.13	0.59	0.11	0.02	0.14	0.00	0.13	1.74	0.01	0.09	0.00	0.07
SR-54_C3	Peloidal grainstone clast	0.14	0.28	0.06	0.01	0.11	0.01	0.00	0.02	0.00	0.04	0.95	0.00	0.02	0.00	0.02
SR-54_C11	Peloidal grainstone clast	0.12	0.30	0.07	0.02	0.14	0.01	0.00	0.03	0.00	0.04	0.93	0.00	0.02	0.00	0.02
SR-54_M5	Matrix	0.19	1.49	0.30	0.03	0.14	0.02	0.00	0.02	0.00	0.01	1.16	0.00	0.00	0.00	0.00
SR-54_M7	Matrix	0.22	2.58	0.62	0.27	1.18	0.19	0.04	0.28	0.02	0.28	4.53	0.05	0.21	0.01	0.15
SR-54_C7	Peloidal grainstone clast	0.38	7.99	2.42	0.86	3.33	0.49	0.13	0.68	0.08	0.67	10.43	0.16	0.54	0.07	0.47
SR-101_S1	Wackestone	0.36	1.20	1.19	0.14	0.61	0.11	0.01	0.13	0.00	0.11	1.71	0.00	0.07	0.00	0.04
SR-101_V1	Calcite vein	0.91	1.53	1.68	0.21	0.93	0.19	0.02	0.24	0.00	0.24	2.89	0.02	0.14	0.00	0.11
SR-101_R5	Wackestone	0.68	0.90	1.36	0.18	0.77	0.15	0.02	0.18	0.00	0.20	2.40	0.02	0.12	0.00	0.09
SR-101_V16	Calcite vein	0.21	5.52	1.53	0.47	1.70	0.21	0.10	0.28	0.01	0.24	4.58	0.04	0.16	0.00	0.10
SR-101_R14	Wackestone	0.09	0.25	0.06	0.02	0.10	0.01	0.00	0.02	0.00	0.02	0.73	0.00	0.02	0.00	0.02
PR-71.5_V19	Calcite vein	0.24	4.92	1.43	0.51	1.89	0.28	0.06	0.39	0.04	0.38	5.90	0.08	0.32	0.03	0.28
PR-71.5_V1	Calcite vein	0.44	5.53	1.77	0.64	2.74	0.47	0.11	0.68	0.08	0.74	11.92	0.17	0.58	0.06	0.44
PR-71.5_R1	Wackestone	0.15	2.32	0.68	0.21	0.82	0.11	0.05	0.18	0.01	0.16	3.28	0.02	0.11	0.00	0.08
PR-71.5_V13	Calcite vein	0.76	1.50	2.16	0.26	1.12	0.18	0.02	0.24	0.00	0.20	2.72	0.00	0.12	0.00	0.10
PR-71.5_R12	Wackestone	0.22	2.49	0.71	0.29	1.25	0.22	0.05	0.34	0.03	0.34	5.34	0.07	0.25	0.02	0.17
PR-71.5_V15	Calcite vein	0.36	5.79	1.75	0.64	2.41	0.37	0.08	0.53	0.06	0.52	7.94	0.12	0.44	0.05	0.36

Lu	Sum REE	La/La*	Y/Ho	Eu/Eu*	Gd/Gd*	Pr/Pr*	Ce/Ce*
0.00	3.10	2.84	142.26	1.10	3.58	0.91	1.18
0.00	0.57	0.57	-3.70	0.00	10.52	0.77	1.01
0.00	0.66	-3.79		0.00	9.54	0.85	0.75
0.00	2.01	35.00		0.17	3.54	0.80	1.57
0.01	5.90	4.27	82.52	1.08	1.98	1.34	0.32
0.07	17.94	2.54	67.28	1.28	1.50	1.44	0.33
0.00	3.62	3.24	603.96	1.05	4.54	0.94	1.12
0.00	5.33	3.23	121.26	0.85	4.02	0.94	1.10
0.00	3.99	2.11	119.80	1.15	3.79	0.96	1.05
0.00	10.36	2.85	124.91	2.96	2.53	1.45	0.37
0.00	0.53	-11.33		0.00	10.16	0.97	0.68
0.03	10.64	2.47	70.52	1.03	1.73	1.48	0.33
0.04	14.04	3.20	70.76	1.10	1.48	1.34	0.36
0.00	4.77	2.94	135.70	2.96	3.06	1.41	0.38
0.00	5.90	2.19	562.89	1.05	4.87	0.95	1.10
0.02	6.25	3.62	75.62	1.04	1.73	1.34	0.34
0.04	13.15	2.38	63.92	1.11	1.57	1.47	0.32

Table 2B. Trace element contents of calcite veins and bulk rocks from Early Mississippian carbonates

Sample No.	Mineral/rock	P	Zn	Sr	Mo	Ba	Th	U
SR-54_M4	Matrix	0.46	9.32	164.94	0.04	3.01	0.02	0.23
SR-54_C3	Peloidal grainstone clast	10.01	2.44	507.56	0.03	2.29	0.00	0.05
SR-54_C11	Peloidal grainstone clast	26.95	3.76	327.38	0.02	2.18	0.16	0.15
SR-54_M5	Matrix	0.67	2.73	264.22	0.01	4.22	0.00	0.10
SR-54_M7	Matrix	352.98	8.08	680.46	0.01	7.72	0.00	0.41
SR-54_C7	Peloidal grainstone clast	259.64	25.72	223.71	0.04	5.15	0.03	0.44
SR-101_S1	Wackestone	48.68	8.33	272.33	0.04	4.27	0.02	0.56
SR-101_V1	Calcite vein	10.28	7.68	312.89	0.08	5.03	0.03	0.55
SR-101_R5	Wackestone	29.34	4.56	259.32	0.05	3.67	0.00	0.44
SR-101_V16	Calcite vein	21.64	17.99	351.21	0.02	3.22	0.00	0.09
SR-101_R14	Wackestone	62.79	3.43	331.60	0.03	2.88	0.00	0.06
PR-71.5_V19	Calcite vein	180.84	14.45	89.67	0.04	6.19	0.00	0.38
PR-71.5_V1	Calcite vein	654.40	14.62	1150.61	0.04	15.13	0.00	1.09
PR-71.5_R1	Wackestone	67.76	18.79	233.33	0.03	1.59	0.00	0.05
PR-71.5_V13	Calcite vein	44.23	11.55	428.67	0.07	6.40	0.09	1.09
PR-71.5_R12	Wackestone	902.23	7.72	667.79	0.02	7.68	0.00	0.91
PR-71.5_V15	Calcite vein	234.68	20.99	175.12	0.01	5.66	0.03	0.48

Table 2C. Major element contents of calcite veins and bulk rocks from Early Mississippian carbonates

Sample No.	Mineral/rock	Mg	Al	Ca	Mn	Fe	Sr	Mg/Ca
SR-54_M4	Matrix	5150.82	271.41	263399.32	29.37	284.08	167.44	0.02
SR-54_C3	Peloidal grainstone clast	1742.45	53.83	228407.57	29.53	287.91	503.32	0.01
SR-54_C11	Peloidal grainstone clast	857.88	33.31	119893.10	20.91	262.26	212.07	0.01
SR-54_M5	Matrix	2787.27	60.78	263255.65	29.69	119.84	234.61	0.01
SR-54_M7	Matrix	1991.08	38.95	206486.50	26.57	102.34	490.11	0.01
SR-54_C7	Peloidal grainstone clast	2915.25	460.32	247653.55	163.66	240.88	195.71	0.01
SR-101_S1	Wackestone	3810.85	174.78	292619.64	28.80	290.39	230.65	0.01
SR-101_V1	Calcite vein	9053.84	426.71	383637.96	39.40	451.48	246.86	0.02
SR-101_R5	Wackestone	8681.43	231.52	377099.39	36.80	440.64	229.50	0.02
SR-101_V16	Calcite vein	2033.17	134.03	202073.06	273.84	484.25	301.70	0.01
SR-101_R14	Wackestone	929.83	24.12	124983.23	20.44	131.10	277.89	0.01
PR-71.5_V19	Calcite vein	26873.73	160.22	165980.30	93.62	236.97	80.68	0.16
PR-71.5_V1	Calcite vein	4107.65	217.24	425076.05	58.46	920.78	1070.85	0.01
PR-71.5_R1	Wackestone	1841.29	41.54	193988.92	364.22	114.72	205.54	0.01
PR-71.5_V13	Calcite vein	6410.33	480.69	474649.72	48.50	413.06	362.11	0.01
PR-71.5_R12	Wackestone	2180.34	64.62	230504.45	29.75	86.39	588.95	0.01
PR-71.5_V15	Calcite vein	30281.11	300.77	228648.77	181.61	628.41	149.35	0.13

Table 3. Fluid inclusion data from calcite veins in the Early Mississippian carbonates.

Sample No	Minerals	No. of inclusions	Th (°C)	Tm_{ice} (°C)	Average, Tm_{ice}	Salinity (wt.% Nacl)	$\delta^{18}O_{carb}$ (‰)	Sampling points
SR-101-K1	Calcite vein	1	172-172.5	0.3-0.4	0.35	0.62	-32.8	V2
SR-101-K1	Calcite vein	2		0.5-0.6	0.55	0.97	-32.8	V2
SR-101-K1	Calcite vein	2		0.4-0.5	0.45	0.79	-32.8	V2
SR-101-K1	Calcite vein	3	172-174.5	0.4-0.5	0.45	0.79	-32.8	V2
SR-101-K1	Calcite vein	1	170-173	0.2-0.3	0.25	0.44	-32.8	V2
SR-101-K1	Calcite vein	1		0.5-0.6	0.55	0.97	-32.8	V2
SR-101-K1	Calcite vein	1		0.3-0.4	0.35	0.62	-32.8	V2
SR-101-K1	Calcite vein	2		0.6-0.7	0.65	1.14	-32.8	V2
SR-101-K1	Calcite vein	2		0.5-0.6	0.55	0.97	-33.88	V5 and V5a
SR-101-K3	Calcite vein	1		0.2-0.3	0.25	0.44	-33.88	V5 and V5a
SR-101-K3	Calcite vein	1	170-175	0-0.2	0.1	0.18	-33.88	V5 and V5a
SR-101-K3	Calcite vein	1	165-170	0-0.2	0.1	0.18	-33.88	V5 and V5a
SR-101-K3	Calcite vein	1		0.6-0.7	0.65	1.14	-33.88	V5 and V5a
SR-101-K3	Calcite vein	1	160-165	0.4-0.6	0.45	0.79	-33.88	V5 and V5a
SR-101-K3	Calcite vein	1		0.4-0.6	0.45	0.79	-33.88	V5 and V5a
SR-101-K3	Calcite vein	1		0.2-0.4	0.25	0.44	-33.88	V5 and V5a
SR-101-K3	Calcite vein	1	165-170	0.4-0.6	0.45	0.79	-33.88	V5 and V5a
SR-101-K3	Calcite vein	1	165-170	0-0.2	0.1	0.18	-33.88	V5 and V5a
SR-101-K3	Calcite vein	2	165-170	0.6-0.7	0.65	1.14	-33.88	V5 and V5a
SR-101-K3	Calcite vein	1	160-165	0.6-0.7	0.65	1.14	-33.88	V5 and V5a
SR-101-K3	Calcite vein	1	170-175	0.6-0.7	0.65	1.14	-33.88	V5 and V5a
SR-101-K3	Calcite vein	1	>175	0.5-0.7	0.6	1.05	-33.88	V5 and V5a
SR-101-K3	Calcite vein	1	160-165	0.6-0.7	0.65	1.14	-33.88	V5 and V5a
SR-101-K3	Calcite vein	1	150-155	0.6-0.8	0.7	1.22	-33.88	V5 and V5a
SR-101-K3	Calcite vein	1	170-175	0.6-0.8	0.7	1.22	-33.88	V5 and V5a
SR-101-K3	Calcite vein	2	155-160	0.8-0.9	0.85	1.48	-33.88	V5 and V5a
SR-101-K3	Calcite vein	1	170-175	0.8-0.9	0.85	1.48	-33.88	V5 and V5a
SR-101-K3	Calcite vein	1	>180	0.4-0.6	0.5	0.88	-33.88	V5 and V5a
PR-71.5-P1	Calcite vein	1	105-110	5-5.2	5.1	8.00	-20.92	V2

Th = minimum homonization temperature

Tm_{ice} = ice melting temperature = ø

Salinity (Wt. %) = $0.00 + 1.78\ ø - 0.0442\ ø^2 + 0.000557\ ø^3$

7. References

Allan, J.R., and Matthews, R.K., 1982. Isotope signatures associated with early meteoric diagenesis. Sedimentology 29, 797-817.

Allen, D.E., Seyfried Jr., W.E., 2005. REE controls in ultramafic hosted MOR hydrothermal systems: An experimental study at elevated temperature and pressure. Geochimica et Cosmochimica Acta 69, 675-683.

Bau, M., 1996. Controls on the fractionation of isovalent trace elements in magmatic and aqueous systems: evidence from Y/Ho, Zr/Hf, and lanthanide tetrad effect. Contributions to Mineralogy and Petrology 123, 323-333.

Bau, M., 1991. Rare-earth element mobility during hydrothermal and metamorphic fluid-rock interaction and the significance of the oxidation state of europium. Chemical Geology 93, 219-230.

Bau, M., Balan, S., Schmidt, K., Koschinsky, A., 2010. Rare earth elements in mussel shells of the Mytilidae family as tracers for hidden and fossil high-temperature hydrothermal systems. Earth and Planetary Science Letters 299, 310-316.

Bau, M., Dulski, P., 1996. Distribution of yttrium and rare-earth elements in the Penge and Kuruman iron-formations, Transvaal Supergroup, South Africa. Precambrian Research 79, 37-55.

Bindeman, I.N., Serebryakov, N.S., 2011. Geology, Petrology and O and H isotope geochemistry of remarkably ^{18}O depleted Paleoproterozoic rocks of the Belomorian Belt, Karelia, Russia, attributed to global glaciation 2.4 Ga. Earth and Planetary Science Letters 306, 163-174.

Blattner, P., Grindley, G., Adams, C., 1997. Low-^{18}O terranes tracking Mesozoic polar climates in the South Pacific. Geochimica et Cosmochimica Acta 61, 569-576.

Bowen, G.J., Wilkinson, B., 2002. Spatial distribution of $\delta^{18}O$ in meteoric precipitation. Geology 30, 315-318.

Buggisch, W., Joachimski, M.M., Sevastopulo, G., Morrow, J.R., 2008. Mississippian $\delta^{13}C_{carb}$ and conodont apatite $\delta^{18}O$ records — Their relation to the Late Palaeozoic Glaciation. Palaeogeography, Palaeoclimatology, Palaeoecology 268, 273-292.

Byrne, R.H., Liu, X., Schijf, J., 1996. The influence of phosphate coprecipitation on rare earth distributions in natural waters. Geochimica et Cosmochimica Acta 60, 3341-3346.

Cai, C., Li, K., Li, H., Zhang, B., 2008. Evidence for cross formational hot brine flow from integrated $^{87}Sr/^{86}Sr$, REE and fluid inclusions of the Ordovician veins in Central Tarim, China. Applied Geochemistry 23, 2226-2235.

Criss, R.E., Taylor Jr, H.P., 1986. Meteoric-hydrothermal systems. Reviews in Mineralogy 16, 373-424.

Dallai, L., Ghezzo, C., Longinelli, A., 2001. Fossil hydrothermal systems tracking Eocene climate change in Antarctica. Geology 29, 931-934.

Derry, L.A., Jacobsen, S.B., 1990. The chemical evolution of Precambrian seawater: Evidence from REEs in banded iron formations. Geochimica et Cosmochimica Acta 54, 2965-2977.

Epstein, S., Mayeda, T., 1953. Variation of O^{18} content of waters from natural sources. Geochimica et Cosmochimica Acta 4, 213-224.

Epstein, S., Buchsbaum, R., Lowenstam, H.A., Urey, H.C., 1953. Revised carbonate-water isotopic temperature scale. Geological Society of America Bulletin 64, 1315-1326.

Faure, G., Hoefs, J., Jones, L.M., Curtis, J.B., Pride, D.E., 1988. Extreme ^{18}O depletion in calcite and chert clasts from the Elephant Moraine on the East Antarctic ice sheet. Nature 332, 352-354.

Feng, D., Chen, D., Peckmann, J., 2009. Rare earth elements in seep carbonates as tracers of variable redox conditions at ancient hydrocarbon seeps. Terra Nova 21, 49-56.

Feng, D., Chen, D., Peckmann, J., Bohrmann, G., 2010. Authigenic carbonates from methane seeps of the northern Congo fan: Microbial formation mechanism. Marine and Petroleum Geology 27, 748-756.

Fielding, C.R., Frank, T.D., Birgenheier, L.P., Rygel, M.C., Jones, A.T., Roberts, J., 2008. Stratigraphic record and facies associations of the late Paleozoic ice age in Eastern

Australia (New South Wales and Queensland), in: Fielding, C.R., Frank, T.D., Isbell, J.L. (Eds.), Resolving the Late Paleozoic Ice Age in Time and Space. Geological Society of America Special Paper 441, pp. 41–57.

Franchi, F., Hofmann, A., Cavalazzi, B., Wilson, A., Barbieri, R., 2015. Differentiating marine vs hydrothermal processes in Devonian carbonate mounds using rare earth elements (Kess Kess mounds, Anti-Atlas, Morocco). Chemical Geology 409, 69-86.

German, C.R., Elderfield, H., 1990. Application of the Ce anomaly as a paleoredox indicator: the ground rules. Paleoceanography 5, 823-833.

Gianelli, G., Ruggieri, G., Mussi, M., 1997. Isotopic and fluid inclusion study of hydrothermal and metamorphic carbonates in the Larderello geothermal field and surrounding areas, Italy. Geothermics 26, 393-417.

Giles, K.A., 1996. Tectonically forced retrogradation of the lower Mississippian Joana Limestone, Nevada and Utah, in: Longman, M.W., Sonnenfeld, M.D. (Eds), Paleozoic systems of the Rocky Mountain region. Rocky Mountain Section, Society for Sedimentary Geology, pp. 145-164.

Giles, K.A., Dickinson, W.R., 1995. The interplay of eustasy and lithospheric flexure in forming stratigraphic sequences in foreland settings: An example from the Antler foreland, Nevada and Utah, in: Dorobek, S.L., Ross, G.M. (Eds), Stratigraphic Evolution of Foreland Basin. Society for Sedimentary Geology Special Publication 52, pp. 187-211.

Goldstein, R.H., Reynolds, T.J., 1994. Systematics of fluid inclusions in diagenetic minerals: SEPM Short Course 31. Society for Sedimentary Geology 199.

Harbaugh, D.W., Dickinson, W.R., 1981. Depositional facies of Mississippian clastics, Antler foreland basin, central Diamond Mountains, Nevada. Journal of Sedimentary Research 51, 1223-1234.

Herwartz, D., Pack, A., Krylov, D., Xiao, Y., Muehlenbachs, K., Sengupta, S., Di Rocco, T., 2015. Revealing the climate of snowball Earth from $\delta^{17}O$ systematics of hydrothermal rocks. Proceedings of the National Academy of Sciences of the United States of America 112, 5337-5341.

Jacobsen, S.B., Kaufman, A.J., 1999. The Sr, C and O isotopic evolution of Neoproterozoic seawater. Chemical Geology 161, 37-57.

Jaffrés, J.B.D., Shields, G.A., Wallmann, K., 2007. The oxygen isotope evolution of seawater: A critical review of a long-standing controversy and an improved geological water cycle model for the past 3.4 billion years. Earth-Science Reviews 83, 83-122.

Jaguin, J., Boulvais, P., Boiron, M., Poujol, M., Gapais, D., Ruffet, G., Briant, N., 2014. Stable isotopes (O, C) and fluid inclusion study of quartz-carbonate veins from the antimony line, Murchison Greenstone Belt. American Journal of Science 314, 1140-1170.

Jakubowicz, M., Dopieralska, J., Belka, Z., 2015. Tracing the composition and origin of fluids at an ancient hydrocarbon seep (Hollard Mound, Middle Devonian, Morocco): A Nd, REE and stable isotope study. Geochimica et Cosmochimica Acta 156, 50-74.

Katz, D.A., Eberli, G.P., Swart, P.K., Smith Jr, L.B., 2006. Tectonic-hydrothermal brecciation associated with calcite precipitation and permeability destruction in Mississippian carbonate reservoirs, Montana and Wyoming. American Association of Petroleum Geologist Bulletin 90, 1803-1841.

Lawrence, M.G., Greig, A., Collerson, K.D., Kamber, B.S., 2006. Rare earth element and yttrium variability in South East Queensland waterways. Aquatic Geochemistry 12, 39-72.

Li, D., Chen, H., Zhang, L., Hollings, P., Chen, Y., Lu, W., Zheng, Y., Wang, C., Fang, J., Chen, G., 2016. Ore geology and fluid evolution of the giant Caixiashan carbonate-hosted Zn–Pb deposit in the Eastern Tianshan, NW China. Ore Geology Reviews 72, 355-372.

Machel, H.G., Krouse, H.R., Sassen, R., 1995. Products and distinguishing criteria of bacterial and thermochemical sulfate reduction. Applied Geochemistry 10, 373-389.

Mathieu, J., Kontak, D., Turner, E., Fayek, M., Layne, G., 2015. Geochemistry of Phanerozoic diagenesis on Victoria Island, NWT, Canada. Chemical Geology 415, 47-69.

Middleton, A.W., Uysal, I.T., Golding, S.D., Förster, H., Allen, C.M., Feng, Y., Rhede, D., Marshall, V.J., van Zyl, J., 2014. Geochronological (U–Pb, U–Th–total Pb, Sm–Nd) and geochemical (REE, $^{87}Sr/^{86}Sr$, $\delta^{18}O$, $\delta^{13}C$) tracing of intraplate tectonism and associated fluid flow in the Warburton Basin, Australia. Contributions to Mineralogy and Petrology 168, 1-22.

Mii, H., Grossman, E.L., Yancey, T.E., 1999. Carboniferous isotope stratigraphies of North America: Implications for Carboniferous paleoceanography and Mississippian glaciation. Geological Society of America Bulletin 111, 960-973.

Murray, R.W., Brink, M.T.B.T., Gerlach, D.C., Russ III, G.P., Jones, D.L., 1991. Rare earth, major, and trace elements in chert from the Franciscan Complex and Monterey Group, California: Assessing REE sources to fine-grained marine sediments. Geochimica et Cosmochimica Acta 55, 1875-1895.

Nothdurft, L.D., Webb, G.E., Kamber, B.S., 2004. Rare earth element geochemistry of Late Devonian reefal carbonates, Canning Basin, Western Australia: confirmation of a

seawater REE proxy in ancient limestones. Geochimica et Cosmochimica Acta 68, 263-283.

Olivier, N., Boyet, M., 2006. Rare earth and trace elements of microbialites in Upper Jurassic coral- and sponge-microbialite reefs. Chemical Geology 230, 105-123.

O'Neil, J.R., Clayton, R.N., Mayeda, T.K., 1969. Oxygen isotope fractionation in divalent metal carbonates. The Journal of chemical Physics 51, 5547-5558.

Poole, F.G., Sandberg, C.A., 1991. Mississippian paleogeography and conodont biostratigraphy of the western United States, in: Cooper, J.D., Stevens, G.H. (Eds.), Paleozoic Paleogeography of the Western United States. Pacific Section, Society of Economic Paleontologists and Mineralogists Special Publication 42, pp. 109–124.

Reynard, B., Lécuyer, C., Grandjean, P., 1999. Crystal-chemical controls on rare-earth element concentrations in fossil biogenic apatites and implications for paleoenvironmental reconstructions. Chemical Geology 155, 233-241.

Rongemaille, E., Bayon, G., Pierre, C., Bollinger, C., Chu, N., Fouquet, Y., Riboulot, V., Voisset, M., 2011. Rare earth elements in cold seep carbonates from the Niger delta. Chemical Geology 286, 196-206.

Sando, W., 1976. Mississippian history of northern Rocky Mountains region. Journal of Research of the United States Geological Survey 4, 317-338.

Shields, G.A., Webb, G.E., 2004. Has the REE composition of seawater changed over geological time? Chemical Geology 204, 103-107.

Simmons, S.F., Christenson, B.W., 1994. Origins of calcite in a boiling geothermal system. American Journal of Science 294, 361-400.

Smith, M.T., Dickinson, W.R., Gehrels, G.E., 1993. Contractional nature of Devonian-Mississippian Antler tectonism along the North American continental margin. Geology 21, 21-24.

Soreghan, G.S., Soreghan, M.J., Poulsen, C.J., Young, R.A., Eble, C.F., Sweet, D.E., Davogustto, O.C., 2008. Anomalous cold in the Pangaean tropics. Geology 36, 659-662.

Speed, R., Sleep, N., 1982. Antler orogeny and foreland basin: A model. Geological Society of America Bulletin 93, 815-828.

Sverjensky, D.A., 1984. Europium redox equilibria in aqueous solution. Earth and Planetary Science Letters 67, 70-78.

Taylor, S.R., McLennan, S.M., 1985. The continental crust: its composition and evolution. United States, Blackwell Scientific Publications, 138 p.

Wallace, M.W., Hood, A.v., Shuster, A., Greig, A., Planavsky, N.J., Reed, C.P., 2017. Oxygenation history of the Neoproterozoic to early Phanerozoic and the rise of land plants. Earth and Planetary Science Letters 466, 12-19.

Wang, W., Zhou, C., Guan, C., Yuan, X., Chen, Z., Wan, B., 2014. An integrated carbon, oxygen, and strontium isotopic studies of the Lantian Formation in South China with implications for the Shuram anomaly. Chemical Geology 373, 10-26.

Webb, G.E., Kamber, B.S., 2000. Rare earth elements in Holocene reefal microbialites: a new shallow seawater proxy. Geochimica et Cosmochimica Acta 64, 1557-1565.

Zhao, Y., Zheng, Y., 2015. Geochemistry of vein and wallrock carbonates from the Ediacaran system in South China: Insights into the origins of depositional and post-depositional fluids. Chemical Geology 404, 71-87.

Zhao, Y., Zheng, Y., 2010. Stable isotope evidence for involvement of deglacial meltwater in Ediacaran carbonates in South China. Chemical Geology 271, 86-100.

Zhao, Y., Zheng, Y., Chen, F., 2009. Trace element and strontium isotope constraints on sedimentary environment of Ediacaran carbonates in southern Anhui, South China. Chemical Geology 265, 345-362.

Dev K Maharjan

Department of Geoscience
University of Nevada Las Vegas, Las Vegas, NV 89154-4010
Email: devkmaharjan@gmail.com
Phone: (702) 285-8408 (Cell), Fax: (702) 895-4064

EDUCATION

Ph.D., *Current*	**Department of Geoscience, University of Nevada Las Vegas (UNLV)**
	Expected graduation-Spring 2017
	Environmental changes across the Early Mississippian carbon isotope excursion
M.S., 2010	**School of Geosciences, University of Louisiana at Lafayette**
	Climate signals in Lake Sediments, East African rift valley
M.Sc., 2001	**Central Department of Geology, Tribhuvan University, Kiritipur, Kathmandu, Nepal**
	Quality of siltstones for concrete aggregate
B.Sc., 1999	**Trichandra College, Tribhuvan University, Kathmandu, Nepal**
	Geological mapping of Tansen Group, Western Nepal

EMPLOYMENT

2016	Teaching Assistant of GEOG 104, Department of Geoscience, UNLV
2015	Research Assistant, Department of Geoscience, UNLV
2010-2014	Teaching Assistant of GEOL 101/GEOG 104, Department of Geoscience, UNLV
2008-2010	Research Assistant, School of Geosciences, University of Louisiana at Lafayette
2006-2007	Assistant Lecturer, Department of Environment Science, Patan Multiple Campus, Nepal
2005-2007	Lecturer, Department of Environment Science, Bishwa Niketan Science Campus, Nepal
2002-2005	Teacher, Part time teacher at several High schools in Kathmandu.

RESEARCH AWARDS:

2016	Bernada French Scholarship, UNLV
2014	Edwards and Olswang Scholarship, UNLV
2014	Bernada French Scholarship, UNLV
2013-2014	The Graduate Professional Student Association (GPSA), UNLV
2011	The Nevada Petroleum Society Graduate Student Research Awards in Geosciences
2011	Bernada French Scholarship, UNLV

PUBLICATIONS

Goman, M., Ashley, G.M., Owen, R.B., Hover, V.C., **Maharjan, D.K.**, 2017, Late Holocene environmental reconstruction from Lake Solai, Kenya. The Professional Geographer, DOI: 10.1080/00330124.2016.1266948

Maharjan, D.K., 2010, Elemental and Isotopic Variations in Organic Matter in Wetland and Lake Sediment as Potential Paleoclimate Indicators, Lake Solai Area, East African Rift Valley, Kenya. M.S. Thesis, University of Louisiana Lafayette.

Maharjan D. K., Tamrakar, N.K., 2004, Quality of siltstones for concrete aggregate from Nallu Khola area, Kathmandu, Jour. Nepal Geol. Society, Vol. 30, pp. 167-176.

Sah, R.B., Joshi, G.R., Panday, P.R., Zakaria, A.R., Devkota, B., Yadav, K., **Maharjan, D.K.**, Neupane, N.R., 2003, Geology and mining of cement grade limestone deposit of Sindali, Udayapur, Eastern Nepal, Jour. Stratigraphic Association of Nepal, Vol. 4, pp. 26-31.

ABSTRACTS

Maharjan, D.K., Jiang, G., Peng, Y., 2015, The sulfur cycle across the Early Mississippian positive $\delta^{13}C$ excursion: GSA abstracts with programs Vol. 47, No. 7, p. 126.

Jiang, G., Morales, D., **Maharjan, D.**, 2015, Cerium anomaly across the mid-Tournaisian carbon isotope excursion (TICE). AGU Fall Meeting, Abstract #PP31B-2245.

Hover, V.C, Ashley, G.M, Goman, M.F., **Maharjan, D.K.**, Owen, R.B., Jeremy, S., 2015, Playa lake and marginal wetland sediments record over 1000 years of climate shifts at lake Solai, east African rift, Kenya. GSA abstracts with programs Vol. 47, No. 7, p. 284.

Maharjan, D.K., Jiang, G., Peng, Y., Sahoo, S.K., Henry, R.A., 2014, Coupling organic carbon and nitrogen Isotope with carbonate carbon isotope excursion across the Early Mississippian Kinderhookina-Osagean boundary in Great Basin, Western USA. AGU Fall Meeting, Abstract #PP41A-1337.

Goman, M.F., Ashley, G.M., Owen, R.B., Shilling, A.M., Barboni, D., Hover, V.C., **Maharjan, D.K.**, 2013, The link between little ice age rainfall and modern freshwater wetlands in the east African rift valley. GSA abstracts with programs Vol. 45, No. 7, p. 423.

Goman, M.F., Ashley, G.M., Owen, R.B., Hover, V.C., **Maharjan, D.K.**, 2012, Reconstructed hydrological changes during the little ice age, lake Solai wetlands, Kenya. GSA abstract with programs Vol. 44, No. 7, p. 359.

Taufani, L., **Maharjan, D. K.**, Jiang, G., 2012, Detrital carbonates in a sequence stratigraphic framework: Example from Furongian slope environment in the Hot Creek Range of central Nevada. GSA abstracts with programs Vol. 44, No. 7, p. 223.

Maharjan, D.K., Hover, V.C., Ashley, G.M., Goman, M.F., Owen, R.B., Park, L.E., 2009, Evidence for centennial-scale climate variation recorded by organic matter in a freshwater wetland, lake Solai, Kenya. GSA abstracts with programs Vol. 41, No. 7, p. 143.